ACOUSTICS OF TURBULENT NON-PREMIXED SYNGAS COMBUSTION

Sjoerd Pater

De promotiecommissie is als volgt samengesteld:

Voorzitter en secretaris:	
Prof. Dr. H. Eising	Universiteit Twente
Promotor:	
Prof. Dr. Ir. Th.H. van der Meer	Universiteit Twente
Assistent Promotor:	
Dr. Ir. J.B.W. Kok	Universiteit Twente
Leden:	
Prof. Dr. Ir. A. Hirschberg	Universiteit Twente
Prof. Dr. Ir. A. de Boer	Universiteit Twente
Prof. Dr. Ir. B.J. Geurts	Universiteit Twente
Prof. Dr. L.P.H. de Goey	Technische Universiteit Eindhoven
Dr.-Ing. habil. B.E. Noll	Institut für Verbrennungstechnik, DLR Stuttgart

This research has been performed in the framework of the EU project HEGSA.

Acoustics of turbulent non-premixed syngas combustion
Pater, Sjoerd Gerardus Maria
PhD thesis, University of Twente, Enschede, The Netherlands
November 2007

ISBN 978-90-365-2516-9

Printed by Print Partners Ipskamp

The cover is a photo of Battersea Power Station, South Bank of the River Thames at Battersea, London, taken by Viola Mashoed.

ACOUSTICS OF TURBULENT NON-PREMIXED SYNGAS COMBUSTION

PROEFSCHRIFT

ter verkrijging van
de graad van doctor aan de Universiteit Twente,
op gezag van de rector magnificus,
prof. dr. W.H.M. Zijm,
volgens besluit van het College voor Promoties
in het openbaar te verdedigen
op vrijdag 2 november 2007 om 15.00 uur

door

Sjoerd Gerardus Maria Pater

geboren op 18 november 1977

te Anna Paulowna

Dit proefschrift is goedgekeurd door de promotor

Prof. Dr. Ir. Th.H. van der Meer

en door de assistent promotor

Dr. Ir. J.B.W. Kok

Summary

Coal gasification is one of the options for clean coal technology. Gasification of coal takes place when coal is exposed to superheated steam. During this process, a mixture of hydrogen H_2, carbon monoxide and inert components (usually CO_2 and H_2O) are produced in a carrier flow of nitrogen. This product gas is called syngas, which can be fired in a gas turbine.
The turbulent flame in the combustion chamber of a gas turbine can act as a source of sound. As the syngas is a low calorific gas (the calorific value of syngas is approximately 5 MJ/kg which is a factor of 8 lower than natural gas), the mass flows are high. To prevent a too high pressure drop over the fuel line, the cross-sectional areas of the fuel lines are relatively large. The acoustic field generated by the turbulent syngas flame can induce a fluctuation in the fuel mass flow. These fluctuations are then transported to the flame front and can result in heat release fluctuations. As a result the flame radiates more noise, which is fed back to fuel mass flow fluctuations. The amplitudes of the fluctuations will increase in time and a so-called thermoacoustic instability may occur. During such a thermoacoustic instability the acoustic pressure can become excessively high. Often, already within a minute very serious damage can occur at the burner or other parts of the combustor.
This thesis is written to add insight in the processes that take place during the formation and break down of thermoacoustic instabilities in turbulent syngas combustion. Additional to this, methods are investigated to predict acoustic fields and instabilities during this type of combustion.
First of all, a laboratory scale experimental setup is designed and manufactured. A syngas burner which is designed specifically for this project was built. The setup is used to validate all models that were used. The setup has a nominal thermal power of 100 kW at a pressure of 5 bar. It is equipped with dynamic pressure transducers to measure acoustic pressures. It is also possible to observe the flame with a high speed camera.

To predict acoustic pressures in the combustion chamber, a one dimensional acoustic model is used. One dimensional modelling is sufficiently accurate as the axial component by far is the most important. The temperature gradient in the combustor has a great influence on the generated acoustic field. For this reason, additional attention is paid to this gradient. The results show that the model is capable of predicting the most important elements of the acoustics in the combustion chamber. This model is also applied to identify the acoustic sources of the flame.
Thermoacoustic instabilities are not only related to the acoustics in the combustion chamber. They arise due to a coupling between several processes. Important is the so-called flame transfer function which characterises the coupling between aerodynamics and combustion. This transfer function represents the relation between a perturbation in the fuel mass flow and the response of the flame. To predict this flame transfer function, unsteady CFD simulations are applied. At a certain moment in time, during the simulations, the fuel mass flow is disturbed by an impulse function. The reaction of the flame is monitored by calculating the volume integrated heat release fluctuations of the flame. Using spectral analysis, the frequency dependent flame transfer function can be determined. It appears that the applied method works well within certain limits. The results of the measurements are also cast in a correlation model called the n-τ-model. It is shown that the n-τ-model can be applied to non-premixed flames.
The CFD calculations are carried out with commercially available combustion models as well as with a combustion model that is developed in the research group of Thermal Engineering. This combustion code is called Cfi. The code of Cfi is applied on two set points and produces very good results.
Finally, all models are integrated to predict thermoacoustic instabilities. The one dimensional acoustic model is used as a base for this thermoacoustic model. This model needs the flame transfer function as input. It is not possible to predict acoustic pressures with this model, but it can identify frequencies at which instabilities occur. The experimental setup has been unstable only once. The unstable frequency of this set point was predicted within 4%.

Samenvatting

Terwijl de verbranding van steenkool in Europa steeds minder voorkomt, neemt de vergassing van steenkool toe in populariteit. Vergassing van steenkool gebeurt door oververhitte stoom te leiden over steenkool. Bij dit proces ontstaat een mengsel van waterstof (H_2), koolstofmono-oxide (CO) en inerte componenten (meestal koolstofdioxide CO_2 en H_2O op een dragergas van N_2). Dit productgas wordt synthesegas genoemd. Met een aantal aanpassingen kan een gasturbine gestookt worden op dit synthesegas.
De verbranding van het synthesegas gebeurt turbulent. De vlam in de verbrandingskamer gedraagt zich hierdoor als geluidsbron. Aangezien het synthesegas een laagcalorisch gas is (ongeveer factor 8 lager dan Groninger aardgas) zijn de massastromen hoog. Om ervoor te zorgen dat de drukval over de brandstofinlaat van de branders niet te groot wordt, zijn de doorsneden van de brandstofinlaten groot. Het akoestische veld dat de turbulente synthesegas vlam genereert kan de brandstofstroom laten fluctueren. Deze fluctuaties worden naar het vlamfront getransporteerd en kunnen de vlam een extra impuls geven om sterker geluid af te stralen. Indien de omstandigheden er naar zijn, kan dit proces zich herhalen. De amplitudes van de fluctuaties zullen opslingeren in tijd en snel zal er een zogenaamde thermo-akoestische instabiliteit zijn ontstaan. Tijdens een dergelijke thermo-akoestische instabiliteit kunnen de akoestische drukken erg hoog oplopen. Zo hoog dat er binnen zeer korte tijd (vaak al binnen de minuut) ernstige schade optreedt aan de brander en andere onderdelen die zich in de nabijheid van de verbrandingkamer begeven.
Dit proefschrift is geschreven om meer inzicht te bieden in de processen die zich afspelen bij het opbouwen en afbreken van thermo-akoestische instabiliteiten bij turbulente synthesegas verbranding. Ook wordt er gekeken naar methoden om geluidsvelden en instabiliteiten te voorspellen bij dit type verbranding.
Als eerste is een ontwerp gemaakt voor een laboratorium opstelling. In deze opstelling zit een synthesegas brander die ook speciaal voor dit project is

ontworpen. Deze opstelling is gebruikt om alle modellen te valideren. De opstelling heeft een thermisch vermogen van 100 kW bij 5 bar. Hij is uitgerust met dynamische druksensoren om akoestische drukken te meten. Ook is het mogelijk om door een venster de vlam met behulp van een snelle camera te bestuderen.
Om de akoestische drukken in de verbrandingskamer van de opstelling te voorspellen is een één-dimensionaal akoestisch model gebruikt. Eén-dimensionaal modelleren is mogelijk omdat voornamelijk de lengterichting in de verbrandingskamer van belang is. De temperatuursgradient in de verbrandingskamer is van grote invloed op het gegenereerde geluidsveld. Daarom is extra aandacht aan deze gradient besteed. Het zal blijken dat het model in staat is de belangrijkste processen van de akoestiek in de verbrandingskamer te voorspellen. Ook wordt het model toegepast om de akoestische bron van de vlam te identificeren.
Thermo-akoetische instabiliteiten ontstaan niet enkel door akoestiek in de verbrandingskamer. Ze ontstaan door een koppeling van meerdere processen. Een belangrijk element is de zogenaamde vlamoverdracht. Deze overdracht geeft de relatie tussen een perturbatie in de massastroom van de brandstof en de reactie van de vlam op deze perturbatie. Om deze vlamoverdracht te kunnen voorspellen wordt gebruik gemaakt van tijdsafhankelijke CFD. Dit wordt gedaan door op een bepaald moment in de simulatie de brandstofstroom te verstoren met een impuls. Vervolgens wordt de reactie van de vlam geregistreerd in de vorm van volume geintegreerde fluctuaties in de warmteafgifte van de vlam. Met spectrale analyse kan de frequentie afhankelijke vlamoverdrachts functie worden bepaald. Uit de resultaten van de metingen blijkt dat deze methode tot op zekere hoogte goed werkt. De resultaten van de metingen zijn gegoten in een correlatie model, het zogenaamde n-τ-model. Dit toont aan dat het n-τ-model ook werkt voor niet voorgemengde vlammen.
De CFD berekeningen zijn uitgevoerd met zowel de beschikbare commerciele verbrandingsmodellen als met een verbrandingsmodel dat in de onderzoeksgroep van Thermische Werktuigbouwkunde is ontwikkeld. Dit verbrandingsmodel heet Cfi. De Cfi code is gebruikt voor twee setpoints en blijkt voor een setpoint zeer mooie resultaten te geven.
Als laatste worden alle modellen geintegreerd tot een model dat thermo-akoestische instabiliteiten kan voorspellen. De basis hiervoor is het eerder genoemde één-dimensionale akoestische model. Verder heeft het model de vlamoverdrachtsfunctie nodig. Dit model is niet in staat om akoestische drukken te voorspellen op instabiele frequenties, maar het kan wel de instabiele frequenties identificeren. De opstelling is eenmaal instabiel geweest. De instabiele frequentie op dit setpoint is binnen 4% voorspeld.

Contents

1
Introduction

1.1 Combustion of fossil fuels

With the invention of the steam-engine it proved to be possible to convert energy from fuel into work. Not directly, but by several steps: combustion leads to heat, heat was transferred to water, water became steam and the high temperature and pressure could drive a machine and produce work. In

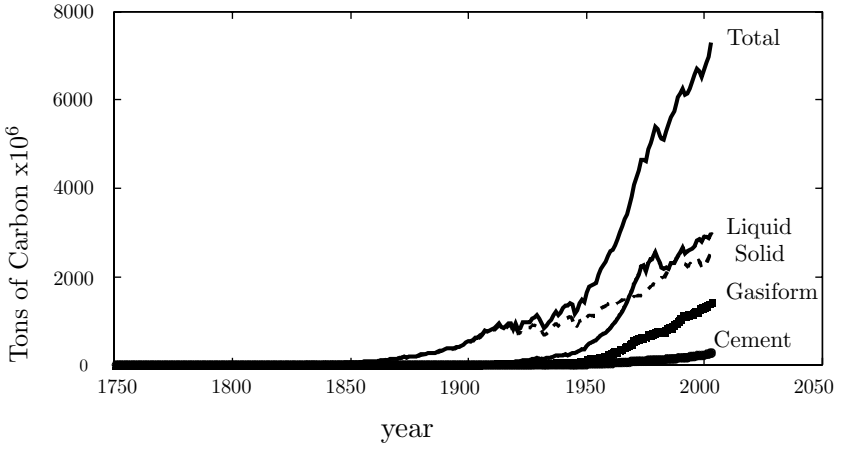

Figure 1.1: Fossil carbon emissions [1].

figure 1.1 a strong increase of carbon emission around 1875 can be noticed. The figure shows that in the last 150 years, the CO_2 emissions have increased tremendously. Contributors of this increase are the steam engine in 1769 and

also the invention of the Otto (1854) and Diesel (1892) engine at the end the 19th century. The development of the jet engine and the gas turbine added more efficient generation of power, but also increased the total power consumption significantly. Thanks to these developments, people changed their way of living, improving levels of prosperity.
All these developments made man more and more dependent on fossil fuels. Man could not live anymore at present living conditions without the help of mechanical work. Most of this work is delivered by combustion of fossil fuels. Beside the huge increase in carbon emissions, the natural resources are exploited at a very high pace. Although there is more than enough oil for the next couple of decades, it is clear that the supplies are finite. Figure 1.2 shows some figures, used by the Oil & Gas Journal [1]. It shows the world reserves for oil, gas and coal in Billion Barrels of Oil Equavalents (BBOE), as well as the daily production in Million Barrels of Oil Equivalents (MBOE) and the prediction how long these world reserves will last. The first figure shows that the amount of energy stored in coal reserves is almost five times bigger than the amount of energy stored in oil and gas reserves. Figure 1.2b depicts that the daily production of coal is comparable to the gas production, but significantly smaller than the oil production. The latter figures are considered the most optimistic. It is obvious that the reserve of coal is by far the biggest. While the oil and gas reserves will last around 30 and 70 years respectively, coal will be available for approximately 250 years with the present production. To prevent further environmental problems, like global warming, clean coal technologies are necessary to utilise these huge coal reserves. Coal gasification is one of the options.

1.2 Clean fossil

1.2.1 Syngas

The gas produced in a coal gasification process is called coal gas, town gas, synthetic gas or syngas. In this report the term syngas will be used. Town gas was originally developed in the 1800s and was produced for lighting and cooking. Natural gas and electricity soon replaced town gas for these applications, but the gasification process has been utilised for the production of synthetic chemicals and fuels since the 1920s.
Coal contains more than 50 mass% carbon which is more than 70 volume% (this includes inherent moisture). The carbon content is dependent on coal rank. A coal type with a higher rank contains more carbon and less hydrogen, oxygen and nitrogen, until 95 % purity of carbon is achieved at the Anthracite

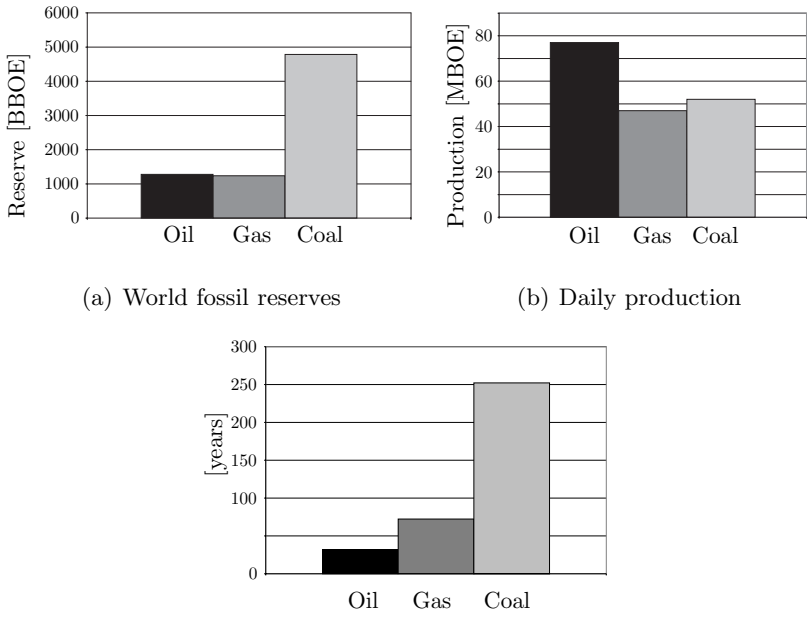

(a) World fossil reserves

(b) Daily production

(c) Years of production left

Figure 1.2: Some figures of the worlds fossil fuel reserves [1].

rank. During gasification of coal, the following global reactions take place:

$$C + O_2 \rightarrow CO_2 \tag{1.1}$$

$$CO_2 + C \rightarrow 2CO \tag{1.2}$$

$$C + H_2O \rightarrow CO + H_2 \tag{1.3}$$

The gasification process occurs as the char reacts with carbon dioxide and steam to produce carbon monoxide and hydrogen. All the advantages of modern gas fired power plants, like combined gas turbine and steam turbine systems, are within reach with this gaseous fuel. These systems have very high high efficiencies. Also, corrosive ash elements such as chloride and potassium may be refined out by the gasification process, allowing high temperature combustion of the gas from otherwise problematic fuels. The high availability of coal makes this an attractive process. The possible application of biomass makes it even more attractive. Biomass is a durable energy source. With the possibility of clean combustion this is also a *clean* energy source. The application of biomass does bring additional challenges. As it is very difficult to

maintain a constant quality of the biomass, the produced gas will change with the input of the gasifier. Using a gas turbine for the conversion of syngas, the whole gas turbine (compressor, burner, combustor and turbine) should be able to cope with the changes in fuel quality. One of the most promising applications of syngas is the so-called IGCC, the Integrated Gasification Combined Cycles.

1.2.2 IGCC

IGCC uses a combined cycle with a gas turbine driven by the combusted syngas, while the heat of the exhaust gases is exchanged with water/steam to generate superheated steam to drive a steam turbine. The IGCC can roughly be divided into three parts: oxygen production, gasification and power production. A high level of integration of these three units is required to achieve a good overall efficiency of the plant. The main features are depicted in figure 1.3. This figure shows the process scheme of the ELCOGAS IGCC in Puertollano in Spain.
The air separation unit (ASU) works at high pressure. The air which is needed

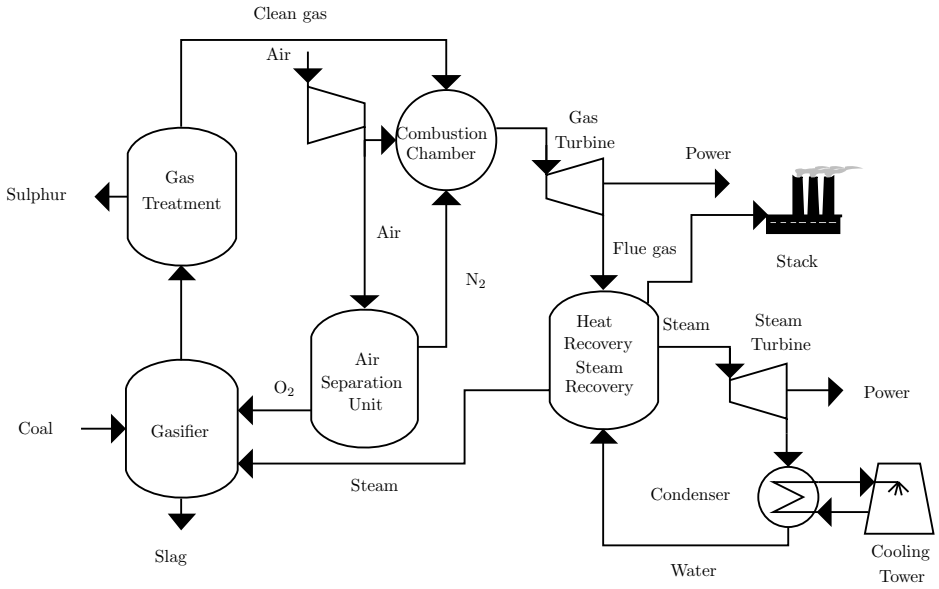

Figure 1.3: Process scheme of the ELCOGAS IGCC in Puertollano, Spain.

for the (ASU) is extracted at the outlet of the compressor of the gas turbine. The waste nitrogen of the ASU is mixed with the clean gas to feed the burner of

the gas turbine. In the gasifier coal gasification takes place in the presence of a controlled 'shortage' of oxygen, thus maintaining reducing conditions (Gasifier in figure 1.3). After cleaning, the syngas produced in the gasifier, it is fed to the combustion chamber. The heat in the air extracted from the compressor is used to heat up the impure nitrogen and the low pressure condensate. A part of this heat is also used to heat the saturated water to produce steam for NO_x control. High pressure and low pressure steam from the gasification unit is further superheated and expanded in the steam turbine of the combined cycle. The exhaust gases of the gas turbine are fed to the Heat Recovery Steam Generator. Here, steam is generated to drive the steam turbine. In Europe three IGCC plants are realised. Puertollano (Spain), Priolo, Sicily (Italy) and Buggenum (The Netherlands). These plants are fed with coal and some also with biomass.
The gas turbine which is installed in the IGCC of Buggenum is a Siemens SGT5-2000E. At the time this gas turbine engine was installed it was called V94.2. A picture of this machine is shown in figure 1.4. This gas turbine combusts syngas in a non-premixed fashion.

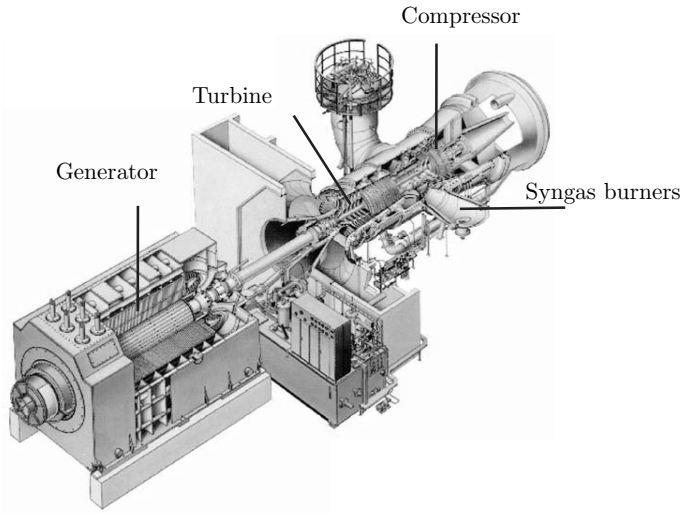

Figure 1.4: The Siemens SGT5-2000E2 Gas Turbine at Buggenum.

1.3 Non-premixed combustion

This thesis will focus on non-premixed combustion of syngas and the processes involved. During non-premixed combustion the fuel and the oxydiser are sup-

plied separately to the combustor. Mixing by (turbulent diffusion) has to take place in the combustion chamber before combustion can occur. For that reason, non-premixed combustion is also called diffusion combustion. Contrary to premixed combustion, when fuel and air are mixed before entering the combustion chamber. As mixing has not yet occurred in diffusion flame type combustors it is one of the main phenomena to be modelled. In figure 1.5 the structure of a (laminar) diffusion flame is presented. With the help of this figure, some general remarks about diffusion flames can be made [2]. Fuel is fed from the left hand side and air from the right. At the interface between fuel and air, mixing takes place by diffusion. As can be seen from figure 1.5, the mixture is combustible in a limited range of fuel and oxydiser mass fractions. This range is limited at the left hand side by the rich limit (too much fuel) and the right hand side by the lean limit (too much air). The stoichiometric mixture lies in between these limits. At this point, fuel and air are mixed in the exact molar ratio for complete combustion, leaving no excess oxygen. So at this point, the highest temperatures can be expected.
A diffusion flame does not have a flame speed as can be defined for premixed combustion. The reason for this is because the flame does not propagate in the opposite direction of one of the flows. For this reason, diffusion flames are more sensitive to velocity perturbations [2].
In diffusion flames the flame thickness can take a wide range of values. The stretching of the flame is a main parameter for the flame thickness. In premixed combustion, the flame thickness can be be coupled to flame speed and fluid properties.
Diffusion flames are very safe as they do not propagate. For this reason they are relevant in industrial applications.

1.4 Acoustics in combustion

1.4.1 Criterion of Rayleigh

A lot of different mechanisms play a role in producing sound and the coupling with the acoustic environment. As already mentioned, there is a difference between autonomous noise and coupled acoustics.

In case of autonomous noise, the flame acts as an acoustic source and does not couple with the acoustic domain. As the combustion process is dominated by turbulent mixing, so is the acoustic source [3]. Noise basically arises from pressure fluctuations due to unsteady heat release and is therefore strongly dependent on the structure of eddies in the mixing region. But the noise not

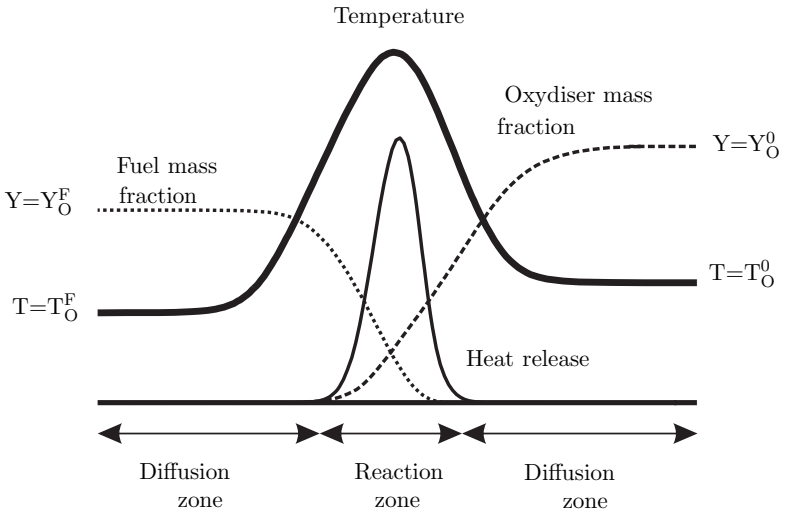

Figure 1.5: Diffusion flame structure

only arises from the mixing, also from the fluctuation in the flame surface area during combustion [4]. Lefebvre [5] distinguishes direct noise (induced by the combustion process) and indirect noise (produced by the flow of hot products through the turbine and exhaust nozzle) in a gas turbine.

Coupled acoustics is an interaction between the source (the flame) and the acoustic properties of the domain (air line, fuel line, combustion chamber and exhaust). In certain situations this coupling can lead to a thermoacoustic instability [6]. When the acoustic boundary conditions are appropriate, this can lead to resonant frequencies of the system and sometimes to a growth of the amplitude in time.

One possible effect of the coupling between combustion and combustion chamber is a so-called *singing flame*. The first one who observed it was Byron Higgins in 1777 [7]. A singing flame can easily be reproduced by placing a flame in a tube which is open at both ends. When varying the length of the fuel supply line, at a certain length the flame will start singing. A longer or shorter fuel supply line will probably stop the singing. Rayleigh [8] was the first who explained this phenomenon by the periodic heat release of the flame. When the fluctuating heat release of the flame is not more than 90 ° out of phase with the pressure oscillations in the combustion chamber, a combustion

instability can occur. He stated that an instability occurs, if:

$$\int_V \int_0^\tau p'Q' dt dV > 0 \tag{1.4}$$

Where τ is a period of oscillation, p' is the unsteady pressure and Q' is the unsteady heat release. Polifke et al. [9] mention that this criterion provided merely a necessary, but not a sufficient condition for instability, as it does not take into account the stabilising influence of dissipation of acoustic energy and losses at system boundaries. Poinsot and Veynante [2] question the widely accepted Rayleigh criterion. Because many experiments do not actually support this result in a straightforward manner. Therefore they propose an extended Rayleigh criterion:

$$\frac{(\gamma - 1)}{\gamma p_0} \int_V \int_0^\tau p'Q' dt dV > \int_A \int_0^\tau p'\mathbf{u} dt dA \tag{1.5}$$

In words this can be explained as follows. When more acoustic energy is added to the system (LHS) than is dissipated by the system (or flows away through the border, RHS) the system becomes unstable. Furthermore Poinsot and Veynante [2] question the use of acoustic energy as a measure for instabilities anyway: the acoustic energy has the same definition in non-reacting and reacting flows, but lacks entropy. Moreover, the derivation of the Rayleigh criterion assumes that combustion instability occurs if the acoustic energy grows. This is not necessarily the case. Poinsot and Nicoud [10] introduced a fluctuating variable other than the acoustic energy, which does take into account the fluctuating entropy.

1.4.2 Rijke tube

The unstable character can be demonstrated by the Rijke tube [11]. Figure 1.6 shows such a tube. At the left hand side of the figure, the tube geometry is depicted and at the right hand side, the acoustic pressure and velocity are shown. The two pictures correspond with each other. So at the top of the tube, the acoustic pressure is zero and the acoustic velocity maximum.
The sound comes from a standing wave whose wavelength is about twice the length of the tube, giving the fundamental frequency. Lord Rayleigh, in his book [12], gave an explanation of how the sound is generated. Later, Heckl [13] gave an explanation why the pipe oscillation are supported when the gauze is placed in the lower part and not supported when the gauze is placed in the upper part.
The flow of air passes the gauze in a combination of two motions. There is a uniform upward motion of the air $\overline{u}$ due to a natural convection current

resulting from the gauze heating up the air. Superimposed on this is the motion due to the sound wave u'. The combination of u' and $\overline{u}$ creates and

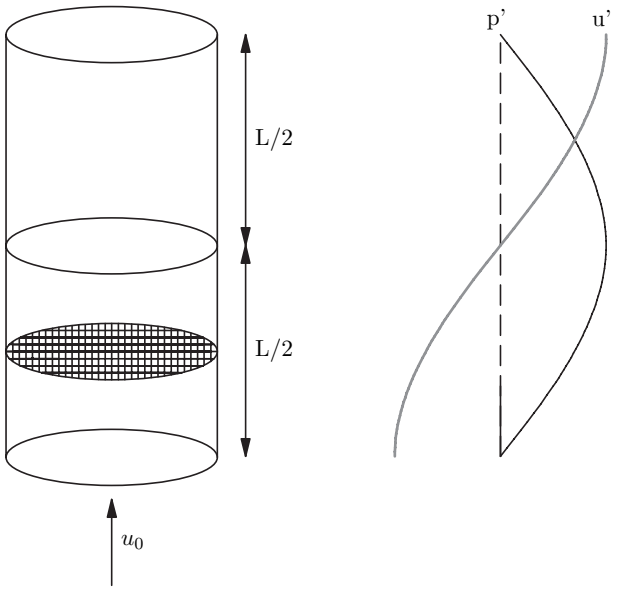

Figure 1.6: A Rijke tube. The grid represents a heated gauze. The RHS of the figure shows the acoustic pressure and velocity distributions.

maintains the time-varying component of heat transfer, q'. To understand this, consider the direction of the flow at the heat source location in the tube due to the combination of u' and $\overline{u}$. For one half the acoustic cycle, both u' and $\overline{u}$ have the same direction, and the heat source communicates with fresh air, enhancing heat transfer. In the other half cycle, the acoustic velocity u' is in the opposite sense to the mean flow and the net fluid velocity is reduced. This means that the heat source is surrounded by preheated air, which in turn reduces the heat transfer in this half of the acoustic cycle. Hence, the unsteady heat transfer q' varies with the changes in u' and is approximately proportional to it: $q'(t) \propto u'$. However, in practice, the response of q' is not instantaneous with changes in u' and it takes a finite time for the changes in u' to get reflected in q'. Thin boundary layers surround the heated gauze and determine the heat transfer. An increase in velocity will reduce the thickness of the boundary layer, but this happens not instantaneous. So q' lags behind u', i.e., $q'(t) \propto u'(t-\tau)$, where τ represents the time lag between q' and u'. The instability in the Rijke tube is naturally sustained in the lower half of the tube and not in the upper half. In figure 1.7 an explanation for that bahaviour is presented. At the bottom of figure 1.7 the acoustic pressure, acoustic velocity

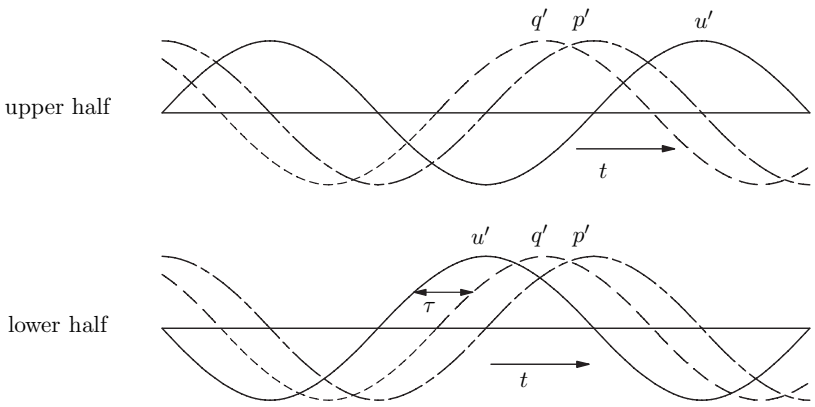

Figure 1.7: Time dependence of the acoustic pressure and acoustic velocity and of the heat transfer at the gauze.

and the heat transfer from the gauze in lower part of the Rijke tube is shown as a function of time. The figure shows that the heat transfer q' lags behind τ on the acoustic velocity. In the top part of the figure, the upper half of the Rijke tube is represented. The phase of the acoustic velocity is opposite to the one in the lower half of the tube. This implies that the flow velocity needed to sound the tube should be three times lower than for the gauze placed in the lower part [14]. In case the velocity is lower, the boundary layers around the gauze are thicker. This reduces the heat transfer and the sound source.

1.4.3 Types of instability

Combustion instabilities can be induced by many different mechanisms. Authors always try to make a certain classification in the types of mechanisms. Lefebvre [5] distinguishes growl and howl with different frequency ranges. Candel and Williams [15, 16] make the following classification based on the origin of three types of instabilities.

System instabilities

System instabilities are usually in the low frequency range. They involve the entire combustion system, like the storage tanks, the supply lines, the combustion chamber and the exhausts. Although these kind of instabilities may occur in all types of installations, they usually occur in rocket engines and power plants.

Chamber instabilities

Chamber instabilities can have two different causes:

- Acoustic instabilities
  Acoustic instabilities correspond to the eigen frequency of the combustion chamber [15]. The singing flame [7] is an example of an acoustic instability. The appearance of acoustic instabilities in practical systems is determined by the characteristic combustion times and the geometrical configuration of the reactive zone [15].

- Hydrodynamic instabilities
  Separation of a boundary layer can cause hydrodynamic instabilities. Another mechanism is the coalesce of the induced vortices to cause feedback of the instabilities [15].

Intrinsic instabilities

Intrinsic instabilities are related to the chemistry and the thermo-diffusive mechanisms. Sivashinsky [17] observes that in cases where the Lewis number Le<1 (the Lewis number is the ratio between the thermal and molecular diffusion, Le=$\frac{\alpha}{\mathcal{D}}$), laminar intrinsic instabilities can arise. In case Le>1, heat is earlier in a combustion region than fuel [18–20]. Hydrogen is well-known for its very fast molecular diffusion. Fast molecular diffusion leads to low Lewis numbers.
Figure 1.8 is a schematic diagram of the type of pattern that can arise from

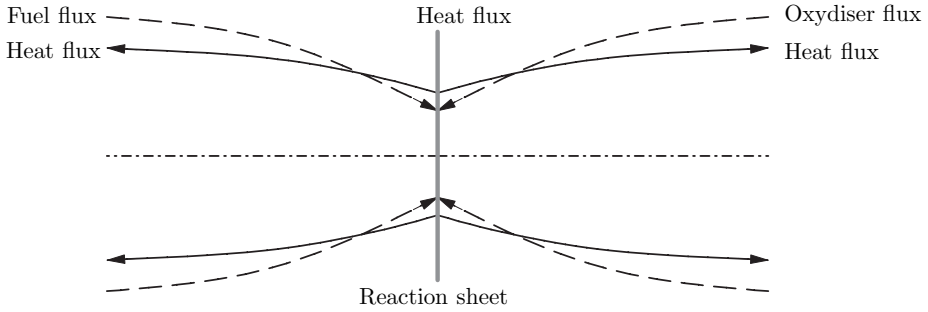

Figure 1.8: Thermo-diffusive instability [21]

a thermo-diffusive instability. In the case that Le<1 the high-diffusivity reactants diffuse preferentially to sinks provided by the strong segments of the reaction sheet, leaving the region between deficient in reactants and therefore

subject to local quenching [21]. This leads to a thermo-diffusive instability.

This study will focus on acoustic instabilities of syngas flames. When gas turbines came into use, the main fuel was high calorific and the combustion was non-premixed. For this type of combustion it was well possible to reach stable operating points. This was usually realised by a high pressure drop in the fuel channel. This can be done at low cost in the efficiency of the gas turbine as the mass flows of high calorific gases are low compared to air mass flows. A high pressure drop in the fuel channel prevents pressure fluctuations from travelling upstream and influencing the power of the flame. The past decade, premixed combustion in gas turbines became preferred, to reduce NO_x emission. Premixed combustion provides a better temperature profile to the turbine inlet, leading to higher possible loads and higher efficiencies. To meet NO_x emission regulations the air excess levels are pushed to their limits. This can also lead to combustion instabilities. In the IGCC setup, syngas is used in a non-premixed combustion regime. As this gas is low calorific, the pressure drop in the fuel line should be low and the system is more vulnerable to acoustic instabilities by a feedback mechanism to the fuel supply line.

1.5 The EU HEGSA project

A three year EU sponsored project called HEGSA was initiated in 2002. At the 1st of January in 2003 the project started. HEGSA is an acronym for **H**igh **E**fficient **G**as turbine for **S**yngas **A**pplication. Several partners with an industrial or academic background participated in the project (see section 1.5.2).

1.5.1 Aims of the project

The goals of the HEGSA projects are:

- Reduction of CO_2-emissions
- Reduction of pollutant emissions (NO_x and CO)
- Highly efficient usage of solid fuel resources(like coal, heavy refinery residues and all kinds of biomass)
- Improved operational and fuel flexibility including high H_2 content fuels
- Improvement of competitiveness of gas turbine manufacturers in new market sectors
- Electricity generation emphasising sustainable environmental protection

- Securing and expanding employment in power plant industry in particular in Europe through progress in technology
- Improving export opportunities in Europe by advanced gas turbine technology

1.5.2 Partners

To enhance the transfer of knowledge between industry and academy, the EU projects have partners from both. The more practical approach of the industry can have positive influence on the direction the academics are doing their research. On the other hand, the academic partners usually are inclined to perform a more fundamental search into matter than industrial partners. Both ways can have positive effects. The project partners are:

From industry:

- Siemens Aktiengesellschaft
- ANSALDO ENERGIA Spa
- Enel Produzione S.p.A.
- NV NUON Energy Trade & Wholesale

From academia:

- Deutsches Zentrum für Luft- und Raumfahrt e.V. (Verbrennings Institut, Stuttgart)
- Universiteit Twente

1.5.3 Tasks

During the project, there was extensive co-operation with the Combustion Research Institute of DLR in Stuttgart. DLR was not involved in acoustic investigations, but did a lot of work on laser diagnostics, reported by Tsurikov et al. [22] and on the modelling of the chemistry of syngas combustion, reported by Slavinskaya [23]. The tasks for the University of Twente during the HEGSA project were:

1. Modelling of flame transfer function for syngas flames
2. Preparation of small scale generic test

3. Execution of small scale generic thermoacoustic tests
4. Validation and optimisation of thermoacoustic syngas flame model
5. Development of thermoacoustic model for advanced gas turbine syngas combustion system/ evaluation of thermoacoustic behaviour

1.6 Objectives

The work which is presented in this thesis has the primary goal of developing a tool which is able to determine the acoustic behaviour of a syngas fired gas turbine during its design phase.
Another goal is to show which influence the combustion air temperature, combustion pressure and fuel composition has on the acoustic behaviour of the flame and the acoustic domain. This includes the influence on the acoustic source of the flame and the influence on the flame transfer function. The fuel mixture is not of a constant quality as IGCC power plants are fed with biomass. The quality of this biomass is not constant.
Additional to that it is the objective to build an experimental setup, execute experiments and validate the results that have been predicted.
Finally, it will be investigated whether it is possible to describe the measured and modelled flame transfer function with some simple distribution functions.

1.7 Outline

To achieve the above mentioned goals, a variety of tools was applied. In general the work can be divided into three parts:

- Acoustics
- Computational Fluid Dynamics (CFD
- Experiments

The acoustics were modelled using a one dimensional model, implemented in MATLAB. This model is capable of predicting acoustic pressures of unexcited flames.
The tool of CFD is used in a wide range of applications. First of all, it was used as a design tool during the design of the burner. Also, CFD could give indications of axial temperature profiles throughout the combustor. This input is necessary for the acoustic model. The main application of CFD was the use for the prediction of the flame transfer function. This was done in two

stages: steady state and transient. The steady state option was used to obtain an indication of the flow field and the temperature field. After that, unsteady CFD was used to obtain a flame transfer function. For all these applications, global chemical reactions were assumed. As the combination of H_2 and CO is hard to catch in simple models, an in house chemical code, called CFI [24] was also applied to two cases. Beside using this code, also the performance of this code is analysed.
A combination of the predicted flame transfer function and a modified acoustic model is used to predict unstable frequencies. This modified model is not capable of predicting acoustic pressures during unstable operation, but the frequencies of instabilities can be predicted.
Finally, the results of the measurements were used to validate all the models. During steady operation power spectra were measured to validate the acoustic model. The setup can also be used to measure flame transfer functions.
All these applications have led to the following selection of chapters. Chapter two explains how the setup (including the burner) works and how it was designed.
Chapter three discusses the theory of the propagation of sound. For situations with and without a temperature gradient, this theory is used to explain the working principle of a one dimensional acoustic model. This model is validated with experimental data.
In the fourth chapter the combustion modelling is discussed. Commercial CFD models were applied, but also more complex and detailed models were used. Especially the chemistry is modelled into more detail, by using the in house developed code called CFI.
Chapter five will show the results that are obtained with the steady CFD. Both the commercial and the in house models are validated with results that are obtained by the DLR in Stuttgart.
In chapter six, the measurement technique for the flame transfer function is described. This flame transfer function is the relation between a fuel mass flow perturbation and the response of the heat release of the flame. The flame transfer function supplies valuable information on the stability of the acoustics of a combustion system. The measured flame transfer functions is used in an n-τ approach. This model is a simplification of the measured results. The simplification allows the model to be used in more complex approaches in predicting the stability of a thermoacoustic system.
In the final chapter, results of unsteady CFD calculations are presented. Unsteady CFD is applied to predict the flame transfer function. Using both the commercial and CFI [24] chemistry model the flame transfer function is predicted. The results are compared with experimental data to validate them.

2
Experimental setup

2.1 Introduction

To validate the modelling work in this thesis, an experimental setup was built. The central component of the test rig is a burner designed to combust syngas. The complete setup is a comprehensive collection of bottled gases, an air compressor, mass flow controllers, electric controlling interface, air preheaters, a pressure vessel, a cooling system, a throttle valve and an exhaust. In the pressure vessel measurement equipment is installed to gain information about the combustion process.

2.2 Description of the experimental setup

The setup can roughly be divided into three sections. All sections are presented in figure 2.1. From top to bottom there is the supply section, the combustion section and the cooling section. All sections are designed to resist a pressure of 5 bar.
The supply section including the burner is depicted in figure 2.2. In the next section more details are presented.
The combustion section consists of a combustion chamber, surrounded by a liner and a cooling channel. The liner is 750 mm in length and has a square diameter of 94 mm. The cooling channel surrounds the liner and is fed with cold air. In the combustion chamber, fuel and air mix and combust. The flame stabilises on the recirculation zone induced by the swirling flows. The combustion section ends with an acoustic decoupler, which is a diaphragm with

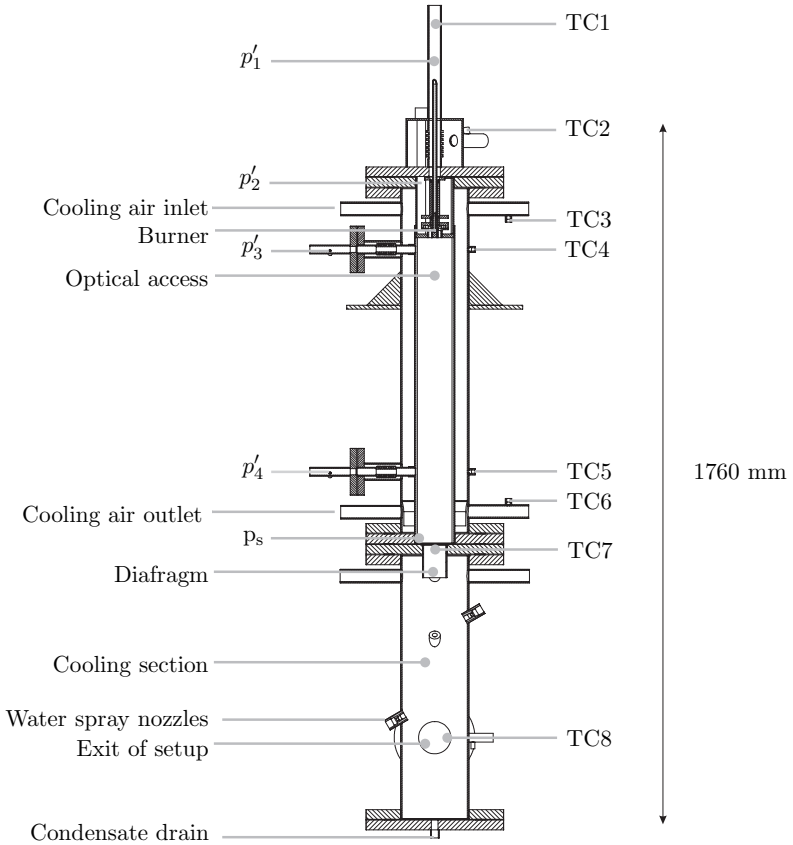

Figure 2.1: Section view of the experimental setup; P1-P4 are dynamic pressure transducers, TC1-TC8 are thermocouples and P_s is a static pressure transducer

an opening radius of 27 mm. This provides a reflective acoustic boundary.
The hot product gases and the cooling air come together in the cooling section. In this section, water fed spray nozzles cool down the mixture below a temperature of 600 K.
In case of firing at elevated pressure, downstream of the cooling section, the product gases are throttled to ambient pressure. Downstream, the gases go to the chimney. In the chimney, gas samples can be checked on composition, for example the O_2 concentration.

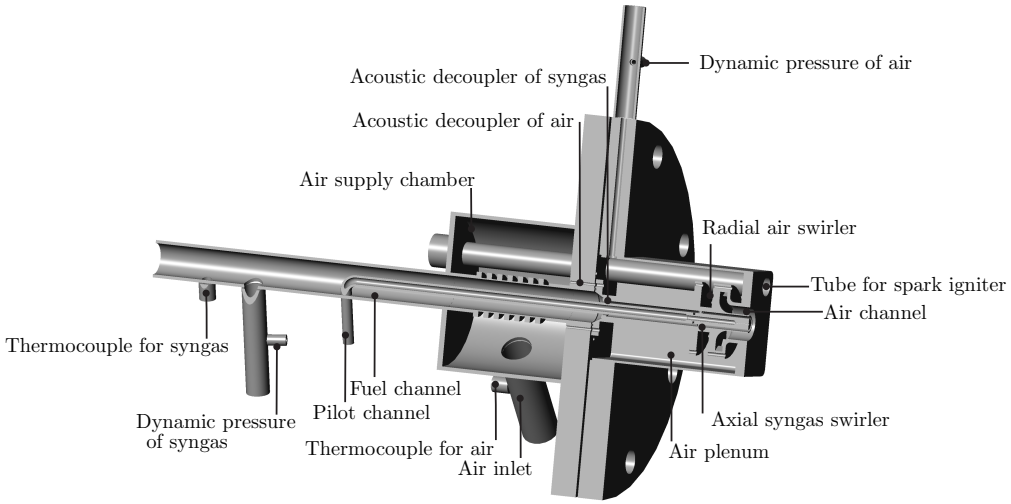

Figure 2.2: Cross section of the burner and the fuel and air supply system

2.3 Burner design

The burner that has been used is specifically designed for the HEGSA project. Both numerical simulations and laboratory experiments are carried out with this burner. The burner is designed to combust syngas and the design is derived from the burner developed for the EU project DESIRE [25]. It is designed at the Laboratory of Thermal Engineering and manufactured in the workshop of the University of Twente. Two pieces were built, one for the DLR in Stuttgart and one for the Laboratory of Thermal Engineering.
To come to an appropriate design, a list of requirements was set up. They are listed below:

- Non-premixing
- Able to combust low calorific fuels with varying compositions and varying calorific values (5-8 MJ/kg)
- Simple geometry for easy manufacturing and computational representation
- High pressure drop on the fuel side, introducing upstream an acoustically hard wall
- Thermal power of 20 kW/bar

As mentioned in the Introduction (chapter 1) the pressure drop on the fuel side of syngas burners in gas turbine applications is usually low. The desired pressure drop in the experimental setup is high. This is done to exclude instabilities induced by low pressure drops in the fuel line.
The details of the resulting design are depicted in figure 2.3. How the burner fits in the whole setup can be seen in figures 2.1 and 2.2.
The burner is a two channel generic syngas non-premixing burner. The syngas is combusted in a non-premixed mode to prevent flashback due to the presence of hydrogen. Both air and fuel are swirled. The air is fed to the burner from a plenum. From the plenum the air flows into the radial swirlers. It is swirled in radial channels by triangular blocks. The fuel flows through an annular tube and is swirled by axial vanes.
As the burner needs to be able to combust low calorific fuels, the area of the fuel opening is much bigger than in burners for high calorific fuels. For fuels containing high concentrations of methane (like natural gas) the stoichiometric mixture fraction is usually around $\phi = 0.06$. For low calorific fuels the mixture fraction increases to values between 0.3 and 0.45. These values in stoichiometry lead to big fuel area's. On the other hand, to meet the requirement of a high pressure drop over the fuel side of the burner, the area of the fuel opening has an optimum.
The burner operates at a constant power/pressures ratio. This is easy to settle. When the pressure increases, so will the mass flow through the burner. So on balance, the velocity will change through the burner as the higher pressure brings a higher density.
The fuel side of the burner is fed by the fuel line, coming from the mass flow controllers. Entering the burner, the fuel passes an acoustic decoupler. This

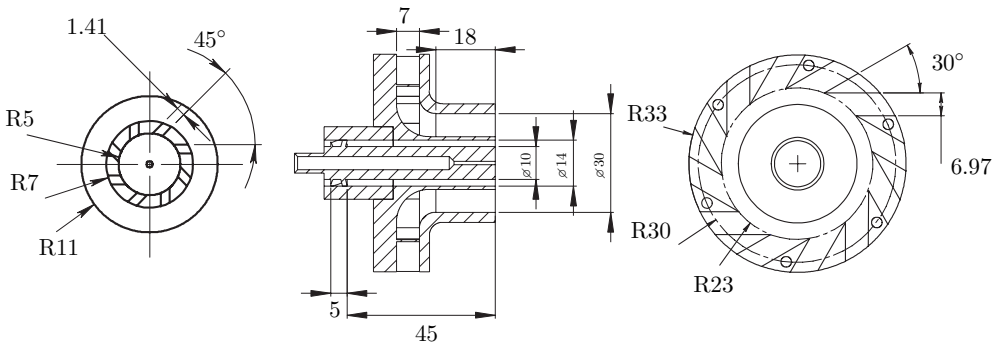

Figure 2.3: Cross section of the burner including dimensions of the air and fuel swirler

decouples all acoustics upstream of the burner from the remaining part of the setup. This is easily achieved by a throttling passage. As the fuel gas is available at 10 bar, some pressure drop can be afforded. Further downstream of the decoupler, the fuel swirler is placed. At the left hand side of figure 2.3, the syngas swirler is displayed. This swirler contains eight axial swirler vanes. These vanes are placed in a 45° angle in the flow. This swirler is 5 mm in length and the channel is 2 mm high. Downstream of the swirler, the fuel enters the combustor through an annular passage.
When the air enters the setup, it first enters the air supply chamber (see figure 2.2. This chamber is connected with the air plenum by an acoustic decoupler. The air speed is increased here up to 70 % of the speed of sound. Once in the air plenum, the air enters the radial swirlers. The swirler consists of a radial inlet and triangular shaped blocks. These blocks are very effective in adding swirl to the flow. During the design process, the air swirler, more specifically the angle of the triangular blocks, was a key aspect. Downstream of the radial swirler, the air goes through a bend and is fed to the combustor. Downstream of the bend in the air channel of the burner, the air flow is a swirling coaxial flow. Both the air and fuel flow have a hub, which improves the axisymmetry of the flow [26].
The fuel swirl and air swirl is co-directional. At the exit of the burner, when fuel and air can meet, the boundary of the inner recirculation zone will also be the mixing plane. In this region the shear will be high and because of the recirculation of hot combustion products, this will also be the region of the flame stabilisation.
Through one of the corners of the air plenum runs a tube. The spark igniter, which is used to start the experiment is mounted in this tube. The actual ignition takes place in the upstream corner of the combustion chamber.
Figure 2.4 shows some pictures of the manufactured burner. The picture on

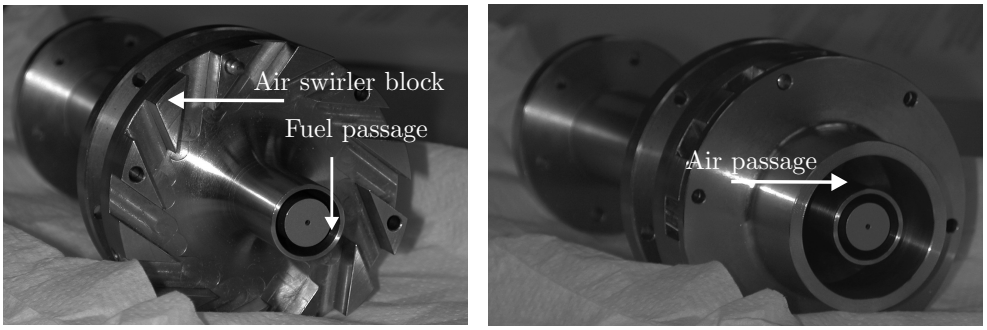

Figure 2.4: Pictures of the burner

the left hand side shows the burner without the top cover of the air passage. In this picture, the air swirler blocks are visualised clearly. The picture on the right hand side shows the burner including the top cover of the air passage.
During the design process, several steps of improvement were made. The first version had a tapered hub. This caused detachment and re-entering of the flow. By giving the hub a blunt edge, this problem was solved. The choice of the ratio between the outer and inner radius of the (fuel and air) channel R_{out}/R_{in} determines whether the flow keeps attached to the hub or not. When the swirl is too high compared to the axial velocity the flow detaches from the hub. Although it is desired that the flame does not attach to the burner hub this is very hard to achieve. In the final design, the flame does attach to the burner hub. However, the fuel has high velocity and is cold compared to the flame. This ensures a sufficient cooling of the hub.

2.4 Controlling and measurement equipment

To control the combustion setup and to do measurements, equipment was installed. In figure 2.1 some parts of this equipment are displayed.

Mass Flow Controllers and heaters

All fuel components are supplied by bottled gases. The mass flow from these bottles is reduced in pressure and fed to the mass flow controllers. These mass flow controllers are used to supply the setup with the desired amounts of fuel and air. As the fuel consists of several species, the number of mass flow controllers is quite extensive. Figure 2.5 gives an overview of the mass flow controllers for fuel and air and the air preheaters. Once the fuel mass flow is controlled, all the components come together in the fuel line. This line is long enough to mix the fuel homogeneously.
Pressurised air is delivered by an air compressor. This air is used for two ends: combustion air and cooling air. Both ends have their own mass flow controllers. Downstream of the mass flow controllers of the combustion air, a possibility to preheat the air is built in. The heaters are temperature controlled electric resistance heaters. The cooling air is provided to the setup in a direct line.

Throttle Valve

When the setup is firing at an elevated pressure, the exhaust gases need to be throttled before they can be fed to the chimney. This is done by a throttle valve. Pressurised air is used to drive the throttle valve.

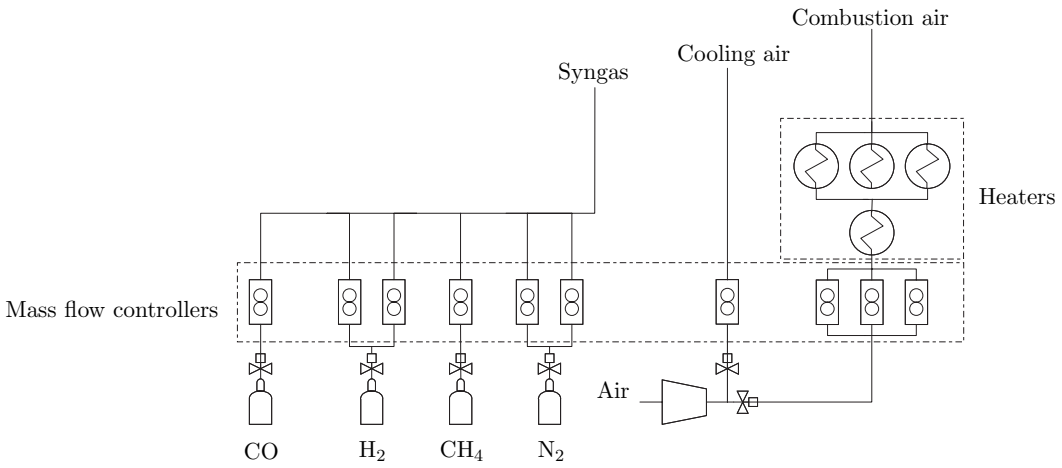

Figure 2.5: The mass flow controllers and the heaters in the setup

Static Pressure Transducers P_s

The static pressure transducer is used to measure the static pressure and to control the throttle valve with that value. The static pressure is measured at the downstream end of the combustion chamber.

Thermocouples TC1-TC8

Eight K-type thermocouples are installed in the setup. It is not possible to measure the flame temperature directly with thermocouples, but the thermocouples can supply valuable combustor information. As depicted in figure 2.1, eight thermocouples are installed to measure the temperatures of: combustion air and fuel, cooling air in out, two liner points, exit of the combustor and exit of the setup.

Kulites P1-P4

The Kulite dynamic pressure transducers can measure the acoustic pressure in the air and the fuel channel and at two positions in the combustion chamber. A pressure wave passing the measuring position can travel to the Kulite. As the temperatures close to the combustion chamber are very high, the Kulite is placed some distance away from it. In figure 2.6 the measuring principle is shown. Travelling to the Kulite, the pressure wave passes through a thermal expansion compensator. This compensator counterbalances the differences in thermal expansion between several parts in the setup. The Kulite itself is

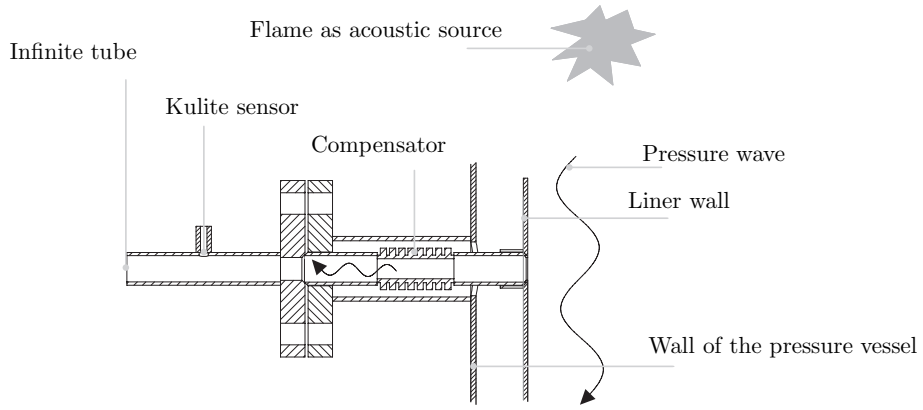

Figure 2.6: Dynamic pressure measurement

mounted flush to the tube where the pressure wave is passing. After being measured, the wave disappears into a semi-infinite tube. This is a hose, filled with acoustic damping material.

MOOG valve

The flame transfer function is defined by the ratio between the heat release rate of the flame and a perturbation in the mass flow of the fuel (see chapter 6). To induce this perturbation, several techniques can be applied. Some researchers use a simple loudspeaker [3,27,28] and others use a siren [6,29–31]. Loudspeakers and sirens can excite up to high frequencies. But the shape of the excitation spectrum of sirens is determined by the sirens geometry [25]. The MOOG valve can perturb the mass flow of the fuel in a controlled way. The valve is placed upstream of the setup. It is depicted in figure 2.7. It consists of a coil which creates a magnetic field. This magnetic field can move a piston operated valve. The piston opens or closes the fuel channel. The position of the piston is checked by a displacement sensor. The resulting acoustic pressure is measured by the Kulite in the fuel channel. Several authors describe this device [25, 32]. Figure 2.8 shows the transfer function between the displacement of the piston of the MOOG valve and the dynamic pressure in the fuel line (p'_1 in figure 2.1). The valve can excitate up to 400 Hz. The transfer function is determined at four different excitation levels. The maximum input signal is +/-1 V. But at 0.60 V the maximum displacement of the piston is reached. From this input level the piston of the MOOG valve started to hit the end limits. Figure 2.8a shows the magnitude of this transfer function and figure 2.8b the angle. Figure 2.8a shows that the excitation levels of 0.10 V

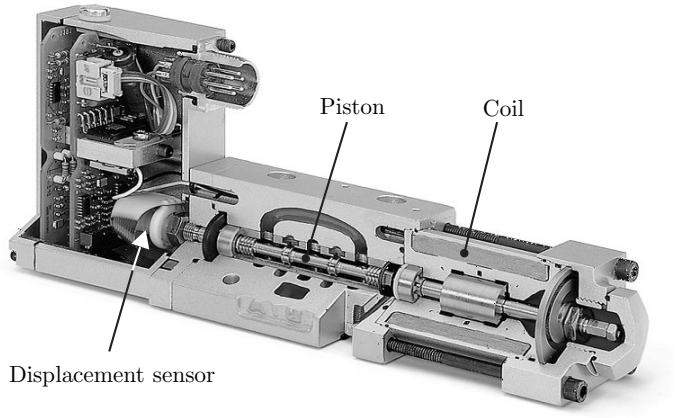

Figure 2.7: The MOOG valve

and 0.25 V have transfer functions that are very close to each other. This can be considered as the linear range. The excitation level of 0.50 V and also 0.60 V show some significant differences, especially in the frequency range of 0-50 Hz. The angles between the measured signals are for all excitation levels very close to each other.

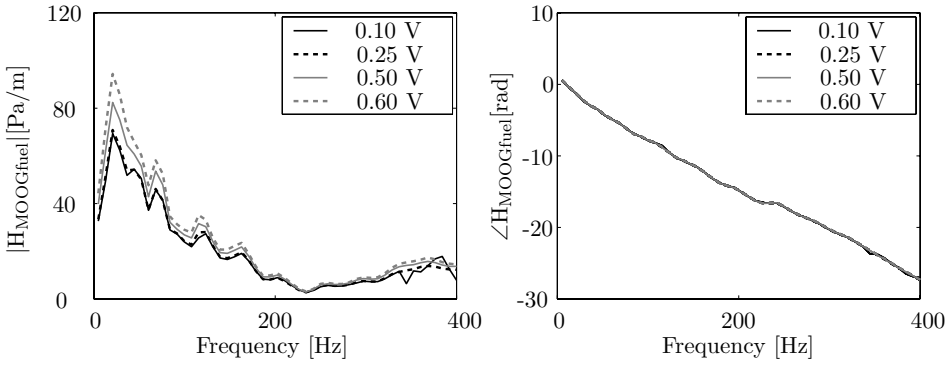

(a) Amplitude (b) Angle

Figure 2.8: Transfer between MOOG and fuel pressure measuring point

LabView

LabView is used to control the complete setup. All the 'slow' equipment is controlled by it. It controls the mass flow controllers, all the magnetic valves, it reads the thermocouples and the static pressure and it controls the throttle valve.

SigLab

SigLab is a system that processes the fast/ dynamic data from the Kulites. It can supply power spectra, cross spectra and transfer functions between different measuring points by using Fourier transforms. It can also control the MOOG valve. The SigLab system is equipped with four ingoing channels of 2^{13} storage positions to store and transform data from the Kulites and has two outgoing (control) channels.

2.4.1 Measuring the flame transfer function

The transfer function which can be measured during combustion is p'_4/p'_1, see figure 2.9. The transfer function targeted in the measurements is defined by $Q'/\dot{m}'_f$. Because the setup is able to operate at elevated pressure, the measurement equipment can not be placed at the ideal positions. Hence, several steps to reconstruct the desired flame transfer function need to be taken. These lead to the following approximation:

$$H_f = \frac{Q'}{\dot{m}'_f} \approx \frac{p'_4}{p'_1} \cdot F \tag{2.1}$$

Chapter 6 describes how F is determined. It shows the estimations, calculations and assumptions that are taken for the reconstruction.

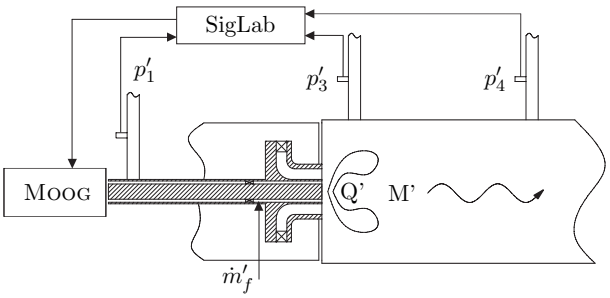

Figure 2.9: Integration of the SigLab system in the experimental setup

2.4.2 Chemiluminescence

Due to the chemical reactions in the combustion process some species become electronically excited so that the molecules are no longer in thermal equilibrium. In this state, a molecule is highly reactive and the lifetime of these species is very short in general (100 ns). After that, the molecule can fall back in its ground state by energy transfer between its vibrational, rotational and electronic states. In that case the energy is released in the form of electromagnetic radiation, a phenomenon also known as natural light emission or chemiluminescence. As a result of the quantified energy levels in an atom, each molecule emits a characteristic spectrum. This makes it possible to identify individual species in a flame with the use of spectral filters and a photomultiplier or CCD camera. This technique can measure the relative concentration of some species. However, the camera collects all the light in its line of sight. To reconstruct this line of sight information, a special deconvolution technique is applied. One of the methods to do this is called the Abel transformation. This assumes that the flame is axisymmetric. This technique is described by Harleman [33].
In the here described setup, OH* chemiluminescence measurements were car-

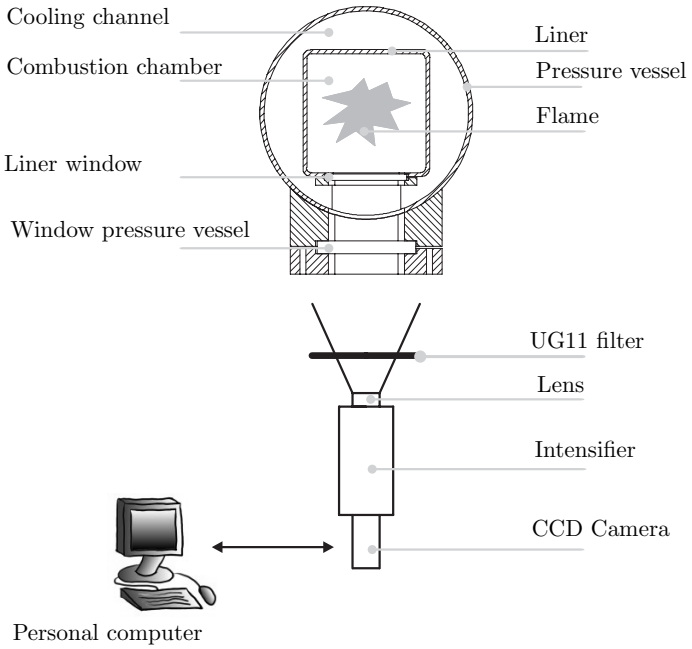

Figure 2.10: OH* measurement equipment installed next to the setup

ried out. CH* is also a measurable intermediate species, but usually, the CH*

signal is very weak. Moreover, the fuel that is planned to be used in the setup does not always contain hydrocarbons. Both hydrogen and carbon is available in the fuel, but not in the same species. This would lead to low concentrations of CH and thus to low signal level.
Light emitted by OH^* radicals has a wave length around 350 nm. This light can be filtered by a UG11 filter. The specifications of this filter are reported in appendix B. Some authors claim that OH^* can be considered as a qualitative indication for the heat release of the flame [34,35]. Others doubt this [36]. But the OH^* chemiluminescence data can at least be used to validate the CFD calculations with the CFI chemistry model.

2.5 Operating points

The operating points presented in table 2.2 are fixed in co-operation with DLR Stuttgart. The maximum pressure possible at DLR is 2 bar. So, during the co-operation this was the limit. In the naming convention, the physical properties of the cases can be recognised. The first part of the name refers to the fact whether the fuel mixture contains methane or not. If the mixture does not contain methane, it is called Syn, if it does contain methane it is called Meth. The number in the names indicates the pressure in the combustor in bar. Finally, the indication hot and cold refer to the inlet air temperature.

mixture	CO [mass%]	H_2 [mass%]	CH_4 [mass%]	N_2 [mass%]	LHV [MJ/kg]
6	31.1	1.5	0.0	67.3	5.0
7	29.2	1.5	6.2	63.1	7.8

Table 2.1: The two types of fuels which are used.

Case name	mixture	T_{air} [K]	Pres [bar]	Power [kW]	λ [-]	T_{ad} [K] @ $\lambda = 2$	T_{ad} [K] @ $\lambda = 1$
Syn1Cold	6	293	1	20	2	1478	1990
Syn2Cold	6	293	2	40	2	1478	1996
Meth1Cold	7	293	1	20	2	1477	2077
Meth2Cold	7	293	2	40	2	1477	2086
Syn1Hot	6	423	1	20	2	1550	2033
Syn2Hot	6	423	2	40	2	1559	2126
Meth1Hot	7	423	1	20	2	1550	2041
Meth2Hot	7	423	2	40	2	1559	2137

Table 2.2: Operating points of all investigated cases.

3
Acoustics in a hot environment

3.1 Introduction

Any gas turbine is susceptible to enter into unstable operation during changes of load or environmental conditions. Exactly for that reason it would be very rewarding to be able to predict the stability of a gas turbine for all its operating conditions. Therefore, acoustics and flame mechanisms need to be predicted in coupled operation.
First of all, this chapter presents the theory on one dimensional acoustics. After that, an acoustic model is presented. This model is set up to predict acoustic pressures based on the analytical solution of the Helmholtz equation. The predicted acoustic pressures can be compared with the measured auto spectra in the experimental setup. The model needs an acoustic source as a boundary condition. In case of combustion noise, the flame will act as acoustic source. Once the measured auto spectra are known, the model can also be applied to reconstruct the acoustic properties of the measured flame.
The acoustic model can be modified to a thermoacoustic model. This model can predict frequencies of thermoacoustic instabilities. The solution of the Helmholtz equation assumes a harmonic relation between position and time. When the flame responds on an aerodynamic perturbation upstream of it, the phase shift between aerodynamics and heat release is important and will induce non-harmonic behaviour. At certain frequencies, the coupling between the heat release of the flame and this phase shifted aerodynamic feedback can result into high amplitude acoustic pressure oscillations. The thermoacoustic

model can take this behaviour into account and predict frequencies at which instabilities occur.

3.2 The analogy of Lighthill

Sir James Lighthill introduced a powerful approach on sound generation by aerodynamics [37–39]. For this purpose he combined the Navier-Stokes equation for momentum conservation and the equation for conservation of mass. The analogy renders an exact wave equation including three types of sources. These sources can be divided in monopoles, dipoles and quadrupoles. In equations 3.1 and 3.2, conservation of mass and momentum are formulated:

$$\frac{\partial \rho}{\partial t} + \nabla \cdot (\rho \mathbf{u}) = 0 \tag{3.1}$$

$$\frac{\partial (\rho \mathbf{u})}{\partial t} + \nabla \cdot \left(\rho \mathbf{u} \otimes \mathbf{u}^T\right) = -\nabla p + \nabla \cdot \sigma + \mathbf{f} \tag{3.2}$$

Here, $\mathbf{u}$ is the velocity vector, $\otimes$ is the dyadic product (product between vectors leading to a tensor), σ is the stress tensor of viscosity and $\mathbf{f}$ is the momentum induced by external forces.
Lighthill suggested to take the time derivative of the equation for mass conservation (equation 3.1) and the divergence of the equation of momentum conservation (equation 3.2). Subtraction of the results of these operations leads to:

$$-\nabla^2 p = \nabla \cdot \left(\nabla \cdot \left(\rho \mathbf{u} \otimes \mathbf{u}^T - \sigma\right)\right) - \frac{\partial^2 \rho}{\partial t^2} - \nabla \cdot \mathbf{f} \tag{3.3}$$

By replacing the instantaneous values with a mean and a fluctuation: $p = \overline{p} + \tilde{p}$, $\rho = \overline{\rho} + \tilde{\rho}$ and adding the term $\frac{1}{c_0^2}\frac{\partial^2 \tilde{p}}{\partial t^2}$ at both sides of the equal sign, the analogy of Lighthill appears:

$$\frac{1}{c_0^2}\frac{\partial^2 \tilde{p}}{\partial t^2} - \nabla^2 \tilde{p} = \nabla \cdot \left(\nabla \cdot \left(\rho \mathbf{u} \otimes \mathbf{u}^T - \sigma\right)\right) - \frac{\partial^2}{\partial t^2}\left(\frac{\tilde{p}}{c_0^2} - \tilde{\rho}\right) - \nabla \cdot \mathbf{f} \tag{3.4}$$

All terms on the right hand side can be considered as sources of sound. From all these terms [25], the only term which should be included when considering combustion is the monopole of the term $\frac{\partial^2}{\partial t^2}\left(\frac{\tilde{p}}{c_0^2} - \tilde{\rho}\right)$. The term $\nabla \cdot \left(\nabla \cdot \left(\rho \mathbf{u} \otimes \mathbf{u}^T - \sigma\right)\right)$ is a quadrupole. This quadrupole represents the turbulence in the flow and can be neglected in case of combustion noise [25]. Also the dipole of $\nabla \cdot \mathbf{f}$ can be neglected as a source term in low Mach-number combustion systems [25]. Klein [3] has dedicated a chapter in his thesis to the noise generation by a flame. This theory is summarised and applied in chapter 4.

3.2.1 The flame as an acoustic source

As mentioned, the term $\frac{\partial^2}{\partial t^2}\left(\frac{\tilde{p}}{c_0^2} - \tilde{\rho}\right)$ is the only Lighthill source term that will be taken into account. In appendix D this expression is rewritten to:

$$\frac{\partial}{\partial t}\left[\frac{\gamma - 1}{c_0^2} q'_f\right] \tag{3.5}$$

in which γ is the ratio of heat capacities c_p/c_v and q'_f is the local rate of heat release. It seems that the derivation in appendix D has converted a second order derivative in time into a first order derivative. However, the term of q'_f is also a time derivative.

3.3 One dimensional wave propagation

3.3.1 Analytical solution

Taking the result of Lighthill's analogy as a starting point, the wave equation can be simplified. Assuming no mean flow, negligible viscous forces and linear acoustics, the wave equation reduces to [2, 40]:

$$\frac{1}{c_0^2}\frac{\partial^2 \tilde{p}}{\partial t^2} - \nabla^2 \tilde{p} = 0 \tag{3.6}$$

Introducing a mean flow $\mathbf{u}_0$, the equation changes to [3, 25]:

$$\frac{1}{c_0^2}\frac{D^2 \tilde{p}}{Dt^2} - \nabla^2 \tilde{p} = 0 \tag{3.7}$$

Where $\frac{D}{Dt}$ represents the material derivative, the time derivative moving with a mean flow $\mathbf{u}_0$. The solution of this equation, assuming acoustics to propagate in only one direction and to be harmonic, then becomes:

$$p'(x) = \hat{p}_A e^{ik_A x} + \hat{p}_B e^{-ik_B x} \tag{3.8}$$

where $\hat{p}_A$ is the wave travelling to the left with speed $c_0 - u_0$ and $\hat{p}_B$ is the wave travelling to the right with a speed of $c_0 + u_0$. k_A therefore reads $\frac{\omega}{c_0 - u_0}$ and k_B equals $\frac{\omega}{c_0 + u_0}$ From the linearised momentum equation, the fluctuating velocity can be derived:

$$u'(x) = \frac{-1}{\rho_0 c_0}\left(\hat{p}_A e^{ik_A x} - \hat{p}_B e^{-ik_B x}\right) \tag{3.9}$$

3.3.2 Temperature gradient

As already mentioned, the syngas combustion is non-premixed. Non-premixed combustion takes place close to the stoichiometric mixture fraction. As twice as much air is supplied than needed for the combustion, the temperature downstream of the flame decreases quickly due to mixing of product gases and fresh air. This mixing will lead to an axial mean temperature gradient in the combustion chamber. Beside this effect, the combustion chamber is mainly bounded by cooled liner walls. Due to the cooling of the wall, the combustion products will also be cooled. The temperature gradient thus caused will influence the local acoustic properties. To account for the temperature gradient in the combustion chamber, Sujith et al. [41] have proposed an exact solution for acoustic fields in ducts with an axial temperature gradient. Van Kampen [25] has also used this approach. The solution does not take the effects of a mean flow into account, thus it is only valid for Mach numbers below 0.1. As the temperatures are high, so is the speed of sound ($\mathcal{O}(700)$ m/s). Velocities are around 40-50 m/s at highest. Hence the low Mach number condition is met easily. The approach of Syjith et al. [41] is as follows. It starts with the equations of state and energy conservation.
Assuming a perfect, inviscid and non-heat-conducting gas [41], the energy equation reads:

$$\frac{\partial p}{\partial t} + \mathbf{u} \cdot \nabla p + \gamma p \nabla \cdot \mathbf{u} = 0 \tag{3.10}$$

And the equation of state for a perfect gas:

$$p = \rho R T \tag{3.11}$$

Assuming one dimensional acoustics and expressing each of the dependent variable as the sums of a mean and a time dependent small amplitude perturbation:

$$p(x,t) = \overline{p} + \tilde{p}(x,t), \quad u(x,t) = \overline{u} + \tilde{u}(x,t), \quad \rho(x,t) = \overline{\rho} + \tilde{\rho}(x,t), \tag{3.12}$$

On condition that the mean flow Mach number is below 0.1, the solution of the steady momentum equation shows that the mean pressure $\overline{p}$ is constant in the duct. Sujith et al. [41] have used a similar approach as Lighthill, but instead of using the equation for conservation of mass, they use the equation for conservation of energy. Taking the derivative to x of the momentum equation and the derivative to t of the energy equation, the wave equation can be derived as [41]:

$$\nabla^2 \tilde{p} - \frac{1}{\overline{\rho}} \frac{d\overline{\rho}}{dx} \nabla \tilde{\rho} - \frac{\overline{\rho}}{\gamma \overline{p}} \frac{\partial^2 \tilde{p}}{\partial t^2} = 0 \tag{3.13}$$

In case that the density can be assumed constant $\frac{d\overline{\rho}}{dx} = 0$ this equation reduces to the general wave equation [2, 40]:

$$\nabla^2 \tilde{p} - \frac{1}{c_0^2} \frac{\partial^2 \tilde{p}}{\partial t^2} = 0 \tag{3.14}$$

Rewriting $\frac{\overline{\rho}}{\gamma \overline{p}}$ to $\frac{1}{c_0^2}$ with the definition of the speed of sound ($c_0^2 = \gamma RT$) and differentiating the equation of state and again assuming that the mean pressure in the duct is constant, the gradients in steady temperature and the density relate as:

$$\frac{1}{\overline{\rho}} \frac{d\overline{\rho}}{dx} + \frac{1}{\overline{T}} \frac{d\overline{T}}{dx} = 0 \tag{3.15}$$

Assuming a periodic time dependence ($\tilde{p}(x,t) = p'(x)e^{i\omega t}$) and introducing a temperature function depending on x, $\overline{T} = \overline{T}(x)$, this can be rewritten to [41]:

$$\left(\frac{d\overline{T}}{dx}\right)^2 \frac{d^2 p'}{d\overline{T}^2} + \frac{1}{\overline{T}} \frac{d}{dx} \left(\overline{T} \frac{d\overline{T}}{dx}\right) \frac{dp'}{d\overline{T}} + \frac{\omega^2}{\gamma R} \frac{p'}{\overline{T}} = 0 \tag{3.16}$$

For a mean temperature distribution:

$$\overline{T} = T_1 + mx \tag{3.17}$$

the solution of equation 3.16 reads [41]:

$$p' = c_1 J_0 \left(\frac{\omega}{a} \sqrt{\overline{T}}\right) + c_2 Y_0 \left(\frac{\omega}{a} \sqrt{\overline{T}}\right) \tag{3.18}$$

where c_1 and c_2 are (complex) constants, J_0 and Y_0 are Bessel and Neumann functions of order zero and a is defined as:

$$a = \frac{\overline{m}}{2} \sqrt{\gamma R} \tag{3.19}$$

The results in this derivation are implemented in the Transfer Matrix Method, presented in the next section.

3.3.3 Attenuation

Not all sound will be propagated. Some of it will be dissipated by viscous damping. As industrial size combustion systems usually are large, so are the characteristic lengths. For this reason, the effects of damping can be neglected. However, at the measuring position and in the burner, the characteristic lengths are still small. Viscosity effects can dissipate acoustic energy in these regions. An additional source of damping is the mean turbulent flow.

Zwikker and Kosten [42] presented the Low Reduced Frequency solution. In this model they modify the wave number to contribute for the attenuation. Tijdeman [43] shows that most of the analytical solutions depend only on the shear wave number s ($= R\sqrt{\overline{\rho}\omega/\mu}$). Where R is the radius of a circular tube, $\overline{\rho}$ is the mean density, ω is the frequency [rad/s] and μ is the dynamic viscosity. To account for the attenuation in the here presented model, the solution of Ingard and Singhal [44] is used. This model takes the acoustic damping into account in case a turbulent mean flow is present in the acoustic domain. See [25] for more details.

3.4 The Transfer Matrix Method

The theory so far presented, was implemented in an acoustic model. This model uses the Transfer Matrix Formulation. In the Transfer Matrix Formulation (TMF) [25,45,46], the acoustic domain will be separated into elements, for example tubes. For each element, the acoustic mass flow $\mathbf{M}'$ and the pressure perturbation $\mathbf{p}'$ at the inlet and outlet of the element can be related to each other by a certain transfer function, based on equation 3.8, the analytical solution of the acoustic wave equation. When the acoustic elements are coupled, these relations can be inserted in one matrix, forming the system matrix $\mathbf{A}$, that relates the pressures to the acoustic mass flows at each coupling point like:

$$\mathbf{A}\mathbf{p}' = \mathbf{M}' \tag{3.20}$$

Now, when adequate boundary conditions are present, the unknown pressure perturbations $\mathbf{p}'$ at each node can be solved by:

$$\mathbf{p}' = \mathbf{A}^{-1}\mathbf{M}' \tag{3.21}$$

3.5 Matrix elements

In figure 3.1, a tube with symbolic conventions is presented. The element is numbered J, the inlet has index 1, the outlet index 2. Note that M_2^J is positive in the opposite direction of M_1^J. When for the inlet and outlet of the tubes, the boundaries are $x = -L/2$ and $x = L/2$ are used, the pressure can be expressed as $\mathbf{p}' = \mathbf{C}\hat{p}$. Note that indication of the element in the notation is in superscript:

$$\left\{ \begin{array}{c} p_1^J \\ p_2^J \end{array} \right\} = \left[\begin{array}{cc} e^{-\mathrm{i}L^J(k_A-k_B)/2} & e^{\mathrm{i}L^J(k_A-k_B)/2} \\ e^{\mathrm{i}L^J(k_A-k_B)/2} & e^{-\mathrm{i}L^J(k_A-k_B)/2} \end{array} \right] \left\{ \begin{array}{c} \hat{p}_A^J \\ \hat{p}_B^J \end{array} \right\} \tag{3.22}$$

For the velocity perturbations can be derived $\mathbf{u}' = \mathbf{D}\{\hat{p}\}$:

$$\left\{ \begin{array}{c} u_1^J \\ u_2^J \end{array} \right\} = \frac{1}{\rho_0 c_0} \left[\begin{array}{cc} -e^{-\mathrm{i}L^J(k_A-k_B)/2} & e^{\mathrm{i}L^J(k_A-k_B)/2} \\ -e^{\mathrm{i}L^J(k_A-k_B)/2} & e^{-\mathrm{i}L^J(k_A-k_B)/2} \end{array} \right] \left\{ \begin{array}{c} \hat{p}_A^J \\ \hat{p}_B^J \end{array} \right\} \tag{3.23}$$

When one is interested in the amplitudes of the left and right travelling waves, the coefficients $\hat{p}_A$ and $\hat{p}_B$ can be found with $\hat{\mathbf{p}} = \mathbf{C}^{-1}\mathbf{p}'$.
With S^J as the area of the tube and M^J it follows:

$$M_1^J = S^J \rho_0 u_1^J \tag{3.24}$$
$$M_2^J = S^J \rho_0 u_2^J \tag{3.25}$$

As $\mathbf{u}' = \mathbf{D}\hat{\mathbf{p}}$ and $\hat{\mathbf{p}} = \mathbf{C}^{-1}\mathbf{p}'$, $\mathbf{u}'$ can be expressed as: $\mathbf{u}' = \mathbf{D}\mathbf{C}^{-1}\mathbf{p}'$. The acoustic mass flow M^J in the cylindrical element J is given by:

$$\frac{S^J}{c_0 \sinh(C_J)} \left[\begin{array}{cc} \cosh(C_J) & -e^{\mathrm{i}L^J(k_A-k_B)/2} \\ e^{\mathrm{i}L^J(k_A-k_B)/2} & -\cosh(C_J) \end{array} \right] \left\{ \begin{array}{c} p_1^J \\ p_2^J \end{array} \right\} = \left\{ \begin{array}{c} M_1^J \\ M_2^J \end{array} \right\}$$

in which $C_J = \mathrm{i}L^J(k_A - k_B)/2$. The coefficients of the element matrix can be written as:

$$A_{ij}^J = \left[\begin{array}{cc} A_{11}^J & A_{12}^J \\ A_{21}^J & A_{22}^J \end{array} \right] \left\{ \begin{array}{c} p_1^J \\ p_2^J \end{array} \right\} = \left\{ \begin{array}{c} M_1^J \\ M_2^J \end{array} \right\} \tag{3.26}$$

3.5.1 Coupling of elements

When two tubes are coupled to each other, like in figure 3.2, the matrix is extended with one dimension. Note that the exit of element J is the inlet of element $J+1$. At the node between two coupled elements, acoustic mass flow $\mathbf{M}'$ and acoustic pressure are conserved.
With two coupled tubes, the matrix is given by:

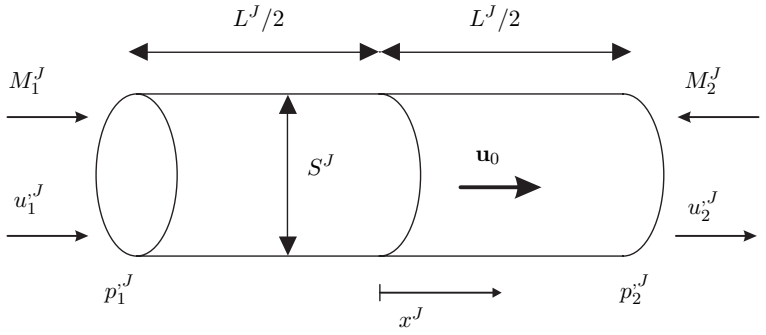

Figure 3.1: Symbolic conventions for a single tube

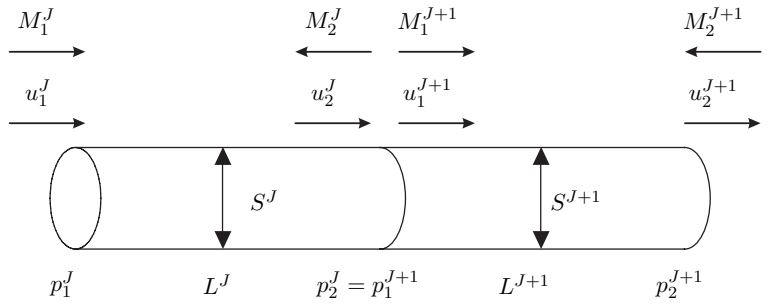

Figure 3.2: Symbolic conventions for two coupled tubes

$$\begin{bmatrix} A_{11}^J & A_{12}^J & 0 \\ A_{21}^J & A_{22}^J + A_{11}^{J+1} & A_{12}^{J+1} \\ 0 & A_{21}^{J+1} & A_2^{J+1} \end{bmatrix} \begin{Bmatrix} p_1^J \\ p_2^J \\ p_2^{J+1} \end{Bmatrix} = \begin{Bmatrix} M_1^J \\ M_2^J \\ M_2^{J+1} \end{Bmatrix} \tag{3.27}$$

In the case that the flow area of two coupled elements changes significantly, the conservation of pressure does not hold. For this purpose van Kampen [25] has derived a new element coupling, called flow coupling. Before the area change, the velocity of the flow has a normal flow profile. It can not be assumed that immediately downstream the area change, the velocity has a similar profile as upstream of the area jump. A jet, which separates at the trailing edge is formed. The kinetic energy of the jet is not completely converted into potential energy (pressure). The part that is not converted into potential energy is dissipated. This process takes places in the area which is indicated as the turbulent mixing region in figure 3.3.
The resulting matrix is:

$$\begin{bmatrix} A_{11}^J & A_{12}^J & 0 & 0 \\ A_{21}^J & A_{22}^J - R & R & 0 \\ 0 & R & -A_{11}^{J+1} - R & -A_{12}^{J+1} \\ 0 & 0 & -A_{21}^{J+1} & -A_{22}^{J+1} \end{bmatrix} \begin{Bmatrix} p_1^J \\ p_2^J \\ p_1^{J+1} \\ p_2^{J+1} \end{Bmatrix} = \begin{Bmatrix} M_1^J \\ 0 \\ 0 \\ -M_2^{J+1} \end{Bmatrix} \tag{3.28}$$

In this formulation: $R = S_{J+1}\overline{u_{1,J+1}}^{-1}\left[\left(\frac{S_{J+1}}{S_j} - 1\right)^2 - \left(\frac{S_{J+1}^2}{S_j^2} - 1\right)\right]^{-1}$.

3.5.2 Boundary conditions

To be able to solve the system of equations, boundary conditions are required. The acoustic model contains several types of boundary conditions.

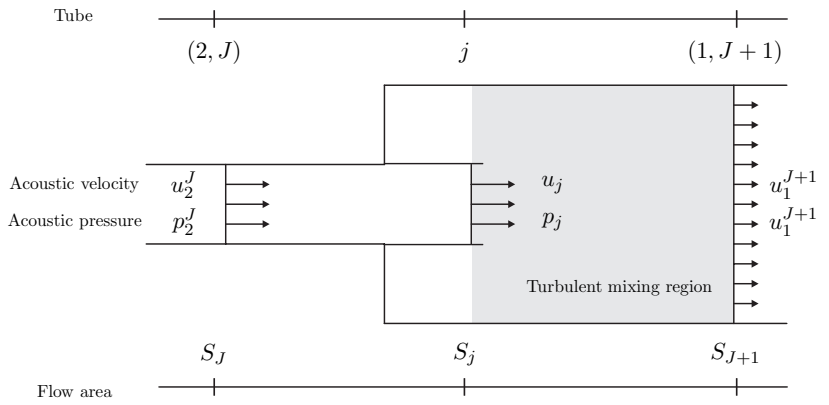

Figure 3.3: Symbolic conventions for two coupled tubes with a mean flow and a step in flow area, implemented in the so-called flow coupling element.

Impedance boundary

Impedance is the relationship between the acoustic pressure and the acoustic velocity. Usually the dimensionless impedance is used. This is:

$$\zeta = \frac{1}{\rho_0 c_0} \frac{p'}{u'} \tag{3.29}$$

An impedance end condition can take the surroundings of the network model into account. The impedance condition at the end of a tube J can be written as:

$$M_{J+1} = -\frac{S_J}{c_0} \frac{1}{\zeta_{J+1}} p_{J+1} \tag{3.30}$$

Using this relation and by eliminating $M_{J=1}$ the element matrix for a single tube terminated with an impedance ζ_{J+1} becomes:

$$\begin{bmatrix} A_{11}^J & A_{12}^J \\ A_{21}^J & A_{22}^J + A_\zeta \end{bmatrix} \begin{Bmatrix} p^J \\ p^{J+1} \end{Bmatrix} = \begin{Bmatrix} M^J \\ 0 \end{Bmatrix} \tag{3.31}$$

where A_ζ equals $\frac{S_J}{c_0} \frac{1}{\zeta_{J+1}}$. And so, a known impedance condition at the end of a tube can be taken into account with an extra term in the element matrix of that tube.

Pressure boundary

In case of a prescribed pressure p_J the J^{th} column is subtracted from the **A** matrix. The J^{th} row and column of the system matrix are set to zero and the

element A_{jj} is set to 1. In the case of two tubes connected to a volume and a prescribed pressure p_0 at node 1 of tube J the system will read:

$$\begin{bmatrix} 1 & 0 & 0 \\ 0 & A_{22}^{J} + A_{11}^{J+1} & A_{12}^{J+1} \\ 0 & A_{21}^{J+1} & A_{22}^{J} \end{bmatrix} \begin{Bmatrix} p_1^J \\ p_2^J \\ p_2^{J+1} \end{Bmatrix} = \begin{Bmatrix} p_0 \\ -p_0 \cdot A_{21}^{J} \\ M_2^{J+1} \end{Bmatrix} \tag{3.32}$$

Volume source

In the acoustic model, a volume source can be applied on one of the nodes. This monopole source M_s' equals the acoustic mass flow in the model: $M_s' = S^J \rho_0 u'$. At the node where the flame is located in the model, this volume source is specified. The source term can be considered as the driving force of the acoustic model.
The acoustic source of a flame is frequency dependent. Usually, the source strength decays with frequency. Singh [47] reports sources independent of the frequency up to 1000 Hz. Experience with the validation of the model in section 3.6 shows that the flame, acting as an acoustic source is dependent on the frequency. In chapter 5, the strength of the acoustic source is predicted by the noise model.
For now, first of all, three generic sources are assumed. Two sources are independent of the frequency at $0.5{\cdot}10^{-5}$ kg/s and $2{\cdot}10^{-5}$ kg/s and one source is decaying with the frequency linearly between the two first mentioned sources. These sources are depicted in figure 3.4.
The acoustic model can also be applied to reconstruct the volume source. In this fashion, the acoustic source will be adjusted until the model prediction meets the experimental results. This method is explained in section 3.7.

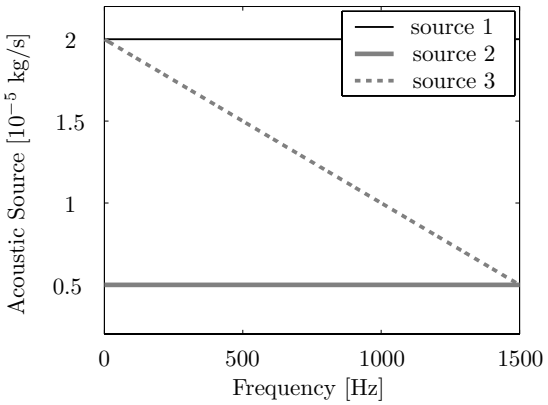

Figure 3.4: The three types of sources that were applied.

3.5.3 Solving

To solve the nodal pressures and nodal velocities of a given network of tubes and volumes the first step is to solve the nodal pressures by solving the system: $\mathbf{p}' = \mathbf{A}^{-1}\mathbf{M}'$. In the second step the nodal velocities are solved through: $\mathbf{u}' = A^J/\rho_0 S^J \mathbf{M}'$, where the vector $\mathbf{u}'$ is arranged per tube as follows:

$$\{u_1^J \ -u_2^J \ u_1^{J+1} \ -u_2^{J+1} \ ..\}^T \tag{3.33}$$

The index J indicates that for a tube J a cross-section S^J has to be used. The advantage of the transfer matrix formulation described above, is that the exact analytical solutions are used between nodal points whereas in standard finite element formulations linear or quadratic functions are used. Hence, in this TMF method there is no need for a discrete number of elements per wavelength; a single element can be used for a tube regardless of the number of wavelengths that fits in the tube. As a result the system matrix remains small, while still retaining accuracy.

3.6 Validation

The acoustic model is validated in this section. As the model can predict steady noise, the measurements that are used are also from an unperturbed flame. The Syn1Hot case (syngas without methane and air preheating temperature of 150 °C) is used for validation.

Figure 3.5 shows the model that has been implemented for this purpose. The model starts at the left hand side of the figure with the air plenum. The plenum can act like a Helmholtz resonator. Downstream of the air plenum, the air side of the burner is located. Entering the combustion chamber, a flow coupling element is used. In the combustion chamber, the solution with a temperature gradient is used. This temperature gradient can be fitted linearly between the adiabatic flame temperature and the exit temperature, but can also be based on calculations with Cfx. Appendix C gives an extensive overview of the possible temperature profiles.
In the combustion chamber, a mean flow does not need to be taken into account, as the speed of sound has risen so high that the Mach number is below 0.1. Between the combustion chamber and the cooling section, again a flow coupling is applied. The end condition of the cooling section is taken as fully reflective.
The network model has two side branches in the combustion chamber. Here, the Kulites are placed for measuring the acoustic pressure (p_3' and p_4'). In

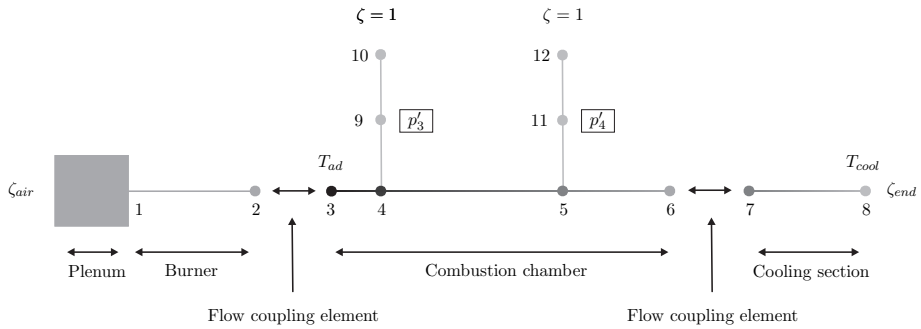

Figure 3.5: One dimensional modelling approach of the combustion chamber

the acoustic model, the measuring points are conform to the points 9 and 11. Downstream of these measuring points the impedance equals 1, assuming that no sound waves are reflected by the semi-infinite hose.
Figure 3.6 presents the comparison between the modelled and the measured

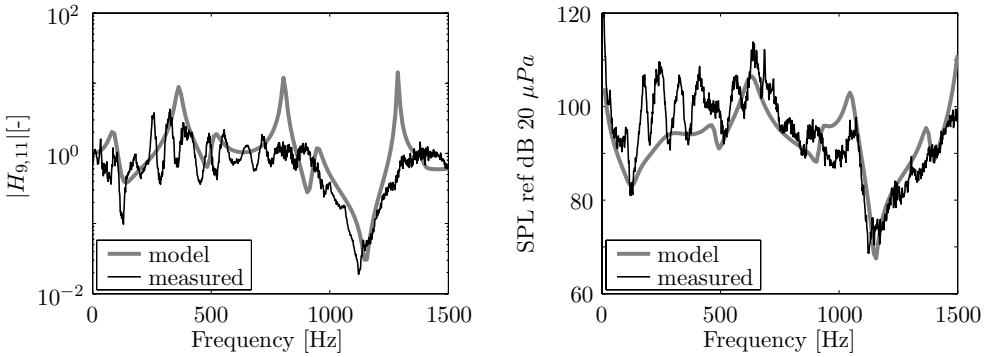

(a) $H_{9,11}$ (b) SPL point 11

Figure 3.6: Results with source 3 for $H_{9,11}$ and SPL at point 11.

acoustics. Extensive results can be found in appendix C. Figure 3.6 (a) shows the transfer between the measuring points in the combustion chamber and (b) shows the sound pressure level (with a reference pressure of 20 μPa) of point 11. The two plots show that the model captures the most important features of the acoustics. The eigen frequencies of the combustion chamber are predicted very well. In the low frequency range some of the details are missing. This is probably due to the imperfectness of the semi-infinite hoses downstream of the measuring points. It is assumed that these hoses do not reflect any pressure waves, but in practice they do reflect the waves to some

extent. As the hoses are 10 metres in length the corresponding frequencies are low. Assuming that the speed of sound is 330 m/s in these hoses, the end of the hose is reflective, this effect can already start at 8 Hz. And although probably minor, the cooling channel can also have an influence on the acoustic properties of the system. Just like the imperfectness of the semi-infinite hose, it is hard to take this effect into account.
For high temperature processes in a non-adiabatic environment (like combustion) it is hard to predict the temperature at every point in the reactor. For diffusion flames it is even harder, as the mixing process is playing an important role. Probably for this reason the peaks are not exactly in the right frequency. As one peak is predicted at a too low frequency and the other at a too high frequency it is not simply a single temperature that is wrongly chosen. Extensive axial temperature information during combustion is necessary for a good prediction of the sound pressure field. It is hard to withdraw this from CFD calculations performed here, as these calculations are all adiabatic. Another issue is, that in a diffusion flame the pressure field may be one dimensional, but the temperature field certainly is not. The air flow enveloping the flame has a much lower temperature, and hence also lower speed of sound.
The source in these modelling results is chosen to be $1 \cdot 10^{-5}$ kg/s. That can be considered as a very strong source. Weaker sources show less response.
In appendix C, more extensive results of this case can be found. In this appendix the source strength is varied and also the temperature gradient. This analysis shows that the input parameters are of great importance. To get a good temperature profile, extensive measurements along the axis of the acoustic domain should be carried out. For the source term, the noise model of chapter 5 can provide additional information, but the acoustic model can also be used in an inverse way as will be shown in the next section.

3.7 Inverse acoustics

So far, the acoustic model has been applied for forward acoustics. An acoustic source is imposed as a boundary condition and together with the acoustic domain, it results in acoustic pressures on the predefined nodes in the model. Those acoustic pressures can be compared with measured values and this way the model can be validated. It is shown that the model captures the most important features of the steady acoustics during combustion (it captures the resonance frequencies). However, it is also shown in appendix C that the imposed acoustic source has a large influence on the resulting acoustic pressures. Instead of forward acoustics (predicting acoustic pressures using a source as input) it is also possible to predict the acoustic source by measuring

acoustic pressures in the nodes of the model. This is what is called inverse acoustics in literature. Inverse acoustics are used to reconstruct a source in an acoustic domain. The same model as described in figure 3.5 has been used to determine the acoustic source, the acoustic strength of the flame.
The model however does not return a unique acoustic source using inverse acoustics. It is possible to apply the measured acoustic pressures as boundary conditions. It is also possible to reconstruct the acoustic mass flows with these boundary conditions, like:

$$\begin{bmatrix} A_{1,1} & \cdots & A_{1,j} \\ \vdots & & \vdots \\ A_{i,1} & \cdots & A_{ij} \end{bmatrix} \begin{Bmatrix} p_1 \\ \vdots \\ p_j \end{Bmatrix} = \begin{Bmatrix} M_1 \\ \vdots \\ M_j \end{Bmatrix} \tag{3.34}$$

This is not sufficient to return a unique acoustic source.

The flame acoustic source is reconstructed in another fashion. The forward model is looped using a condition to open the loop. By using a step by step increasing source, the source at point 11 is evaluated every step. By doing this for every frequency, the acoustic model will meet the measured pressure at every frequency.
The resulting source is presented in figure 3.7a. It looks similar to the decaying source that has been used in the sensitivity analysis. The bumpy behaviour is not physical but generated by the imperfections of the model.
To project the reconstructed source on a smooth correlation, it is correlated with a least squares method. In figure 3.7 the linear fit is shown. The general decay (expressed by the linear fit) can be assumed as the acoustic source of the flame. In figure 3.7b, the model uses the fitted source. It shows a good fit with the experiments. This shows not only that the source was reconstructed well, but also that the linearisation was justified.
By using this method to reconstruct the acoustic source, all differences between the measured and the modelled acoustic pressures are minimised by the adjusted source. The deviations of the model from the measurements between 200 and 500 Hz are probably caused by the imperfectness of the semi-infinite hoses in the experimental setup. Figure 3.7 shows that the reconstructed source fits well the behaviour of the experimental setup.
When experimental data are not available source information of others [48] can also be used.

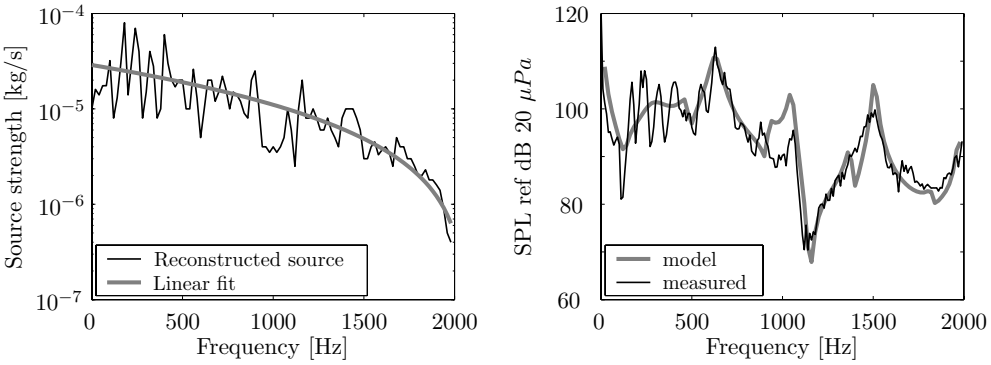

(a) Reconstructed source

(b) SPL 2 with reconstructed source

Figure 3.7: Reconstruction of the source.

3.8 Thermoacoustic instabilities

So far, the focus has been on the accurate prediction of the stationary acoustics in the combustion chamber. It is shown in the previous sections that this is possible within some margin. However, it would be very interesting to be able to predict transient acoustic behaviour and instabilities in a combustion system.
An instability occurs, when at a certain frequency, the input of acoustic energy exceeds the dissipation. The input of acoustic energy is caused by the flame. It was shown that heat release fluctuations can result in an acoustic source. In this thesis, only heat release fluctuations are considered. When this fluctuation of the heat release rate is dependent on an earlier perturbation, the system is not harmonic any more.

Now, equation 3.21 is considered again. When the determinant of $\mathbf{A}$ in this equation becomes small, this equation runs towards a non-trivial solution. The smallest disturbance in the system can result in large pressure perturbations. When no time delays are present in the system, det $\mathbf{A}$ equals 0 for the real eigen frequencies of the system. However, when time delays are present in the system det $\mathbf{A}$ becomes zero for complex frequencies $(\omega_r + i\omega_i)$ in which ω_r is the frequency of the thermoacoustic oscillation and ω_i the growth rate of this oscillation in time. To find this instability, the following problem needs to be solved:

$$|\det\ \mathbf{A}(\omega_\mathrm{r}, \omega_\mathrm{i})| = 0 \tag{3.35}$$

This is a non-linear problem which can be solved in MATLAB by finding the

minimum value of det $|\mathbf{A}(\omega_r, \omega_i)|$. For this purpose, MATLAB contains a search method, based on the Nelder-Mead simplex search method (see [25,49]). When the absolute value of the determinant of $\mathbf{A}$ becomes smaller than $1 \cdot 10^{-4}$, the frequency is considered unstable. This behaves in time as follows:

$$e^{i\omega t} = e^{i(\omega_r + i\omega_i)t} = e^{-\omega_i t} e^{i\omega_r t} \tag{3.36}$$

So when a negative ω_i is found ($\omega_i < 0$) an oscillation will grow in time.

3.8.1 Heat release coupled to inlet variables

To give an idea of how this search tool can be applied in our model, an example will be shown.
Figure 3.8 shows how the coupling between the flame and the acoustics can

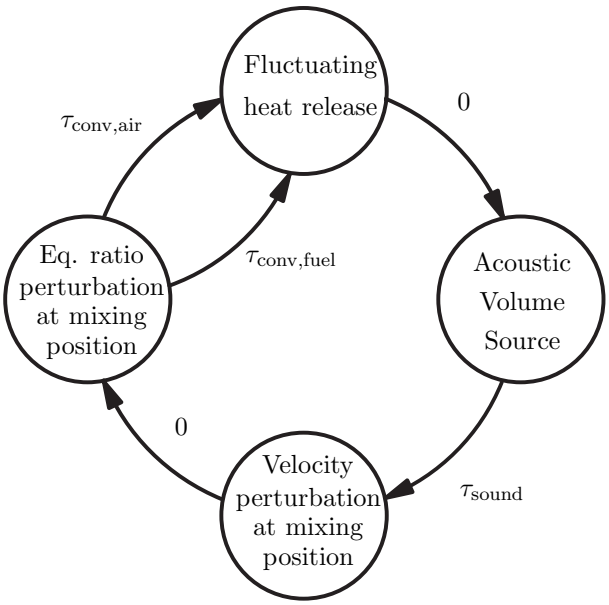

Figure 3.8: Mechanism that can initiate a thermoacoustic instability (0 indicates a time delay of 0).

initiate and sustain pressire oscillations. First of all, there is a fluctuation in the heat release of the flame. This fluctuation causes an acoustic volume source. The acoustic waves, initiated by this volume source, can travel in two directions. The least harmful is the downstream wave. No strong coupling with the flame dynamics can be found downstream of the volume source. However, after a certain time delay τ_{sound} upstream of the acoustic volume

source, a velocity perturbation at the mixing position of fuel and air can arise. This velocity perturbation can have its origin in the air side or the fuel side of the combustor. With a velocity perturbation at the mixing position, the equivalence ratio is immediately influenced. This equivalence ratio fluctuation can travel downstream again following two different paths. With delay at the air side, or with a delay at the fuel side of the flame. Arriving at the flame, the heat release rate of the flame can be influenced and the circle is closed.

Following a derivation [50] for an originally premixed model the instantaneous heat release of a flame can be written as:

$$q(t)|_f = y_f \rho \overline{\dot{V}} h_f \tag{3.37}$$

In this equation subscript $flame$ indicates the flame front, $\overline{\dot{V}}$ is the volume flow, y_f is the fuel mass fraction and h_f is the local flame transfer function. The unit of h_f is [J/kg]. When assuming small perturbations in the fuel mass fraction y_f and density ρ, equation 3.37 can be linearised:

$$q'_f(t) = h_f \left[y_f \overline{\dot{V}} \rho'(t)|_{flame} + \overline{\rho} \overline{\dot{V}} y'_f(t - \tau_{conv})|_m \right] \tag{3.38}$$

In this equation, the mean values are indicated by over bars and the linearised values by an apostrophe. The subscript m refers to the mixing position. τ_{conv} is the convection time for a fluctuation to reach the burner mouth. Note that convection time is different for air and fuel.
This model is not a complete overview of possible influences, but needs to be seen as an example. Equation 3.38 represents the *perturbations in the fuel mass fraction*. Other perturbations can be for example an oscillation of the area of the flame front or a variation of the flame position. These processes are not included in the model.
Figure 3.9 shows the one dimensional model on which this theory is applied. The H_f in the figure represents the acoustic result of the perturbations in the fuel mass fraction. When this loop is open, the flame acts as a normal acoustic source. When this loop is closed, the fuel mass fraction perturbations are taken into account. With the naming convention of figure 3.9, equation 3.38 can be rewritten:

$$q'_f(t) = h_f \left[y_f \frac{\overline{\dot{V}}}{c^2_{el3}} p_4 + \overline{\rho} \overline{\dot{V}} y'_f|_3 e^{-i\omega\tau_{conv}} \right] \tag{3.39}$$

The first term of equation 3.38 was evaluated in the flame. This point is represented by node 7 in figure 3.9. The second term was evaluated at the burner mouth. This point is represented by node 6 in figure 3.9.

The mass fraction of fuel is a fraction containing both air and fuel mass flows. So on both the air side and the fuel side of the burner, the mass fraction of fuel in the combustion chamber can be influenced. The fuel mass fraction is defined as:

$$y_f = \frac{\dot{m}_f}{\dot{m}_a + \dot{m}_f} \tag{3.40}$$

with $\dot{m}_f$ is the mass flow of fuel and $\dot{m}_a$ is the mass flow of air. This equation is given in instantaneous values.
The fuel mass fraction y_f can be rewritten to:

$$y_f = \overline{y_f} + y'_f = \overline{y_f}^2 \frac{\overline{\dot{m}_a}}{\overline{\dot{m}_f}} \left[\frac{\overline{\dot{m}_a}}{\overline{\dot{m}_a} + \overline{\dot{m}_f}} + \frac{\dot{m}'_f}{\overline{\dot{m}_f}} - \frac{\dot{m}'_a}{\overline{\dot{m}_a}} \right] \tag{3.41}$$

When equation 3.41 can be rewritten for the model of figure 3.9. This be-

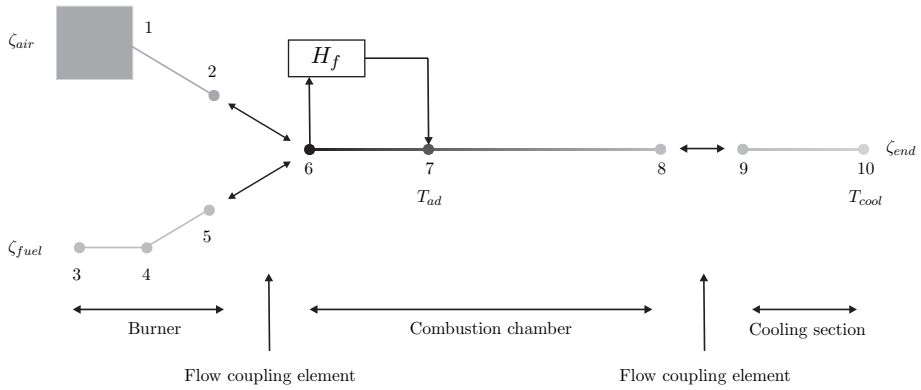

Figure 3.9: Modelling approach of the combustion chamber to predict unstable frequencies

comes:

$$q'_7 = h_f \overline{y_f}^2 \frac{\overline{\dot{m}_a}}{\overline{\dot{m}_f}} \left[\frac{\overline{\dot{V}}}{c_{67}} \frac{\overline{\dot{m}_a} + \overline{\dot{m}_f}}{\overline{\dot{m}_a}} p_7 + \frac{\overline{\rho}\overline{\dot{V}}}{\overline{\dot{m}_f}} \overline{\rho_f} S_{fuel} u'_4 e^{-i\omega\tau_{conv,fuel}} + \right.$$
$$\left. \frac{\overline{\rho}\overline{\dot{V}}}{\overline{\dot{m}_a}} \overline{\rho_a} S_{air} u'_1 e^{-i\omega\tau_{conv,air}} \right] \tag{3.42}$$

and therefore, the fluctuating heat release becomes:

$$q_7' = h_f \overline{y_f}^2 \frac{\overline{\dot{m}_a}}{\overline{\dot{m}_f}} \begin{bmatrix} p_1 \\ p_4 \\ p_6 \\ p_7 \end{bmatrix}^T \cdot \begin{bmatrix} \frac{\overline{\dot{\rho}\dot{V}}}{\overline{\dot{m}_a}} \overline{\rho_a} C^{air} e^{-\mathrm{i}\omega\tau_{conv,air}} \\ -\frac{\overline{\dot{\rho}\dot{V}}}{\overline{\dot{m}_f}} \overline{\rho_f} C^{fuel} e^{-\mathrm{i}\omega\tau_{conv,fuel}} \\ \frac{\overline{\dot{\rho}\dot{V}}}{\overline{\dot{m}_f}} \overline{\rho_f} C^{fuel} \cosh(F^{fuel}) e^{-\mathrm{i}\omega\tau_{conv,fuel}} .. \\ .. - \frac{\overline{\dot{\rho}\dot{V}}}{\overline{\dot{m}_a}} \overline{\rho_a} C^{fuel} \cosh(F^{air}) e^{-\mathrm{i}\omega\tau_{conv,air}} \\ \frac{\overline{\dot{V}}}{c_{6-7}^2} \frac{\overline{\dot{m}_a} + \overline{\dot{m}_f}}{\overline{\dot{m}_a}} \end{bmatrix} \tag{3.43}$$

where the C is a prefactor of $\frac{S^J}{c_0 \sinh(\mathrm{i}(k_A - k_B)L)^J}$, $F^{air} = \mathrm{i}(k_A - k_B)L^{air}$ and $F^{fuel} = \mathrm{i}(k_A - k_B)L^{fuel}$.

3.8.2 Open or closed loop

Figure 3.10 shows that the closing of the feedback loop can initiate thermoacoustic instabilities. The open loop contains an acoustic source in node 7 of figure 3.9, without any relation to an other node in the model, beside the acoustic relations. Making a stability analysis of this system results in figure 3.10 (solid squares). Only two unstable frequencies are found in this fashion. But the growth rate (imaginary frequency) is positive, so the instability is not sustained but damped in time.
Closing the loop, hence relating the acoustic source in node 7 to an equivalence ratio perturbation in node 6 (induced by the air side or the fuel side of the burner) results in the closed loop stability plot (solid bullets). It shows that the closing of the loop turns a stable system into an unstable system. The system also has more points of instability, as the system is changed by closing the loop.

3.9 Conclusions

In this chapter, an acoustic model was presented. It was used for the prediction of acoustic pressures in a combustion chamber. The model takes flow, a temperature gradient and area changes into account. The model has been validated and it showed that the modelling results compare very well with the experimental results. The most important acoustic features, like resonance frequencies, are all captured by the model. Some errors are made in the model. These errors can probably be contributed to the lack of temperature

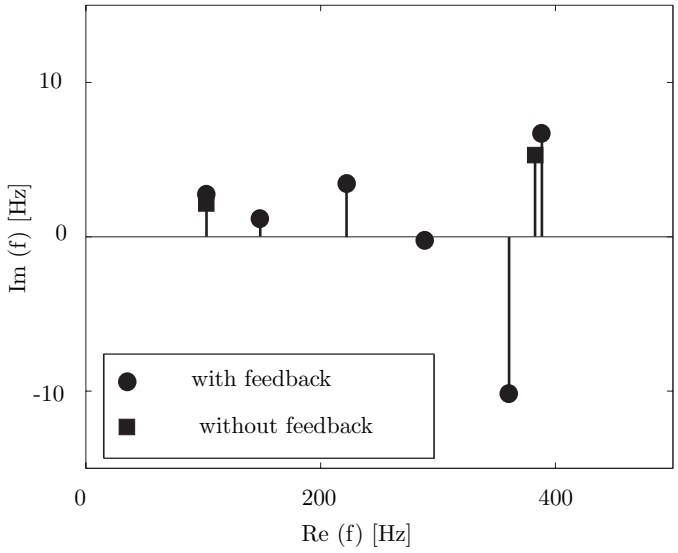

Figure 3.10: Stability maps of an open and a closed loop system.

information from the combustion chamber and the imperfectness of the semi-infinite tubes downstream of the measuring points. For a good prediction of the sound pressure field, accurate and extensive axial temperature information is necessary. As this is very hard to obtain, this is a limitation of the model. However, with the input used in the validation of this chapter, the limited temperature information gave good results.
Beside the acoustic model, a thermoacoustic model was presented. The working principle of this model is shown, but the thermoacoustic model is not yet validated. Validation of the thermoacoustic model will take place in chapter 7.

4
Combustion modelling

4.1 Introduction

This chapter will focus on the modelling of the combustion process. The tools that will be presented in this chapter will be applied to reach two research goals.
The combustion modelling will first be applied to predict the noise that is radiated by the flame. Flame noise is mainly caused under the influence of turbulence. For this reason, the turbulence model is important.
Secondly, the combustion modelling will be applied for the prediction of the flame transfer function. This flame transfer function is the relation between the heat release fluctuations of the flame and an upstream excitation. Predicting the flame transfer function requires a model that predicts the heat release in the right amounts and in the right position. This requires good modelling of the flow field, mixing and chemistry.
The chapter will start with a simple modelling approach that will explain the main behaviour of non-premixed flames. Afterwards, the CFD models will be presented. The commercial CFD code Cfx was used as a flow solver. Cfx has some chemical models embedded, but it is also possible to couple inhouse procedures to the flow solver. The chemistry models embedded in Cfx are applied in the noise model. The chapter will finish with the presentation of how the in house chemistry code was applied. This chemistry code is called Cfi [24]. The model is based on the so-called CSP reduction of laminar premixed solutions.

4.1.1 Simple model for laminar flames with fast chemistry

To get some feeling for non-premixed flames, a simplified model is presented. A description of this model can be found in the book of Poinsot and Veynante [2]. Laminar flames with infinitely fast chemistry are considered in first instance.

Chemistry

A chemical reaction between a fuel (F) and an oxydiser (O) will lead to products (P). The reaction scheme is denoted by:

$$\nu_F F + \nu_O O \rightleftharpoons \nu_P P \tag{4.1}$$

where ν_i are the stoichiometric coefficients for the fuel, oxydiser and produtcs. For the mass fraction (Y_i) of the three reacting elements (F, O and P), a conservation equation can be given:

$$\frac{\partial \rho Y_i}{\partial t} + \nabla \cdot (\rho \mathbf{u} Y_i) = \nabla \cdot (\rho \mathcal{D} \nabla (Y_i)) + \dot{\omega}_i \tag{4.2}$$

where $\dot{\omega}_i$ is the chemical source term and $\mathcal{D}$ represents the diffusion coefficient. The mass based stoichiometric ratio between fuel and oxydiser can be defined as:

$$s = \frac{\nu_O W_O}{\nu_F W_F} \tag{4.3}$$

where the W's indicates the molar masses.
With Y_F the fuel mass fraction and Y_O the oxydiser mass fraction, the equivalence ratio ϕ can be defined as:

$$\phi = s \frac{Y_F^0}{Y_O^0} \tag{4.4}$$

where the index 0 indicate a variable on the inlet.

Mixing

A reduced and conserved variable is introduced to describe fuel/oxydiser mixing: the fuel mixture fraction (a measure for the local fuel/oxydiser ratio). The mixture fraction can be transported by diffusion or convection, but the mixture fraction can not be consumed or produced by chemical reaction.

$$f = \frac{s Y_F - Y_O^0}{s Y_F^0 - Y_O^0} \tag{4.5}$$

In this fashion, the fuel inlet will have a mixture fraction of 1 and the air inlet a mixture fraction of 0.
For mixture fraction f, it is possible to define a conservation equation with convective and diffusive transport:

$$\frac{\partial \rho f}{\partial t} + \nabla \cdot (\rho \mathbf{u} f) = \nabla \cdot (\rho \mathcal{D} \nabla f) \tag{4.6}$$

It can be assumed that a flame is locally one dimensional and only dependent on the gradient of f perpendicular to the flame front. Gradients along the flame front are neglected. So each element of the flame is a small flame itself. These small flames are called flamelets [2].

Mixing flame structure

At this point, finding $T(x,t)$ and $Y_i(x,t)$ can be divided into two problems:

- A mixing problem: the mixture fraction field $f(x,t)$ needs to be known as a function of space and time
- A flame structure problem: the temperature field $T(x,t)$ and mass fractions $Y_i(x,t)$ need to be coupled to the local value of the mixture fraction f.

When the chemistry is assumed to be infinitely fast, the solution for the temperature of the flame structure is represented by equation 4.7. The mass flows of fuel and oxydiser follow the solution represented in equations 4.8 and 4.9. This solution is usually referred to as the Burke-Schumann approach [2].

$$T(f) = \begin{cases} T(f) = f T_F^0 + (1-f)\, T_O^0 + \frac{Q Y_F^0}{c_p} \frac{(1-f) f_{st}}{1-f_{st}} \text{ for } f \geq f_{st} \\ \\ T(f) = f T_F^0 + (1-f)\, T_O^0 + \frac{Q Y_F^0}{c_p} f \text{ for } f < f_{st} \end{cases} \tag{4.7}$$

$$Y_F = Y_F(f) = Y_F^0 \frac{(f - f_{st})}{(1 - f_{st})} \text{ for the fuel side} \tag{4.8}$$

$$Y_O = Y_O(f) = Y_O^0 \left(1 - \frac{f}{f_{st}}\right) \text{ for the oxydiser side} \tag{4.9}$$

Figure 4.1 shows the solutions of this simple approach. The fuel that is used is mixture 6 (see table 2.1). The stoichiometric mixture fraction of this mixture is 0.43. So at this mixture fraction, the temperature (figure 4.1a) will be at its top. The mass fraction of both fuel and air (figure 4.1b) will have their

minimum at this point as both can react in the perfect ratio. In this figure air is at the left hand side (no fuel, so a mixture fraction of 0) and fuel at the right hand side (all fuel, so a mixture fraction of 1). Only 23 mass% of the air is oxydiser and only 32 mass% of the fuel is combustible.
The graphs of a finite rate combustion process will be smoother.

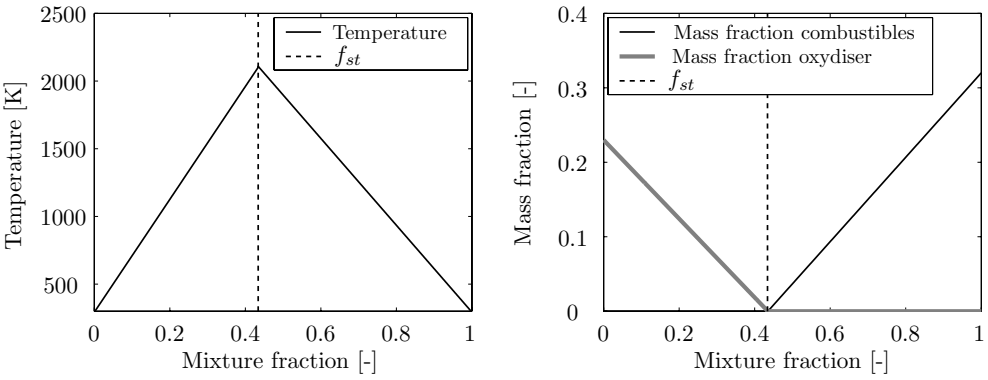

(a) Temperature

(b) Mass fractions

Figure 4.1: Burke-Schumann flame structure, a single step approach of a non-premixed flame of syngas (2 mass% H_2 30 mass% CO, diluted with N_2) and air (23 mass% of O_2, the remainder is N_2).

Finite combustion rates

When the chemistry is not considered as infinitely fast and the flow becomes turbulent, the chemistry profile becomes more complicated.
In case of finite rate chemistry, usually the dimensionless Damköhler number is introduced to compare mixing and chemical time scales:

$$Da^{fl} = \frac{\tau_f}{\tau_c} \tag{4.10}$$

where τ_f represents a characteristic flow mixing time and τ_c the chemical time. In some combustion models, the Damköhler number is used as a threshold for the on and off switching of the chemical reaction in the modelled flame. However, estimating the Damköhler number can be difficult. Assuming that a finite rate chemistry model is available, the chemical time scale τ_c can be calculated using the local concentrations of fuel and air and the local temperature. The mixing time scale τ_f usually has to be estimated. When the value of the Damköhler number takes finite values, finite rate chemistry becomes

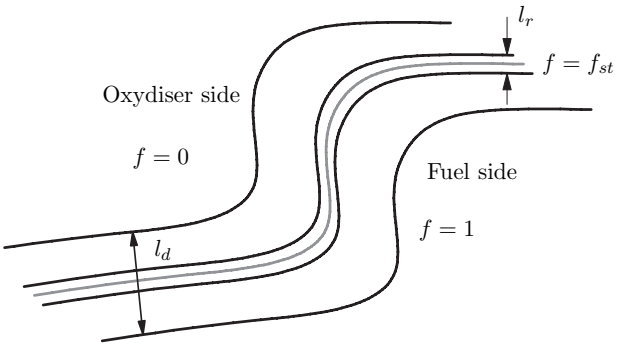

Figure 4.2: Diffusion and reaction layer thickness in a diffusion flame [2].

important [2].
When a flame is laminar, the flame surface is smooth. In case of a turbulent flame it will become curved and bent. This is depicted in figure 4.2.
The diffusion layer is the zone where fuel and oxydiser mix. Beside fuel and oxydiser, reaction products exist in this zone. These products come from the reaction layer. The thickness of this reaction layer is much smaller than the diffusion layer. This is because reaction only takes place in a range which is close to the stoichiometric ratio. The thickness of this layer is estimated by [2, 51]:

$$l_r = l_d \left(Da^{fl} \right)^{-1/a} \tag{4.11}$$

where $a = 1 + \nu_F + \nu_O$. In case of a laminar flame, Da is the already defined Da^{fl} and when the flow is turbulent the Damköhler number is:

$$Da^{turb} = \frac{1}{\tau_c \tilde{\chi}_{st}} \tag{4.12}$$

in which $\tilde{\chi}_{st}$ is the stoichiometric scalar dissipation rate.
It is clear from equation 4.11 that the reaction zone becomes thinner when the Damköhler number increases.

The here described model uses a global reaction for all combustible species. For a fuel like syngas that is a very rough estimation. It is hard to couple one Damköhler number to syngas. The chemical times of CO and H_2 differ a lot. Also the diffusion rate of hydrogen is a lot different from that of CO. Beside that, the mixing behaviour as such is very important and hard to estimate with some rules of thumb. For those reasons, more detailed models are necessary.
Therefore, CFD flow solvers will be used to solve the mixing problem. Beside that, in first instance, the chemical reactions will be modelled by CFX chemical

models. After that, a chemical model, based on a reaction progress variable will be introduced.

4.2 CFD

The tool of Computional Fluid Dynamics (CFD) has been used to several purposes in the project. First of all, CFD was used during the design of the burner. It proved to be a valuable tool for this purpose. Flow field and temperature can be predicted within an accuracy which is hard to get from rules of thumb.
Later in the project CFD has also been applied for the prediction of noise levels (chapter 5) and the flame transfer function (chapter 7).

The Navier-Stokes (NS) equations describe the transport of mass and momentum in a flow. The flow through the burner and in the combustor is turbulent. Solving the NS equations requires a lot of computational power. When the flow is turbulent the computational power increases tremendously. Several different approaches can be applied for the solution of the turbulent NS equations. Figure 4.3 gives an overview of these approaches. The figure shows the wave number of the turbulence on the horizontal axis and the turbulence kinetic energy of the vertical axis. The smaller the wave number, the bigger the turbulence structures.
With Direct Numerical Simulations (DNS) all turbulence structures are calculated, not matter how small they are. With RaNS the effects of turbulence on mixing are modelled. The time averaged equations are solved and the unknown additional terms in these equations are modelled. Finally, Large Eddy Simulation (LES) can be used. In the LES approach, the equations are also time averaged, but only for the small time scales. Larger time scales are directly simulated. This introduces a cut-off wave number k_c. Below the k_c, LES simulates the turbulence directly. Above the cut-off wave number, the turbulence is modelled by time averaging.
Both LES and DNS can be very accurate models. However, these models require huge computational costs. As RaNS models all the turbulence, it is a much cheaper model in terms of computational power. For this reason, RaNS is used in this thesis. Another advantage of RaNS is the possibility of steady state calculations. DNS and LES can only be solved in a transient fashion.

4.2.1 Geometry

In this project two different geometries were used to define the computational domain of the CFD simulations. One, large geometry was used for the steady

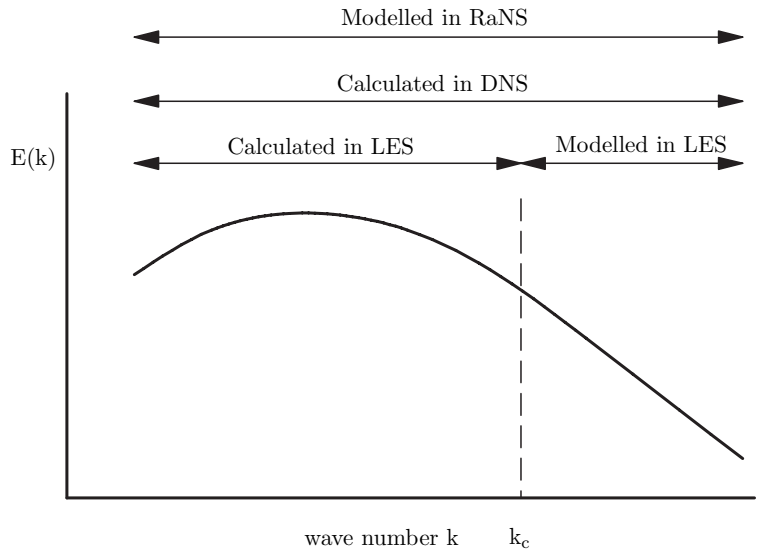

Figure 4.3: Turbulence energy spectrum plotted as function of wave numbers. k_c is the cut-off wave number. [2]

state calculations. A smaller geometry was built for the transient calculations. In figure 4.4, a section view of the large geometry is depicted. This geometry includes all the important flow components. The burner with all swirl vanes is included, the air plenum and the air inlets to the air plenum. The combustor is located downstream of the burner. At the exit of the combustor, a diaphragm is located. The diaphragm is a flow constriction to ensure a reflective boundary condition for acoustic waves. As it also influences the mean flow, it should be included in the CFD calculations as well. Using such a large geometry in a CFD calculation is rather expensive in computational time as those details use a large number of grid cells. The large geometry is built up from approximately 2,500,000 elements.
The smaller geometry is shown in figure 4.5. In this geometry the burner and the air plenum are not included. Moreover, only a quarter of the combustion chamber is included. This saves a lot a elements. However, this approach assumes that the flow in the combustor is periodic. Therefore, periodic boundary conditions can be imposed on the intersection planes. Although the combustor is square, the assumption of periodicity can be done as the corners of the square are dead flow regions, not influencing the flow significantly.
In the case that the burner is not included in the geometry, Mason [52] advises to include an adequate length of the inner passage. This means that the burner mouth and the fuel and air passages upstream should be included in

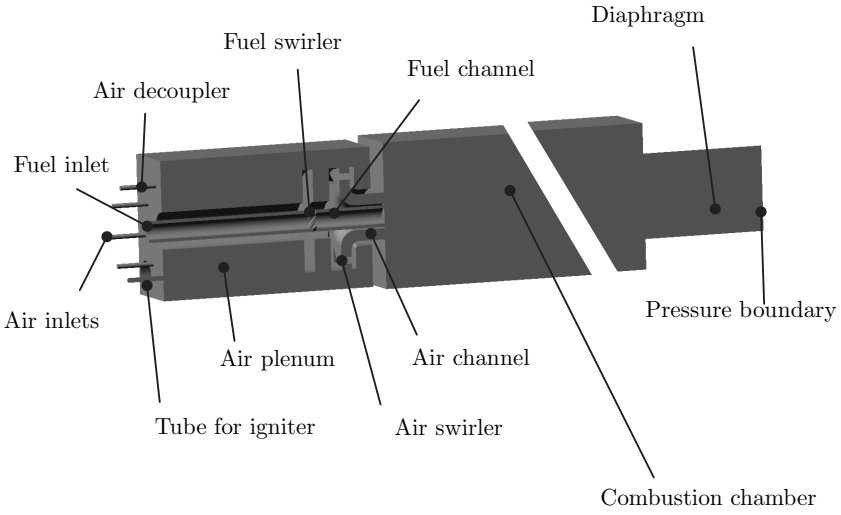

Figure 4.4: A section view of the large geometry

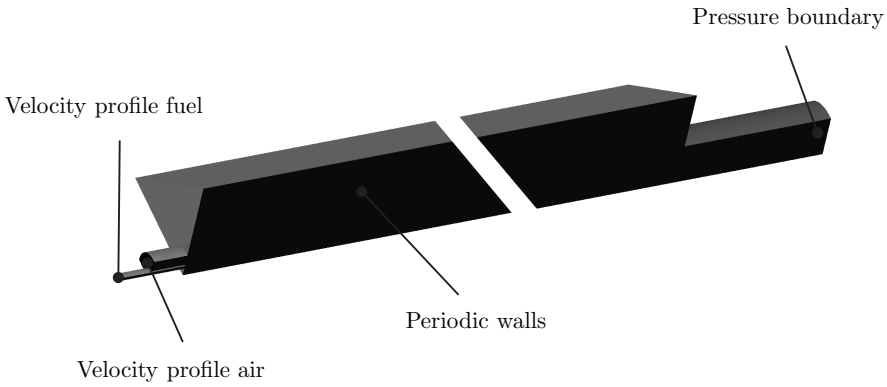

Figure 4.5: The small geometry with the applied boundary conditions

the geometry. This allows the flow to develop in the burner.
The boundary conditions for the small geometry are imported from the large geometry. Velocity and turbulence profiles are exported from the large geometry to the exact locations of the inlets of the small geometry. These velocity profiles include information about the upstream swirlers.
Figure 4.6 shows an overview of how the CFD modelling is set up. It shows which path is followed to the results. It also indicates which geometries are used and which type of calculation (steady state/ transient) was applied.

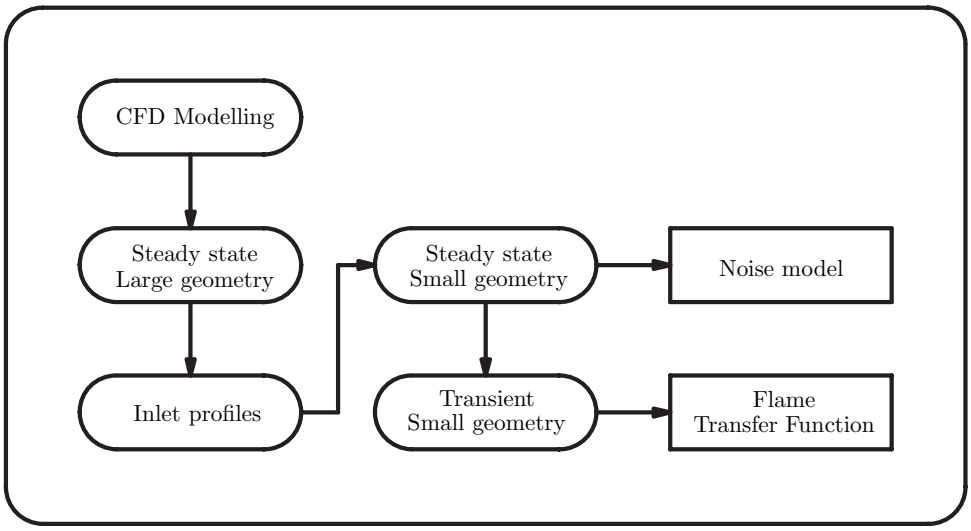

Figure 4.6: Overview of the applied geometries and models

4.2.2 RaNS equations

The Reynolds averaged Navier Stokes (RaNS) equations are obtained by Favre averaging the Navier Stokes equations. The Favre average is defined as [53]:

$$\tilde{A} = \frac{\overline{\rho A}}{\overline{\rho}} \tag{4.13}$$

where $\overline{\rho}$ represents the so-called Reynolds average:

$$\overline{\rho}(\mathbf{x}, t) = \frac{1}{T} \int_{-T/2}^{T/2} \rho(\mathbf{x}, t + \tau) d\tau \tag{4.14}$$

where T is a time scale, larger than those of turbulent fluctuations. Using the Favre method of averaging, the transient, compressible and adiabatic equations for mass, momentum and enthalpy conservation become:

$$\frac{\partial \overline{\rho}}{\partial t} + \nabla \cdot (\overline{\rho}\tilde{\mathbf{u}}) = 0 \tag{4.15}$$

$$\frac{\partial \overline{\rho}\tilde{\mathbf{u}}}{\partial t} + \nabla \cdot \left(\overline{\rho}\tilde{\mathbf{u}} \otimes \tilde{\mathbf{u}}^T\right) = \nabla \cdot \left(\sigma - \widetilde{\overline{\rho}\mathbf{u}''\mathbf{u}''}\right) \tag{4.16}$$

$$\frac{\partial \overline{\rho}\tilde{h}_{tot}}{\partial t} + \nabla \cdot \left(\overline{\rho}\tilde{\mathbf{u}}\tilde{h}_{tot}\right) = \nabla \cdot \left(\overline{\rho}\alpha\nabla\tilde{h}_{tot} - \widetilde{\overline{\rho}h''_{tot}\mathbf{u}''}\right) \tag{4.17}$$

in which the superscript " indicates a fluctuation on the Favre average and σ is the viscous stress tensor:

$$\sigma = 2\mu\dot{D} - \frac{2}{3}\mu\left(\nabla\cdot\tilde{u}\right)\mathbf{I} - \tilde{p}\mathbf{I} \tag{4.18}$$

where $\dot{D} = \frac{1}{2}\left[(\nabla\tilde{u})^T + \nabla\tilde{u}\right]$ is the tensor indicating the rate of strain. Due to the averaging step of the momentum and enthalpy equations, two terms that need more attention are introduced: the product of fluctuating quantities. For the momentum equation this is the so-called Reynolds stress: $-\widetilde{\overline{\rho}\mathbf{u}''\mathbf{u}''}$ and for the enthalpy equation the turbulent convective heat flux: $-\widetilde{\overline{\rho}h''_{tot}\mathbf{u}''}$. The mean quantities are calculated by solving the conservation equations, but these terms need modelling. The problem arising from these terms is often called the closure problem. By introducing the *eddy viscosity hypothesis* the effects of turbulence on the mean flow variables can be modelled:

$$-\widetilde{\overline{\rho}\mathbf{u}''\mathbf{u}''} = 2\mu_t\dot{D} - \frac{2}{3}\left(\mu_t(\nabla\cdot\tilde{u})\mathbf{I} + \rho\tilde{k}\mathbf{I}\right) \tag{4.19}$$

$$-\widetilde{\overline{\rho}h''_{tot}\mathbf{u}''} = \kappa_t\nabla\tilde{h}_{tot} \tag{4.20}$$

where μ_t represents the turbulence viscosity, κ_t the turbulence diffusivity and k the turbulence kinetic energy. The turbulence kinetic energy is determined by the $k-\epsilon$-model [54].
Conservation of k is also calculated by a transport equation:

$$\frac{\partial\overline{\rho}\tilde{k}}{\partial t} + \nabla\cdot\left(\overline{\rho}\tilde{\mathbf{u}}\tilde{k}\right) = \nabla\cdot\left[\left(\mu + \frac{\mu_t}{\sigma_k}\right)\nabla\tilde{k}\right] + P_k - \overline{\rho}\tilde{\epsilon} \tag{4.21}$$

The dissipation of k is called ϵ and is modelled by:

$$\frac{\partial\overline{\rho}\tilde{\epsilon}}{\partial t} + \nabla\cdot\left(\overline{\rho}\tilde{\mathbf{u}}\tilde{\epsilon}\right) = \nabla\cdot\left[\left(\mu + \frac{\mu_t}{\sigma_k}\right)\nabla\tilde{\epsilon}\right] + \frac{\tilde{\epsilon}}{\tilde{k}}\left(C_{\epsilon1}P_k - C_{\epsilon2}\overline{\rho}\tilde{\epsilon}\right) \tag{4.22}$$

where P_k is the turbulence production due to viscous and buoyancy forces and μ_t and κ_t are defined as:

$$\mu_t = C_\mu\overline{\rho}\frac{\tilde{k}^2}{\tilde{\epsilon}} \tag{4.23}$$

$$\kappa_t = \frac{\mu_t}{Pr_t} \tag{4.24}$$

The constants used in the $k-\epsilon$-model are displayed in table 4.1.

$C_{\epsilon 1}$	$C_{\epsilon 2}$	C_μ	σ_k	σ_ϵ	Pr_t	Sc_t
1.44	1.92	0.09	1.0	1.3	0.9	0.9

Table 4.1: Constants used in the $k-\epsilon$ model, as proposed by Launder and Sharma [54].

4.2.3 Discretisation

This section will discuss the discretisation that has been used in the CFD calculations. For spatial discretisation, a first order upwind scheme is applied. When first-order upwinding is selected, the cell face value is set equal to the cell-center value of the upstream cell. Although this does introduce numerical diffusion, second order schemes were not robust enough.
The transient term is approximated by the so-called second order backward Euler scheme:

$$\frac{\partial \phi^n}{\partial t} = \frac{\frac{3}{2}\phi^n - 2\phi^{n-1} + \frac{1}{2}\phi^{n-2}}{\Delta t} \tag{4.25}$$

where ϕ^{n-2} represents the solution field from the time step before the old time level. This scheme is robust, implicit, conservative in time and does not create a time step limitation. It is also second-order accurate in time, but is not bounded and may hence create some non-physical overshoots or undershoots in the solution [55].

4.2.4 Combustion by CFX

Next to the flow and the turbulence, also the combustion process needs to be modelled. In the introduction of the chapter some general properties were already presented. Now, continuing with equation 4.2 from the introduction and applying Favre averaging on this equation gives:

$$\frac{\partial \overline{\rho}\tilde{Y}_i}{\partial t} + \nabla \cdot \left(\overline{\rho}\tilde{\mathbf{u}}\tilde{Y}_i - \left(\overline{\rho}\mathcal{D} + \frac{\mu_t}{Sc_t} \right) \nabla(\tilde{Y}_i) \right) = \overline{\dot{\omega}_i} \tag{4.26}$$

This equation includes the diffusion effects caused by the turbulence by the term of $\frac{\mu_t}{Sc_t}$, where μ_t is defined in equation 4.23 and the turbulence Schmidt number Sc_t is a fitted constant, displayed in table 4.1.
In this equation the term of $\overline{\dot{\omega}_i}$ is the chemical source term. The combustion of syngas is modelled by the following three global reactions:

$$\begin{aligned} 2H_2 + O_2 &\rightarrow 2H_2O \\ 2CH_4 + 3O_2 &\rightarrow 2CO + 4H_2O \\ 2CO + O_2 &\rightarrow 2CO_2 \end{aligned} \tag{4.27}$$

For hydrogen, the mixed-is-burnt estimation is applied, as the combustion reaction of hydrogen is very fast. For both CO and CH_4, a one step global mechanism is used. This global mechanism assumes an Arrhenius temperature dependence:

$$\dot{\omega}_i = A_i T^{\beta_i} e^{-\frac{E_i}{RT}} \tag{4.28}$$

Where A_i is the pre-exponential factor, β_i is the dimensionless temperature exponent, E_i is the activation energy, R is the gas constant and T the absolute temperature.
When more accuracy is desired, the chemistry can also be approached by a model based on a reaction progress variable. This is explained in section 4.3.

4.2.5 Noise prediction by CFD

In thermoacoustics, autonomous noise and coupled acoustics can be dealt with separated. For the prediction of the coupled acoustics, the thermoacoustic model (presented in chapter 3) is used. For the autonomous noise, steady state CFD can be applied. Klein [3] and Kok [56] already presented a model that was able to predict noise, radiated by a turbulent flame. De Jager [57] has made this model applicable for a TFC combustion model and later also for the CFI model [58]. In this section it will be briefly explained how the noise levels were predicted in this project.
First of all, a so-called Von-Kárman turbulence spectrum is assumed. This spectrum is based on steady state RaNS CFD. This method is described in [58]. The Lighthill wave equation for acoustic pressure fluctuations is the base. The flame is assumed to act as a monopole source. The solution for the acoustic pressure (equation 11 from [59]) is defined as a volume integral of the square of the gradient of the mixture fraction f:

$$p'(x_0,t) = \frac{c_0}{S} \int\int\int \rho \mathcal{D} A^* \delta\left(f - f_{st}\right) \nabla f \cdot \nabla f \,\Big|_{\underline{x}, t-\left|\frac{x_0 - x}{c_0}\right|} dV \tag{4.29}$$

where $\mathcal{D}$ is the diffusion coefficient, A^* is a sound generation constant and δ is the Dirac function. To compare the results from this model with the experiments, the acoustic model of chapter 3 is used as an intermediate. This noise model creates results assuming that the flame is situated in an semi-infinite tube. The sound pressure levels during the experiments are measured in a setup which is certainly not semi-infinite. How the setup during firing acoustically behaves can be simulated quite accurately by the acoustic model. Now from experiments, the acoustic source of the flame can be determined by the acoustic model. When this acoustic source is then used as an input for an acoustic model with boundary conditions like the combustion chamber is

a semi-infinite tube, the noise model can be validated.
The noise level finally is calculated with equation 35 from [59]:

$$pp(f) = 2\pi \left[\frac{c_0}{S}\right]^2 \sum_{i=1}^{ncel} \left[\left(\rho \mathcal{D} B \overline{A^*}\right)^2 \frac{J l_{cor,y_2} l_m}{2\overline{u}} E^2 \left(\frac{2\pi f}{2\overline{u}}\right) \right]_i V_i \qquad (4.30)$$

where B is a constant from scalar dissipation, J is the Jacobian of the coordination transformation to flame sheet coordinates, l_{cor} is a correlation length corresponding to the radial location in the flame, $\overline{u}$ is the mean velocity and E is the turbulence energy spectrum. Kok and De Jager [58] have coupled the noise prediction tool to a CFD calculation with the CFI combustion code. The source term of the reaction progress variable, S_c, is used as the source term for the calculation of the sound spectrum. The cases here considered use the CFX combustion models and thus the chemical source of these models is used as input for the noise prediction.
The results of this method are reported in the chapter 5.

4.3 Reduction of chemical databases by CFI

Using chemical models from commercial codes usually can give rather quick and very reasonable results. However, the combustion model presented up to this point simplifies the chemistry. The model does not take any interaction between the fuel components into account. Beside the lack of interaction between the species, the turbulence also does not have an effect on the chemistry. It is shown [25] that the temperature is dependent on turbulence fluctuations. Fluctuation in the temperature can seriously influence the local reaction rate. The CFX-10 embedded model assumes a δ-PDF distribution. Calculating the solution for a turbulent CFD problem including detailed chemistry and turbulence parameters like PDF distribution is very costly in terms of computational effort. A detailed chemical mechanism like GRI 3.0 involves 325 reactions with 53 species. For this reason, the detailed chemistry is often reduced. The big and complex chemistry schemes often carry a lot of reactions which are so fast they do not contribute significantly to the accuracy of the chemical reaction rate. Reduction of these big chemical schems is possible with the so-called Intrinsic Low Dimensional Manifold (ILDM) [60,61]. Another method, analogous to ILDM is called Computational Singular Perturbation (CSP) [60,62,63]. A final method is the intuitive elimination of small reaction time scales [64].
This section will explain the use of the CFI combustion model, based on the reduction method of CSP. The CFI model is a generic tool for reducing big chemical mechanisms. It has been developed in the Laboratory of Thermal

Engineering and has been published in [63, 65–67]. This has all been summarised and generalised for premixed combustion by Derksen [24]. Derksen has used it with the GRI 3.0 mechanism, but De Jager [68, 69] has shown that the tool is generally applicable. He successfully used it for even bigger mechanisms than GRI 3.0. He made it also applicable for non-premixed and non-adiabatic combustion.
Instead of solving the transport equation for all of the species in the chemical mechanism, the CFI combustion model defines composed species mass fractions. The dimensionless deviation of these composed species from equilibrium defines a set of Reaction Progress Variables (RPV's). These composed species mass fractions are linear combinations of all species in the mechanism. Transport equations are solved for the composed species mass fractions. Another variable, the Reaction Progress Variable (RPV) expresses the measure of chemical equilibrium. Together with the fuel mixture fraction, the RPV's determine the chemical composition. The CFI model generates a database where all chemical species, temperature and density are made dependent on the RPV's and the fuel mixture fraction. This is done prior to the actual CFD calculation. It has been shown by Louis et al. [67] that the construction of the composed species can be done intuitively for small reaction mechanisms like the combustion of syngas. For more complex mechanisms a computational tool is used for this purpose. As already mentioned, this tool is called CSP. It was was introduced by Lam and Gousis [62] and Massias et al. [70]. This chapter will explain how the CFI model works and how the CSP reduction is applied. Also the use the CFI combustion model with non-premixed syngas and methane enriched syngas is discussed in this chapter.

4.3.1 The CFI combustion model

The name of the CFI combustion model is derived from the C (reaction progress variable) F (mixture fraction) and I (enthalpy variable). The use of the model can be divided into several stages:

- First of all, a detailed chemical mechanism is chosen. As well as syngas as methane enriched syngas are used as a fuel in this project, so the most convenient mechanism to choose is GRI 3.0. This mechanism consists of 325 reactions, 53 species and 5 elements. As it is not relevant for primary combustion processes, the reactions concerning NO_x production are excluded from the mechanism. In appendix A, the mechanism that is used is presented.

- This detailed mechanism is used as an input for laminar flame solutions. These solutions can be obtained by the packages PREMIX or Cantera.

- The laminar solution is the input for the next step, CSP S-STEP. The CSP algorithm is able to make a division between slow and fast species in the chemical mechanism. A brief introduction to the algorithm is given in section 4.3.3. By applying the CSP algorithm, the non-linear behaviour of the chemical source terms is removed.
- Once slow and fast species are identified, a laminar database is built. All variables in the database are stored as a function of the Reaction Progress Variables and the mixture fraction.
- The last step also takes the turbulence effects into account and lead to the turbulent database, the final step in the CFI model.

4.3.2 Laminar solutions

In figure 4.7 detailed flame solutions are depicted. These solutions are obtained with Cantera. Cantera is an open source, object oriented software package for problems involving chemically reacting flows [71]. In contrast with PREMIX it is also able to calculate diffusion flames. For both cases, the pressure is atmospheric, both inlet temperatures are 293 K and the fuel/air mass flow ratio is stoichiometric.
The profiles presented in figure 4.7 are all normalised. Figure 4.7 shows some typical profiles for counterflow, non-premixed flames. The horizontal axis represents the length of the reactive domain and the vertical axis the normalised temperature or concentration. In these plots the fuel enters the domain from the left and the air from the right. The conditions are taken from the cases Syn1Cold and Meth1Cold.
The main reason why the resulting flame of Meth1Cold is shifted to the left compared to the Syn1Cold case is the mass flow of fuel. The difference in stoichiometric ratio (0.44 for Syn1Cold and 0.30 for Meth1Cold) is another reason. As the fuel of Meth1Cold has a higher calorific value (7.8, compared to 5 MJ/kg), a lower mass flow is needed to meet the same power conditions. For this reason, the flame moves to the fuel side. From the plots it can be concluded that the flame front of the Meth1Cold flame is more narrow than the flame front of the Syn1Cold flame.

4.3.3 CSP algorithm

A big and complicated chemical mechanism like GRI 3.0 usually consists of a wide variety of reaction time scales. The fast time scales make these systems very stiff [70]. Moreover, solving a transport equation for every species is computationally very expensive. In an effort to reduce the solving time and for

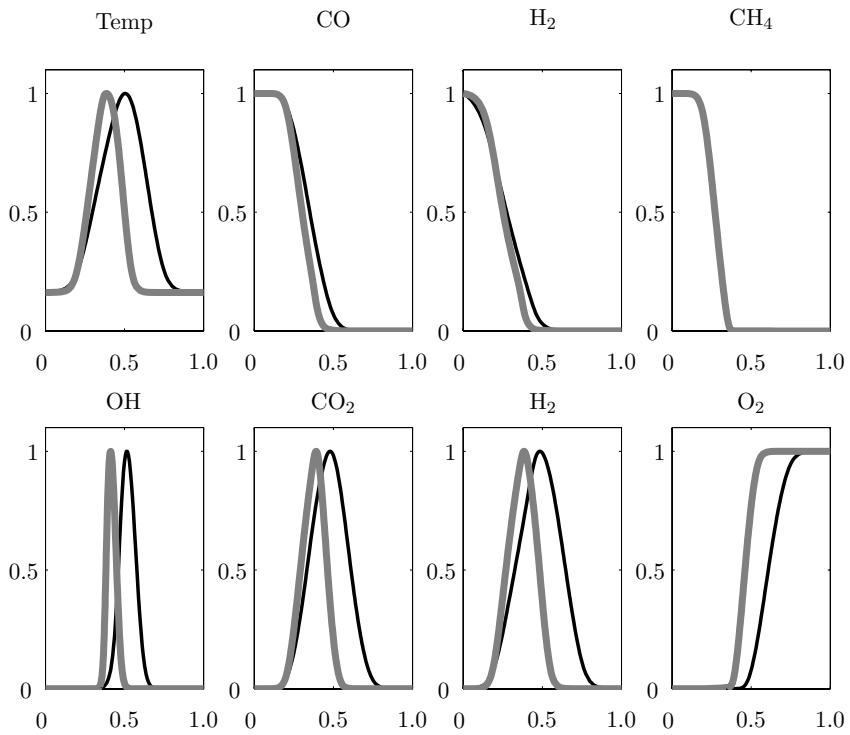

Figure 4.7: Normalised values of the temperature and some species concentrations of the laminar flame solution calculated by Cantera of the Syn1Cold (black) and Meth1Cold (gray) cases. On the horizontal axis , the distance is displayed.

more physical understanding, it is important to identify the most significant physical parameters.

Considering the composition of a chemical system as a point in composition space [25], this composition can be seen as a multi-dimensional space in which each dimension represents the concentration of a chemical species. The composition point will move through this space by the chemical reaction rate. The fast chemical reactions will move this point towards a certain manifold. This manifold can be spanned by the basis vectors consisting of only a part of the complete domain and is usually called the low-dimensional manifold [24]. This manifold can be determined by the method of CSP. This is done by identifying the species which are associated with fast chemical time scales, the so-called steady state species and by setting up element balances.

Starting with an extensive chemical mechanism, consider a vector $\boldsymbol{\eta}$ that has

components composed by:

$$\eta_j = b_{ij} y_i \tag{4.31}$$

In this equation, $\boldsymbol{\eta}$ is a linear combination of all species in the chemical mechanism and is called the composed species. N is the number of species in a chemical mechanism, $\mathbf{b}$ is the matrix indicating which are the fast species, which are the element balances and to what extent the chemical species participate in the composed species. Y is the vector with mass fractions of all species.
The matrix $\mathbf{b}$ can be divided into three parts:

$$\mathbf{b}^r = [b^1, .., b^M]^T \tag{4.32}$$

Where $\mathbf{b}^r$ is the vector containing the steady state species. This vector contains the fast part of the chemical system. M is the number of time scales that is faster than the locally dominant ones and varies from 0 to N-1.

$$\mathbf{b}^c = [b^{S+1}, .., b^N]^T \tag{4.33}$$

The vector $\mathbf{b}^c$ represents the element conservation relations. The number of elements E.

$$\mathbf{b}^s = [b^{M+1}, .., b^S]^T \tag{4.34}$$

The vector of $\mathbf{b}^s$ is the vector with the slow species. This vector contains the species represented in the composed species. Moreover, $S = N - M - E$ is the dimension of the low dimensional manifold.

$$\mathbf{b}^c = [b^{S+1}, .., b^N]^T \tag{4.35}$$

Finally, the vector $\mathbf{b}^c$ represents the element conservation relations. The number of elements E.
At this point, enough equations are defined to solve a system of N equations. Now, $\boldsymbol{\eta}^s = \mathbf{b}^s \mathbf{Y}$ is the low dimensional manifold. The dimension of this manifold is equal to the number of CSP reactions. The progress of these reactions is expressed in so-called Reaction Progress Variables (RPV's). Despite the name, the RPV's actually indicate the measure of equilibrium of the CSP reaction. The RPV value runs from 0 to 1. An RPV value of 1 indicates full chemical equilibrium. A value of 0 is the furthest away from chemical equilibrium. For a more extensive description of the CSP method, the reader is referred to the PhD thesis of Derksen [24] and the article of Massias et al. [70].
Once the CSP has been carried out and the matrices $\mathbf{b}$ and $\boldsymbol{\eta}$ are known, the j^{th} RPV reads:

$$c_j = \frac{\eta_j - \eta_j^u}{\eta_j^{eq} - \eta_j^u} \tag{4.36}$$

Where the superscript u stands for an unburnt and eq for an equilibrium situation. The mixture fraction is defined as:

$$f = \frac{\eta - \eta^{air}}{\eta^{fuel} - \eta^{air}} \tag{4.37}$$

Where the superscript air indicates the air inlet and $fuel$ the fuel inlet.
In contrast to the RPV's, the mixture fraction does not have a source term. And so, in case of a premixed situation, f will be constant. As this thesis only considers non-premixed cases, the mixture fraction will vary throughout the domain as a conserved variable. For the RPV's as well as the mixture fraction, a transport equation is solved. This transport equation is derived in appendix B of [24] by Derksen.

4.3.4 Laminar databases

One of the important outputs of the CSP algorithm is the $\mathbf{b}^s$ vector, the vector with the participation factors of every species in the composed variable. De Jager [69] has shown that this vector is not unique: *multiple vectors will allow for a mathematical correct solution for the definition of this* $\mathbf{b}^s$*, but it is found that not all of these vectors will behave correctly in physical space.*
To check whether the calculated $\mathbf{b}^s$ behaves correctly in physical space, the $\mathbf{b}^s$ vector can be used in the solution of a laminar flame calculation as is done in figures 4.10, 4.11 and 4.12. These plots show a monotone relation between the reaction progress variable and the source term, temperature and OH concentration. In case the $\mathbf{b}^s$ vector is not valid in physical space the monotone behaviour would be lost [69].
Figure 4.8 shows the three different possible $\mathbf{b}^s$ vectors. All $\mathbf{b}^s$ vectors are mathematically correct vectors for a CSP reduction with one RPV. All these vectors are representing one (and also the same) equation: the description of the slow system. The vector at the left hand side shows that from the fuel and air components (O_2 N_2, H_2 and CO), only O_2 is represented in the composed species. The second and third vector do contain values for H_2 and CO. They also include large values of intermediant species. All vectors showed to behave correctly in physical space. Following Derksen [24] the vector on the left hand side in figure 4.8 is used for further applications.
CSP reduction can also point out differences between two cases. Figure 4.9 shows the difference between the $\mathbf{b}^s$ vectors of the Syn1Cold and the Meth1Cold cases. This figure points out the influence of methane addition to syngas on the $\mathbf{b}^s$ vectors. It shows that $\mathbf{b}^s$ does not change for species concerning CO and H_2 combustion. As both CO and H_2 do not appear in the $\mathbf{b}^s$ of Syn1Cold this makes sense. It does also not change for O_2, a component that does appear in $\mathbf{b}^s$ of Syn1Cold.

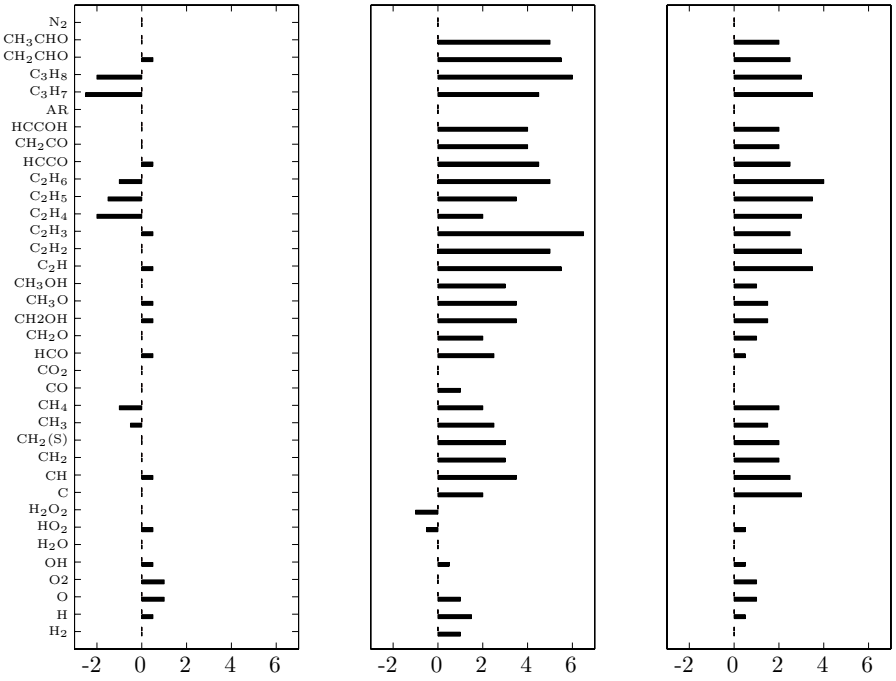

Figure 4.8: Different CSP definitions for the slow chemical manifold in a stoichiometric Syn1Cold flame.

4.3.5 Laminar database validation

Using the results of the CSP reduction a database can be built. This database is a storage of temperature and species concentration. The running variables in this database are the mixture fraction and one RPV. Two databases are assessed. One for the case Syn1Cold and one for Meth1Cold. In this section, the quality of these databases will be determined by validation.

A validation is carried out with PREMIX. PREMIX is a one dimensional flame solver, using detailed chemistry. Two cases will be compared, based on the source term of the RPV, the temperature and the OH concentration. To be able to make a comparison, at each location x of the detailed solution, the value of $c_j(x)$ is obtained. Using this value of $c_j(x)$, the database results can be plotted for this location. The PREMIX data can also be plotted as a function of $c_j(x)$. Now, the database and the PREMIX solution can be compared. Figure 4.10 shows the differences in the source for the reaction progress variable and agreements between the databases of the Syn1Cold and Meth1Cold cases. The black line represents a database quantity in every plot and the

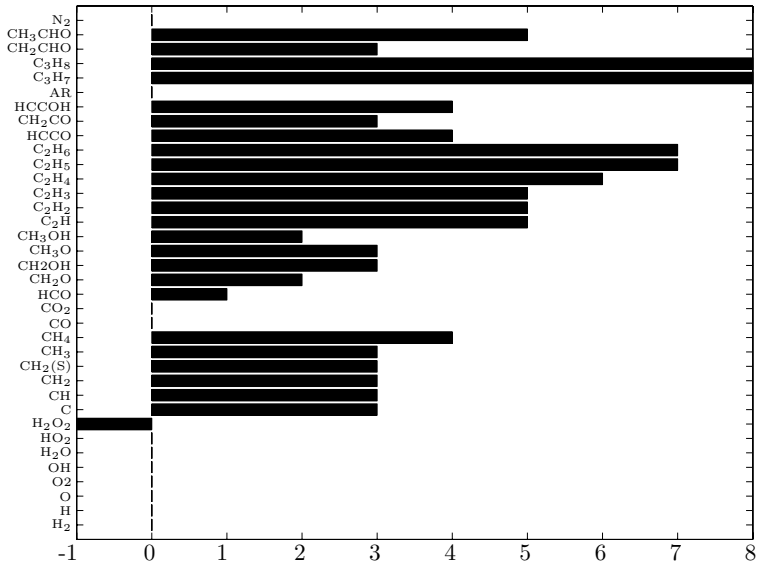

Figure 4.9: Difference between CSP definitions for the slow chemical manifold between the Syn1Cold and Meth1Cold case in a stoichiometric flame.

gray line the PREMIX solution. In figure 4.10a, a large deviation between the database and PREMIX solution can be noticed. However, this will not disturb the usage of the database in a CFD calculation. Both the inlet of air and fuel will have an RPV value of 1. This represents chemical equilibrium. When mixing between fuel, air and hot products occurs, the mixture will be pushed away from this equilibrium, but not further than RPV=0.7 as results in chapter 5 show. From RPV=0.7 the system again moves back to equilibrium. This holds for the case Syn1Cold as well as for Meth1Cold. Taking this into account, the deviations from the PREMIX solution will not be large. The source for the Meth1Cold case shows even a better agreement for the relevant RPV interval.

Figure 4.11 shows the temperature from both the PREMIX and the database solution. Especially in the high temperature region the agreement between the two sets of data is very good. In figure 4.11b it is very clear that the software that calculates the databases starts to interpolate between the imposed value of RPV=0 and the calculated value of RPV=0.2. This behaviour can be observed in most of the plots, but in figure 4.11b it is very obvious. Also here, the slight deviations of the database solution and the PREMIX solution will not cause deviations in the CFD calculations as these deviations all appear in the region below RPV=0.7.

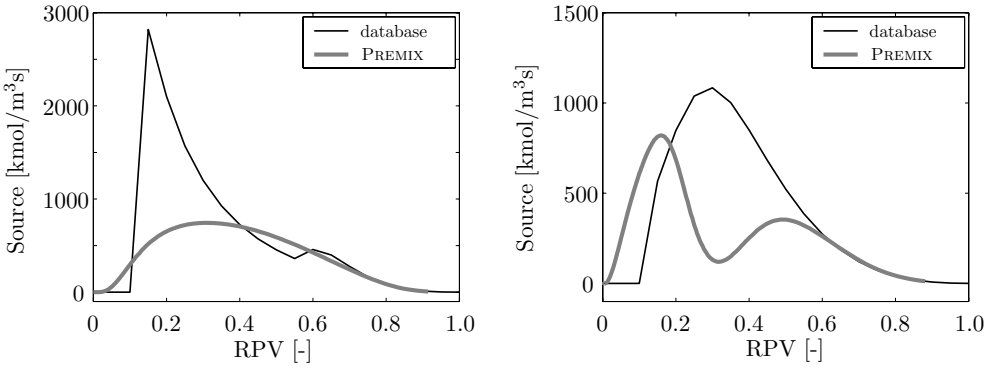

(a) Source Syn1Cold (b) Source Meth1Cold

Figure 4.10: Comparison of chemical source term of Syn1Cold and Meth1Cold case between the laminar database and the PREMIX solution, based on the Reaction Progress Variable.

In figure 4.12 the validation of the OH prediction of the databases is depicted. Again, for values above RPV=0.7, the agreement is very good. Below RPV=0.7, the trend of the PREMIX solution is followed quite well. Compared to Derksen using the CFI code [24], the OH results are very accurate. In figures F.1 and F.2 in the appendices, the source term and the temperature are depicted for the databases of Syn1Cold and Meth1Cold. They are plotted dependent on the one and only RPV and the mixture fraction. Depending on those two variables, the source term and temperature can be presented as a surface. Similar effects as in the figures 4.10 can be noticed: an excessive growth of the chemical source term for low values of the RPV. However, as already mentioned, it is most unlikely that the database will be accessed for these low values by the flow solver.

4.3.6 Laminar database behaviour

In the previous section (in figure 4.10), the laminar database of Syn1Cold showed some extraordinary behaviour. At low values for the RPV, the chemical source term climbed to extreme values. When approaching the RPV value of 0, the code interpolates the chemical source to 0. This extreme value of the source term could point out a shortcoming of the CFI model. For that reason, more attention to the completion of the laminar database is paid. As already mentioned, the $\mathbf{b}^s$ vector indicates which species take part in the composed variable.
Taking a closer look at this vector, it shows that some species have an influ-

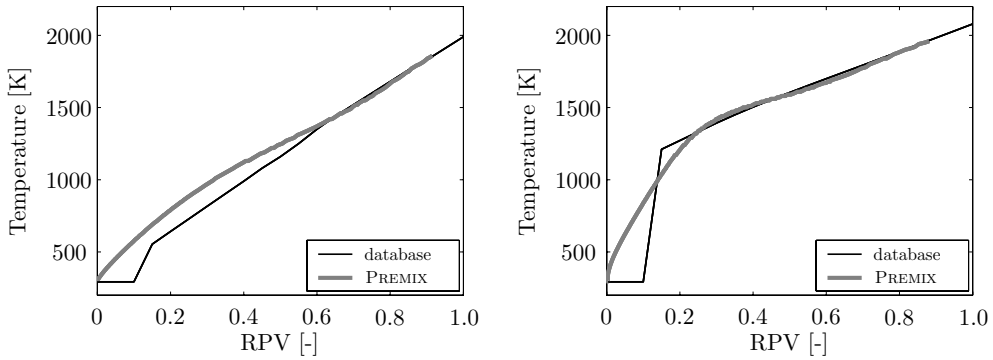

(a) Temperature Syn1Cold (b) Temperature Meth1Cold

Figure 4.11: Comparison of the temperature of Syn1Cold and Meth1Cold case between the laminar database and the PREMIX solution, based on the Reaction Progress Variable.

ence which at first sight seems to be out of proportion. Some species with very low concentration ($< \mathcal{O}(10^{-4})$ mass%) do contribute to the chemical source term. To gain insight in this phenomenon, the contribution of each species to the source term was specified. It shows that some species with very low concentrations have large contributions. In the case of Syn1Cold these species are HO_2 and H.
Figures 4.13 and 4.14 present the effect of several manual modifications in the $\mathbf{b}^s$ vector. Figure 4.13a shows the unmodified laminar database. In figure 4.13b the database only contains species that meet a manually chosen concentration criterion. Species with a lower concentration than 10^{-4}mass% are no longer contributing to the chemical source term. In this specific case, the contributions from the species HO_2 and H were eliminated. In a next step, only contributions from species considered as major species (CO, CO_2, H_2, H_2O and O_2) are allowed in the chemical source term. Of course, this contribution is only accredicted in the case that the $\mathbf{b}^s$ also allows that. This means that only O_2 determines the source term in figure 4.14. This has an even stronger effect and is depicted in 4.14. So, in this specific case the global reaction is controlled by major species only. This seems very straight forward, but it is not. Application of these modifications to other cases (the Meth1Cold case) showed that it was not possible to build the global reaction only from major species. So the CFI code can supply mathematically correct solutions, but they should always be interpreted with care.

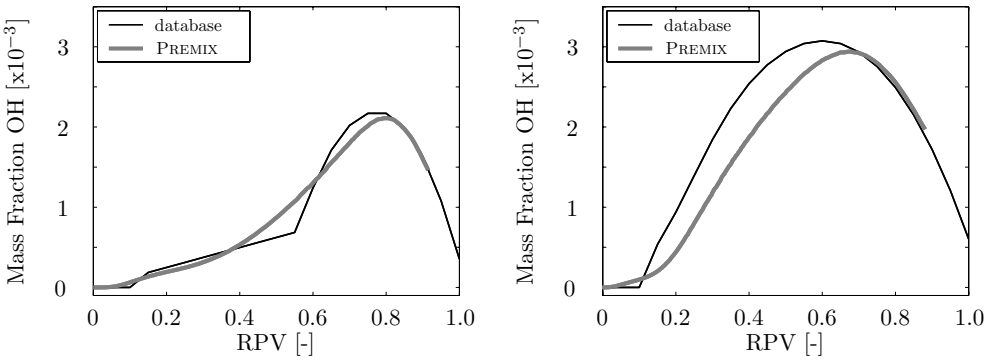

(a) OH Syn1Cold (b) OH Meth1Cold

Figure 4.12: Comparison of the OH concentration of Syn1Cold and Meth1Cold case between the laminar database and the PREMIX solution, based on the Reaction Progress Variable.

4.3.7 Turbulent database

To make the transport equations applicable in turbulent combustion calculations with a RaNS code, the running variables c_j and f need to be decomposed into a mean and a turbulence fluctuation. In the database for laminar combustion, all variables (temperature, density and mass fractions of species) are stored as a function of c_j and f. In the database for turbulent combustion these variables will become functions of $\mathbf{c}$, $\mathbf{c}''$, f and f''. In case of an adiabatic flow:

$$\widetilde{T} = \widetilde{T}\left(\widetilde{\mathbf{c}}, \widetilde{\mathbf{c}''^2}, \widetilde{f}, \widetilde{f''^2}\right) \tag{4.38}$$

$$\widetilde{\mathbf{Y}} = \widetilde{\mathbf{Y}}\left(\widetilde{\mathbf{c}}, \widetilde{\mathbf{c}''^2}, \widetilde{f}, \widetilde{f''^2}\right) \tag{4.39}$$

$$\overline{\rho} = \overline{\rho}\left(\widetilde{\mathbf{c}}, \widetilde{\mathbf{c}''^2}, \widetilde{f}, \widetilde{f''^2}\right) \tag{4.40}$$

The Favre averaged of these variables will then read:

$$\widetilde{\phi} = \frac{1}{\overline{\rho}} \int_{\mathbf{c}=\mathbf{0}}^{1} \int_{f=0}^{1} \rho\phi\left(\mathbf{c}, f\right) P\left(\mathbf{c}\right) P\left(f\right) \mathrm{d}\mathbf{c}\mathrm{d}f \tag{4.41}$$

In this expression $P(\mathbf{c})$ and $P(f)$ are the probability density functions (PDF) of $\mathbf{c}$ and f respectively. It is assumed that $\mathbf{c}$ and f are statistically independent. Also, for $\mathbf{c}$ and f a β-PDF is assumed. Derksen [24] presents a more detailed derivation of the Favre averaging of scalars and transport equations.

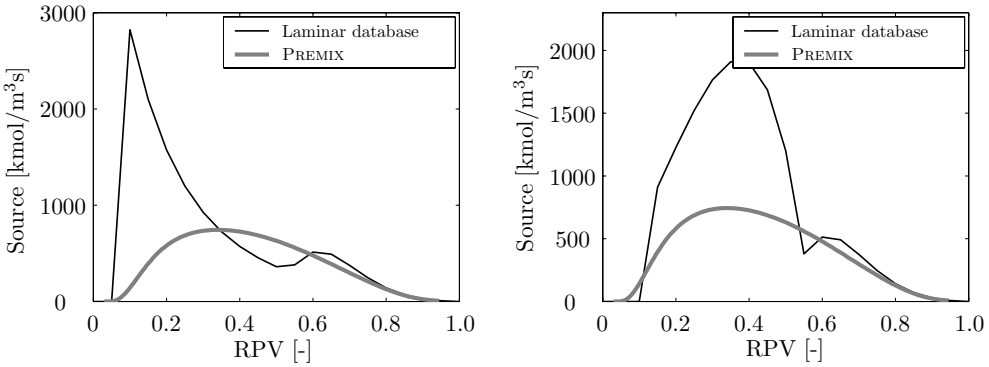

(a) Complete database

(b) Database with a concentration condition

Figure 4.13: Several influences on the laminar database of case Syn1Cold.

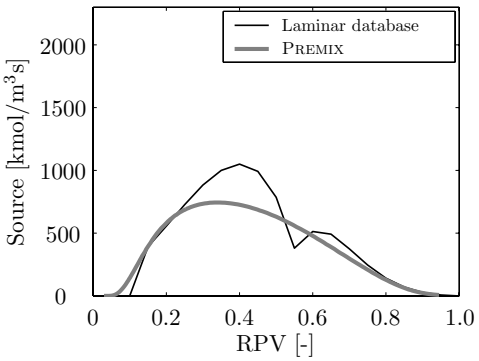

Figure 4.14: Database of Syn1Cold with only major species.

4.4 Conclusions

In this chapter, the modelling approaches of the combustion process were described. For the CFI model, some analysis work has been carried out. The results of the database are compared with results from PREMIX. Especially for high values of the reaction progress variable, the results of the database look very promising. For low values the results from the database and from PREMIX show major differences, but the flow solver will not access this part of the database as will be shown in the next chapter.

5
Steady state results

5.1 Introduction

This chapter will present and discuss all modelled and measured cases at constant fuel and air mass flow. These cases are considered as turbulent combusting flows in steady state.
First of all, CFD results will be presented. Results for both standard Cfx chemistry models and the Cfi chemistry model are shown. Subsequently, both chemistry models will be validated against experimental data from Tsurikov et al. [22] from Dlr Stuttgart. The Cfx models will be validated based on the heat release. The Cfi model will be compared with the measured chemiluminescence intensity of OH^*.
The noise model, a CFD tool to predict autonomous noise from flames is validated with measured acoustic data. For simplicity, the noise model uses boundary conditions other than present in the experimental setup. For this reason, the acoustic model from chapter 3 is applied to compare the noise model and measurements in a fair fashion.
Finally, the steady state turbulent flame acting as an acoustic source is experimentally analysed for all set points (see chapter 2 for details). Steady state acoustic power spectra are used as an input for the acoustic model to identify the acoustic source. These acoustic sources are compared with high frequency OH^* intensity measurements which are carried out in the Laboratory of Thermal Engineering. The results of these measurements can be reconstructed in frequency dependent OH^* sources. Comparing the OH^* source with the acoustic source gives valuable information on assumptions that are done in modelling.

5.2 CFD results

Steady state CFD calculations have been performed with two types of chemistry models: the CFX chemistry model and the CFI model. These models were presented in chapter 4.

5.2.1 CFX results

First of all, some cases calculated with CFX chemistry are presented. To be able to compare the results with each other, the legends of all results are identical.
Figure 5.1 depicts the steady state results of the Syn1Cold case. The figure is

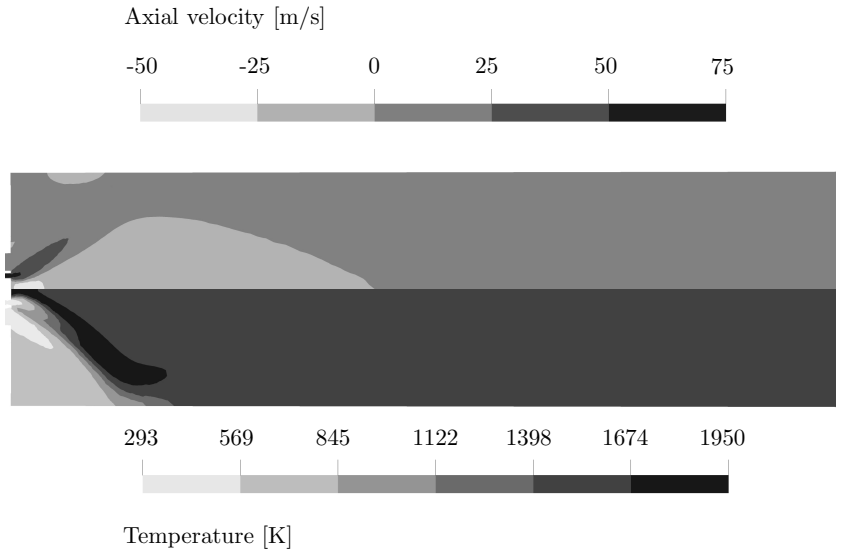

Figure 5.1: Syn1Cold case flow field and temperature contour predicted with the CFX chemistry model.

divided into two parts. The upper part shows a contour plot of the axial flow field and the lower part a contour plot of the temperature field. The axial flow field shows a well defined recirculation zone. At the hub of the burner, the axial velocity reaches high and negative values. The hot product gases are deflected in radial direction by the central part of the burner core. This does not cause any overheating as the burner is cooled well enough by the cold fuel flow surrounding the burner core. These backward flowing hot product gases mix with fresh fuel and air. Heat transfer from the hot gases to the fresh gases ignites them. In the lower part of the figure, the temperature field is

shown. It shows that close to the burner, the high temperature appears inside the recirculation zone. Further downstream the high temperature region coincides with the shear layer between the forward and backward flowing gases.
Figure 5.2 presents the results of case Meth1Cold. That is the case with

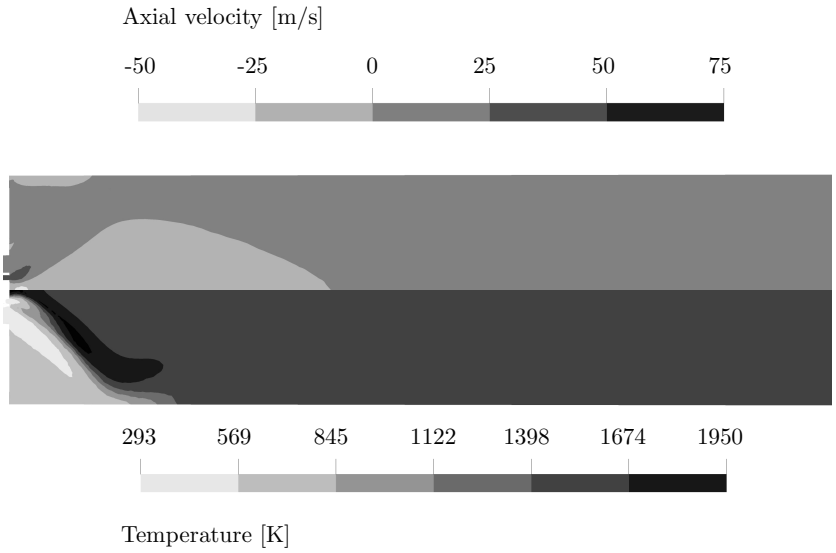

Figure 5.2: The predicted flow field and temperature contour predicted by the CFX chemistry model of the Meth1Cold case.

atmospheric combustion of methane containing syngas with cold combustion air. The results look similar to the results of case Syn1Cold in figure 5.1. However, the recirculation zone of Meth1Cold is shorter. As the calorific value of the methane containing syngas is higher than the syngas without methane (7.8 compared to 5 MJ/kg) the fuel flow velocities are lower. Lower flow velocities induce a smaller recirculation zone.

5.2.2 CFI results

Beside the CFX combustion models, also the combustion model CFI has been applied to some cases. This model is also described in chapter 4. Figure 5.3 shows the flow field and the temperature field of the Syn1Cold case. The recirculation zone is slightly shorter than the Syn1Cold case calculated with the CFX combustion model. In the temperature contour it can be seen that instead of one high temperature contact with the core of the burner, the CFI

case has two contacts. One is in the narrow part of the recirculation zone, close to the burner. The other high temperature contact with the burner is with the partition of the fuel and air. Another difference between the CFX and the CFI model can be found in the temperature field. The CFI model predicts a much smoother temperature field than the CFX chemistry model. The CFX model was used in a three step version, with global kinetic rates for both CO and CH_4 combustion in the flame. For H_2 a mixed-is-burnt assumption was made. In retrospect this consumption of H_2 may have been dependent on kinetic rates as well. Hence, the assumption of global equilibrium being incorrect and leading to steep gradients in the flame. This is handled more accurately by the CFI model.
As described in chapter 4, CFI obtains its information from a preprocessed

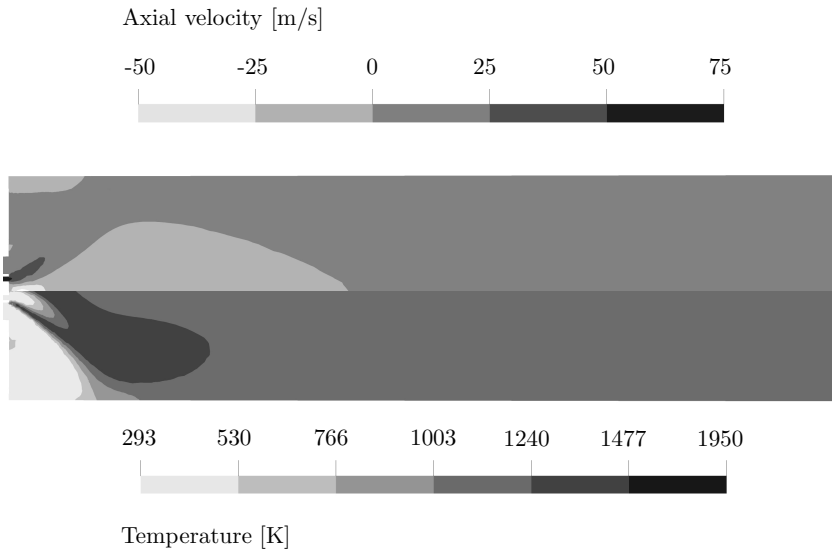

Figure 5.3: Syn1Cold case flow field and temperature contour modelled with CFI chemical model.

database. This database has stored variables like temperature and species concentration based on a varying fuel mixture fraction and a reaction progress variable.
Figure 5.4 shows the fuel mixture fraction field together with the reaction progress variable field. The mixture fraction varies from 0 in the air inlet to 1 in the fuel inlet. The mixing in the combustion chamber leads to a variety of values in the fuel mixture fraction. Also, the recirculation zone has a major influence. This recirculation zone brings back hot products which

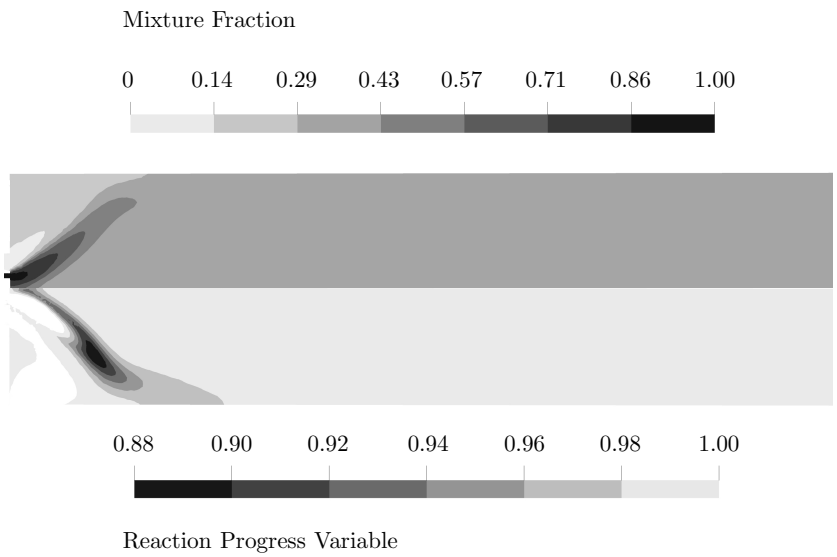

Figure 5.4: Syn1Cold case mixture fraction field and reaction progress variable contour modelled with CFI chemical model.

have a mixture fraction value close to the value of reaction reaction products. The high mixture fraction value from the fuel inlet is curved around the recirculation zone and decays with distance until the mean value is reached. The mixture fraction is a conserved variable. So it is not produced or consumed during mixing or combustion. For this reason, the exit value of the mixture fraction is just the average value of the fuel and air flow, weighted with their mass flows.
The reaction progress variable is 1 on both inlets, fuel and air. So instead of reaction progress variable, chemical equilibrium variable would have been a better name. After all, it is a measure for how far away the mixture is from chemical equilibrium. In the fuel and air inlet, the flows are stable and do not contain any driving forces to react. After mixing, a new chemical equilibrium has to be reached. At this point, the reaction progress variable has two driving forces. Mixing fuel and air makes the mixture chemically less stable, it drives the variable away from equilibrium, away from unity. Chemical reaction (in this case combustion) brings back stability in the mixture. And so, it brings the reaction progress variable back to unity. As combustion of hydrogen containing fuels is fast, the reaction progress variable will not be driven away very far from equilibrium. For infinitely fast combustion, the reaction progress variable would be 1 in the entire domain. According to

figure 5.4, the reaction progress variable is 1 in large areas, but goes down to 0.88 in a small region. This is the region where the flame is located. In chapter 4 the applicability of the database was checked. It showed that the database for the case of Syn1Cold can be applied with good accuracy for values of the reaction progress variable between 0.7 and 1. The reaction progress variable for this case has a bottom value of 0.88. So the dependent values from the database are applied in a high accuracy range.

5.2.3 Noise model

Another steady state phenomenon is the autonomous noise from turbulent flames. The noise model as introduced in chapter 4 is able to predict sound pressure levels at the upstream end of the combustor based on steady state CFD calculations. It uses the Green's solution of a semi-infinite length combustion chamber. However, the acoustic pressures in the experimental setup

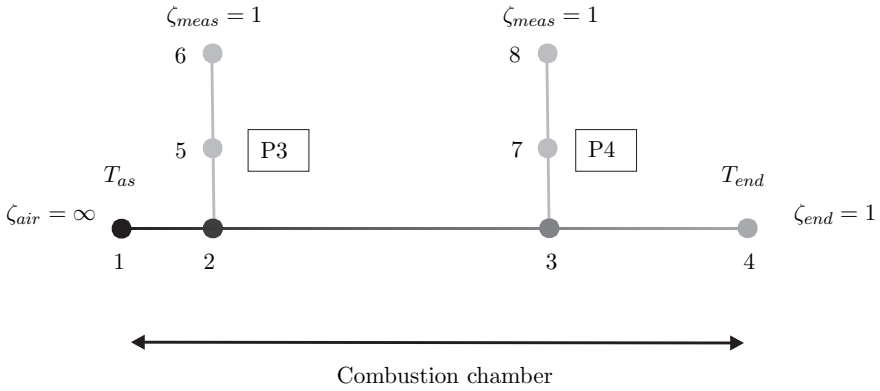

Figure 5.5: The acoustic model used for validation of the noise model.

are measured in a finite length combustion chamber. To compare the results from the noise model with the measurements, the acoustic model from chapter 3 is used again. First of all, the acoustic source from a measurement is reconstructed using the inverse method (see chapter 3 for more details and section 5.4.2 for all the reconstructed acoustic sources). After this, the reconstructed acoustic source is now used as an *input* of the acoustic model for the semi-infinite length combustor. Hence, the acoustic model is now applied with new boundary conditions, meeting the boundary conditions of the semi-infinite combustion chamber as used in the noise model. This means that a non-reflecting boundary (ζ=1) is used at the exit of the combustion chamber.

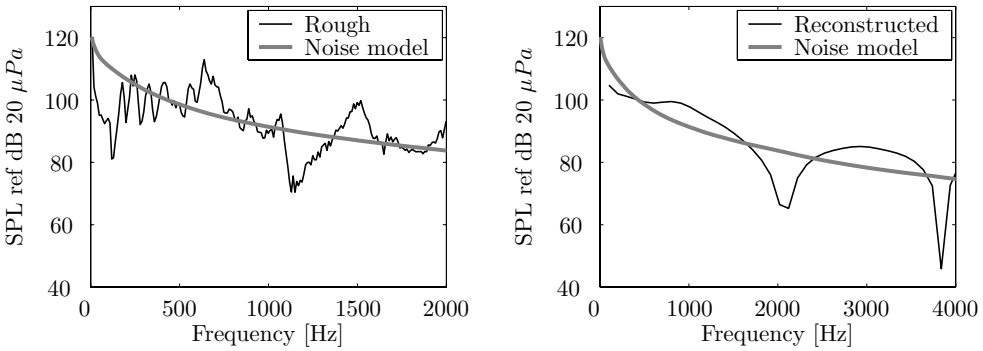

(a) Rough measurement (b) Reconstructed measurement

Figure 5.6: The modelled sound pressure level by the noise model validated by the measured sound pressure level and validated by the reconstructed measurement for case Syn1Hot.

The measured reconstructed acoustic pressure can now be compared with the noise modelled by the noise model.
Figure 5.5 shows the acoustic model as it is used for the comparison between the measured acoustic pressures and modelled noise by the noise model. Like the Green's solution in the noise model, only the combustion chamber is included in the acoustic model. Apart from the hard boundary at the entrance ($\zeta_{air} = \infty$) of the combustion chamber, all boundaries are non-reflective ($\zeta_{meas} = \zeta_{end} = 1$).
Figure 5.6 presents at the left hand side the results of the comparison between the sound pressure level (SPL) predicted by the noise model and measured SPL for the case of Syn1Hot. At the right hand side, the noise model is compared with the reconstructed measurements.
The comparison with the rough measurements shows agreement in the general trend. The resonance frequencies in the experimental setup are not predicted by the noise model as this is not incorporated.
In the reconstructed measurements, the resonance frequencies of the system are still present, but have shifted as the impedance at the exit has changed from hard reflective to non-reflective. In the results of chapter 3, a resonance frequency around 1000 Hz could be identified. With the noise model, this resonance frequency is present at approximately 2000 Hz. As the first standing wave has changed from half a wave length into a quarter wave length, this makes sense. The noise model predicts the overall trend due to the Von Kárman spectrum. The noise model does not predict the deviation from the Von Kárman spectrum. At frequencies below 100 Hz, the noise model is pre-

dicting significantly higher levels than is measured. This is because of the assumption of the Von Kárman spectrum in the noise model. This spectrum is known for its limitations in low frequencies regions [72]. As proved in chapter 3, the acoustic model captures all important acoustic features of the combustion chamber. So this method should provide a good validation of the noise model.
At this point, only case Syn1Hot is validated. Investigation of the other cases showed that this case is representative for all investigated cases.

5.3 OH^* Measurements DLR Stuttgart

Measurements have been carried out at the DLR Combustion Institute in Stuttgart by Tsurikov et al. [22] and at the Laboratory of Thermal Engineering of the University of Twente. The DLR has focused on the OH^* chemiluminescence measurements in a fashion that was introduced in chapter 2. Their data are used to validate the CFD results in this study. Measurements

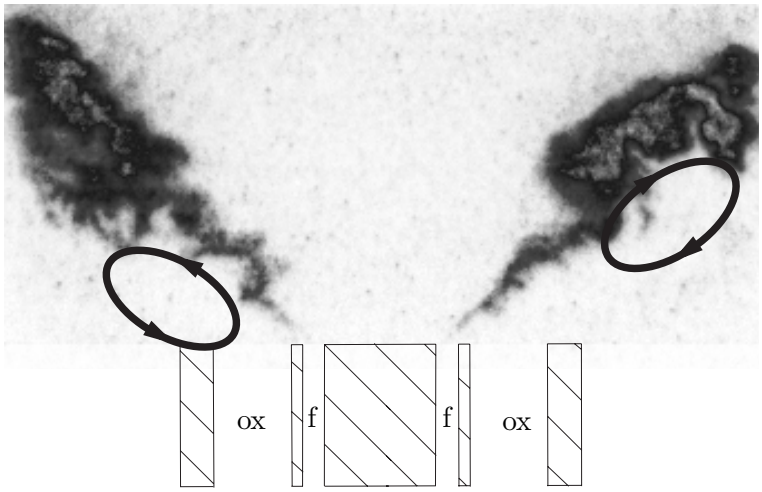

Figure 5.7: A single shot OH PLIF measurement of one of the investigated cases from DLR Stuttgart.

that are carried out in the Laboratory of Thermal Engineering also include OH^* chemiluminescence, but these measurements were more focused on the frequency dependent flame source identification based on OH^* intensity. The results of these measurements are presented in the next section (section 5.4).
OH concentrations have also been measured by PLIF: Planar Laser Induced Fluorescence. Instead of measuring the spontaneous light, OH molecules are

excited by a laser beam. For a very short period in time, the molecules jump to another energy level. When the excited molecules fall back in their original state, light is emitted. This light can be measured. More information about PLIF can be found in [73, 74].
The chemiluminescence measurements of the DLR [22] showed good agreement with the and the PLIF measurements. For validation ends, the chemiluminescence data were used.
Figure 5.7 shows a single shot OH PLIF measurement of the HEGSA combustor

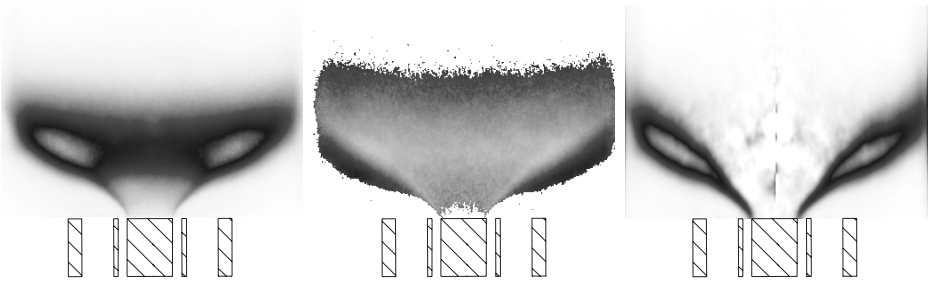

(a) Averaged (b) Fluctuation (c) Deconvolved

Figure 5.8: Chemiluminescence measurement of Syn2Cold case from DLR Stuttgart [22].

at DLR Stuttgart [22]. With this single measurement, the mixing behaviour of the burner can be shown to a certain extent. As the velocities in the fuel channel are significantly higher than the velocities in the air channel, a shear force will build up at the interface of these two flows. When this shear force becomes large enough, one side of the flow can roll over to the other side (indicated by the circular arrows). In this case the fuel flow rolls into the air flow indicated by the arrows. The large shear force leads to fast mixing.
In figure 5.8 the processing of an OH* chemiluminescence measurement is depicted. The fuel and air are fed from below. In the figure at the left hand side, the average value of the light emitted by the OH* radicals is shown. This is an average of 2600 images. The area surrounding the flame does not contain any excited OH*. In the flame region, the darker the figure, the more OH* was measured. However, the enclosed areas containing lighter colours indicate more intense light emission than the dark zones. Next to the average, the fluctuating value can be determined, this is shown in figure 5.8b. In the near region of the flame large fluctuations can be noticed. Further away the fluctuations decrease until a value of zero is reached. Finally, a deconvolution method is applied to the data. This deconvolution method (Abel transforma-

tion) was mentioned in chapter 2. The result is shown in figure 5.8c. In this figure, a well defined flame can be observed. Immediately after leaving the burner, the fuel and the air start reacting and both flows bend outward. At a certain point the flame gets more intense. Finally the flame bends slightly to the top of the combustor. Note that the flame stabilises at the burner core. Results like in figure 5.8c can be compared with CFD calculations.

5.3.1 CFD validation with DLR measurements

The CFD calculations will be validated in this section in two different ways. First of all, PIV measurements are used to validate the flow field. After that, the combustion is validated by OH^* chemiluminescence measurements.

PIV Measurements

At the DLR in Stuttgart some PIV measurements [22] were carried out. PIV is an acronym for Particle Image Velocimetry. In this method small inert particles are added to the reacting flow. A high speed camera captures

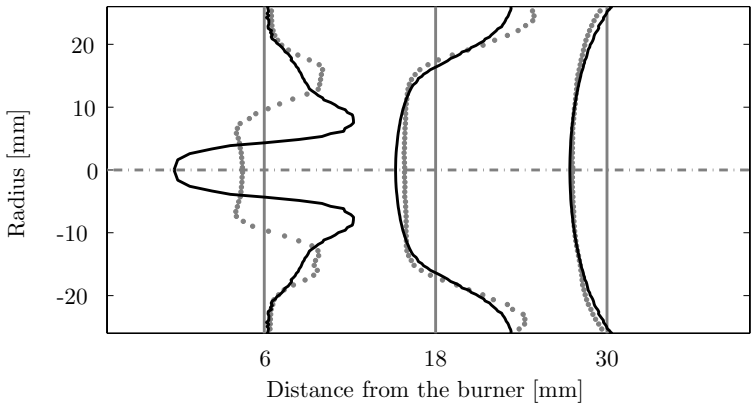

Figure 5.9: Mean dimensionless axial velocity profiles of simulation results of mixture 6 (——) and PIV measurements (. . .).

the motion of these particles. In order to measure the velocity at least two exposures are needed [22]. They can be recorded on one or several frames. The frames are split in a large number of interrogation areas, often called tiles. It is then possible to calculate a displacement vector for each tile with help of signal processing (auto-correlation/cross-correlation). This is converted to a velocity using the time between image exposures. This method is only reliable

up to a certain maximum velocity. For this reason, the PIV measurements were carried out at half the power of the project set points and atmospheric pressure . This means that the velocities are also halved. For more details, the reader is referred to [22]. The PIV measurements were carried out for two different set points. One with mixture 6 and one with mixture 7 (see chapter 2). Preheating was omitted.
Figures 5.9 and 5.10 shows the validation of three cross-sectional planes in

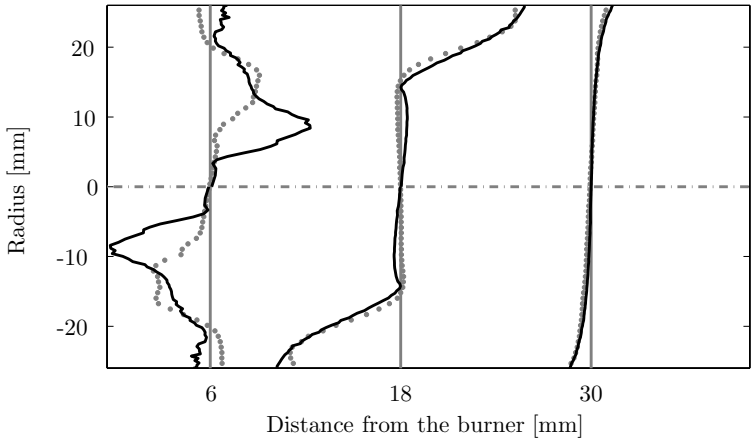

Figure 5.10: Mean dimensionless radial velocity profiles of simulation results of mixture 6 (——) and PIV measurements (. . .).

the combustor. The cross-sections are located at 6 mm, 18 mm and 30 mm from the burner exit. The PIV camera was able of capturing approximately 58 mm of the flow field in cross dimension. Figure 5.9 presents the mean dimensionless axial velocity and figure 5.10 shows the mean dimensionless radial velocities. Close to the burner, at 6 mm from the burner exit, the CFD calculation deviates from the measurements. The recirculation zone is predicted stronger and more narrow. At 18 mm the CFD is much more in agreement with the PIV measurements. Towards the investigated boundaries there is some deviation, but in the centre of the flow it is very similar to the PIV data. The cross-section at 30 mm shows also good agreement. Although it seems that at 30 mm, the entire flow has a negative velocity, in reality this view is limited by the capturing width of the camera. Outside the image the flow is positive.

In figures 5.11 and 5.12, the PIV validation of mixture 7 is depicted. These figures show similar results. Close to the burner, the CFD simulation deviates

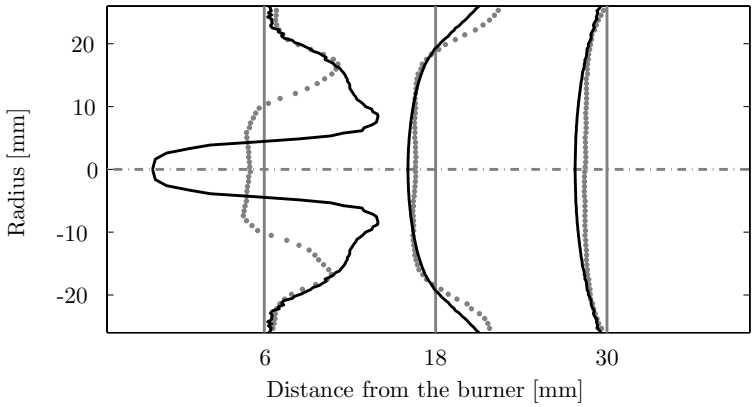

Figure 5.11: Mean dimensionless axial velocity profiles of simulation results of mixture 7 (——) and PIV measurements (. . .).

from the PIV measurements, but further away from the burner agreement increases. It should be noted that close to the burner PIV measurements can be inaccurate. In this region, the velocities are close to the maximum handling velocity of the PIV method. For this reason, the measurements can become inaccurate [75]. Validation is hence not carried out close to the burner.

OH* chemiluminescence

Beside the flow field also, OH* radicals can be measured. As shown in the previous section, the DLR in Stuttgart has carried out those experiments [22]. The figures in this section show the qualitative comparison between the heat release field and the OH* measurement of DLR Stuttgart for the CFX calculations. The results from the CFI model will be validated based on OH concentration. Although the OH* measurements could not capture the whole combustion chamber, the whole flame is visible. The width of the chamber is 45 mm and the camera can capture 33 mm. The presentation of the predicted data takes this into account and is also plotted for this radius. Both prediction and measurement will not be accompanied by a legend as it is a qualitative comparison, using chemiluminescence it is not possible to quantify the measured species.
Figure 5.13 shows the prediction of the heat release by the CFX chemical model validated with the measured OH* data for the Syn1Cold case. On the left hand side, the predicted heat release is depicted and the measured OH* is shown at the right. At a first glance prediction and measurement do not look

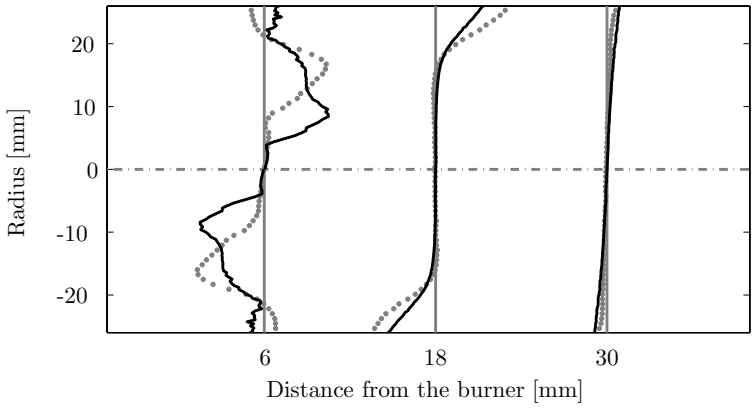

Figure 5.12: Mean dimensionless radial velocity profiles of simulation results of mixture 7 (——) and PIV measurements (. . .).

alike very much. The CFX model predicts a combustion front at the hub and one between the fuel and the air. Only the hub combustion front is measured. This latter front thrives on the oxygen remaining in the hot circulated flow. But a property that is very important for flame dynamics, the flame length, is predicted well. At the resolution of the acoustic length scales the comparison between CFD and the measurement is very good.
The two combustion models (for CO and H_2 combustion) that were applied in this prediction can both be distinguished. The dark area near the burner exit shows the rapid combustion of hydrogen. The length of the flame points out the slow combustion of carbon monoxide. As a result of high turbulence in the recirculation zone, some additional chemical activity can be seen in the centre of the combustor. In the measurement data some disturbance can be seen on the axis. This is probably not OH*, but a result of the Abel transform of the measurement. Although the coupling of OH* concentration and heat release is questionable, a better agreement between modelling and measuring result would be expected. Nevertheless, Tribuzi [76] has shown that using a very rough grid (which did not even capture the recirculation zone of the flow), the main acoustic phenomena could still be identified.

Figure 5.14 shows the OH* concentration for the Syn1Cold case, predicted by the CFI model on the left hand side and the measured OH* concentration by DLR Stuttgart [22]. In the predicted OH* field, the recirculation zone in plotted. As mentioned before there is a difference between measured OH and

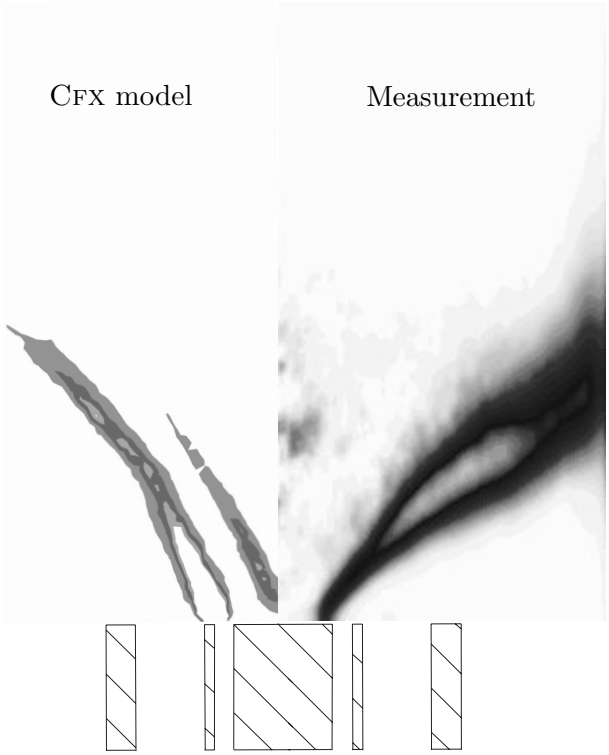

Figure 5.13: Qualitative comparison between heat release prediction, modelled by a Cfx model and measured OH* by chemiluminescence at Dlr Stuttgart [22] for the Syn1Cold case.

excited OH*. The latter is emitting light spontaneously. The Cfi model does not predict OH*, but OH. Although for validation of predicted OH excited OH* is used, this does not introduce any errors.
The predicted OH can be correlated with the reaction progress variable in figure 5.4. The lower the RPV value, the more OH is produced. The OH production takes place on the border of the recirculation zone.
Figure 5.14 shows that the prediction of OH by the Cfi is in good agreement with the measured OH*. The Cfi model predicts one combustion front, like the measured data: at the hub in the mixing zone of fuel and flue gases. The angle of the flame with the central axis shows good agreement and also the length is well predicted. In both predictions and measurements the flame stabilises at the burner hub and not on the partition between the fuel channel and the air channel. The fresh cold air will be heated by the flame and will

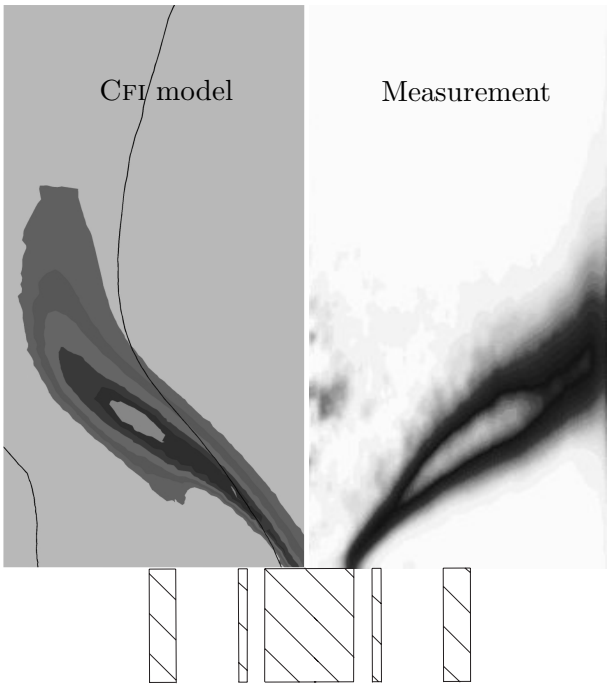

Figure 5.14: Qualitative comparison between OH* prediction, modelled by the Cfi model and measured OH* by chemiluminescence at Dlr Stuttgart [22] for case Syn1Cold.

then be recirculated. Fuel and hot recirculated air will mix and ignite. The predicted OH on the centre of the hub is probably an effect of the definition of the chemical source term of the Cfi model and the flow solver. The flow solver predicts significant negative axial velocities on the axis of the combustor. These high velocities cause high values of k and ϵ. Both of these variables are used in the chemical source term of the Cfi model. So when the flow field will be predicted more accurately, the Cfi model will also achieve better results. The influence of the turbulence will be discussed later in this section.

In figure 5.15 the case of Meth1Cold is validated. This is methane containing syngas with cold combustion air. The predicted OH concentration from the Cfi model is compared with OH* measured by chemiluminescence. The

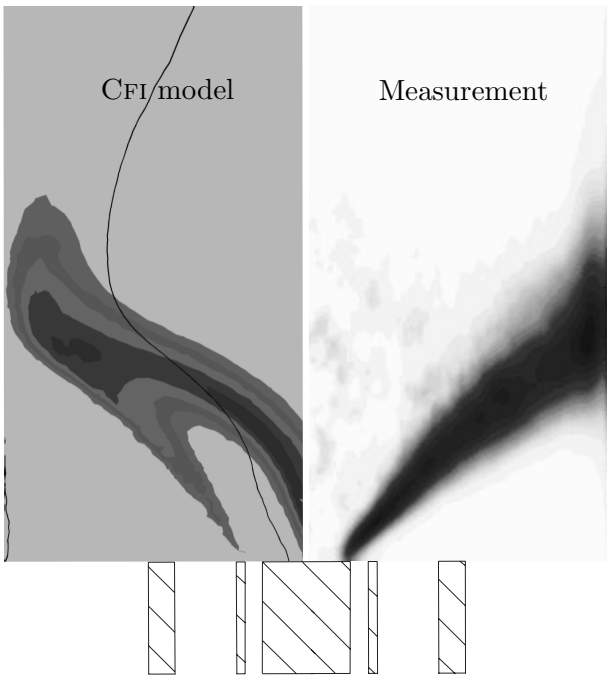

Figure 5.15: Qualitative comparison between OH* prediction, modelled by the CFI model and measured OH* by chemiluminescence at DLR Stuttgart for case Meth1Cold.

figure shows that the angle of the flame with the central axis is again well predicted. Moreover, at the far end of the flame, the prediction agrees well with the measurement. However, the effect that could already be observed in some extent in the Syn1Cold case has become more distinct, the back flow on the burner hub, introduces chemical activity on the hub. This chemical activity results in predicted OH that does not appear in the measurement.

5.3.2 Discussion

Turbulence

In the previous section it has been indicated that the predicted turbulence might have influence in the results predicted by the CFI model. This is not surprising as both k and ϵ show up in the mixing term ([24]):

$$\overline{\phi'' \mathbf{u}''} \propto \frac{k^2}{\epsilon} \tag{5.1}$$

When the recirculation zone is overpredicted, the mixing term is over predicted. This leads to a large driving force for chemical activity. Oxygen is still available as λ=2.
Figure 5.16 depicts the turbulence kinetic energy of the Meth1Cold case, using the CFI model. Also the recirculation zone is included. It shows that the turbulence kinetic energy is concentrated in and around the first diameter length of the recirculation zone. On the axis of symmetry, where the OH is predicted in high concentrations, the turbulence kinetic energy is also very high. Although the turbulence eddy dissipation also reaches its highest values in this region, the turbulence kinetic energy appears squared in the mixing term.

OH concentration and heat release correlation

Beside the turbulence, another discussion can be started on this validation. It is questionable whether the light, emitted by OH* radicals gives us information about the heat release of the flame. Schuermans [28] doubts this and Ayoola [36] claims that the heat release is best represented by the pixel by pixel mulitiplied product of PLIF measured OH and CH_2O concentration and not by OH only. Measuring CH_2O however, is more difficult than measuring OH. The OH* produced by H_2 combustion is probably a fair measure for the heat release by H_2 combustion. However, in the flame, CO is also present. First of all, the presence of CO influences the OH* production. Some reactions in the GRI 3.0 mechanism indicate an influence of CO on the OH concentration. Although it is hard to point out how big this influence is, the presence of this influence is clear.
Secondly, it is not possible to use the amount of OH* (produced by H_2) as a measure for the heat release of CO. Maybe these two properties do correlate, but it is impossible to indicate the extent of it.
Finally, there is the contribution of CH_4 to the OH* production. More emitted OH* light can not gratuitously be attributed to more heat release.

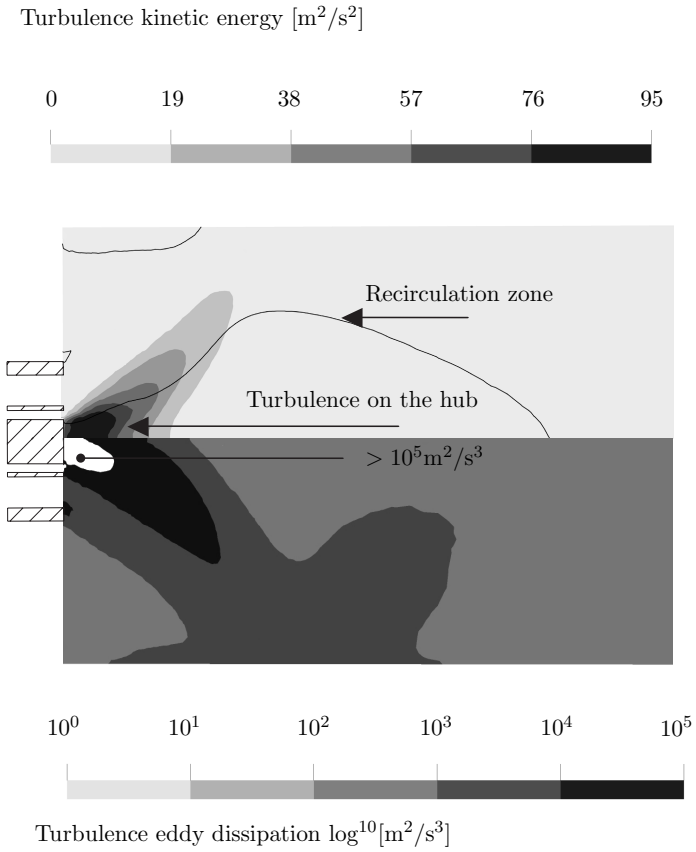

Figure 5.16: The turbulence kinetic energy (k) in the Meth1Cold case, using the CFI model.

The complex chemical system needs to be understood very well before one can conclude this.

5.4 Measurements UT

At the Laboratory of Thermal Engineering mainly thermoacoustic experiments were carried out. But during these experiments also OH^* intensity was measured. So a combination of acoustic data together with OH^* chemiluminescence data could be collected. Beside the different parts of information these experiments supply, the results can also be compared with each other.

LHS		RHS	Pre Exp Fact	Order	T_{act}
$O + HCO$	$\rightleftharpoons$	$OH + CO$	3.000E+13	.000	.00
$OH + CO$	$\rightleftharpoons$	$H + CO_2$	4.760E+07	1.228	70.00
$OH + HCO$	$\rightleftharpoons$	$H_2O + CO$	5.000E+13	.000	.00

Table 5.1: Some reactions from the GRI 3.0 mechanism which can influence the OH^* concentration due to the presence of CO.

5.4.1 Source identification by OH^* measurements

The OH^* intensity of each flame can be measured with a sampling rate of up to 1000 Hz. The intensity of the light integrated over each image can be put into a Fourier transform to process the time data into frequency spectral data. As the maximum frequency is 1000 Hz, the Nyquist frequency is 500 Hz. According to literature [77] data are accurate up to half the Nyquist frequency. As the chemiluminescence measurement is a qualitative method, all cases are normalised by the mean intensity value between 10 and 50 Hz. In this fashion, qualitative comparisons between the cases can be made.
Figure 5.17 shows the frequency dependent OH^* intensity spectrum for all four set points with cold combustion air. The spectrum shows significant noise levels, with amplitudes of approximately 25%. In the range of 0-500 Hz the OH^* chemiluminescence spectrum can be considered alomost flat, with a minor decay with increasing frequency. In most cases, a peak arises. For case Syn2Cold, this peak is around 300 Hz. The methane containing fuels Meth1Cold and Meth2Cold do not show this peak.

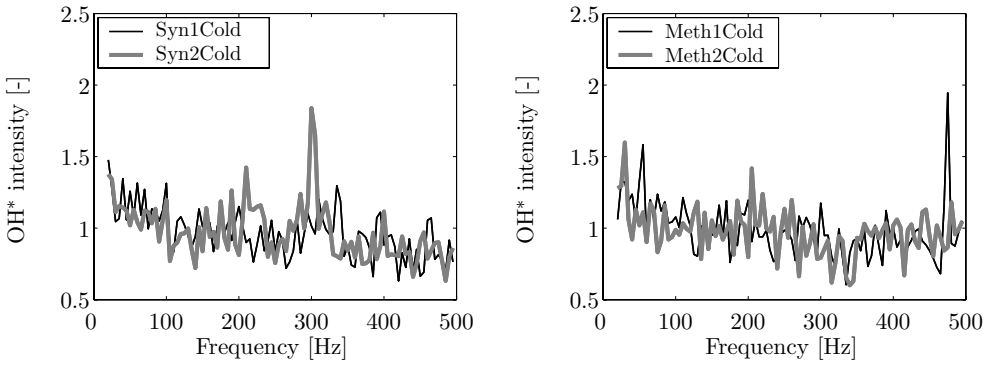

(a) Syn1Cold and Syn2Cold (b) Meth1Cold and Meth2Cold

Figure 5.17: OH^* chemiluminescence for the cold combustion air cases.

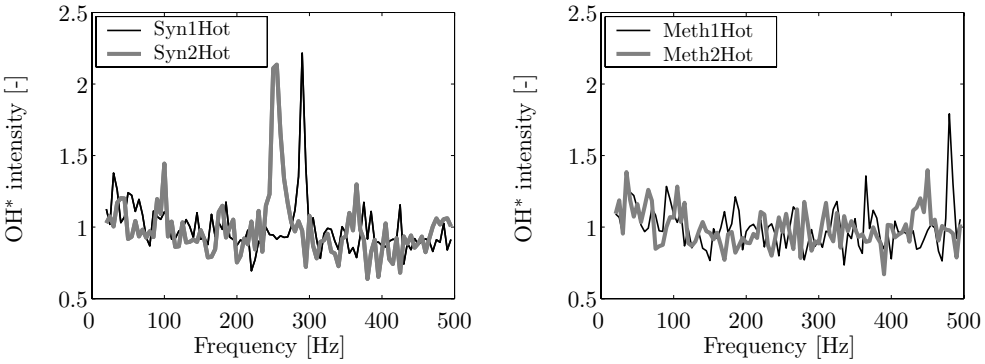

(a) Syn1Hot and Syn2Hot (b) Meth1Hot and Meth2Hot

Figure 5.18: OH* chemiluminescence for the hot combustion air cases.

Figure 5.18 shows similar results, but now for all set points with hot combustion air. The slight decay seems to be gone. The peaks in the OH* spectra have moved and have also become stronger. Again there are no such peaks for the methane containing cases. A peak in the OH* spectrum might be explained by the time scale of the chemical reaction producing OH* linking with the major time scale of the turbulence eddies. Hence methane changes the chemical time scale to uncouple this link. However, when this was the case, the increase in activity at those specific frequencies should also be observed in the acoustic measurements. This however is not the case. Figure 5.19

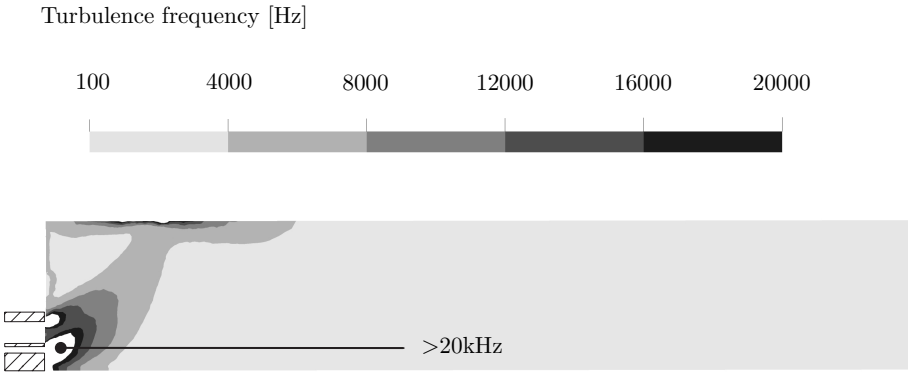

Figure 5.19: Typical turbulence frequency.

shows a typical contour plot of the turbulence frequency as it is present in the combustion chamber according to the CFD calculation. The turbulence

frequency is here defined as the eddy dissipation frequency, ϵ/k. This figure shows that in the flame zone, the turbulence frequency is much higher than the frequencies at which the peaks in OH* chemiluminescence appear. For this reason, it is not likely that those peaks are due to a coupling with major turbulence time scales.
In the previous figures, the raw OH* chemiluminescence data were presented. From these data it is very hard to observe any trends. For this reason, the data will be linearised using a least squares method of MATLAB. The linearisation was already applied on the acoustic sources in chapter 3. In those cases it showed to be a very good approximation of the reconstructed source. To be able to compare the reconstructed acoustic source and the measured chemiluminescence source, the same linearisation is applied on the chemiluminescence data.
In figure 5.20 the measured OH* intensity and the linearised OH* source for the cases of Syn1Hot and Syn2Hot are presented. Both are normalised to unity. The capricious behaviour of the OH* source is smeared out in this linerisation. In this fashion, comparison with the acoustic reconstructed source has become easier.

Figure 5.21 shows the linearised intensities. At the left hand side the cold combustion air cases and on the right hand side the hot combustion air cases are depicted. It shows that the hot cases have a stronger OH* intensity at higher frequency, resulting in a flatter profile. Higher temperature induces faster combustion as combustion rates scale exponentially with temperature.

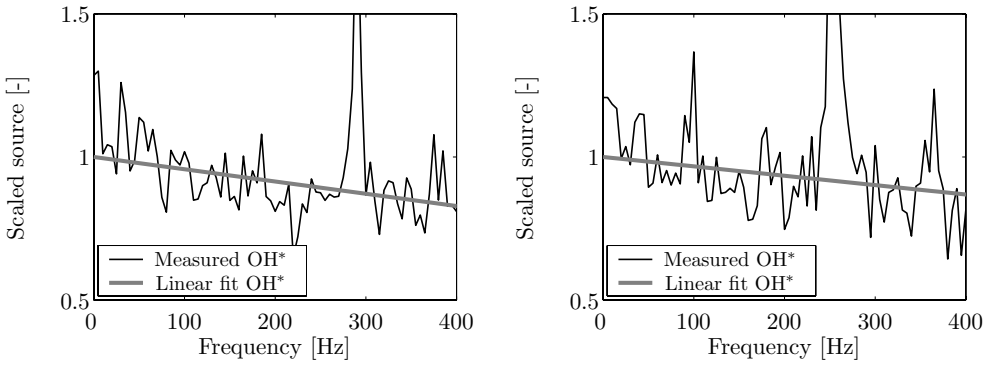

(a) Syn1Hot (b) Syn2Hot

Figure 5.20: Measured OH* spectrum and its linearisation of cases Syn1Hot and Syn2Hot.

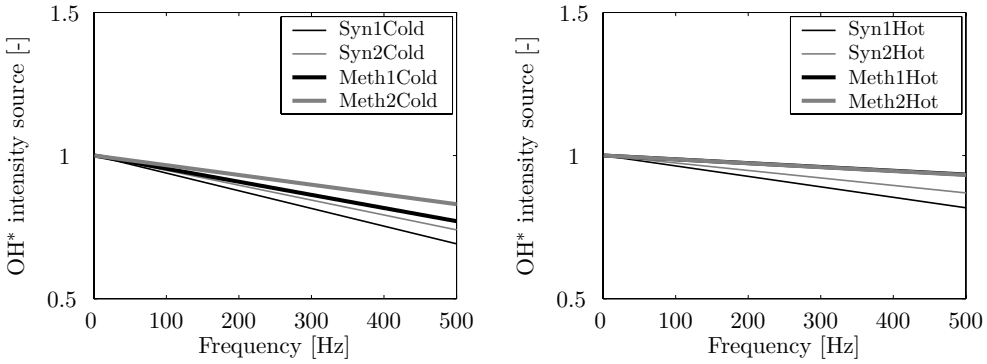

(a) Cold cases (b) Hot cases

Figure 5.21: Linearised OH* chemiluminescence

For this reason the flame is more active at higher frequencies.
Remarkable is the fact that the set points with methane show a profile of intensity that decreases less with frequency than the cases without. It was expected that methane would reduce the source strength at higher frequencies. However, as can be seen in the next section, this effect of methane appears for frequencies above 500 Hz. In other words, the OH* intensity measurements were not able to capture them, due to the Nyquist frequency of 500 Hz.
The pressure on the other hand does have an influence that would be expected. The OH* intensity is stronger at higher frequencies for set points at elevated pressures. In case of turbulent combustion, higher pressure leads faster combustion and thus again, the flame can be more active in the high frequency range.

5.4.2 Acoustic source identification

As described in chapter 3, during the experiments, the acoustic pressure is measured at several points in the experimental setup. Using the results of these acoustic measurements as an input to the acoustic model, the acoustic source of the flame can be reconstructed. In this section, the reconstructed acoustic sources for all cases are presented. The influences of pressure, fuel composition and combustion air temperature will be estimated from these results.
Figure 5.22 shows all the reconstructed acoustic sources. In figure 5.22a, the cases with cold combustion air are depicted and in b the cases with preheated (150 °C) combustion air. Especially in the cold cases, the influences of both pressure and methane can be observed.

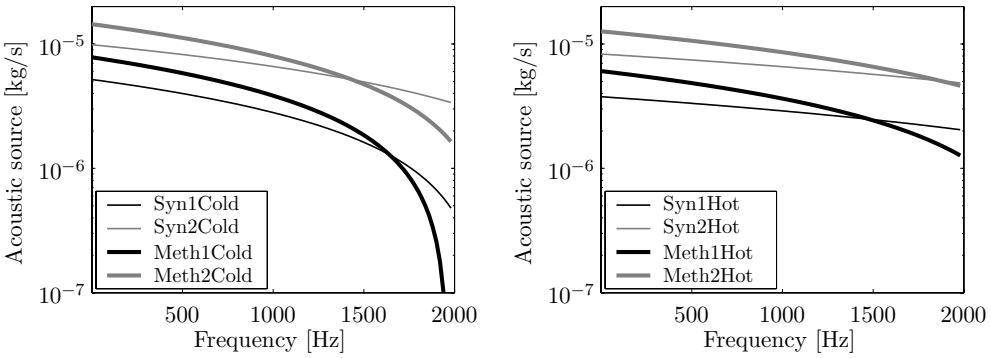

(a) Cold cases (b) Hot cases

Figure 5.22: Reconstructed acoustic sources for all cases

Case	10 Hz	1000 Hz	2000 Hz
SynCold	1.9	2.6	7.1
MethCold	1.8	2.2	80.0
SynHot	2.2	2.3	2.4
MethHot	2.1	2.4	3.6

Table 5.2: Ratios of acoustic source strengths at several frequencies.

It shows that a higher combustion pressure induces a larger acoustic source. However, at an elevated pressure in the combustion chamber also the thermal power is higher.
Now it is the question whether the acoustic pressures are increased by the higher specific thermal power or by the effect of pressure on combustion. Table 5.2 shows the ratios of the acoustic sources at 2 bar to its value at 1 bar. This is done for each combustion case at three different frequencies, 10, 1000 and 2000 Hz. From this table it can be observed that the ratio for SynHot is almost independent of frequency. Also the MethHot cases are only slightly influenced by the frequency. Considering the source strength ratios at low frequency (10 Hz), the ratios for cold combustion air cases is a little less than the pressure ratios for both mixtures, about 1.90. For the hot combustion air cases, the source strength ratio is larger than the pressure ratio, about 2.10. For all cases, the source strength ratios increase. This means that the higher pressure not only induce a stronger acoustic source, but also that the pressurised cases are less dependent on the frequency. Very remarkable are the differences in increase between the four cases. For the case SynHot, the

source strength ratio increases from 2.20 at 10 Hz to 2.37 at 2000 Hz. These cases are almost invariant to frequency. Also the MethHot cases increase only slightly from 2.08 at 10 Hz to 3.63 at 2000 Hz. The chemical time scales are probably smaller than $5{\cdot}10^{-4}$ s for all hot cases. The cold combustion air cases are much more influenced by the increase in pressure. The SynCold cases have an acoustic source strength ratio of 1.90 at 10 Hz and 7.06 at 2000 Hz. The MethCold cases react even stronger on the pressure increase. The source strength ratio increase from 1.84 at 10 Hz to approximately 80 at 2000 Hz. Hence the effect of pressure depends on combustion air temperature and even stronger on the fuel composition. This suggests a strong sensitivity to chemical kinetics.
Rajaram and Lieuwen [78] give an overview of the sound spectrum radiated by a premixed flame. They state that for a fixed burner diameter, the turbulent flame's acoustic spectrum has a nearly universal shape whose total power is a function of the equivalence ratio and flow velocity. Increasing the burner diameter leads to a shift to lower frequencies of peak acoustic emissions. Singh et al. [47] have done a variation study for noise emission from non-premixed flames. They claim that the fall-off frequency is determined by the flow velocity. However, these studies are all done with open flames and thus with atmospheric pressure. Strahle, [48] mentions a scaling law for combustion generated noise. He shows that the acoustic power for several types of combustion models scale with the density ρ_0 linearly. Stahle does not take into account the chemical kinetics of the flame. This would confirm the trend in the measured noise levels. But this still does not give a confirmation whether the sound pressure scales with pressure or with specific thermal power. This insight can be given by combustion models, as here all the detailed data are available.

5.4.3 Comparison of measured OH^* intensity sources and the measured acoustic sources

In the previous sections, the separate measured acoustic sources and the OH^* intensity sources were presented. Comparing both results with each other can give insight in the coherence between the two measurement techniques.
Figure 5.23 shows the ratio of the linearised measured OH^* intensity and the linearised measured acoustic source. This is done for the cases Meth1Cold, Meth2Cold, Syn1Hot and Syn2Hot. For all cases a very good agreement can be noticed. The case of Syn1Hot has the largest disagreement, but still, only a small deviation can be noticed at the frequency limit. The agreement between these two models has a very nice implication. The acoustic model, that is

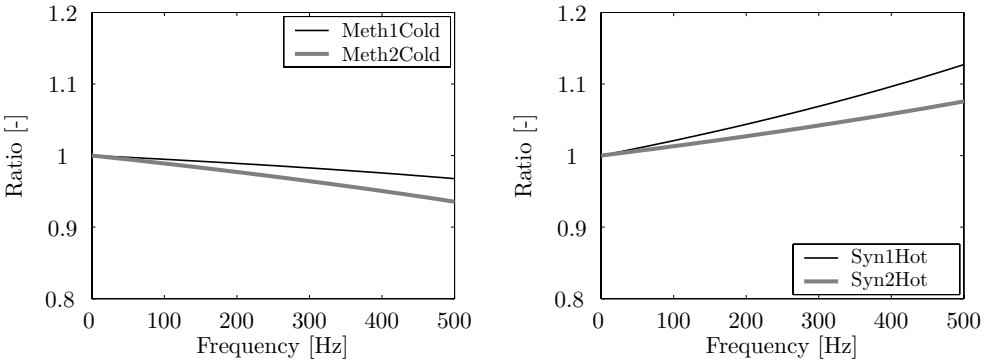

(a) Cold cases (b) Hot cases

Figure 5.23: Ratios between reconstructed measured acoustic source and the OH* intensity measurements for three cases.

used to reconstruct the acoustic source, assumes that this acoustic source is not disturbed by its surroundings. As the measured OH* intensity by chemiluminescence shows good agreement with the reconstructed acoustic source, the assumption that is made in the acoustic model is a valid assumption. Because during the chemiluminescence experiments, the OH* production is certainly subject to the influence of the acoustic field. Nevertheless, the OH* source shows good agreement with the acoustic source, reconstructed with this assumption.

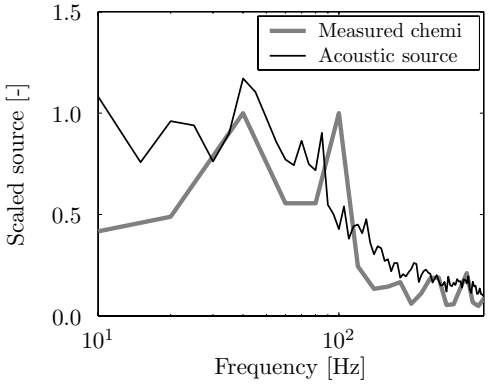

(a) OH* and acoustic spectrum

Figure 5.24: Measured chemiluminescence in a CO/N_2 flame

The last measurement which will be presented in this section is shown in figure 5.24. This figure shows the comparison between the measured chemiluminescence source and reconstructed acoustic source for a fuel containing only CO and N_2. The resulting *flame* (reaction zone) was not well stabilised and it was completely detached from the burner. This reaction zone was located approximately 15 cm downstream of the burner. As only CO was available, the chemical branching was probably delayed. Therefore the flame was detached. In case that CO is accompanied by hydrocarbons or hydrogen, OH radicals can initiate the CO decomposition. Without OH, the only possibility that CO can be consumed is by O radicals. Breaking O_2 is only possible at high temperatures and moreover, it is a slow process. Nevertheless, the chemiluminescence measurement gave a strong signal. Similar to the previous measurements, the filter described in appendix B was used. Because only a narrow band of wavelengths can pass this filter it was expected that only light emitted by OH^* would be detected with this filter. However, the chemiluminescence signal was strong. And the source representations in figure 5.24, determined by chemiluminescence and reconstruction by the acoustic model show good agreement. But, as only CO was combusted, hardly no OH^* could have been formed. The flame was completely blue, so soot was not a disturbing factor. Drabbels [79] have shown that CO only emits light that does not pass the filter as the wave length is shorter. Ayoola et al. [36] demonstrated that in some cases, excited carbon dioxide, CO_2^* can also emit light in a broadband of 350 to 600 nm. This light is partially in the region of the passing bandwidth of the filter. As CO_2 is produced in great quantities this can be a plausible explanation for the observed phenomena.
It has been shown that not only OH^*, but at least one other light emitting radical scales with the reconstructed acoustic source. It is hard to say whether this can be made general, but at least this would be an interesting point for the future. To this end a systematic evaluation can be made of flames without hydrogen and flames compared with flames without carbon.

5.5 Conclusions

The reconstructed acoustic source behaves in a well defined and characteristic way. In case the pressure increases, the acoustic source of the non-premixed syngas flame also increases. At low frequencies, this increase scales approximately with the pressure in the combustion chamber at constant specific thermal power (kW/kg) of the flame. At higher frequencies, combustion air temperature and composition play a role.

A higher temperature of the combustion air leads to a flatter profile of the acoustic source. The value at low frequencies is somewhat lower, but it does not fall-off with frequency as quickly as the cold cases do. Finally, addition of methane introduces a faster fall-off of the acoustic source. At low frequencies the source is stronger, but at higher frequencies it falls off quicker than the equivalent not containing methane. All these findings suggest a great sensitivity of the acoustic source to chemical kinetics.
The acoustic source of the flame is used as a boundary condition in the acoustic model, as presented in chapter 3. This way of implementation assumes that the acoustic source is not influenced by the acoustic field in the combustion chamber. The OH^* intensity measurements are determined inside the combustion chamber. Its environment and thus the measurement are subject to the acoustic field. Still, the reconstructed acoustic source and the OH^* intensity source compare well. This confirms that the measured acoustic source is very well correlated to the measured combustion source processes.
The last presented results show that it is well possible that in the narrow band of the UG11 filter not only spontaneous emissions of OH^* are measured. Also a radical of the CO combustion process emits light. As with the other measurements, the source measured by chemiluminescence and the reconstructed acoustic source, compares well for CO combustion. Not only OH^*, but also other radicals can be used as an indication of the acoustic source strength.

6
Measurements of the flame transfer function

6.1 Introduction

In the previous chapters, results from modelling and experiments on steady state, unperturbed flames were discussed. Besides, the coupling between flame source, acoustics and aerodynamics was discussed shortly in chapter 3. Combustor instabilities are usually caused by the coupling of these processes.
Figure 6.1 shows how a fluctuation is transported through the combustor. When a disturbance is sustained by the coupling functions for a certain frequency, an instability can occur.
In the previous chapter the measured flame transfer function was presented. This function describes the relation between the aerodynamics and the source of the flame. The acoustic model (chapter 3) described how an acoustic source in a hot environment induces an acoustic field. In this model it is assumed that the acoustics do not have a significant influence on the flame source. This was demonstrated in chapter 5. For this reason it is dashed in figure 6.1. The influence of the acoustics of the combustor on the aerodynamics can be captured in the thermoacoustic model. This model was already presented in chapter 3.
This chapter will explain how the flame transfer function is determined from experiments and will show the results from that. Additionally, the n-τ-model will be applied to correlate the resulting flame transfer functions. This model is also known as the time lag model. It was originally introduced by Crocco [80–82], and has been applied by many other researchers. The n-τ-

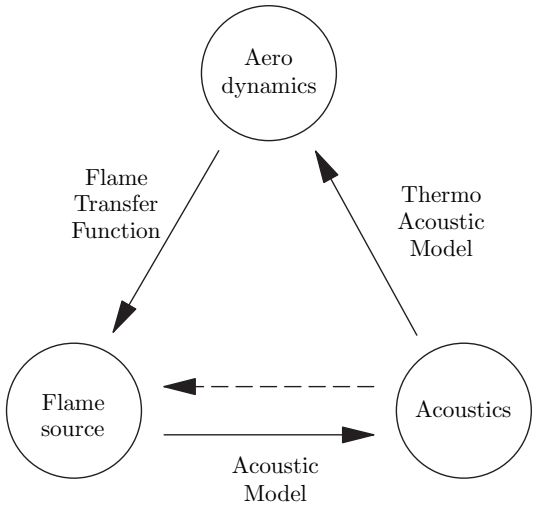

Figure 6.1: The coupling mechanisms in a combustor.

model can project a perturbation in the fuel line (isolated from all physical phenomena) on an absolute part called n and a time lag called τ.

6.2 Measurement of the flame transfer function

In chapter 2, the design of the experimental setup was described. Also the measurement equipment was shown. However, the determination of the flame transfer function was only described briefly. Therefore, in this section it will be shown how the measurements for the determination of the flame transfer function were executed. It is also presented how the measured data is used to reconstruct the flame transfer function and can be compared with the modelled results.

6.2.1 Flame transfer function

The flame transfer function is widely reported in literature [9, 31, 32, 83, 84] as it can provide valuable information about the thermoacoustic properties of a combustion system. Some authors call it the flame transfer function [31,32,83], others report on the flame transfer matrix [9]. It all comes down to the same: a relation between an excitation upstream of the flame and the response to that excitation of the flame in terms of heat release. Once the flame transfer function is known, it can be applied in acoustic models for the determination of the thermoacoustic stability. Also in this thesis, the flame transfer function

will be applied in the thermoacoustic model that is presented in chapter 3.
In case of non-premixed combustion, the flame transfer function can be seen as the function that relates a perturbation on one of the inlets of the burner with the response of the heat release of the flame. This is a function, which is dependent on the frequency:

$$H_f(\omega) = \frac{Q'}{\dot{m}'} \tag{6.1}$$

where ω is the angular frequency and Q' is the heat release fluctuation of the flame and $\dot{m}'$ is a perturbated mass flow. This mass flow can be either the fuel mass flow or the air mass flow.
To facilitate comparison of different flame transfer functions, the function is usually presented in a normalised version:

$$H_f^*(\omega) = \frac{Q'/\dot{m}'}{\overline{Q}/\overline{\dot{m}}} \tag{6.2}$$

where a bar indicates mean values.

A typical syngas flame is non-premixed, and the burner has a fuel and an air inlet. For this reason, both fuel and air mass flows can be perturbed.
To determine which whether the fuel or the air mass flow should be used

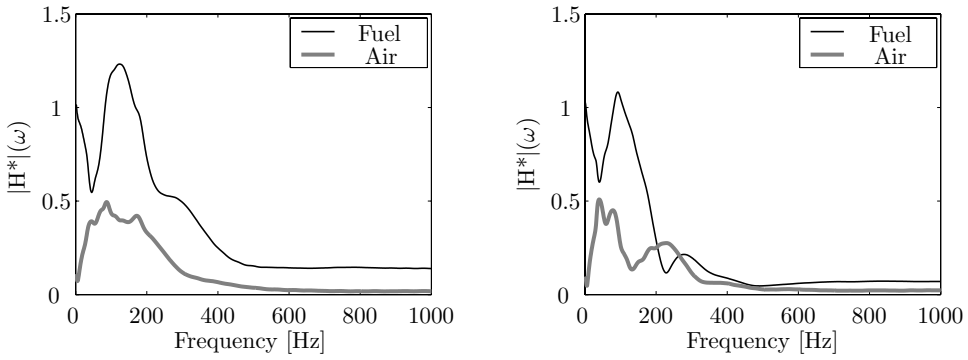

(a) Syn1Cold (b) Meth1Cold

Figure 6.2: Comparison of amplitudes of flame transfer functions excited by fuel and air mass flow perturbations.

in the flame transfer function, four CFD calculations were carried out. For two different cases, the fuel mass flow and the air mass flow were perturbed separately. Figure 6.2 shows the results of these four CFD calculations. The

details of these CFD simulations are described in chapter 7. The figure shows only the amplitudes of the flame transfer functions. From figure 6.2 it becomes clear that a perturbation of the fuel mass flow gives a much higher response in amplitude than a perturbation of the air mass flow. Perturbation of the fuel mass flow leads to a fluctuation of the power of the flame. And so, the relation between a fuel mass flow perturbation and a heat release fluctuation is much stronger.
As a result of this the flame transfer function is defined from here on as the ratio between the heat release response of a flame and the perturbed fuel mass flow:

$$H_f^*(\omega) = \frac{Q'/\dot{m}'_f}{\overline{Q}/\overline{\dot{m}}_{fuel}} \tag{6.3}$$

The flame transfer function is a complex function and is in this thesis represented by an amplitude and a phase angle. The amplitude gives information about the amplification of the ingoing signal and the phase angle indicates the phase shift between the input and the response signal.
To be able to compare the measured and modelled values of the flame transfer function, the definition also needs to include the position of the perturbation and the response. The perturbed fuel mass flow m'_f is defined 34 mm upstream of the burner exit.
The flame is considered as a point source. This means that all acoustic energy is assumed to be released in one single point in the acoustic domain. This is a valid assumption as the actual distributed source can be considered as small (approximately 4 cm) compared to its acoustic domain (order of 0.75 m). A large acoustic domain involves long acoustic resonance waves. Due to the hard boundaries, these resonance waves are of the order of 1.5 m. These long waves do not influence a small acoustic source.

6.2.2 Reconstruction of the measured transfer function

In the experimental setup, presented in chapter 2, a device to perturb the fuel mass flow is built in. This is the MOOG valve.
Figure 6.3 shows the schematic layout of the experimental setup including the devices needed for the measurement of the flame transfer function. The MOOG valve is installed approximately 1.5 m upstream of the burner. At measuring point p'_1 in figures 2.1 and 6.3, the dynamic pressure in the fuel line is determined. However, as mentioned in the previous section, the fuel mass flow perturbation is defined at a position downstream of this measuring point $\dot{m}'_f$ in figure 6.3.
The definition of the flame transfer function also contains the rate of heat release. The rate of heat release can be measured in this experimental setup,

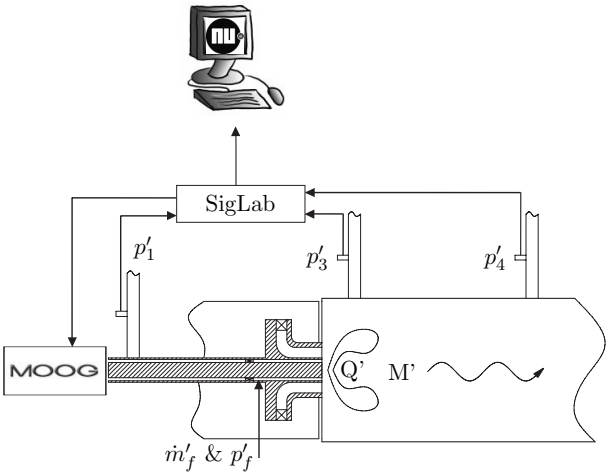

Figure 6.3: Integration of the SigLab system in the experimental setup

but not fast enough for the determination of the flame transfer function. The dynamic pressure in the combustor (p'_3 and p'_4 in figure 6.3) *can* be measured fast enough. As a result, the transfer function that can be measured in the setup reads p'_4/p'_1. The desired flame transfer function was defined as $Q'/\dot{m}'_f$. In the next section it will be shown that the flame transfer function $Q'/\dot{m}'_f$ is embedded in the measured dynamic pressure transfer function p'_4/p'_1. To be able to extract the desired flame transfer function from the measured transfer function, a data processing method will be devised.
To start the reconstruction, the desired flame transfer function is written as a product of the measured transfer function and several other transfer functions:

$$H_f = \underbrace{\frac{Q'}{\dot{m}'_f}}_{\text{desired FTF}} \approx \underbrace{\frac{p'_4}{p'_1}}_{\text{measured}} \cdot \underbrace{\frac{p'_1}{p'_f}}_{\text{BTF}} \cdot \underbrace{\frac{p'_f}{\dot{m}'_f}}_{p'\rightarrow m'} \cdot \underbrace{\frac{Q'}{M'}}_{\frac{c_0^2}{\gamma-1}} \cdot \underbrace{\frac{M'}{p'_4}}_{\text{STF}}, \tag{6.4}$$

where BTF stands for Burner Transfer Function, and STF for Source Transfer function. The next section will go into the approximations, calculations and measurements of these separate transfer functions.

Burner Transfer Function

The first unknown transfer function is the burner transfer function: p'_1/p'_f. This is the relation between the dynamic pressure p'_1 and the pressure p'_f in figures 6.3 and 6.4. The burner transfer function is determined with the acoustic model introduced in chapter 3, but is also measured in a small experimental

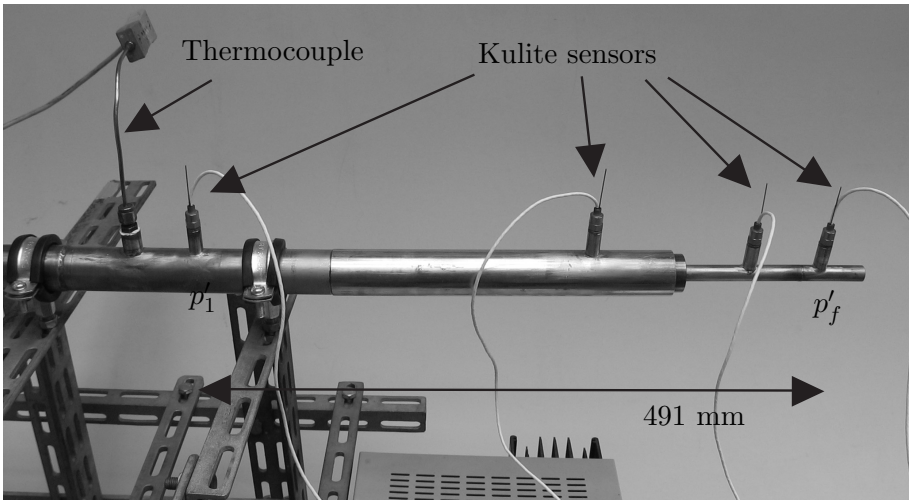

Figure 6.4: Photo of the experimental setup to measure the burner transfer function

setup, shown in figure 6.4 [85].
This setup contains several linked pipes. The diameters of these pipes are in line with the hydraulic diameters in the fuel line of the burner. The dynamic pressure in the setup is measured by four Kulite dynamic pressure transducers at four different positions. The temperature is also measured by a thermocouple at one position. The positions of the Kulites agree with the characteristic points in the combustion setup. The experiments are carried out for different temperatures and Mach numbers. Figure 6.5 depicts a typical result of the burner transfer function between the dynamic pressures of p'_f and p'_1 in figure 6.4. It shows the modelling result together with the results of two different experiments. The figure presents the amplitude of this transfer function in the top plot and the angle between the input signal and response in the middle one. The bottom figure of 6.5 shows the coherence function γ^2. This is the degree of linearity between the excitation and the response signal:

$$\gamma^2 = \frac{S_{14}S_{41}}{S_{11}S_{44}} \tag{6.5}$$

Where S_{14}, S_{41}, S_{11} and S_{44} are the cross and power functions of the acoustic measurements. In the case that the response signal follows the excitation signal perfectly, this coherence function becomes unity for all frequencies. Introduction of noise or non-linearities decreases the coherence. The experiments differ in the way the mass flow was excited. In one case the mass flow was excited by a sweep function and in another case sine functions were used. The

advantage of these sine functions is the high coherence between the input and the response signal. The disadvantage is the large amount of effort it takes to execute all the experiments. The results show that the sine and sweep excitations give similar transfer functions. The model shows good agreement with the measurements.
Figure 6.5 shows a resonance frequency around 300 Hz where the amplitude

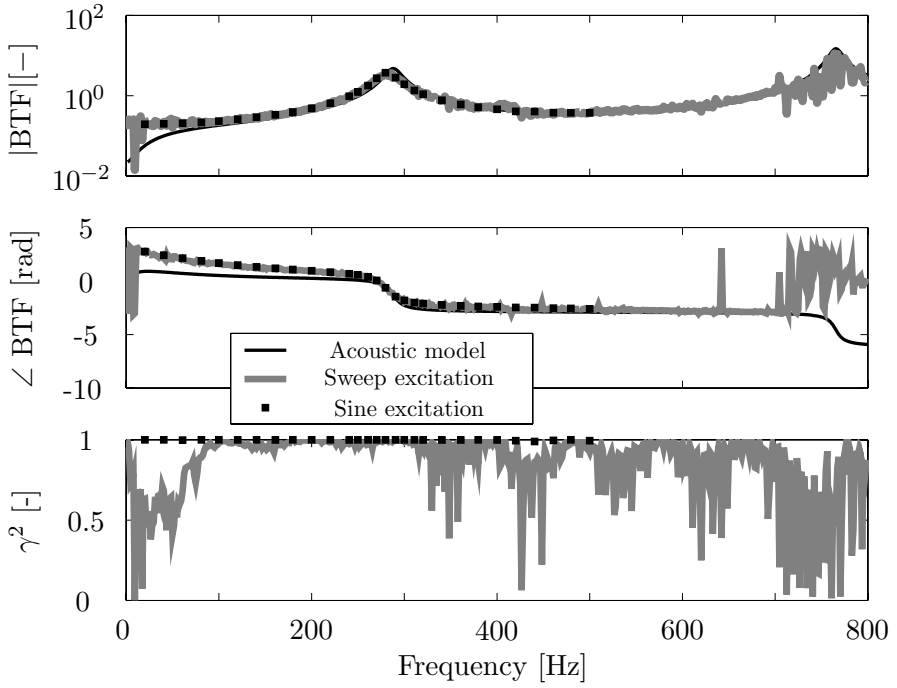

Figure 6.5: Predicted and measured burner transfer function.

increases significantly and the angle decreases π radials. The figure shows that the sine excitations give the best coherence. Although the coherence of the sweep excitation is not as good as the sine excited case, the results for both amplitude and phase angle do not deviate significantly.

Pressure to mass flow perturbation ($p' \rightarrow m'$)

The second unknown factor in equation 6.4 is $p'_f/\dot{m}'_f$. This indicates how a pressure fluctuation will result into a mass flow fluctuation. As the tube is not contracted at the position where $p'_f/\dot{m}'_f$ is evaluated, the impedance $\zeta = 1/\rho_0 c_0 p'/u'$ is assumed to be 1. As a result of this, $p'_f/\dot{m}'_f$ can be assumed

to be the c_0, the speed of sound.

Heat release rate perturbation to acoustic source ($\frac{c_0^2}{\gamma-1}$)

The third unknown transfer function is Q'/M'. This give the ratio of the acoustic source M' to the fluctuating heat release Q'. This transfer function is estimated with $Q'/M' = c_0^2/(\gamma - 1)$. It has been shown [25] that this is a good estimation for the transfer function between the heat fluctuation and the sound source.

Source Transfer Function

The last transfer function of equation 6.4 is M'/p_4'. As the combustion chamber confines the flame, the measured sound field is the result of the source (the flame) together with its acoustic domain, the combustion chamber. The transfer function M'/p_4' expresses the relation between the acoustic source and the acoustic pressure at the measuring point in the combustion chamber (p_4' in figure 6.3). This transfer function can be determined by the acoustic model. However, in chapter 3, it was shown that the results of the acoustic model with a frequency independent source showed some deviation with the measurements. Moreover, the acoustic model did not prove to be accurate enough in the low frequency region. For this reason, the acoustic source M' is replaced by the fitted acoustic source (see chapter 3 and chapter 5):

$$\frac{M'}{p_4'} = \frac{M'_{fitted}}{p_4'} \tag{6.6}$$

In this fashion, the acoustic model is only needed for the determination of the fitted source term and not for the transfer function from source to measuring point.

6.2.3 Results

Using the reconstruction method described in the previous section, the results for the flame transfer function are obtained. To make a good comparison between the different cases, the normalised flame transfer functions are depicted. In appendix G a complete overview of the measured cases is shown. Here, a selection is presented.
All the flame transfer function plots show the amplitude of the flame transfer function at the left figure and the phase angle at the right hand side. The phase angle is usually a negative number and decays with the frequency. The

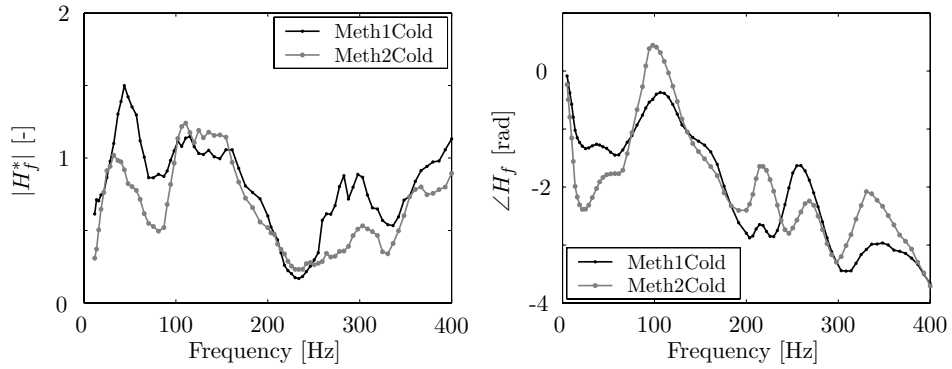

(a) Amplitude (b) Phase angle

Figure 6.6: Comparison of flame transfer functions of cases Meth1Cold and Meth2Cold to show the influence of pressure.

phase angle indicates a time delay between the disturbing and responding signals:

$$\tau = \frac{-\phi}{2\pi f} \tag{6.7}$$

with τ indicating the time delay and ϕ the phase angle.
Most of the measurements of the flame transfer function show some irregular behaviour in the low frequency range (from 5-50 Hz). In this region, the amplitude shows values below unity and the phase angle is very small. In the discussion section, more attention is paid to this.
Figure 6.6 depicts the results of both the Meth1Cold and Meth2Cold cases. Case Meth2Cold is similar to Meth1Cold, but has a pressure of 2 bar instead of 1 bar. The amplitude of Meth1Cold has a dip around 80 Hz and rises above unity between 110 and 160 Hz. The amplitude of case Meth1Cold falls off around a frequency of 170 Hz and reaches a very low amplification value around 225 Hz. Above this frequency, the amplitude rises again. As the excitation frequency was limited, it is not clear what will happen above 400 Hz. The case of Meth2Cold shows similarities with Meth1Cold, but also some differences. The dip around 80 Hz is much deeper and also the increases after the first major fall-off is less.
The phase angle of both cases shows, with some deviation, a general decay. In case that the decay rate would be constant, the time lag between the excitation and response signal would be equal for every frequency. This is obviously not the case. The pressure also has an influence on the phase

angles, but in general the phase angles of the Meth1Cold and the Meth2Cold are similar.
According to Tsurikov et al. [22] from the DLR in Stuttgart who did extensive OH^* measurements, no clearly identifiable trends for flame structure could be noticed.
Figure 6.7 shows the influence methane has on the flame transfer function.

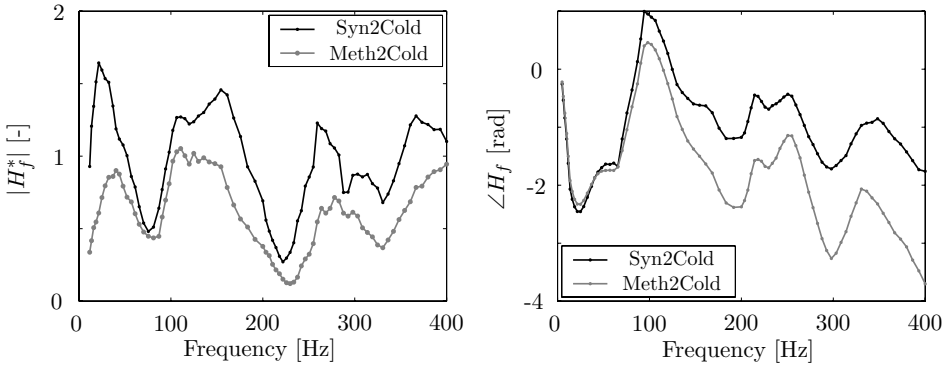

(a) Amplitude (b) Phase angle

Figure 6.7: Comparison of flame transfer functions of cases Syn2Cold and Meth2Cold to show the influence of methane addition to syngas.

The cases of Syn2Cold and Meth2Cold are depicted. Case Meth2Cold contains methane. Also in the amplitude of case Syn2Cold, the dip around 80 Hz can be observed. In the fall-off, the influence of methane is shown. The amplitude of Meth2Cold, the methane containing mixture starts approximately 20 Hz earlier to fall off. This effect was already observed by Klein [3]. Meth2Cold also decreases 0.2 amplitude points more than the Meth1Cold case. After arriving at the lowest amplitude this difference maintains. Also when the amplitude rises again, this difference is preserved.
A difference in phase angle can also be observed. As the methane containing fuel mixture has a higher calorific value, the mass flow and thus the velocity is lower than the fuel mixture without methane. But the excitation in the fuel mass flow is propagated with the speed of sound. When entering the combustion chamber the propagation velocity becomes equal to the convective velocity. Literature is discordant on acoustic perturbations arriving in a combustion chamber. Some authors mention that the disturbance becomes aerodynamic when the flow area increases [31] (like in a backward facing step) and some claim that the transition from acoustic to aerodynamic occurs

during mixing of fuel and air [25]. In the combustor that is evaluated here this question is not relevant as these events coincide. Summarising, when a perturbation enters the combustion chamber, the propagation speed decreases to the convective speed of the mixture. Moreover, the methane containing mixture will also be slower from chemical point of view. This explains the slower response of the methane containing fuel mixture.
As will be described in the next section, the methane addition also had an influence on the OH* chemiluminescence measurements at the DLR from Stuttgart [22]. This supports the findings of the influence of methane during the measurements of the flame transfer functions.
Figure 6.8 depicts the influence of the increased temperature of the combus-

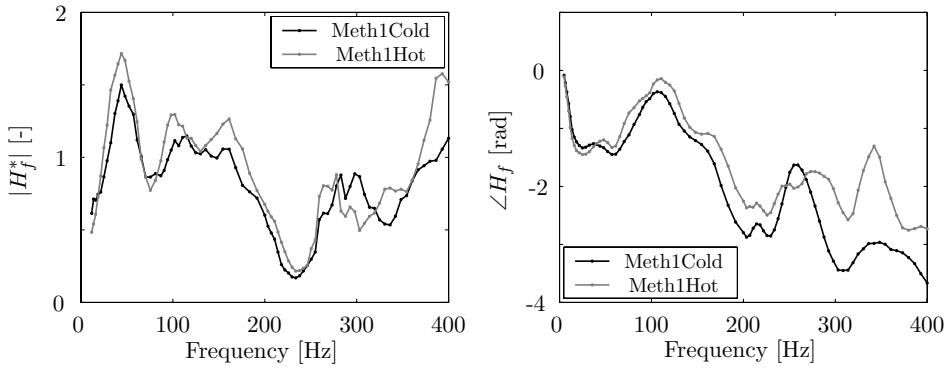

(a) Amplitude (b) Phase angle

Figure 6.8: Comparison of flame transfer functions of cases Meth1Cold and Meth1Hot to show the influence of a higher combustion air temperature.

tion air. The cases Meth1Cold and Meth1Hot are shown. Case Meth1Hot has a combustion air temperature of 150 °C. Peaks and dips appear at the same frequencies. The phase angle shows a very slight difference. It seems, especially at higher frequencies that Meth1Hot case has a smaller phase shift. This is very sensible as a higher temperature induces faster combustion.
The OH* chemiluminescence experiments at DLR in Stuttgart [22] showed no influence of the hot combustion air.

6.2.4 Discussion

Comparison with OH^* chemiluminescence experiments

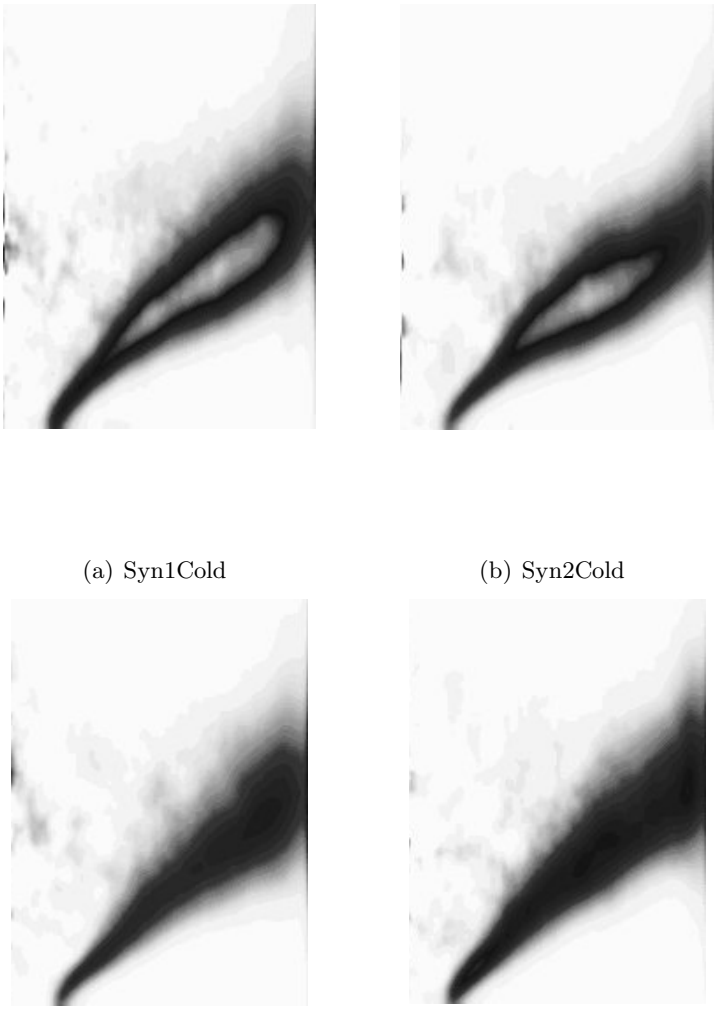

(a) Syn1Cold (b) Syn2Cold

(c) Meth1Cold (d) Meth1Hot

Figure 6.9: OH^* chemiluminescence measurements of Syn1Cold, Syn2Cold, Meth1Cold and Meth1Hot [22].

As mentioned earlier, Tsurikov et al. [22] from the DLR Stuttgart has measured the OH* intensity of all specified cases. In figure 6.9 the OH* chemiluminescence results for the cases Syn1Cold, Syn2Cold, Meth1Cold and Meth1Hot are shown. All results are plotted with the same linear colour scale. Although small differences can be observed, the two flames at the upper side (Syn1Cold and Syn2Cold) do not differ much. This indicates that the pressure influence at these pressures is not very high. The addition of methane (Meth1Cold and Meth1Hot) has more implications. Considering a cross-section perpendicular to the flame, the addition of methane decreases the gradient of measured OH*. This will have implications on the heat release distribution. Finally, the increase of combustion air temperature (Meth1Hot, compared with Meth1Cold) also does not affect the flame much.
The OH* chemiluminescence results, observed by DLR Stuttgart [22] agree with the flame transfer functions measurements in Twente with respect to sensitivity of combustion air temperature, fuel mixture and pressure.

Low frequency behaviour

For all the presented cases, the phase angle shows high values at low frequencies. Much higher values than would be expected, according to the general trend of the phase angle. It has visually been observed that the flames in this frequency region started to pulsate and even became detached from the burner during a certain part of the sine excitation. This means that the flame is further away from the point of excitation resulting in a larger phase angle.In the measurement of the burner transfer function, the correlation function between 0 and 100 Hz was far away from unity. Moreover, the phase angles in the flame transfer function are small anyway. Every measuring error increases because of the small measured value.

6.3 n-τ-model

The results of the flame transfer function measurements have been processed now. At this point the n-τ-model will be introduced. This model uses two parameters (n and τ) to describe the flame transfer function. The parameter n represents the non-dimensionless amplification (comparable with the absolute part of the flame transfer function) and τ represents the time lag between a perturbation in the fuel mass flow and the response of the flame. The parameter τ is comparable with the phase angle of the flame transfer function (see equation 6.7). The n-τ-model was proposed by Crocco and Cheng during their research into liquid rocket instabilities [80–82]. The simplicity of the model

allows to incorporate the n-τ-model into more complex models to assess the effect of thermoacoustic oscillations [86].
Once the parameters n and τ are determined, further parameterisation can be applied. This is shown in section 6.3.1.
Also in th n-τ-model, it is assumed that Q' depends only on the longitudinal wave amplitudes upstream and downstream, the effects of pressure fluctuations on combustion are neglected compared to velocity fluctuations, $Q'(p') \ll Q'(u')$ and the acoustic wavelength is assumed to be much larger than the flame length ($\lambda_{acoustic} \ll L_{flame}$).
The parameters n and τ can be extracted from the measured data. Assuming that all variables oscillate harmonically in time [2], the fuel mass flow perturbation m'_f, heat release fluctuation Q' and parameters n and τ relate like [2]:

$$\frac{Q'}{m'_f} = \frac{c_0^2}{\gamma - 1} n e^{i\omega\tau} \tag{6.8}$$

Combining expression 6.8 and expression 6.3:

$$H_f^*(\omega) = \frac{\overline{\dot{m}_f}}{\overline{Q}} \cdot \frac{c_0^2}{\gamma - 1} n e^{i\omega\tau} \tag{6.9}$$

where $H_f^*(\omega)$ can be expressed as:

$$H_f^*(\omega) = \left|H_f^*(\omega)\right| \cdot e^{i\omega\tau} \tag{6.10}$$

By combining expression (6.9) and (6.10), n-τ parameters can be obtained as a function of ω:

$$n = \frac{\gamma - 1}{c_0^2} \frac{\overline{Q}}{\overline{\dot{m}_f}} \left|H_f^*(\omega)\right| \tag{6.11}$$

Using expression 6.11, the parameter n can be identified from the measured flame transfer function.
Also the time delay τ need to be extracted from the measurements. As mentioned, this can be done with equation 6.7.
The parameter τ depends much on the nature of the combustion process. For example, for the rocket applications the time delay is associated with the droplet evaporation and the consequent heat release, dependent on reaction rate. These processes are affected by pressure, and it was determined by Crocco that τ varies with p^k only [80]. For premixed combustion, Putnam provided a simple way of estimating τ:

$$\tau = \frac{\delta}{V_p} \tag{6.12}$$

where V_p is the mean flow velocity and δ is the distance between the fuel injection and the flame front (convective time) [7]. For the non-premixed case considered here, the time lag between perturbation in the fuel mass and response of the flame can be divided into two parts. Before the mixing of fuel and air, the perturbation will travel with the speed of sound. Downstream of this mixing, the perturbation will be transported in a convective way. The convective time however is assumed to be so dominant that the acoustic time will be neglected.

6.3.1 Further parameterisation of n and τ

At this point, the n and τ parameters are determined. To be able to describe both parameters with just a few characteristic numbers, n and τ will be further parameterised. The n parameter will be modelled as a Gaussian distribution:

$$n(f, N, \sigma^2, F) = N \cdot e^{\frac{-(f-F)^2}{2\sigma^2}} \tag{6.13}$$

where σ^2 is the variance and F is the frequency at which the n parameter is maximum, N. It should be taken into account that the effect of different distributions can overlap. If two sets of n-τ parameters (two different processes) are considered, $n_1(f), \tau_1(f)$ and $n_2(f), \tau_2(f)$, the 'global' n parameter can be calculated as:

$$n(f) = n_1(f) + n_2(f) + ground \tag{6.14}$$

and the 'global' τ parameter as a weighted average of the individual time delays:

$$\tau(f) = \frac{\tau_1(f) \cdot n_1(f) + \tau_2(f) \cdot n_2(f)}{n_1(f) + n_2(f) + ground} \tag{6.15}$$

This method allows the introduction of as many peaks as are needed to fit the parameters obtained from the estimated transfer function (accounting of different phenomena). Only two were introduced in order to obtain a small set of parameters which reproduce reasonably the n-τ parameters (peaks which lead the behaviour). Four parameters are needed in order to describe each of the peaks: three to define the Gaussian function (N_i, σ_i^2, F_i) and the time delay (τ_i). Then, if two peaks are chosen to model the parameters, only eight parameters are sufficient to describe them.

6.3.2 n-τ Results

With the theory introduced in the previous section, the parameterisation of the measured flame transfer function is carried out. For all measurements,

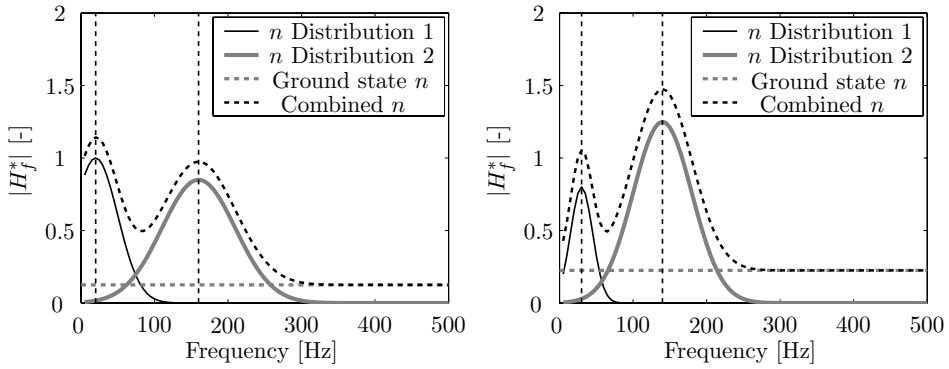

(a) Syn1Hot (b) Syn2Hot

Figure 6.10: The building blocks of the parameterisation of n and τ.

two distributions were applied. All resulting parameters can be found in appendix E.

Figure 6.10 shows how the n parameter for both Syn1Hot and Syn2Hot is constructed from two distributions and a ground state, like in equation 6.13 and 6.14. The two central frequencies for Syn1Hot are 20 ad 160 Hz. For Syn2Hot they are 30 and 140 Hz. Together, the parameters can be compared with the original flame transfer function. This is done in figure 6.11.

Figure 6.11 shows the comparison between measured flame transfer function and the parameterised function for both Syn2Cold and Meth2Cold. Again, the parameterisation is performed with two distributions. Around these two frequencies, the distributions model the flame transfer function very well. Away from these distributions, deviations occur. Actually, four distributions should have been used to describe the whole flame transfer function. However, these cases show the difference between frequency regions which are described by the distributions and which are not.
Although this method is applied in these cases with only two distributions, in some cases it would be more convenient to apply more distributions. As an example this is done with the prediction of case Syn1Hot. This is shown in figure 6.12.

In figure 6.13 the parameter of τ is validated for two cases with the actual measured delay time. The parameter τ is determined as in equation 6.15.

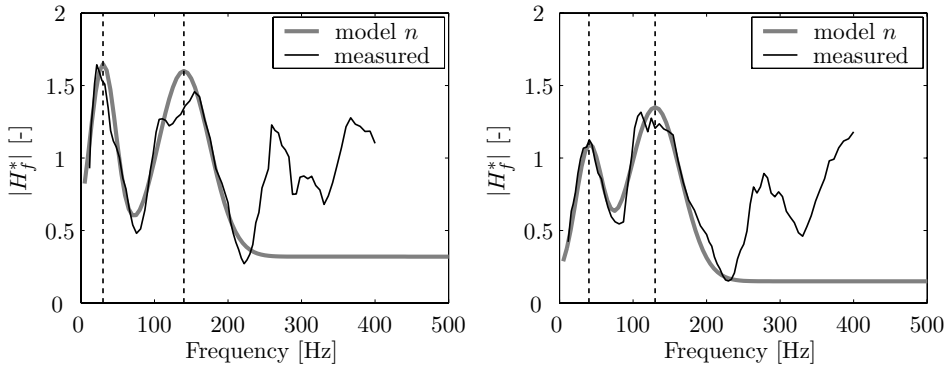

(a) Syn2Cold (b) Meth2Cold

Figure 6.11: Validation of the parameterisation by n with the actual measurements.

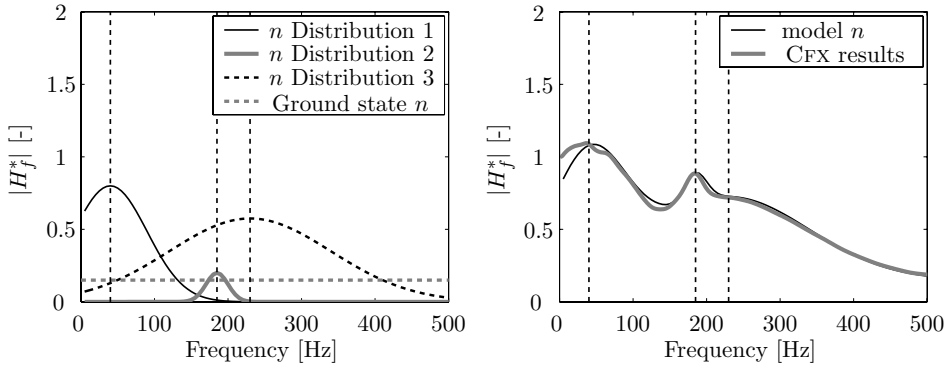

(a) Three distributions with ground state (b) Validation of n

Figure 6.12: Parameterisation of n of case Syn1Hot with three Gaussian distributions.

Despite the large variation of the time delay in the range 0-100 Hz, a good comparison is achieved for the τ parameter.
Using equation 6.12, the values of the τ parameter can be compared with the assumption that convection is dominant in the time lag τ. The CFD calculations, presented in chapter 5 can be used for an estimation of the convective speed, needed in this expression. The results of these CFD calculations show that the average velocity in the considered domain is approximately 20 m/s.

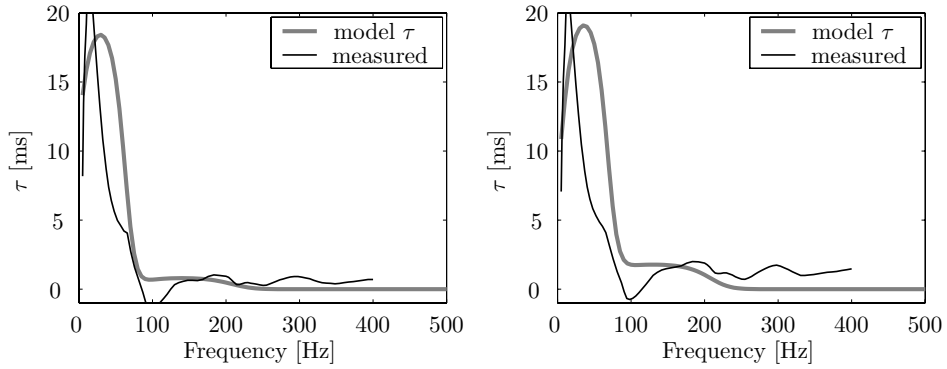

(a) Syn2Cold (b) Meth2Cold

Figure 6.13: Validation of the parameterisation by τ with the actual measurements.

Heat release will take place from the base of the flame up to the tip. Convective transport takes place over an average length of approximately 20 mm. This will take 1 ms with 20 m/s. The acoustic time will be one order of magnitude lower (34 mm with a speed of sound of 380 m/s). So although the acoustic time does have some significance, the time lag is dominated by the convective delay.

6.4 Conclusions

In this chapter it is described how the measurement data are postprocessed in order to extract the flame transfer function. It shows the results of variations in the set points. It seems that the flames transfer function is invariant to combustion air temperature and pressure. Addition of methane however did have an influence. Addition of methane to syngas introduces a lower fall-off frequency.
In the second part of this chapter, the n-τ-model was applied to the measured results. It was shown that this model is very effective in parameterising the flame transfer function. For further research it is recommended to determine which phenomena influence the frequency F and σ.

7
Predicting combustor dynamics

7.1 Introduction

In the previous chapters, several models have been discussed and validated to describe the combustion processes and the acoustics in the combustor. The final goal is the prediction of the combustor's acoustical *dynamics*. This means the prediction of the flame transfer function, but also the prediction of the combustor stability.
During experiments, several unstable modes of the combustor were observed. Only one of these unstable modes, was close to a set point. This set point, together with its unstable behaviour will be discussed at the end of this chapter. The model that was presented at the end of chapter 3 is used for this purpose. The model seems to be capable of predicting the first instability mode with a accuracy of 4%.
First of all, the modelled flame transfer function will be presented and validated with the experimentally determined flame transfer functions. Although both the modelled and the measured results contain uncertainties, the validation shows that the flame transfer function can be predicted.

7.2 Flame Transfer Function predicted by CFD

As already mentioned in previous chapters, the flame transfer function can be determined either by measurements or by CFD. During this project transient

CFD was applied to determine the flame transfer function. Van Kampen [25] proves that it is also possible to use steady state CFD for this purpose, but up to now, this method is only applicable to small-sized grids.

$$H_f^*(\omega) = \frac{Q'/\dot{m}'_f}{\overline{Q}/\overline{\dot{m}}_{fuel}} \tag{7.1}$$

The flame transfer function was defined in chapter 6 as the relation between a perturbation in the fuel mass flow and the heat release fluctuation of the flame as in expression 7.1. Also in the CFD simulation a perturbation needs to be applied to the steady state flame simulation. This can be done in several ways. In general, this is a choice between four excitation methods. Sine excitation, white (or random) noise, a step function and an impulse function. These methods need different processing.
Sine excitations [87] are easy to apply and give a very good correlation between the excitation and the response signal. However, only one frequency at the time can be investigated. For this reason, the sine excitation is usually only applied after a calculation in which a wide frequency range is investigated. In this fashion, frequencies with deviant behaviour can be investigated in more detail.
White noise or random noise [25, 87] can also be used for excitation. This method can provide data distributed over a wide range of frequencies. On the other hand, these calculations are usually rather lengthy. The duration of the simulation is determined by the frequency resolution Δf. The frequency resolution scales with the number of time steps n and the time interval ΔT like : $\Delta f = 1/(n\Delta T)$. So, the higher the frequency resolution should be, the longer the simulation will take.
Another possibility is the step function [9, 83]. At a certain moment in time, an important flow variable (equivalence ration, fuel mass flow) is increased.
Finally, also the impulse function [25,88] can be applied. An impulse excitation is a short pulse in time. This type of excitation is like hitting a table with a hammer. All frequencies are excited at the same time, but not with the same amplitude. However, this is an easy method of extracting the flame transfer function from a transient CFD simulation. Not many time steps are needed to complete the simulation. For these reasons, the impulse excitation is used for the simulations presented in this thesis. The method was implemented by exciting the fuel mass flow with an impulse. The level of excitation needs to be high enough to excite the flame. On the other hand, a too strong excitation can introduce non-linearities. These considerations have resulted in an impulse excitation of 3% of the mean of the fuel mass flow. This excitation level does not excite non-linearities, but at the same time does excite the flame

sufficiently to overcome the noise.
The heat release response of the flame is calculated by integrating the heat release over the entire domain:

$$Q' = \int_V q'_f dV \tag{7.2}$$

where q'_f is the local heat release. It is valid to use this integral, as the flame (acting as a sound source) can be considered small compared to the whole domain. Use of the volume integrated heat release source assumes that the source, distributed over the flame domain, is projected in a point source. This is also not a problem as the actual distributed source, again, can be considered small compared to its acoustic domain.
The excitation pulse travels through the domain and causes heat release perturbations in the flame front. This fluctuation in the heat release is captured by the volume integration. This results in a time signal of the heat release. From discrete signal analysis [77, 89] it can be learned that the resulting time signal of an impulse perturbation can be transformed into a frequency dependent transfer function:

$$H_f = \sum_{j=1}^{n} \frac{Q'(\tau_j)}{m'_f} e^{-j\omega\tau_j} \tag{7.3}$$

Where j is the number of the time step, n is the total number of time steps in the simulation and $Q'(\tau_j) = Q(\tau_j) - Q(\tau_n)$. This is the difference between the heat release at the j^{th} time step and the last time step (mean heat release).
The time step was chosen to be $5{\cdot}10^{-4}$ s. This corresponds to a sampling frequency f_s of 5000 Hz and a Nyquist frequency f_n of 2500 Hz. According to Tijdeman [77], the frequency dependent results will be reliable up to half the Nyquist frequency, 1250 Hz. The results will be presented up to 500 Hz as the amplitude has negligible values above this frequency. Moreover, the experimental data only go up to 400 Hz.

In the case that the chemistry is modelled by the CFI model, the heat release is extracted in a different way. It can be shown [25] that the local heat release of the flame can be written as the material derivative of the integrated heat capacity:

$$q_f = \rho \frac{D}{Dt} \int_{T_0}^{T} c_p(T,t) dT \tag{7.4}$$

By volume integrating this expression, the total derivative disappears [25] and the total heat release reduces to:

$$Q' = \int_V \rho \frac{\partial}{\partial t} \left(\int_{T_0}^{T} c_p(T,t) dT \right) dV \tag{7.5}$$

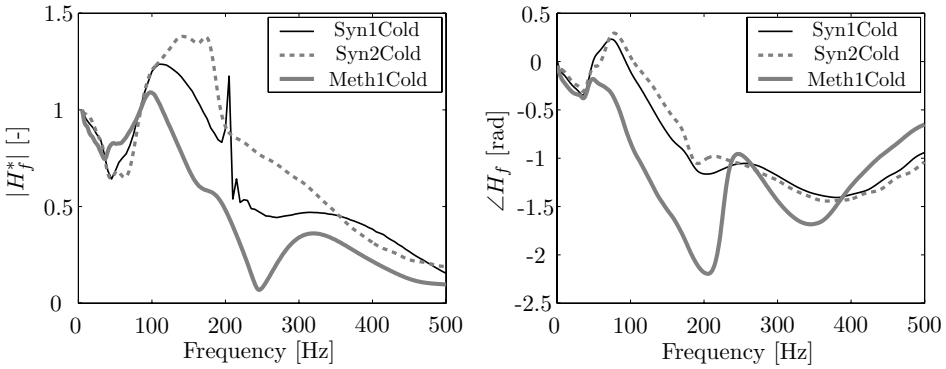

(a) Amplitude (b) Phase angle

Figure 7.1: Predicted flame transfer functions as a function of frequency of the cases Syn1Cold, Syn2Cold and Meth1Cold.

In figure 7.1 the predicted flame transfer functions of the cases Syn1Cold, Syn2Cold and Meth1Cold are depicted. The Syn1Cold case will be used as a base case to compare other cases with. At the left hand side the amplitude of the transfer function is shown and at the right hand side the phase angle, as a function of frequency.

The amplitude of the base case Syn1Cold has a dip around 40 Hz of 0.7, and a peak around 120 Hz of 1.2. At 180 Hz the amplitude beomes less than 1. Around 200 Hz a very small peak can be observed. Supposedly, this is an anomaly. A sine excitation at this frequency did not show any high amplification behaviour. At frequencies above 200 Hz, the amplitude decays quickly. Between 200 and 400 Hz it remains constant at about 0.5, above 400 Hz the amplitude decays to low values. The phase angle of case Syn1Cold decays at a constant rate between 100 and 200 Hz. Very remarkable: around 100 Hz, the phase angle exceeds 0. This suggests a response of the flame before it was excited, which is not possible. Further on in this chapter, this positive phase angle will be studied in more detail. Above 200 Hz the response signal loses coherence with the excitation. This is expressed by a more or less constant phase angle, above 400 Hz the coherence of the data is too small to calculate the phase angle acuurately. In the amplitude plot, the influence of an increased pressure (Syn2Cold) and the addition of methane can

be well observed. Increasing the pressure leads to a slightly shifted amplitude spectrum. The dip at low frequency has become wider and the peak amplitude has become higher and wider. Above approximately 180 Hz it decays slowly to low amplitude. The phase angle of case Syn2Cold shows that pressure does not affect the time lag between excitation and response. This is sensible as all velocities in the combustor are kept constant and only the pressure has been changed.
The influence of the addition of methane (Meth1Cold) is more striking. In this case, the whole spectrum is shifted to a lower frequency. The initial dip and peak appear at lower frequencies. The phase angle shows that the combustion of the methane containing mixture is slower than the other mixtures. The phase angle decreases faster, indicating a larger time lag. Also in the case of Meth1Cold, the coherence gets lost around 400 Hz.
It seems that the addition of methane causes damping in the absolute part of the flame transfer function. To explain this, the time scales that are involved need to be considered. First of all, the convective time scale is considered. Although this time scale does have influence on the total time lag between excitation and response of the flame, for the absolute part of the flame transfer function, the convective time scale is not important. This can be demonstrated by exciting the fuel mass flow much further upstream. The absolute part of the flame transfer function is the same, only the time lag changes. For this reason, the damping effect of methane is probably caused by slowness of the reaction of methane combustion.

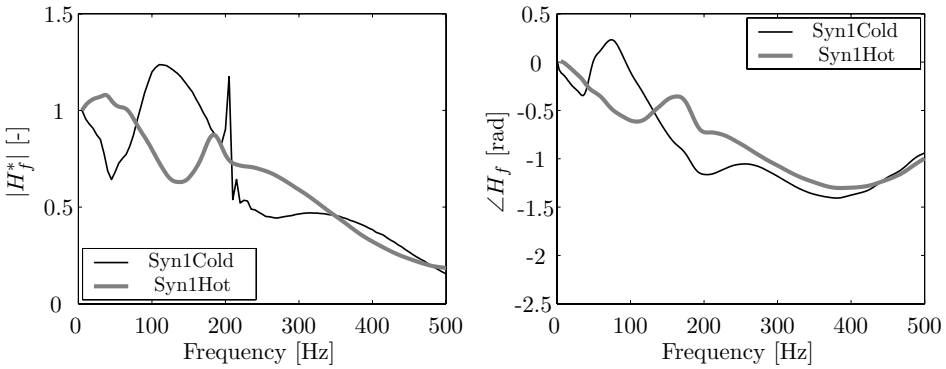

(a) Amplitude (b) Phase angle

Figure 7.2: Predicted flame transfer functions of the cases Syn1Cold and Syn1Hot.

In figure 7.2 the predicted flame transfer functions of the cases Syn1Cold and Syn1Hot are shown. In this fashion the influence of an increased combustion air temperature can be demonstrated. The dip that appears in the Syn1Cold case at 40 Hz is shifted to 150 Hz. This can be explained by the increase of chemical speed. A higher temperature results in faster chemistry and thus into higher frequencies. Also for this reason, the peak that originally showed up at 120 Hz has shifted to almost 200 Hz in the Syn1Hot case. However, this peak is low and does not exceed unity. Above this frequency of 200 Hz the amplitude decays. It decays similar to the Syn1Cold case. This damping effect can also be caused by the higher temperature. Under influence of higher temperatures, the turbulence structures become smaller. The smaller turbulence structures are, the easier it is to dissipate them.
The phase angle of Syn1Hot shows a linear decay shifted to the 150-400 Hz range. The decay is less steap than in the cold case. At 150 Hz there is again the large decrease in phase angle, with linear decay again at lower frequencies. Remarkable is that the phase angle does not exceed the value of 0.
In appendix H all predicted cases are shown.

7.3 Validation

In this section, the results of the flame transfer function, determined by transient CFD, are validated. The results of the CFD simulations are presented in the previous section. The measurements, as described in chapter 6 were used for this validation.
Figure 7.3 shows the validation of the Syn2Cold case. In the range 40-200 Hz the measured and predicted amplitude compare very well. This includes the dip at 40 Hz (measured at 60 Hz), the location heigth and width of the peak and its fall-off at 200 Hz. Around 200 Hz the deviation starts. The predicted amplitude decreases with increasing frequency, while the measured flame transfer function goes up again for a new peak. In the next section, more attention is paid to this behaviour.
The measured phase angle compares well with the predictions in the range of 120 to 200 Hz. Here, the phase angle decreases linearly with frequency. Interesting is that the measurements, like the predictions, show a positive phase angle around 100 Hz. Above 200 Hz the measurements show oscillating behaviour of the phase angle. The CFD predictions obviously here have lost accuracy in the noise.

In figure 7.4 the validation of case Meth1Cold is shown. The amplitude plot points out that the fall-off, that starts in the measurements at approximately

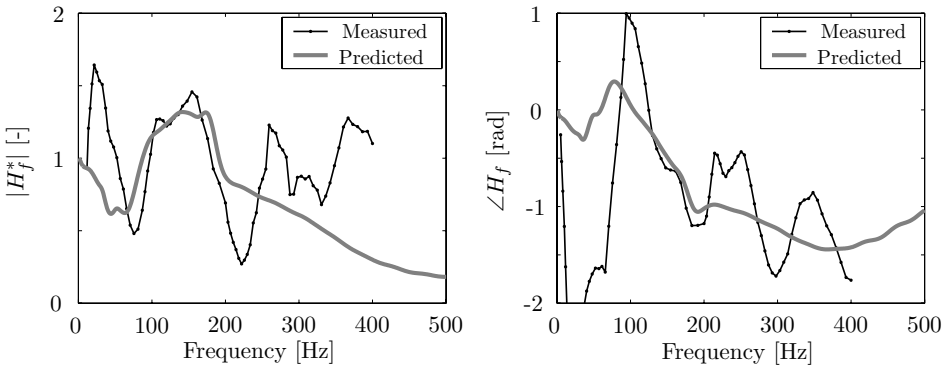

(a) Amplitude (b) Phase angle

Figure 7.3: Validation of predicted flame transfer function of case Syn2Cold.

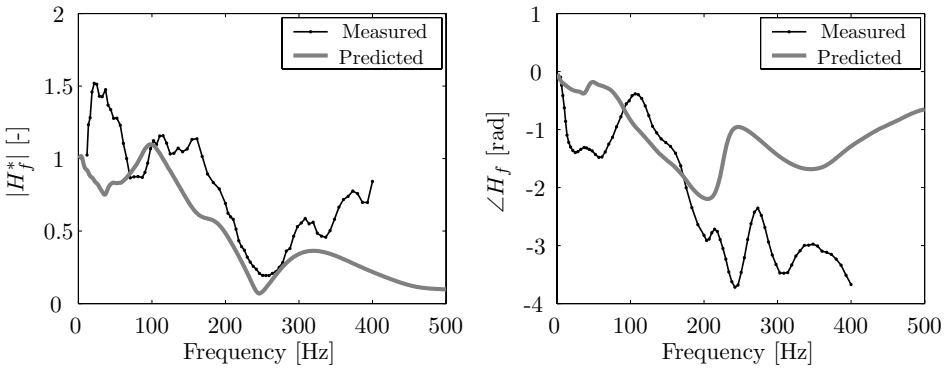

(a) Amplitude (b) Phase angle

Figure 7.4: Validation of predicted flame transfer function of case Meth1Cold.

160 Hz, is predicted at a too low frequency. The lowest amplification, at 250 Hz is predicted well. In frequencies above this 250 Hz, both prediction and measurement increase again. However, the difference between prediction and measurement also increases. The phase angle of the predicted flame transfer function decays at a steady rate from 100 to 200 Hz in both measurement and prediction. The predicted rate is slightly higher. Above 200 Hz it increases again in the prediction. This latter behaviour is not observed in the

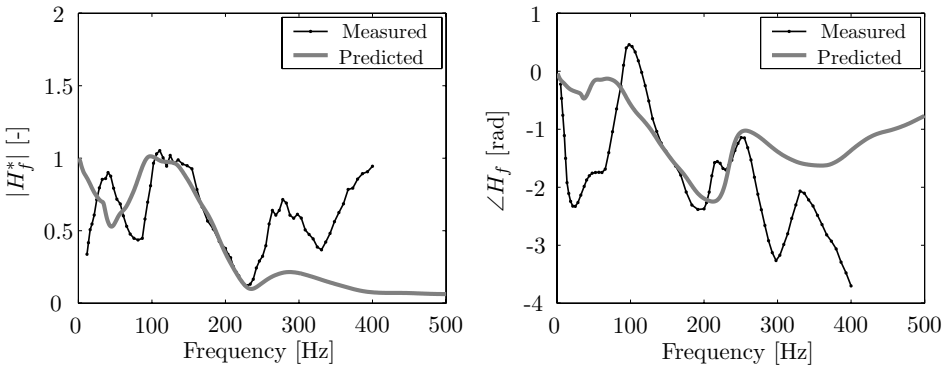

(a) Amplitude (b) Phase angle

Figure 7.5: Validation of predicted flame transfer function of case Meth2Cold.

measurement. The phase angle of the measurement decreases until 250 Hz and then stabilises.

Figure 7.5 depicts the validation of the flame transfer function of the Meth2Cold case. Both prediction and measurement show a maximum amplitude of 1 at 100 Hz, followed by a steady decrease to 0.2 at 220 Hz. Above 250 Hz the predictions have lost correlation and the amplitude remains low. The measurement shows an increase of amplitude until 300 Hz, followed by a decrease and another increase with frequency. For the phase angle, the predicted and measured phase angle shows behaviour similar to the other cases.

Figure 7.6 shows the validation of a flame tranfer function that is determined with the use of the Cfi combustion model. At the left hand side, where the aboslute value is depicted, the oscillating behaviour is captured well. Between 200 and 250 Hz, the measured values are overpredicted. In that frequency range, the dip in the measurement is predicted, but the dip is deeper. Around 150 Hz, the model also predicts a dip which is not measured. Above a frequency of 350 Hz, the two deviate. In the phase angle, the behaviour of the measurement is not followed very well, but the general trend is captured.

From the validation of the flame transfer functions can be concluded the following. Although both the measurements and the modelling results contain uncertainties, it seems that the flame transfer function can be predicted very

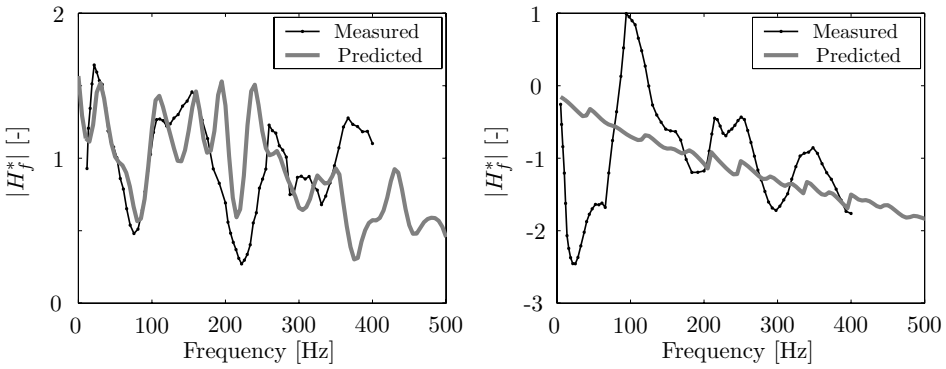

(a) Amplitude (b) Phase angle

Figure 7.6: Validation of predicted flame transfer function using the CFI combustion modelof case Syn2Cold.

reasonably by CFD.

7.4 Discussion

Some of the results presented in the previous section draw the attention because of their odd nature. In this section, three of the results that seem to deviate at first sight, are considered in more detail. First of all, two modelled flame transfer functions that exceed unity are highlighted. In first instance, these two cases were only predicted using an impulse excitation. Now, at discrete frequencies, sine excitations are used in CFD.
Another point that draws the attention is the underprediction of the amplitude at higher frequencies. Around 400 Hz, the impulse excited CFD flame transfer function under predicts the measured results to a significant extent. To find out what happens at higher frequencies, also at 400 Hz, a sine excited case is evaluated.
Finally, some cases show a positive phase angle at certain frequency. This would indicate a response before the flame was excited. In an attempt to explain this, also for these specific cases, sine excitations were carried out.

7.4.1 Exceeding unity by absolute FTF

In the figures that show the normalised amplitude of the flame transfer function, unity is an important state. Unity means that the excess heat release

equals the oscillation of chemical energy. The flame releases heat proportional to the amplitude of excitation at that frequency. And thus, a response below 1 gives a lower rate of heat release than the amplitude of excitation at that frequency. Assuming complete combustion at all times, this means that part of the thermal energy is released at other not excited frequencies or buffered and released with a phase lag. This does not suggest a dissipation of the excitation signal, but indicates that the heat is released in a dfferent part of the frequency spectrum. Another explanation is that the flame acts like a fuel buffer. During a rise in the oscillation of fuel mass flow, it can store chemical energy, and release it later, when the fuel mass flow decreases again. This also explains how at some frequencies the amplitude can increase above unity. In that case, the chemial energy is stored at a point of minimum excitation and released at a point of maximum excitation. This behaviour can be achieved in case that the flame varies in length, or more precise, in volume. An amplitude rising above unity has been observed before. Bohn et al [83], Gentemann et al. [30] and Freitag et al. [31], all have seen the same phenomenon. This section will try to point out why the amplitude of the flame transfer function would be smaller than unity and why it would exceed 1. For this purpose, for two cases, Syn2Cold and Meth1Cold CFD simulations have been carried out with a sine excitation at several frequencies.

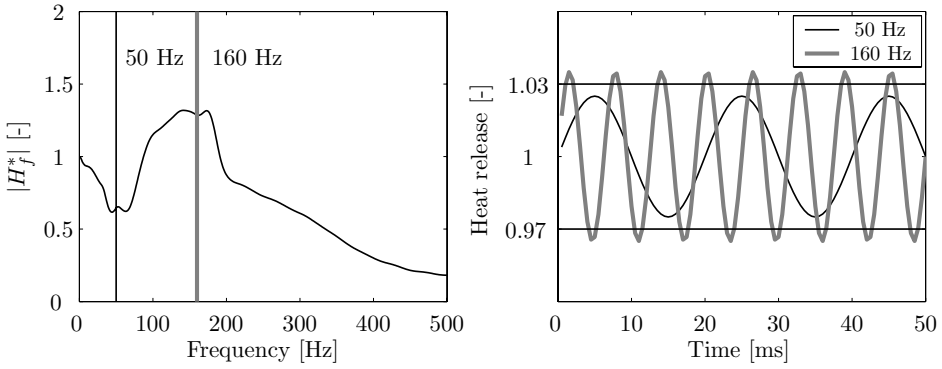

(a) FTF with impulse

(b) Sine excitations at 50 and 160 Hz

Figure 7.7: The FTF calculated by impulse excitation, with an indication at which frequencies sine excitations were carried out for Syn2Cold.

Figure 7.7a shows the amplitude of the flame transfer function of the Syn2Cold

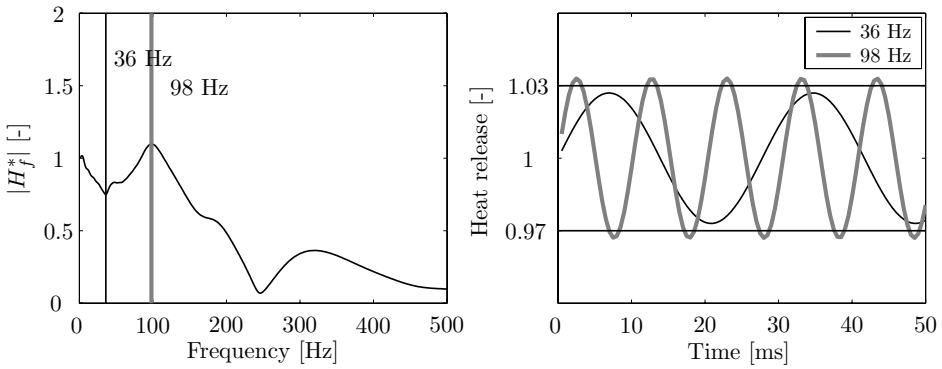

(a) FTF with impulse

(b) Sine excitations at 50 and 160 Hz

Figure 7.8: The FTF calculated by impulse excitation, with an indication at which frequencies sine excitations were carried out for Meth1Cold.

case, obtained by an impulse excitation. Two frequencies are highlighted in this figure. At a frequency of 50 Hz, the amplitude is lower than unity and at 160 Hz the amplitude exceeds 1. In figure 7.7b the resulting heat releases of sine excitations at these two frequencies are shown. The excitation amplitude was 3%, this is also indicated in the figure. The results of the additional computations with sine excitations agree very well with the results of the impulse excitations. At the minimum of the cycle of 160 Hz, the flame releases less heat than supplied. The chemical energy is buffered and released at the maximum point of the cycle. This way the amplitude becomes larger than the amplitude of excitation.
The influence of chemical kinetics and the interaction of different chemical time scales will be discussed in section 7.4.2.
Numerical experiments for the case of Meth1Cold show similar results. The numerical experiment has been carried out for 36 Hz and 98 Hz. The presence of methane moves the minimum and the maximum amplitude to lower frequencies, but it also damps the amplitudes of them. Figure 7.8b depicts the amplitude of the modelled flame transfer function of the Meth1Cold case and the resulting amplitudes of two sine excited simulations, one at 36 Hz and one at 98 Hz. Although a similar result can be observed as in the Syn2Cold sine excitations, the amplitudes of the Meth1Cold sine excitations were less extreme. This could already be expected from figure 7.8a, where the peak in the amplitude of the flame transfer function is lower than the peak of the

Syn2Cold case. This damping effect can be contributed to the methane addition.

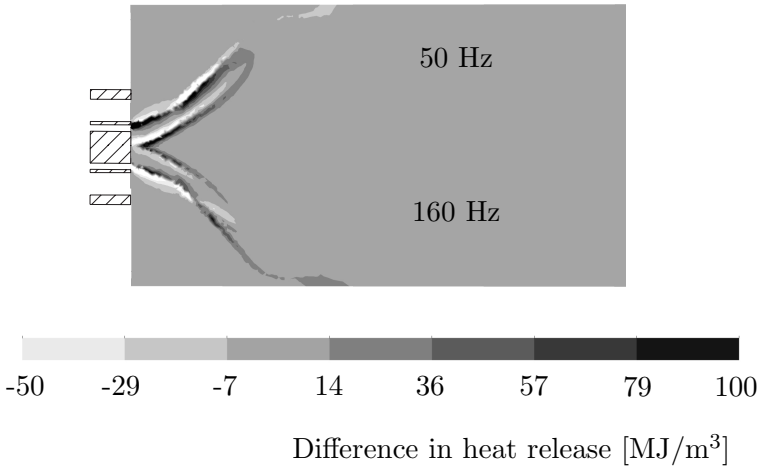

Figure 7.9: Difference in heat release between maximum and minimum of the response to sine excitation for Syn2Cold case.

To be able to get an impression of how the flame volume (and so the amount of energy buffered in the flame) changes during an excitation, the results of the sine excited cases of Syn2Cold are also processed in a different way. By showing the difference between the maximum and minimum response of a single frequency, the movement of the flame can be captured in one figure. In figure 7.9 those differences are shown for the case of Syn2Cold. In the upper plot, the difference between the maximum and minimum of the 50 Hz sine excitation and in the lower plot, the difference between the maximum and minimum values of the 160 Hz excitations is plotted. In figure 7.9 can be seen that the flame length for the 50 Hz case does not change much. The flame moves forward as a whole and it also moves to the centre of the combustor. The 160 Hz case, in the bottom part of the figure, does show a change in flame length. This is the frequency that exceeds unity in the flame transfer function. Close to the burner the flame also moves to the centre of the combustor. Halfway the flame this behaviour changers. From that point the flame moves outward instead of inward.
For the Meth1Cold, similar data processing has been carried out. This case showed similar behaviour. However, as this case also showed less amplitude in the flame transfer function, the differences between the maximum and minimum response of the sine excited flame were also smaller.

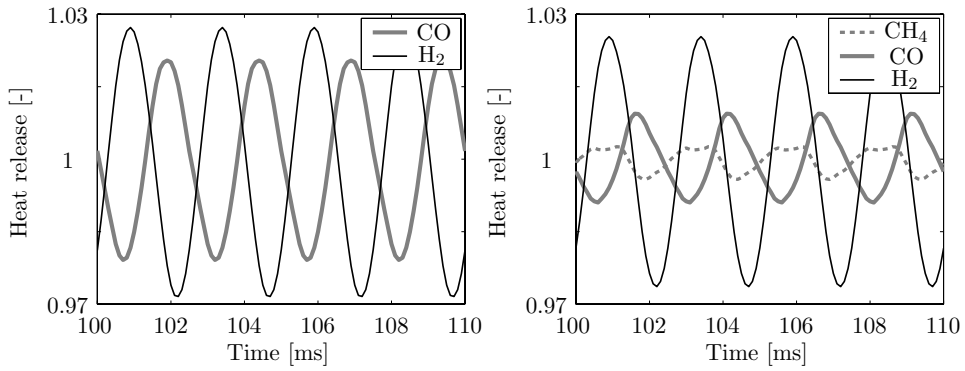

(a) Syn2Cold (b) Meth1Cold

Figure 7.10: Cases Syn2Cold and Meth1Cold excited at 400 Hz.

7.4.2 Under prediction at 400 Hz

It was noticed that for higher frequencies, the simulation under predicted the measured amplitude of the flame transfer function (see figures 7.3, 7.4 and 7.5). This under prediction related to all the validated cases. A further analysis was carried out for several cases. The under prediction could be contributed to the numerical scheme for spatial discritisation. An upwind scheme has been used for this and upwind is well known for its numerical diffusive behaviour [55]. The higher the frequency, the more sensitive the numerical scheme becomes to dissipation. To investigate whether this was the case, a sine excitation has been executed at 400 Hz for both the Syn2Cold and the Meth1Cold case. Figure 7.10 shows the results for these simulations. It shows the time dependent contribution to the heat release fluctuations of all combustible species in the fuel mixtures. The figure reveals that not the dissipative nature of the upwind scheme caused the damping in the flame transfer function, but interference of two chemistry time scales. Figure 7.10a points out that at 400 Hz carbon monoxide reacts completely different than hydrogen. To be more exact, the responses of the two species is completely out of phase. This is why the simulation with impulse excitation decays for higher frequencies. Of course, in reality, hydrogen and carbon monoxide do not combust completely independent. Nevertheless, this does point out that chemical processes, both responding on an excitation, can have such different time scales that the combined contribution to the total heat release goes to zero.
Figure 7.10b shows a similar behaviour for the Meth1Cold case. This simu-

lation also nicely points out that methane does not respond on excitations of 400 Hz. Probably the chemical time scale of methane is such that it can not respond in time anymore on an excitation.
At low frequencies (20 Hz), the responses for the H_2, CO and CH_4 reactions are in phase with each other.

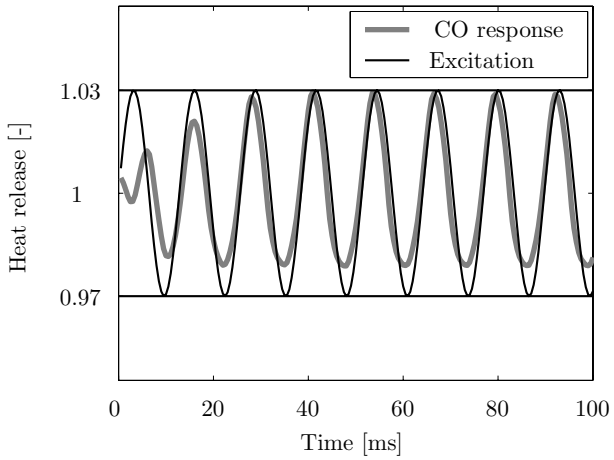

Figure 7.11: Syn2Cold case excited at 78 Hz.

7.4.3 Positive phase angles

Finally, some attention will be paid to the positive phase angle in the Syn2Cold case. A positive value of the phase angle would point out a response before the excitation. Figure 7.11 shows the excitation signal together with the response of the CO contribution to the heat release fluctuation. The response of hydrogen was acting in a normal fashion. This figure shows indeed a response of CO before the excitation. Moreover, it is striking that the positive amplitude is bigger than the negative amplitude. It is unclear whether this has something to do with the negative time lag.
As a positive phase angle psysically is impossible, it is very plausible that the response is very negative ($\phi - 2\pi$) instead of positive. In case the flame deflects strongly due to excitation, the time lag can also increase.

7.5 Prediction of instabilities

In the introduction of chapter 6, a closed feed back loop was presented. This explained which processes interact and lead to thermoacoustic instabilities. Up

to here, all processes of this scheme were modelled and validated individually. In this section, the combined influences of all these processes meet. In this section, thermoacoustic instabilities will be predicted. The model that has been presented in chapter 3 will be put into practice.

Measurements showed that all set points were stable. However, during changes in settings the combustor could run into an unstable mode. Most of those unstable points were far away from the modelled set points. One instability had operating conditions very close to the Syn1Hot case. The system ran unstable and sound pressure levels of more than 140 dB could be measured.
The thermoacoustic model has been applied using the predicted flame transfer function of the Syn1Hot case. Figure 7.12 shows the result of the measured sound pressure level (upper plot) together with the predicted instability plot. The upper plot also shows the SPL of stable operation of case Syn1Hot. In the measured SPL, a strong tonal peak can be identified at 220 Hz during the instability. There is a weaker tonal peak at 440 Hz. The remaining frequencies show similar or even lower sound pressure levels than during stable operation. The thermoacoustic model predicts one unstable frequency with negative imaginary frequency. This means that only one unstable frequency really builds up an instability. The unstable frequencies with a positive imaginary frequency will damp out in time. At an unstable point with a negative imaginary frequency the acoustic pressure will grow in time. The unstable point with negative imaginary frequency is predicted at 212 Hz. This is equivalent to the measured value with a deviation of 8 Hz. This 8 Hz is an error of 3.8 %. The second tonal peak at 440 Hz is also predicted to some extent by the point with the lowest damping rate (and hence still stable) at approximately 400 Hz. In the measurements, this peak is approximately 20 dB lower and thus not the main instability. Another well predicted phenomenon is a frequency with high damping rate around 315 Hz. In the measurement of the SPL, a very low value can be identified in this frequency range.
The differences between the prediction and the measurement can have several causes: the acoustic model, but also other influences. The acoustic model needs very accurate input of temperature data. When the temperature input is not accurate enough, the tonal peaks will appear immediately at a different frequency. Also, the model misses accuracy in some frequency regions, especially in low frequencies. Moreover, the amount of cooling air surrounding the liner also has influence. First of all, it withdraws heat from the liner and so from the combustion and dilution zone. But it also has a damping influence on the liner. The instability of figure 7.12 disappeared by adding more cooling air. It is not possible to say which of the effects has the most influence.

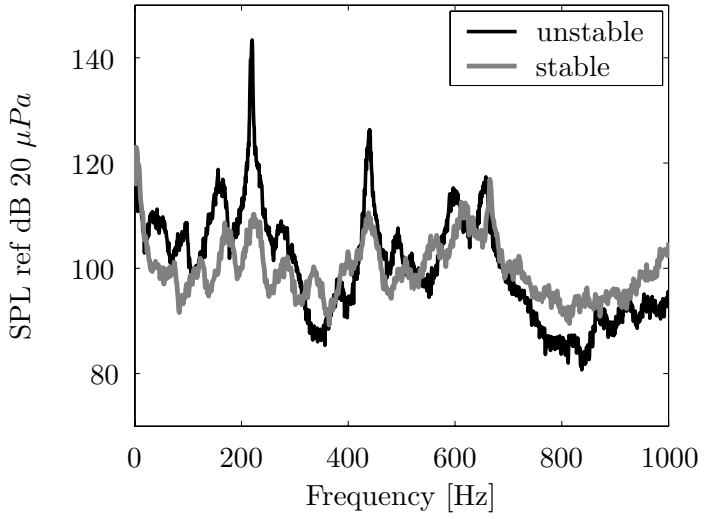

(a) SPL

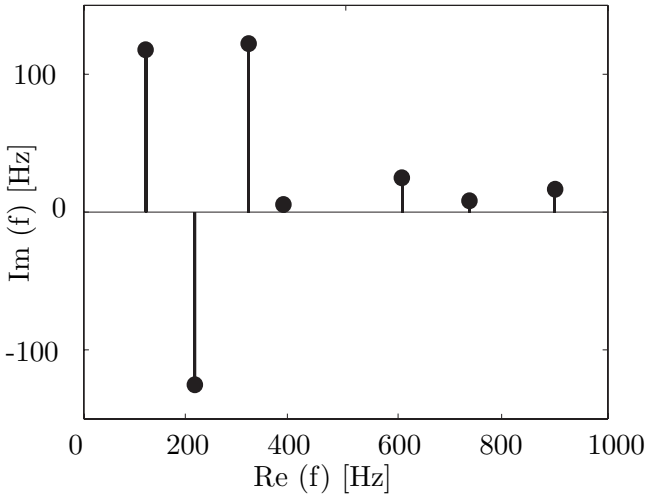

(b) Stability map

Figure 7.12: Sound pressure level of stable and unstable operation.

7.6 Conclusions

It has been shown that the flame transfer function can be predicted with unsteady CFD simulations. Validation with experimental data pointed out that

particular in the frequency range of 50-250 Hz, the simulations compared well with the measurements. Above this frequency, deviations could be noticed. This was not caused by numerical damping. The responses of the hydrogen and carbon monoxide combustion were approximately 90° out of phase. Although this apparently does not happen in reality, this does point out that two different chemical processes can both have a strong response to an excitation without any effective result in the total response. Next to this, to improve the prediction of the flame transfer function, the time scales of chemical kinetics need to be taken into account more accurately.
This chapter showed that it is possible to predict an instability in a non-premixing turbulent syngas combustor. Although only one case could be validated, the instability was predicted within 4% accuracy.

8
Conclusions and Recommendations

8.1 Conclusions

In this thesis a study to the acoustic phenomena in turbulent syngas combustion was presented. This was a study in the framework of the EU project called HEGSA. This project aimed at the development of a new type of gas turbine in which syngas would be the primary fuel.
In the study of the acoustic phenomena, several paths are followed. Both analytical and numerical models have been used to predict sound pressure levels. Flame transfer functions were predicted by numerical models. All predictions have been validated by data from an experimental setup, which was designed and manufactured during the project.
With the experimental setup it was possible to measure acoustic pressures in the fuel and air supply as well as at several positions in the combustion chamber. From the experimental data, acoustic auto spectra and flame transfer functions could be obtained. The acoustic auto spectra were used to validate the acoustic model. The measured flame transfer function was used to validate the modelled flame transfer function. The setup was also equipped to measure OH^*, an intermediate species, marking the flame front. From these data acoustic sources could be identified and numerical models could be validated.
To be able to predict acoustic pressures in a combustion chamber, a one-dimensional acoustic model model has been developed. This model uses the analytical solution of the Helmholtz equation and assumes that the acoustics in the experimental setup are mainly one-dimensional. The model was also

used to determine the acoustic source of the flame using experimental data as input. The results in chapter 5 showed that the model is well-capable of capturing the main acoustic phenomena like the resonance frequencies of the combustion chamber. In the lower frequency region, the model lacks accuracy. The model showed great sensitivity to the temperature gradient. Detailed temperature information from the combustion chamber is needed for a correct use of the model.

The model shows that the acoustic source can be influenced significantly by the combustion air temperature, the combustion pressure and fuel composition.

A higher temperature of the combustion air leads to a flatter profile of the acoustic source. The strength of the acoustic source at low frequencies is somewhat smaller, but it does not fall-off with frequency as quickly as the cold cases do. Addition of methane to the syngas introduces a faster fall-off of the acoustic source. At low frequencies the source is stronger, but at higher frequencies it falls off more quickly than the equivalent fuel without methane. All these findings suggest a great sensitivity of the acoustic source to chemical kinetics. A higher combustion air temperature causes a higher reaction rate. This results in less fall-off of the acoustic source with frequency. As the chemical time scales of methane differ a lot from those of hydrogen and carbon monoxide, methane addition reduces the acoustic source with frequency.

With an increasing pressure in the combustor, the acoustic source of the non-premixed syngas flame also increases. At low frequencies, this increase scales approximately with the pressure in the combustion chamber at constant specific thermal power (kW/kg) of the flame. At higher frequencies, combustion air temperature and composition play a role.

The acoustic source of the flame is used as a boundary condition in the acoustic model, as presented in chapter 3. This way of implementation assumes that the acoustic source is not influenced by the acoustic field in the combustion chamber. The OH^* intensity was determined inside the combustion chamber. Its environment and thus the measurement are subject to the acoustic field. Still, the reconstructed acoustic source and the OH^* intensity source compare well. This confirms that the measured acoustic source is very well correlated to the measured combustion source processes.

The reacting flow in the combustor was modelled by CFD. First, a steady solution was determined. Subsequently, to determine the flame transfer function, the fuel mass flow was perturbed and the heat release rate was monitored in a transient calculation. The steady solution was validated with PIV data. Remarkably, close to the burner a deviation between the modelled and the measured data was observed. Further downstream only minor differences

were noticed. The data from the OH^* measurements deviated from the CFX results obtained with the simplified chemistry model. The chemical in-house code called CFI shows much better results. It showed that the CFI model is also capable of modelling syngas combustion using the GRI30 mechanism. In chapter 4 it was shown that it should always be checked to what extent the reaction flow is pushed away from equilibrium. The CFI model is only accurate between RPV values of 0.7 and 1.

An experimental setup was built and experiments have been executed. To obtain the flame transfer function from the measurements, a reconstruction method was used. In that method assumptions concerning the flame and system behaviour were included. In chapter 6, the measured flame transfer functions are shown. Only little variation can be observed between the set points. It seems that the flame transfer function is invariable to combustion air temperature and pressure. Addition of methane to syngas however did have an influence. It introduces a lower fall-off frequency.

In chapter 7, the flame transfer function has been predicted with transient CFD calculations. The predictions showed that both the temperature of the combustion air, pressure and the fuel composition have influence on the resulting flame transfer function. A higher combustion air temperature introduces lower amplitudes and a shift of the whole spectrum to a higher frequency. This also involves the phase angle.

A higher combustion pressure leads to a higher peak in the amplitude. The higher pressure also introduces a fall-off at a higher frequency. The phase angle is not significantly influenced.

Addition of methane to the mixture introduces lower amplitudes and a fall-off at lower frequency. The response was also slower, leading to a larger phase angle.

The results of the modelled flame transfer function should be interpreted with care. A first order upwind scheme was used in the spatial discretisation in these calculations. This numerical scheme is known for its diffusive behaviour. Second order schemes however were not robust enough.

Validation of the predicted flame transfer function with experimental data in chapter 7, pointed out that particular in the frequency range of 50-250 Hz, the simulations compared well with the measurements.

The measured flame transfer functions were used for an n-τ description in chapter 6. This model describes the flame transfer function with a magnitude and a time delay at several frequencies. Together with a distribution, the whole flame transfer function is described. It has been shown that it is well possible to describe a measured flame transfer function with very few variables. The description was carried out with two distributions. More distributions would

have been more convenient, but it has been shown that the methods works properly.
In the last chapter the thermoacoustic model is applied. This model can predict thermoacoustic instabilities in the combustion chamber. The experimental setup once has run unstable close to an operation point. The instability occurred at a frequency of 220 Hz and it was predicted at 212 Hz. This means that the instability was predicted within an accuracy of 4%.
Also the results from this model need interpretation. When the model predicts an instability it does not necessarily mean this instability will occur. It shows that boundary conditions are available.

8.2 Recommendations

To improve the results that were presented, some recommendations will be given here.
A first order upwind scheme was used for spatial discretisation. A second order can be used to improve the results.
The determination of the flame transfer function by means of transient CFD is a labour intensive job. Moreover, as transient calculations are needed, additional errors can occur. For that reason it would be very rewarding to continue with the so-called Linear Coefficient Method by van Kampen [25]. This method can transform a steady solution into a state space description. It has already been shown that this is an effective way of retrieving the flame transfer function. Moreover, as the description follows from a steady solution, transient errors do not occur.
The experimental setup has been used up to a pressure of 2 bar. It was designed for a pressure of 5 bar. It would be very interesting to investigate whether the pressure effect that has been observed holds for higher pressures than 2 bar.
Concerning the Cfi combustion code, the effectiveness can be mentioned. It has been shown that the code can predict combustion chemistry in more detail and with more accuracy than the commercially available models. However, when the code would be quicker in usage it becomes even more attractive.
Finally, not only the conventional methods should be applied in tackling the thermoacoustic problems. It has already been shown by Choi et al. [90] that adding a plasma to an unstable flame is an extremely successful method in stabilising the flame. The radicals in the plasma can fill in 'gaps' in the chemical branching created by the instability. A drawback of the method is that plasmas are extremely reactive. The radicals will also react with the burner and the liner material.

Another suggestion came forward during discussions [91]. It was suggested to excite molecules locally by microwaves. Microwaves can excite water molecules, so it should also be possible to excite molecules in fuels.

Nomenclature

Roman

a	power of Damköhler number $=1 + \nu_F + \nu_O$	[-]
A_i	pre-exponential factor of species i	[-]
A^*	sound generation constant	[-]
$\mathbf{A}$	system matrix in TMF model	[-]
$\mathbf{b}$	matrix indicating to what extent species participate in $\boldsymbol{\eta}$	[-]
$\mathbf{b}^r$	vector containing steady state species	[-]
$\mathbf{b}^c$	vector representing element conservation relations	[-]
$\mathbf{b}^s$	vector with slow species	[-]
c_0	speed of sound at observers position	[m/s]
c_{67}	speed of sound in element 6-7	[m/s]
$c_{1,2}$	complex constants in solution of acoustic pressure with temperature gradient	[J/kgK]
c_j	reaction progress variable of j^th composed species	[-]
c_p	heat capacity at constant pressure	[J/kgK]
c_v	heat capacity at constant volume	[J/kgK]
$\mathbf{C}$	matrix in TMF model	[-]
C	prefactor in TMF solutions, $C^J = \frac{S^J}{c_0 \mathrm{sinh}(\mathrm{ikL})^\mathrm{J}}$	[-]
$C_{\epsilon 1}$	constant, $C_{\epsilon 1} = 1.44$ in $k-\epsilon$-model	[-]
$C_{\epsilon 2}$	constant, $C_{\epsilon 2} = 1.92$ in $k-\epsilon$-model	[-]
C_μ	constant, $C_\mu = 0.09$ in $k-\epsilon$-model	[-]
d	duct diameter	[m]
$\dot{D}$	strain tensor	[1/s]
$\mathcal{D}$	molecular diffusion coefficient	[m^2/s]
$\mathbf{D}$	matrix in TMF model	[-]

Da^{fl}	Damköhler number, ratio between flow time scales and chemical reaction time scales τ_f/τ_c	[-]
Da^{turb}	turbulence Damköhler number	[-]
E	turbulence energy spectrum	[m]
E	number of elements	[-]
E_i	activation energy of species i	[J/kg]
$\mathbf{f}$	momentum vector induced by external forces	[N/m^3]
f	mixture fraction	[-]
f	frequency	[Hz]
Δf	frequency resolution	[Hz]
f_n	Nyquist frequency = 1/2 sampling frequency	[Hz]
f_s	sampling frequency	[Hz]
F	frequency in which parameter n of n-τ-model reaches N	[Hz]
h	specific enthalpy	[J/kg]
h_f	local flame transfer function	[J/kg]
H	Heaviside function	[-]
$H_{9,11}$	acoustic transfer function between points 9 and 11	[-]
H_f	flame transfer function	[Ws/kg]
H_f*	normalised flame transfer function	[-]
G	Green's function	[-]
J	Jacobian	[-]
J_0	Bessel function of order zero	[-]
k	thermal conduction constant	[W/mK]
k	turbulence kinetic energy	[m^2/s^2]
k_A	wave number including mean flow, $k_A = \omega/(c_0 - u_0 x)$	[rad/m]
k_B	wave number including mean flow, $k_B = \omega/(c_0 + u_0 x)$	[rad/m]
k_c	cut-off wave number for LES	[rad/m]
l_{cor}	correlation length, related to radial location in the flame	[m]
l_d	thickness of diffusion layer	[m]
l_m	thickness of mixing layer	[m]
l_r	thickness of reaction layer	[m]
L	length	[m]
Le	Lewis number $\alpha/\mathcal{D}$	[-]
$\dot{m}_a$	air mass flow	[kg/s]
$\dot{m}_f$	fuel mass flow	[kg/s]
m	mass	[kg]
m	constant in temperature distribution	[-]
M	number of chemical time scales faster than locally dominant	[-]
$\mathbf{M}'$	vector of acoustic mass flows in TMF model	[-]
n	number of time steps	[-]

n	interaction parameter, amplification factor in n-τ-model	[-]
$ncel$	number of grid cells	[-]
N	maximum value of n in n-τ-model	[-]
N	number of species	[-]
p	pressure	[Pa]
$\tilde{p}$	acoustic pressure in non-harmonic acoustics	[Pa]
p'	acoustic pressure in harmonic acoustics	[Pa]
$\hat{p}_{A,B}$	complex pressure amplitude of travelling wave	[Pa]
pp	sound spectrum in noise model	[Pa^2]
P	probability density function	[-]
P_k	production of turbulence kinetic energy	[m^2/s^2]
Pr_t	turbulence Prandtl number $Pr_t = 0.9$ in $k-\epsilon$-model	[-]
q_f	local heat release	[W]
Q	volume integrated heat release	[W]
R	correction factor TMF model	[ms]
R	radius of circular tube	[m]
R	specific gas constant	[J/kgK]
R_u	universal gas constant = 8.3144	[J/molK]
s	stoichiometric ratio $\nu_O W_O / \nu_F W_F$	[m^2]
S	dimension of the low-dimensional manifold	[-]
S	area	[m^2]
S_{11}	acoustic power spectrum of measuring point 1	[m^2]
S_L	laminar flame speed in premixed flames	[m/s]
Sc_t	turbulence Schmidt number $Sc_t = 0.9$ in $k-\epsilon$-model	[-]
SPL	sound pressure level	ref dB [20μPa]
t	time	[s]
T	temperature	[K] or [°C]
T	time scale much larger than turbulence fluctuations	[s]
ΔT	time interval	[s]
$\mathbf{u}$	velocity vector	[m/s]
u_{0x}	velocity mean flow in x-direction	[m/s]
V	volume	[m^3]
$\dot{V}$	volume flow	[m^3]
W_i	molar mass of species i	[g/mol]
x, y, z	Cartesian coordinates	[m^3]
y_f	fuel mass fraction	[-]
Y_0	Neumann function of order zero	[-]
Y_i	mass fraction of species i	[-]
Y_i^0	initial mass fraction of species i	[-]

Sub and Supers

$_{ad}$	adiabatic flame temperature
$_{a}$	the air flow
$_{b}$	burner
$_{air}$	at air side of the setup
$_{cool}$	at cooling chamber
$_{end}$	at exit of the setup
$_{eq}$	equilibrium value
$_{flame}$	at the location of the flame
$_{f}$	the fuel flow
$_{fuel}$	fuel side of the setup
$_{meas}$	measuring point
$_{J}$	number index of acoustic element
$_{st}$	at stoichiometry
$_{tot}$	total
$_{u}$	unburnt

Greek

α	thermal diffusivity, $k/(\rho c_p)$	[m^2/s]
β	temperature exponent of species i	[-]
γ	ratio of heat capacities, c_p/c_v	[-]
γ^2	coherence function	[-]
δ	Dirac delta function	[-]
ϵ	dissipation rate of turbulence kinetic energy	[m^2/s^2]
ζ	dimensionless impedance $1/(\rho_0 c_0)p'/u'$	[-]
$\boldsymbol{\eta}$	vector of composed species in CSP	[-]
κ_t	turbulence diffusivity	[kg/ms]
λ	acoustic wave length	[m]
μ	dynamic viscosity	[kg/ms]
μ_t	turbulence viscosity	[kg/ms]
ν	kinematic viscosity	[m^2/s]
ν_i	stoichiometric coefficients for species i	[kg/ms]
ρ	density	[kg/m^3]
σ	viscosity stress tensor	[Pa]
σ^2	variance in n-τ-model	[-]

σ_k	constant, $\sigma_k = 1.0$ in $k-\epsilon$-model	[-]
σ_ϵ	constant, $\sigma_\epsilon = 1.3$ in $k-\epsilon$-model	[-]
τ	period of oscillation	[s]
τ_c	chemical time scale	[s]
τ_{conv}	convection time delay	[s]
$\tau_{conv,air}$	convection time delay in air channel	[s]
$\tau_{conv,fuel}$	convection time delay in fuel channel	[s]
τ_f	flow time scale	[s]
τ_{flame}	time delay in the flame	[s]
τ_j	discrete time at time step j	[s]
τ_{sound}	time delay of a sound wave	[s]
ϕ	phase angle	[rad]
ϕ	equivalence ration	[-]
ϕ	discretised variable	[-]
χ	dissipation rate	[-]
$\dot{\omega}_i$	chemical reaction source term	[kg/m^{3}s]
ω	angular velocity	[rad/s]
ω_i	imaginary part of angular velocity	[rad/s]
ω_r	real part of angular velocity	[rad/s]

Operators

det$\mathbf{A}$	determinant of matrix $\mathbf{A}$
$\frac{\partial}{\partial x}$	partial derivative to x
$\frac{D}{Dt}$	material derivative
dx	increment of x
x'	linearised fluctuation in x
$\tilde{x}$	Favre averaged value of x $\tilde{x} = \overline{\rho x}/\overline{\rho}$
x''	fluctuation on the Favre averaged value of x $\tilde{x} = \overline{\rho x}/\overline{\rho}$
i	imaginary unit number $i = \sqrt{(}-1)$
$\mathbf{I}$	identity matrix
$\overline{x}$	average of x
x_0	mean of x
$\mathbf{x} \otimes \mathbf{x}$	dyadic product of vector $\mathbf{x}$
∇x	gradient of scalar x
$\nabla \cdot \mathbf{x}$	divergence of vector $\mathbf{x}$
$\mathbf{x}^T$	transpose of vector $\mathbf{x}$
$\sum$	summation

A
The GRI 3.0 Mechanism without NO_x production

O	H	C	N	AR

Table A.1: Elements in the detailed mechanism

H2	H	O	O2	OH	H2O	HO2	H2O2
C	CH	CH2	CH2(S)	CH3	CH4	CO	CO2
HCO	CH2O	CH2OH	CH3O	CH3OH	C2H	C2H2	C2H3
C2H4	C2H5	C2H6	HCCO	CH2CO	HCCOH	AR	
C3H7	C3H8	CH2CHO	CH3CHO	N2			

Table A.2: Elements in the detailed mechanism

LHS		RHS	Pre Exp Fact	Order	T_{act}
2O+M	$\rightleftharpoons$	O2+M	1.200E+17	-1.000	.00
O+H+M	$\rightleftharpoons$	OH+M	5.000E+17	-1.000	.00
O+H2	$\rightleftharpoons$	H+OH	3.870E+04	2.700	6260.00
O+HO2	$\rightleftharpoons$	OH+O2	2.000E+13	.000	.00
O+H2O2	$\rightleftharpoons$	OH+HO2	9.630E+06	2.000	4000.00
O+CH	$\rightleftharpoons$	H+CO	5.700E+13	.000	.00
O+CH2	$\rightleftharpoons$	H+HCO	8.000E+13	.000	.00
O+CH2(S)	$\rightleftharpoons$	H2+CO	1.500E+13	.000	.00
O+CH2(S)	$\rightleftharpoons$	H+HCO	1.500E+13	.000	.00
O+CH3	$\rightleftharpoons$	H+CH2O	5.060E+13	.000	.00
O+CH4	$\rightleftharpoons$	OH+CH3	1.020E+09	1.500	8600.00
O+CO(+M)	$\rightleftharpoons$	CO2(+M)	1.800E+10	.000	2385.00
O+HCO	$\rightleftharpoons$	OH+CO	3.000E+13	.000	.00
O+HCO	$\rightleftharpoons$	H+CO2	3.000E+13	.000	.00
O+CH2O	$\rightleftharpoons$	OH+HCO	3.900E+13	.000	3540.00
O+CH2OH	$\rightleftharpoons$	OH+CH2O	1.000E+13	.000	.00
O+CH3O	$\rightleftharpoons$	OH+CH2O	1.000E+13	.000	.00
O+CH3OH	$\rightleftharpoons$	OH+CH2OH	3.880E+05	2.500	3100.00
O+CH3OH	$\rightleftharpoons$	OH+CH3O	1.300E+05	2.500	5000.00
O+C2H	$\rightleftharpoons$	CH+CO	5.000E+13	.000	.00
O+C2H2	$\rightleftharpoons$	H+HCCO	1.350E+07	2.000	1900.00
O+C2H2	$\rightleftharpoons$	OH+C2H	4.600E+19	-1.410	28950.00
O+C2H2	$\rightleftharpoons$	CO+CH2	6.940E+06	2.000	1900.00
O+C2H3	$\rightleftharpoons$	H+CH2CO	3.000E+13	.000	.00
O+C2H4	$\rightleftharpoons$	CH3+HCO	1.250E+07	1.830	220.00
O+C2H5	$\rightleftharpoons$	CH3+CH2O	2.240E+13	.000	.00
O+C2H6	$\rightleftharpoons$	OH+C2H5	8.980E+07	1.920	5690.00
O+HCCO	$\rightleftharpoons$	H+2CO	1.000E+14	.000	.00
O+CH2CO	$\rightleftharpoons$	OH+HCCO	1.000E+13	.000	8000.00
O+CH2CO	$\rightleftharpoons$	CH2+CO2	1.750E+12	.000	1350.00
O2+CO	$\rightleftharpoons$	O+CO2	2.500E+12	.000	47800.00
O2+CH2O	$\rightleftharpoons$	HO2+HCO	1.000E+14	.000	40000.00
H+O2+M	$\rightleftharpoons$	HO2+M	2.800E+18	-.860	.00
H+2O2	$\rightleftharpoons$	HO2+O2	2.080E+19	-1.240	.00
H+O2+H2O	$\rightleftharpoons$	HO2+H2O	11.26E+18	-.760	.00
H+O2+N2	$\rightleftharpoons$	HO2+N2	2.600E+19	-1.240	.00
H+O2+AR	$\rightleftharpoons$	HO2+AR	7.000E+17	-.800	.00
H+O2	$\rightleftharpoons$	O+OH	2.650E+16	-.6707	17041.00
2H+M	$\rightleftharpoons$	H2+M	1.000E+18	-1.000	.00
2H+H2	$\rightleftharpoons$	2H2	9.000E+16	-.600	.00
2H+H2O	$\rightleftharpoons$	H2+H2O	6.000E+19	-1.250	.00
2H+CO2	$\rightleftharpoons$	H2+CO2	5.500E+20	-2.000	.00
H+OH+M	$\rightleftharpoons$	H2O+M	2.200E+22	-2.000	.00
H+HO2	$\rightleftharpoons$	O+H2O	3.970E+12	.000	671.00
H+HO2	$\rightleftharpoons$	O2+H2	4.480E+13	.000	1068.00
H+HO2	$\rightleftharpoons$	2OH	0.840E+14	.000	635.00
H+H2O2	$\rightleftharpoons$	HO2+H2	1.210E+07	2.000	5200.00

LHS		RHS	Pre Exp Fact	Order	T_{act}
H+H2O2	$\rightleftharpoons$	OH+H2O	1.000E+13	.000	3600.00
H+CH	$\rightleftharpoons$	C+H2	1.650E+14	.000	.00
H+CH2(+M)	$\rightleftharpoons$	CH3(+M)	6.000E+14	.000	.00
H+CH2(S)	$\rightleftharpoons$	CH+H2	3.000E+13	.000	.00
H+CH3(+M)	$\rightleftharpoons$	CH4(+M)	13.90E+15	-.534	536.00
H+CH4	$\rightleftharpoons$	CH3+H2	6.600E+08	1.620	10840.00
H+HCO(+M)	$\rightleftharpoons$	CH2O(+M)	1.090E+12	.480	-260.00
H+HCO	$\rightleftharpoons$	H2+CO	7.340E+13	.000	.00
H+CH2O(+M)	$\rightleftharpoons$	CH2OH(+M)	5.400E+11	.454	3600.00
H+CH2O(+M)	$\rightleftharpoons$	CH3O(+M)	5.400E+11	.454	2600.00
H+CH2O	$\rightleftharpoons$	HCO+H2	5.740E+07	1.900	2742.00
H+CH2OH(+M)	$\rightleftharpoons$	CH3OH(+M)	1.055E+12	.500	86.00
H+CH2OH	$\rightleftharpoons$	H2+CH2O	2.000E+13	.000	.00
H+CH2OH	$\rightleftharpoons$	OH+CH3	1.650E+11	.650	-284.00
H+CH2OH	$\rightleftharpoons$	CH2(S)+H2O	3.280E+13	-.090	610.00
H+CH3O(+M)	$\rightleftharpoons$	CH3OH(+M)	2.430E+12	.515	50.00
H+CH3O	$\rightleftharpoons$	H+CH2OH	4.150E+07	1.630	1924.00
H+CH3O	$\rightleftharpoons$	H2+CH2O	2.000E+13	.000	.00
H+CH3O	$\rightleftharpoons$	OH+CH3	1.500E+12	.500	-110.00
H+CH3O	$\rightleftharpoons$	CH2(S)+H2O	2.620E+14	-.230	1070.00
H+CH3OH	$\rightleftharpoons$	CH2OH+H2	1.700E+07	2.100	4870.00
H+CH3OH	$\rightleftharpoons$	CH3O+H2	4.200E+06	2.100	4870.00
H+C2H(+M)	$\rightleftharpoons$	C2H2(+M)	1.000E+17	-1.000	.00
H+C2H2(+M)	$\rightleftharpoons$	C2H3(+M)	5.600E+12	.000	2400.00
H+C2H3(+M)	$\rightleftharpoons$	C2H4(+M)	6.080E+12	.270	280.00
H+C2H3	$\rightleftharpoons$	H2+C2H2	3.000E+13	.000	.00
H+C2H4(+M)	$\rightleftharpoons$	C2H5(+M)	0.540E+12	.454	1820.00
H+C2H4	$\rightleftharpoons$	C2H3+H2	1.325E+06	2.530	12240.00
H+C2H5(+M)	$\rightleftharpoons$	C2H6(+M)	5.210E+17	-.990	1580.00
H+C2H5	$\rightleftharpoons$	H2+C2H4	2.000E+12	.000	.00
H+C2H6	$\rightleftharpoons$	C2H5+H2	1.150E+08	1.900	7530.00
H+HCCO	$\rightleftharpoons$	CH2(S)+CO	1.000E+14	.000	.00
H+CH2CO	$\rightleftharpoons$	HCCO+H2	5.000E+13	.000	8000.00
H+CH2CO	$\rightleftharpoons$	CH3+CO	1.130E+13	.000	3428.00
H+HCCOH	$\rightleftharpoons$	H+CH2CO	1.000E+13	.000	.00
H2+CO(+M)	$\rightleftharpoons$	CH2O(+M)	4.300E+07	1.500	79600.00
OH+H2	$\rightleftharpoons$	H+H2O	2.160E+08	1.510	3430.00
2OH(+M)	$\rightleftharpoons$	H2O2(+M)	7.400E+13	-.370	.00
2OH	$\rightleftharpoons$	O+H2O	3.570E+04	2.400	-2110.00
OH+HO2	$\rightleftharpoons$	O2+H2O	1.450E+13	.000	-500.00
OH+H2O2	$\rightleftharpoons$	HO2+H2O	2.000E+12	.000	427.00
OH+H2O2	$\rightleftharpoons$	HO2+H2O	1.700E+18	.000	29410.00
OH+C	$\rightleftharpoons$	H+CO	5.000E+13	.000	.00
OH+CH	$\rightleftharpoons$	H+HCO	3.000E+13	.000	.00
OH+CH2	$\rightleftharpoons$	H+CH2O	2.000E+13	.000	.00
OH+CH2	$\rightleftharpoons$	CH+H2O	1.130E+07	2.000	3000.00
OH+CH2(S)	$\rightleftharpoons$	H+CH2O	3.000E+13	.000	.00

LHS		RHS	Pre Exp Fact	Order	T_{act}
OH+CH3(+M)	$\rightleftharpoons$	CH3OH(+M)	2.790E+18	-1.430	1330.00
OH+CH3	$\rightleftharpoons$	CH2+H2O	5.600E+07	1.600	5420.00
OH+CH3	$\rightleftharpoons$	CH2(S)+H2O	6.440E+17	-1.340	1417.00
OH+CH4	$\rightleftharpoons$	CH3+H2O	1.000E+08	1.600	3120.00
OH+CO	$\rightleftharpoons$	H+CO2	4.760E+07	1.228	70.00
OH+HCO	$\rightleftharpoons$	H2O+CO	5.000E+13	.000	.00
OH+CH2O	$\rightleftharpoons$	HCO+H2O	3.430E+09	1.180	-447.00
OH+CH2OH	$\rightleftharpoons$	H2O+CH2O	5.000E+12	.000	.00
OH+CH3O	$\rightleftharpoons$	H2O+CH2O	5.000E+12	.000	.00
OH+CH3OH	$\rightleftharpoons$	CH2OH+H2O	1.440E+06	2.000	-840.00
OH+CH3OH	$\rightleftharpoons$	CH3O+H2O	6.300E+06	2.000	1500.00
OH+C2H	$\rightleftharpoons$	H+HCCO	2.000E+13	.000	.00
OH+C2H2	$\rightleftharpoons$	H+CH2CO	2.180E-04	4.500	-1000.00
OH+C2H2	$\rightleftharpoons$	H+HCCOH	5.040E+05	2.300	13500.00
OH+C2H2	$\rightleftharpoons$	C2H+H2O	3.370E+07	2.000	14000.00
OH+C2H2	$\rightleftharpoons$	CH3+CO	4.830E-04	4.000	-2000.00
OH+C2H3	$\rightleftharpoons$	H2O+C2H2	5.000E+12	.000	.00
OH+C2H4	$\rightleftharpoons$	C2H3+H2O	3.600E+06	2.000	2500.00
OH+C2H6	$\rightleftharpoons$	C2H5+H2O	3.540E+06	2.120	870.00
OH+CH2CO	$\rightleftharpoons$	HCCO+H2O	7.500E+12	.000	2000.00
2HO2	$\rightleftharpoons$	O2+H2O2	1.300E+11	.000	-1630.00
2HO2	$\rightleftharpoons$	O2+H2O2	4.200E+14	.000	12000.00
HO2+CH2	$\rightleftharpoons$	OH+CH2O	2.000E+13	.000	.00
HO2+CH3	$\rightleftharpoons$	O2+CH4	1.000E+12	.000	.00
HO2+CH3	$\rightleftharpoons$	OH+CH3O	3.780E+13	.000	.00
HO2+CO	$\rightleftharpoons$	OH+CO2	1.500E+14	.000	23600.00
HO2+CH2O	$\rightleftharpoons$	HCO+H2O2	5.600E+06	2.000	12000.00
C+O2	$\rightleftharpoons$	O+CO	5.800E+13	.000	576.00
C+CH2	$\rightleftharpoons$	H+C2H	5.000E+13	.000	.00
C+CH3	$\rightleftharpoons$	H+C2H2	5.000E+13	.000	.00
CH+O2	$\rightleftharpoons$	O+HCO	6.710E+13	.000	.00
CH+H2	$\rightleftharpoons$	H+CH2	1.080E+14	.000	3110.00
CH+H2O	$\rightleftharpoons$	H+CH2O	5.710E+12	.000	-755.00
CH+CH2	$\rightleftharpoons$	H+C2H2	4.000E+13	.000	.00
CH+CH3	$\rightleftharpoons$	H+C2H3	3.000E+13	.000	.00
CH+CH4	$\rightleftharpoons$	H+C2H4	6.000E+13	.000	.00
CH+CO(+M)	$\rightleftharpoons$	HCCO(+M)	5.000E+13	.000	.00
CH+CO2	$\rightleftharpoons$	HCO+CO	1.900E+14	.000	15792.00
CH+CH2O	$\rightleftharpoons$	H+CH2CO	9.460E+13	.000	-515.00
CH+HCCO	$\rightleftharpoons$	CO+C2H2	5.000E+13	.000	.00
CH2+O2	$\rightarrow$	OH+H+CO	5.000E+12	.000	1500.00
CH2+H2	$\rightleftharpoons$	H+CH3	5.000E+05	2.000	7230.00
2CH2	$\rightleftharpoons$	H2+C2H2	1.600E+15	.000	11944.00
CH2+CH3	$\rightleftharpoons$	H+C2H4	4.000E+13	.000	.00
CH2+CH4	$\rightleftharpoons$	2CH3	2.460E+06	2.000	8270.00
CH2+CO(+M)	$\rightleftharpoons$	CH2CO(+M)	8.100E+11	.500	4510.00
CH2+HCCO	$\rightleftharpoons$	C2H3+CO	3.000E+13	.000	.00

LHS		RHS	Pre Exp Fact	Order	T_{act}
CH2(S)+N2	$\rightleftharpoons$	CH2+N2	1.500E+13	.000	600.00
CH2(S)+AR	$\rightleftharpoons$	CH2+AR	9.000E+12	.000	600.00
CH2(S)+O2	$\rightleftharpoons$	H+OH+CO	2.800E+13	.000	.00
CH2(S)+O2	$\rightleftharpoons$	CO+H2O	1.200E+13	.000	.00
CH2(S)+H2	$\rightleftharpoons$	CH3+H	7.000E+13	.000	.00
CH2(S)+H2O(+M)	$\rightleftharpoons$	CH3OH(+M)	4.820E+17	-1.160	1145.00
CH2(S)+H2O	$\rightleftharpoons$	CH2+H2O	3.000E+13	.000	.00
CH2(S)+CH3	$\rightleftharpoons$	H+C2H4	1.200E+13	.000	-570.00
CH2(S)+CH4	$\rightleftharpoons$	2CH3	1.600E+13	.000	-570.00
CH2(S)+CO	$\rightleftharpoons$	CH2+CO	9.000E+12	.000	.00
CH2(S)+CO2	$\rightleftharpoons$	CH2+CO2	7.000E+12	.000	.00
CH2(S)+CO2	$\rightleftharpoons$	CO+CH2O	1.400E+13	.000	.00
CH2(S)+C2H6	$\rightleftharpoons$	CH3+C2H5	4.000E+13	.000	-550.00
CH3+O2	$\rightleftharpoons$	O+CH3O	3.560E+13	.000	30480.00
CH3+O2	$\rightleftharpoons$	OH+CH2O	2.310E+12	.000	20315.00
CH3+H2O2	$\rightleftharpoons$	HO2+CH4	2.450E+04	2.470	5180.00
2CH3(+M)	$\rightleftharpoons$	C2H6(+M)	6.770E+16	-1.180	654.00
2CH3	$\rightleftharpoons$	H+C2H5	6.840E+12	.100	10600.00
CH3+HCO	$\rightleftharpoons$	CH4+CO	2.648E+13	.000	.00
CH3+CH2O	$\rightleftharpoons$	HCO+CH4	3.320E+03	2.810	5860.00
CH3+CH3OH	$\rightleftharpoons$	CH2OH+CH4	3.000E+07	1.500	9940.00
CH3+CH3OH	$\rightleftharpoons$	CH3O+CH4	1.000E+07	1.500	9940.00
CH3+C2H4	$\rightleftharpoons$	C2H3+CH4	2.270E+05	2.000	9200.00
CH3+C2H6	$\rightleftharpoons$	C2H5+CH4	6.140E+06	1.740	10450.00
HCO+H2O	$\rightleftharpoons$	H+CO+H2O	1.500E+18	-1.000	17000.00
HCO+M	$\rightleftharpoons$	H+CO+M	1.870E+17	-1.000	17000.00
HCO+O2	$\rightleftharpoons$	HO2+CO	13.45E+12	.000	400.00
CH2OH+O2	$\rightleftharpoons$	HO2+CH2O	1.800E+13	.000	900.00
CH3O+O2	$\rightleftharpoons$	HO2+CH2O	4.280E-13	7.600	-3530.00
C2H+O2	$\rightleftharpoons$	HCO+CO	1.000E+13	.000	-755.00
C2H+H2	$\rightleftharpoons$	H+C2H2	5.680E+10	0.900	1993.00
C2H3+O2	$\rightleftharpoons$	HCO+CH2O	4.580E+16	-1.390	1015.00
C2H4(+M)	$\rightleftharpoons$	H2+C2H2(+M)	8.000E+12	.440	86770.00
C2H5+O2	$\rightleftharpoons$	HO2+C2H4	8.400E+11	.000	3875.00
HCCO+O2	$\rightleftharpoons$	OH+2CO	3.200E+12	.000	854.00
2HCCO	$\rightleftharpoons$	2CO+C2H2	1.000E+13	.000	.00
O+CH3	$\rightarrow$	H+H2+CO	3.370E+13	.000	.00
O+C2H4	$\rightleftharpoons$	H+CH2CHO	6.700E+06	1.830	220.00
O+C2H5	$\rightleftharpoons$	H+CH3CHO	1.096E+14	.000	.00
OH+HO2	$\rightleftharpoons$	O2+H2O	0.500E+16	.000	17330.00
OH+CH3	$\rightarrow$	H2+CH2O	8.000E+09	.500	-1755.00
CH+H2(+M)	$\rightleftharpoons$	CH3(+M)	1.970E+12	.430	-370.00
CH2+O2	$\rightarrow$	2H+CO2	5.800E+12	.000	1500.00
CH2+O2	$\rightleftharpoons$	O+CH2O	2.400E+12	.000	1500.00
CH2+CH2	$\rightarrow$	2H+C2H2	2.000E+14	.000	10989.00
CH2(S)+H2O	$\rightarrow$	H2+CH2O	6.820E+10	.250	-935.00
C2H3+O2	$\rightleftharpoons$	O+CH2CHO	3.030E+11	.290	11.00

LHS		RHS	Pre Exp Fact	Order	T_{act}
C2H3+O2	$\rightleftharpoons$	HO2+C2H2	1.337E+06	1.610	-384.00
O+CH3CHO	$\rightleftharpoons$	OH+CH2CHO	2.920E+12	.000	1808.00
O+CH3CHO	$\rightarrow$	OH+CH3+CO	2.920E+12	.000	1808.00
O2+CH3CHO	$\rightarrow$	HO2+CH3+CO	3.010E+13	.000	39150.00
H+CH3CHO	$\rightleftharpoons$	CH2CHO+H2	2.050E+09	1.160	2405.00
H+CH3CHO	$\rightarrow$	CH3+H2+CO	2.050E+09	1.160	2405.00
OH+CH3CHO	$\rightarrow$	CH3+H2O+CO	2.343E+10	0.730	-1113.00
HO2+CH3CHO	$\rightarrow$	CH3+H2O2+CO	3.010E+12	.000	11923.00
CH3+CH3CHO	$\rightarrow$	CH3+CH4+CO	2.720E+06	1.770	5920.00
H+CH2CO(+M)	$\rightleftharpoons$	CH2CHO(+M)	4.865E+11	0.422	-1755.00
O+CH2CHO	$\rightarrow$	H+CH2+CO2	1.500E+14	.000	.00
O2+CH2CHO	$\rightarrow$	OH+CO+CH2O	1.810E+10	.000	.00
O2+CH2CHO	$\rightarrow$	OH+2HCO	2.350E+10	.000	.00
H+CH2CHO	$\rightleftharpoons$	CH3+HCO	2.200E+13	.000	.00
H+CH2CHO	$\rightleftharpoons$	CH2CO+H2	1.100E+13	.000	.00
OH+CH2CHO	$\rightleftharpoons$	H2O+CH2CO	1.200E+13	.000	.00
OH+CH2CHO	$\rightleftharpoons$	HCO+CH2OH	3.010E+13	.000	.00
CH3+C2H5(+M)	$\rightleftharpoons$	C3H8(+M)	.9430E+13	.000	.00
O+C3H8	$\rightleftharpoons$	OH+C3H7	1.930E+05	2.680	3716.00
H+C3H8	$\rightleftharpoons$	C3H7+H2	1.320E+06	2.540	6756.00
OH+C3H8	$\rightleftharpoons$	C3H7+H2O	3.160E+07	1.800	934.00
C3H7+H2O2	$\rightleftharpoons$	HO2+C3H8	3.780E+02	2.720	1500.00
CH3+C3H8	$\rightleftharpoons$	C3H7+CH4	0.903E+00	3.650	7154.00
CH3+C2H4(+M)	$\rightleftharpoons$	C3H7(+M)	2.550E+06	1.600	5700.00
O+C3H7	$\rightleftharpoons$	C2H5+CH2O	9.640E+13	.000	.00
H+C3H7(+M)	$\rightleftharpoons$	C3H8(+M)	3.613E+13	.000	.00
H+C3H7	$\rightleftharpoons$	CH3+C2H5	4.060E+06	2.190	890.00
OH+C3H7	$\rightleftharpoons$	C2H5+CH2OH	2.410E+13	.000	.00
HO2+C3H7	$\rightleftharpoons$	O2+C3H8	2.550E+10	0.255	-943.00
HO2+C3H7	$\rightarrow$	OH+C2H5+CH2O	2.410E+13	.000	.00
CH3+C3H7	$\rightleftharpoons$	2C2H5	1.927E+13	-0.320	.00

Table A.3: Reactions of the detailed mechanism

B
UG 11 Filter properties

The filter that has been used during the OH^* measurements was of the type UG11. The properties of this filter are shown in figure B.1. Most wave lengths are filtered out by this filter. Two narrow bandwidths can pass the filter. The main narrow band is around 350 nm. Approximately 70 % of the light can pass trought the filter at this wave length. At another band, around 750 nm, only 20 % of the light is transmitted.

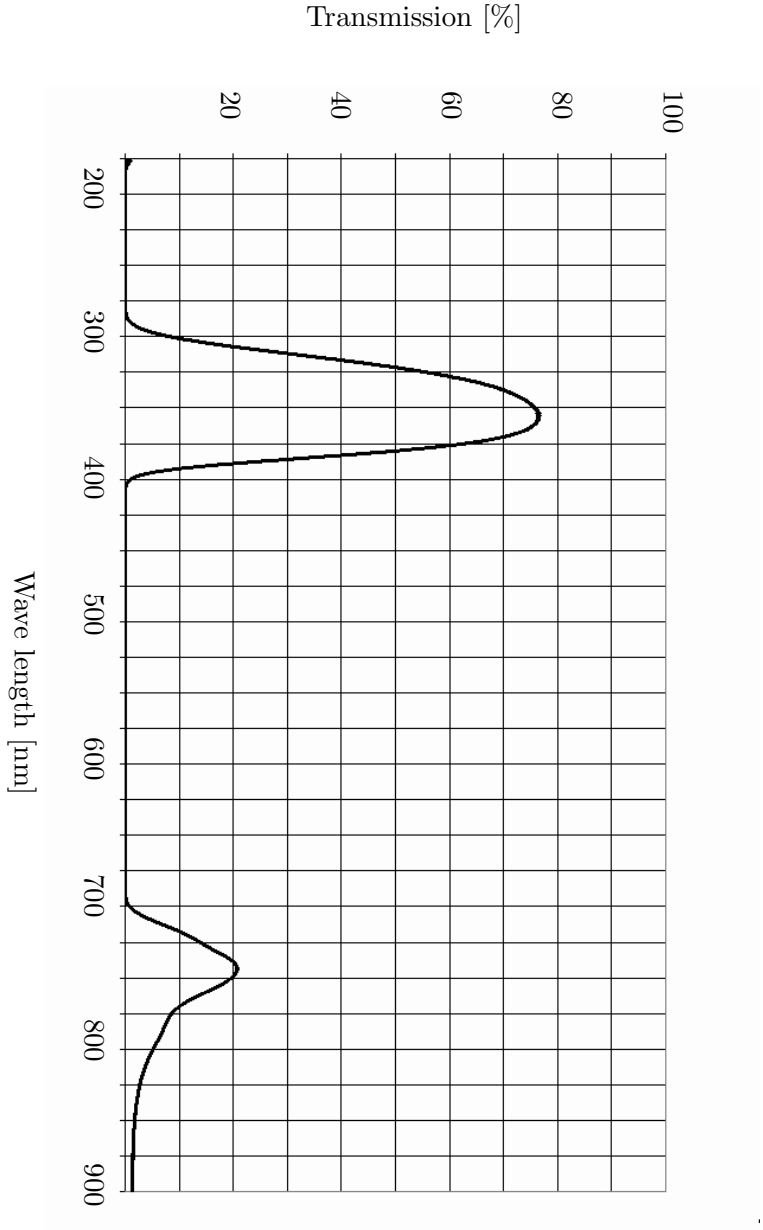

Figure B.1: UG11 Filter properties

C
Sensitivity analysis for acoustic model

Case name	Temp profiel	Source [kg/s]
case 1	derived from CFX	source 1
case 2	derived from CFX	source 2
case 3	derived from CFX	source 3
case 4	linear	source 1
case 5	linear	source 2
case 6	linear	source 3

Table C.1: Investigated cases for acoustic model.

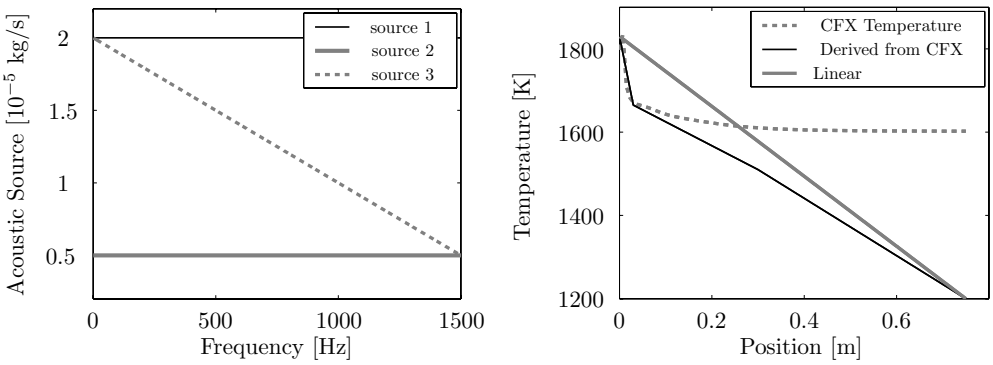

(a) Three sources

(b) Two temperature profiles

Figure C.1: The three types of sources and two temperature profiles that were applied.

According to the temperature profile: The dashed line is the axial temperature development withdrawn from a CFD calculation. However, these calculations are adiabatic. In reality, the heat losses can be considerable. The temperature from CFD decays very quickly at low values for the position (between 0 and 0.03 m). This is caused by the post flame mixing of the product gases and excess air. As this takes place in a small region, it is assumed that the transfer losses outwards of the combustion chamber are smaller than the decay caused by the mixing. Once the mixing is alomost finished (at 0.03 m) the heat losses outwards of the combustion chamber will exceed the temperature decay caused by mixing. From this point (0.03 m), a linear relation between the temperature at at 0.03 m and the exit of the combustion chamber is assumed. This exit temperature is measured during experiments.

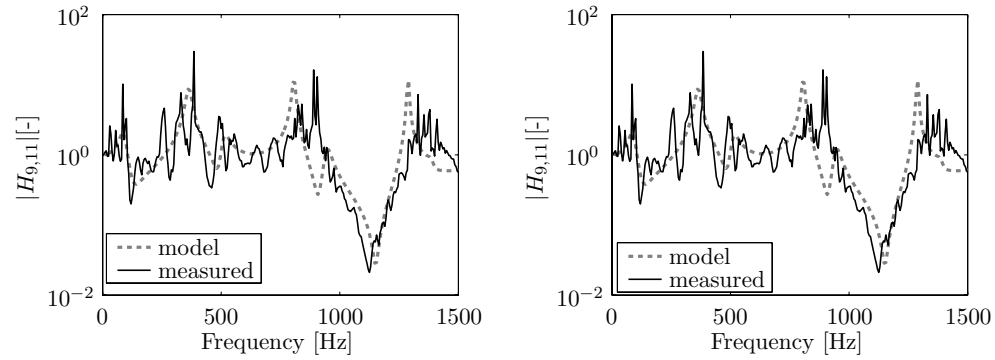

(a) $|H_{9,11}|$ case 1

(b) $|H_{9,11}|$ case 2

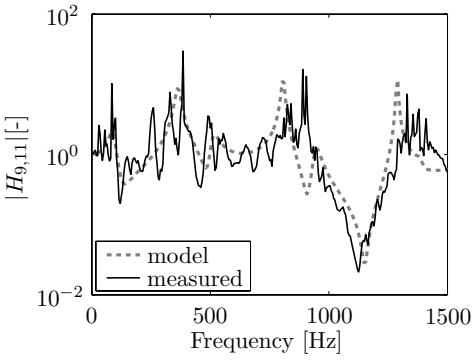

(c) $|H_{9,11}|$ case 3

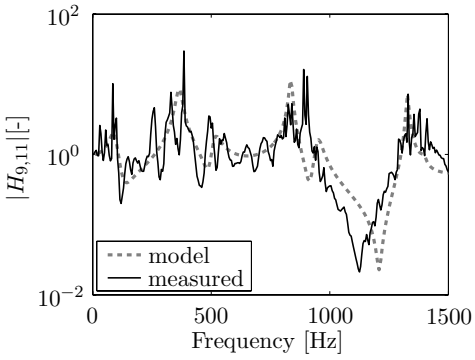

(d) $|H_{9,11}|$ case 4

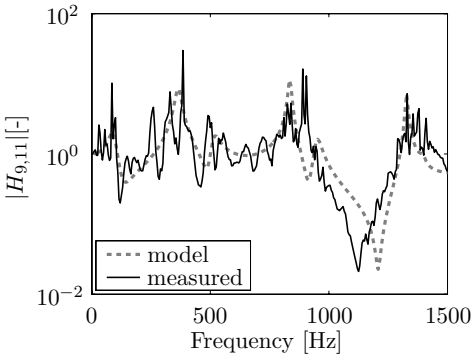

(e) $|H_{9,11}|$ case 5

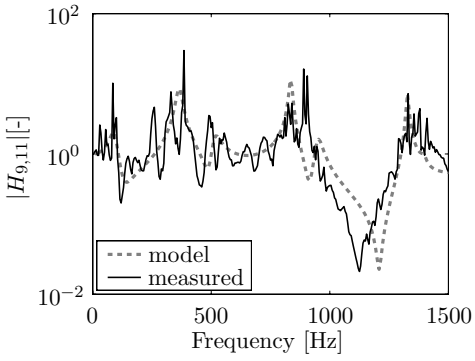

(f) $|H_{9,11}|$ case 6

Figure C.2: Comparison between modelled and measured transfer function between measuring point 1 and 2 with varying source and temperature profile.

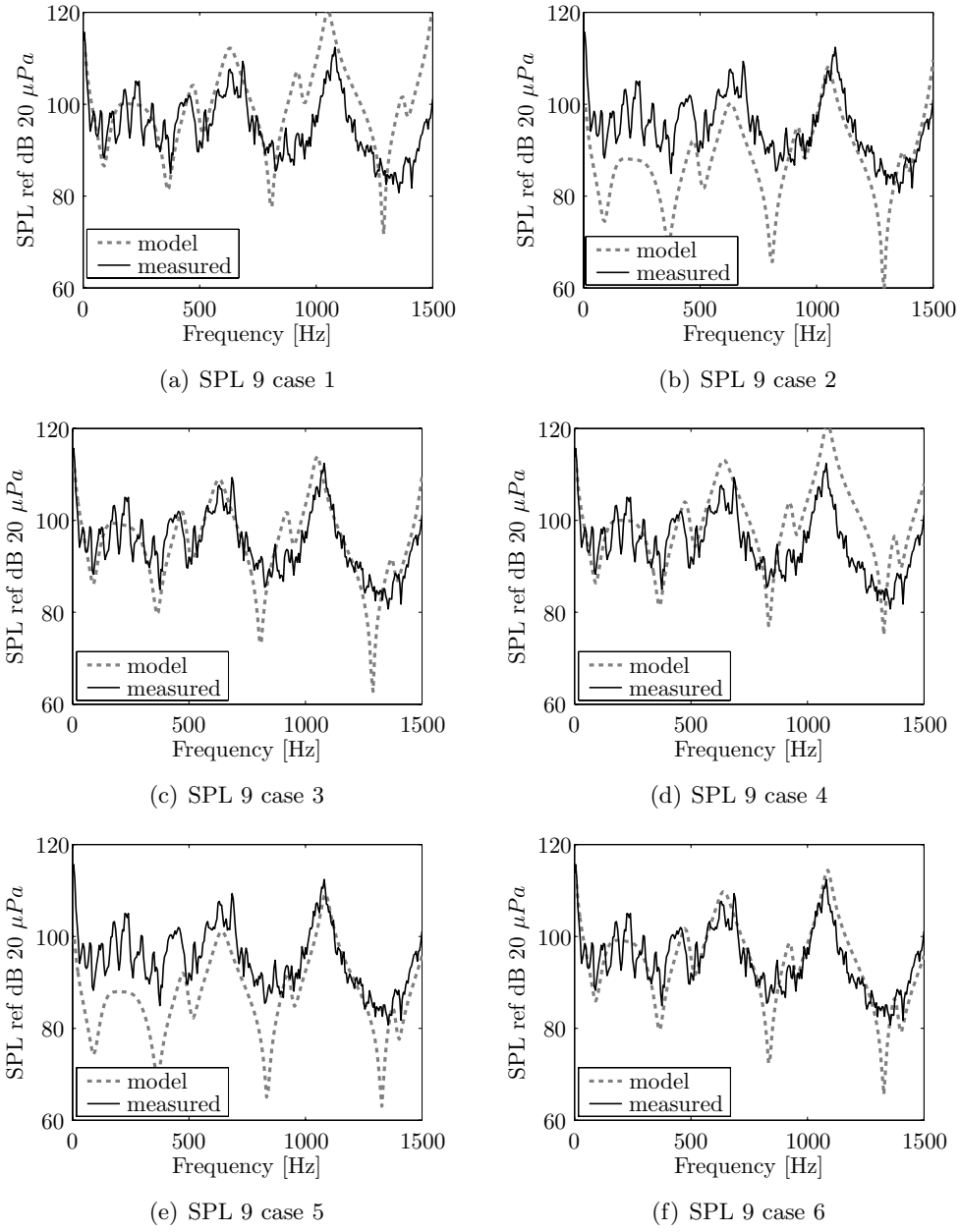

(a) SPL 9 case 1

(b) SPL 9 case 2

(c) SPL 9 case 3

(d) SPL 9 case 4

(e) SPL 9 case 5

(f) SPL 9 case 6

Figure C.3: Comparison between modelled and measured Sound Pressure Level at measuring point 1 with varying source and temperature profile.

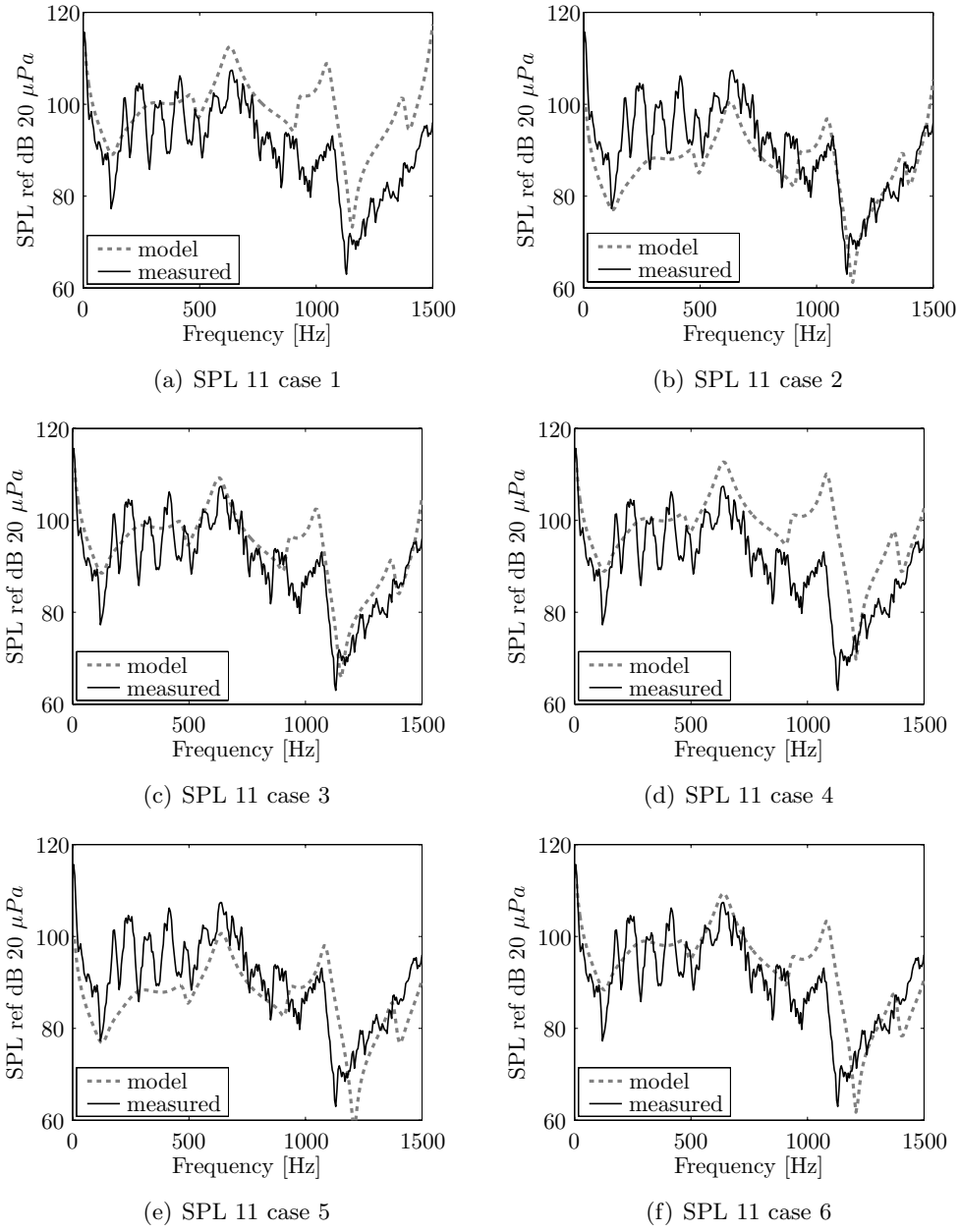

(a) SPL 11 case 1

(b) SPL 11 case 2

(c) SPL 11 case 3

(d) SPL 11 case 4

(e) SPL 11 case 5

(f) SPL 11 case 6

Figure C.4: Comparison between modelled and measured Sound Pressure Level at measuring point 2 with varying source and temperature profile.

D
The flame as an acoustic source

In chapter 3, the analogy of Lighthill was presented.
Assuming that the pressure is a function of the density and the entropy like $p = p(\rho, s)$, then the material derivative of this function can be written as:

$$\frac{\mathrm{D}p}{\mathrm{D}t} = \left.\frac{\partial p}{\partial \rho}\right|_s \frac{\mathrm{D}\rho}{\mathrm{D}t} + \left.\frac{\partial p}{\partial s}\right|_\rho \frac{\mathrm{D}s}{\mathrm{D}t} \tag{D.1}$$

as

$$\frac{\partial p}{\partial \rho} = c_f^2 \tag{D.2}$$

where c_f is the speed of sound at the position of the flame. The linearised version of this equation reads:

$$\frac{\mathrm{D}p'}{\mathrm{D}t} = c_f^2 \frac{\mathrm{D}\rho'}{\mathrm{D}t} + \left.\frac{\partial p'}{\partial s}\right|_\rho \frac{\mathrm{D}s'}{\mathrm{D}t} \tag{D.3}$$

Using the temperature as a so-called dummy variable, the partial derivative of the pressure to the entropy can be rewritten to:

$$\frac{\partial p}{\partial s} = \frac{\left.\frac{\partial p}{\partial T}\right|_\rho}{\left.\frac{\partial s}{\partial T}\right|_\rho} = \frac{\rho T R}{c_v} \tag{D.4}$$

The internal energy, normally a function of entropy and density can be rewritten as a function of pressure and temperature for ideal gases. Then $u = u(s, \rho)$

can be rewritten to $u = u(s, \rho)$, leading to:

$$\left(\frac{\partial u}{\partial p}\right)_T = \left(\frac{\partial u}{\partial s}\right)_v \left(\frac{\partial s}{\partial p}\right)_T + \left(\frac{\partial u}{\partial v}\right)_s \left(\frac{\partial v}{\partial p}\right)_T \tag{D.5}$$

As $du = Tds - Pdv$

$$\left(\frac{\partial u}{\partial p}\right)_T = T\left(\frac{\partial s}{\partial p}\right)_T - p\left(\frac{\partial v}{\partial p}\right)_T \tag{D.6}$$

Using the Maxwell relation $\left(\frac{\partial s}{\partial p}\right)_T = \left(\frac{\partial v}{\partial T}\right)_p$ this results in:

$$\left(\frac{\partial u}{\partial p}\right)_T = -T\left(\frac{\partial v}{\partial T}\right)_p - p\left(\frac{\partial v}{\partial p}\right)_T \tag{D.7}$$

and using the perfect gas law $Pv = RT$ this comes down to:

$$\left(\frac{\partial u}{\partial p}\right)_T = -T\frac{R}{p} + \frac{RT}{p} = 0 \tag{D.8}$$

This means that the internal energy u is not dependent on pressure p for perfect gases. Similarly:

$$\left(\frac{\partial u}{\partial T}\right)_p = \left(\frac{\partial u}{\partial s}\right)_v \left(\frac{\partial s}{\partial T}\right)_p + \left(\frac{\partial u}{\partial v}\right)_s \left(\frac{\partial v}{\partial T}\right)_p \tag{D.9}$$

and thus:

$$\left(\frac{\partial u}{\partial T}\right)_p = T\left(\frac{\partial s}{\partial T}\right)_p - p\left(\frac{\partial v}{\partial T}\right)_p = c_p - R = c_v \tag{D.10}$$

and so $du = Tds - pdv = c_v(T)dT$ for perfect gases. Therefor $du = c_v dT = Tds - pdv$ and so $ds(T, \rho) = \frac{c_v}{T}dT + \frac{p}{T}d\left(\frac{1}{\rho}\right)$. Now, equations D.3 and D.4 can be rewritten: When all terms are devided by c_0^2 and at both sides of the equal sign the term of $\frac{\mathrm{D}\rho'}{\mathrm{D}t}$ is withdrawn,

$$\frac{\mathrm{D}}{\mathrm{D}t}\left(\frac{p'}{c_0^2} - \rho'\right) = \left(\frac{c_f^2}{c_0^2} - 1\right)\frac{\mathrm{D}\rho'}{\mathrm{D}t} + \frac{\rho RT}{c_0^2 c_v}\frac{\mathrm{D}s'}{\mathrm{D}t} \tag{D.11}$$

In this equation, the term $\rho' - \frac{p'}{c_0^2}$ is the so-called excess density ρ'_e. The material derivative of this excess density can be split:

$$\frac{\mathrm{D}\rho'_e}{\mathrm{D}t} = \frac{\partial \rho'_e}{\partial t} + \mathbf{u}\nabla \cdot \rho'_e = \frac{\partial \rho'_e}{\partial t} + \nabla\left(\mathbf{u}\rho'_e\right) - \rho'_e \nabla \cdot \mathbf{u} \tag{D.12}$$

Because of continuity :

$$\nabla \cdot \mathbf{u} = \frac{-1}{\rho} \frac{\mathrm{D}\rho}{\mathrm{D}t} \tag{D.13}$$

and thus:

$$\rho'_e \nabla \cdot \mathbf{u} = \frac{-\rho'_e}{\rho} \frac{\mathrm{D}\rho}{\mathrm{D}t} \tag{D.14}$$

$$-\frac{\partial \rho'_e}{\partial t} = \left(\frac{c_f^2}{c_0^2} - 1 + \frac{\rho'_e}{\rho} \right) \frac{\mathrm{D}\rho'}{\mathrm{D}t} + \frac{\rho R T}{c_0^2 c_v} \frac{\mathrm{D}s'}{\mathrm{D}t} + \nabla \cdot \left(\mathbf{u} \rho'_e \right) \tag{D.15}$$

Taking the time derivative of both sides:

$$-\frac{\partial^2 \rho'_e}{\partial t^2} = \frac{\partial}{\partial t} \left[\left(\frac{c_f^2}{c_0^2} - 1 + \frac{\rho'_e}{\rho} \right) \frac{\mathrm{D}\rho'}{\mathrm{D}t} + \frac{\rho R T}{c_0^2 c_v} \frac{\mathrm{D}s'}{\mathrm{D}t} + \nabla \cdot \left(\mathbf{u} \rho'_e \right) \right] \tag{D.16}$$

Now, the term of the LHS matches the source term of the Lighthill's analogy. Becasue of this, also the RHS of equation D.16 equals this source term. This RHS contains three terms and those will be discussed:

$$\frac{c_f^2}{c_0^2} - 1 + \frac{\rho'_e}{\rho} \tag{D.17}$$

According to van Kampen [25] D.17 becomes 0 for ideal gases with a constant heat capacity.

$$\frac{\partial}{\partial t} \left[\frac{\rho R T}{c_0^2 c_v} \frac{\mathrm{D}s'}{\mathrm{D}t} \right] \tag{D.18}$$

Equation D.17 is the source term due to non-isentropic processes. Combustion is such a non-isentropic process. This term will be developed further down. Finally, there is the term of

$$\nabla \cdot \left(\mathbf{u} \rho'_e \right) \tag{D.19}$$

This term is a source term of sound generated by spatial density fluctuations (movements of the flame). Based on dimension analysis [25, 92], this source can be neglected compared to the remaining source term (see equation D.18) for low Mach number flows. It should be noted that for combustion of low calorific fuels, the spatial density fluctuations are more important than for fuels with high calorific values. However, this term is still neglected.
From thermodynamics can be withdrawn that:

$$q'_f = \rho T \frac{\mathrm{D}s'}{\mathrm{D}t} \tag{D.20}$$

and so that

$$\frac{\partial}{\partial t} \left[\frac{\rho R T}{c_0^2 c_v} \frac{\mathrm{D}s'}{\mathrm{D}t} \right] = \frac{\partial}{\partial t} \left[\frac{R}{c_0^2 c_v} q'_f \right] \tag{D.21}$$

Knowing that $c_p/c_v = \gamma$ and that $c_p - c_v = R$, this becomes:

$$\frac{\partial}{\partial t}\left[\frac{R}{c_0^2 c_v} q_f'\right] = \frac{\partial}{\partial t}\left[\frac{\gamma - 1}{c_0^2} q_f'\right] \tag{D.22}$$

And so:

$$\frac{1}{c_0^2}\frac{\partial^2 p'}{\partial t^2} - \nabla^2 p' = \frac{\partial}{\partial t}\left[\frac{\gamma - 1}{c_0^2} q_f'\right] \tag{D.23}$$

E
n-τ parameters

case	F_1	F_2	N_1	N_2	σ_1	σ_2	τ_1	τ_2	ground
Syn1Cold	120	145	3.4	1.2	13	10	0.0009	0.0013	0.3
Syn2Cold	30	140	1.3	1.3	18	35	0.023	0.001	0.3
Meth1Cold	30	130	1.4	1.1	25	40	0.013	0.002	0.2
Meth2Cold	40	130	0.9	1.2	18	35	0.023	0.002	0.2
Syn1Hot	20	160	1	0.9	30	50	0.012	0.0009	0.1
Syn2Hot	30	140	0.8	1.3	15	40	0.0013	0.0007	0.2
Meth1Hot	45	135	2.0	2.2	12	50	0.015	0.002	0.3
Meth2Hot	45	140	1.6	1.8	15	35	0.0075	0.0005	0.3

Table E.1: n-τ parameters for the measured flame transfer functions

F
Laminar CFI databases

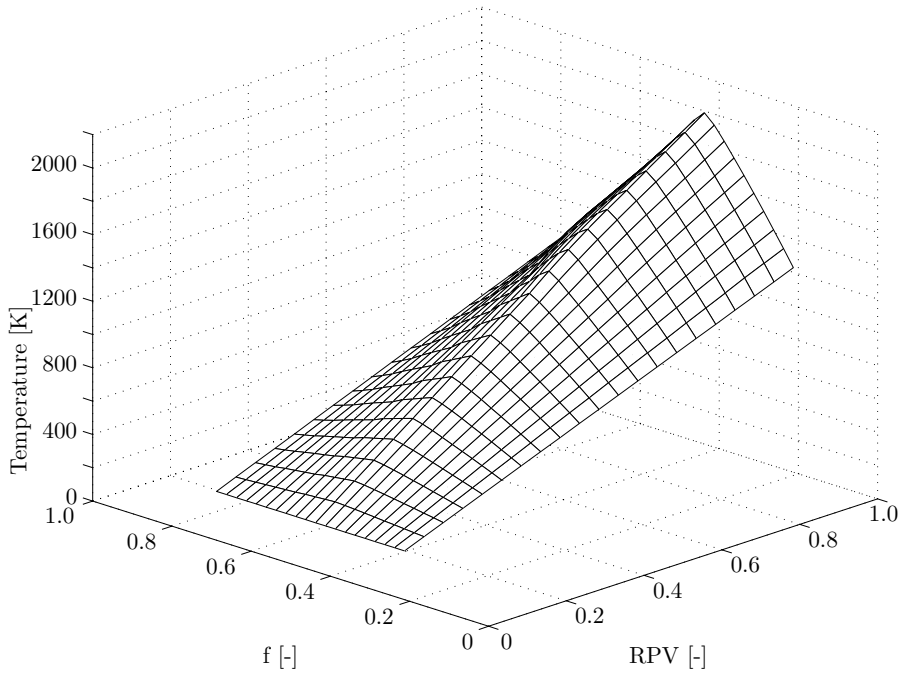

(a) Temperature

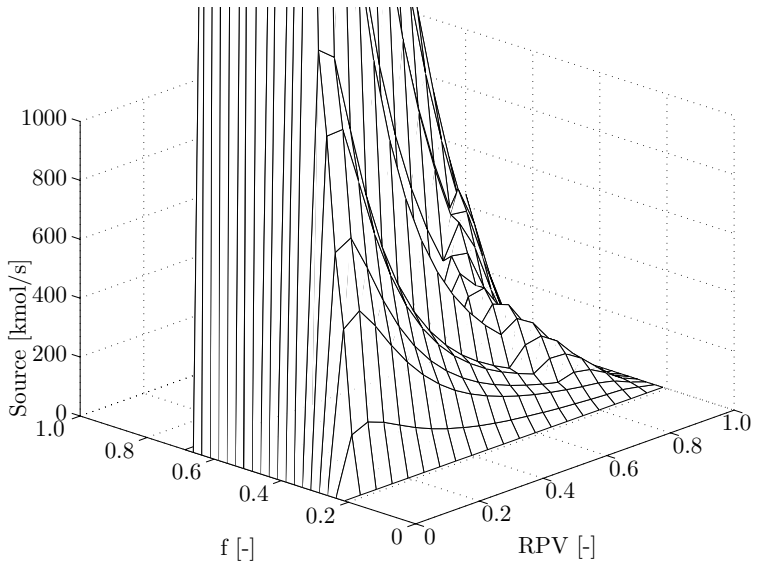

(b) Source

Figure F.1: Chemical source term dependent on the RPV and mixture fraction in the laminar database of Syn1Cold.

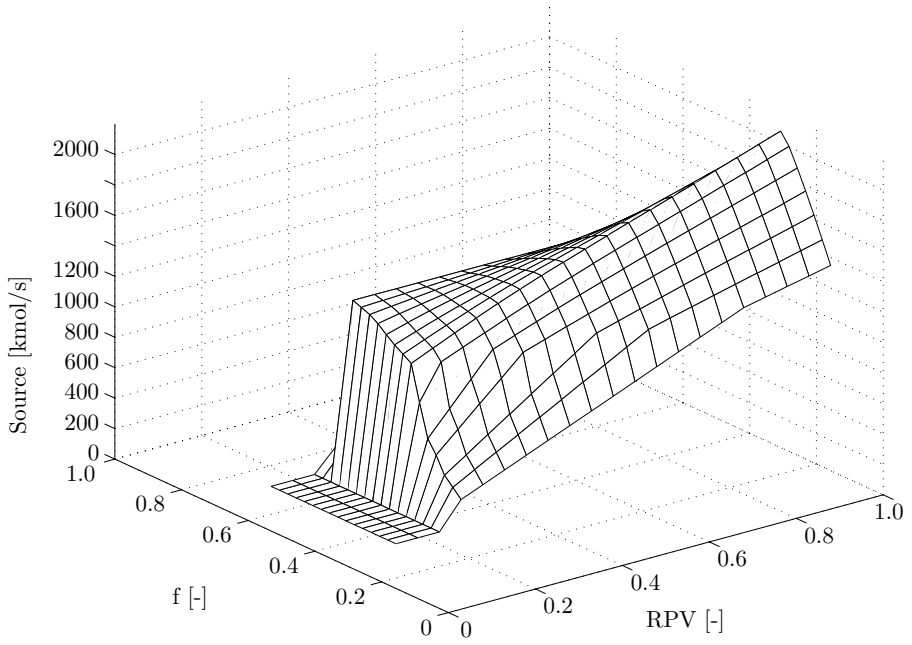

(a) Temperature

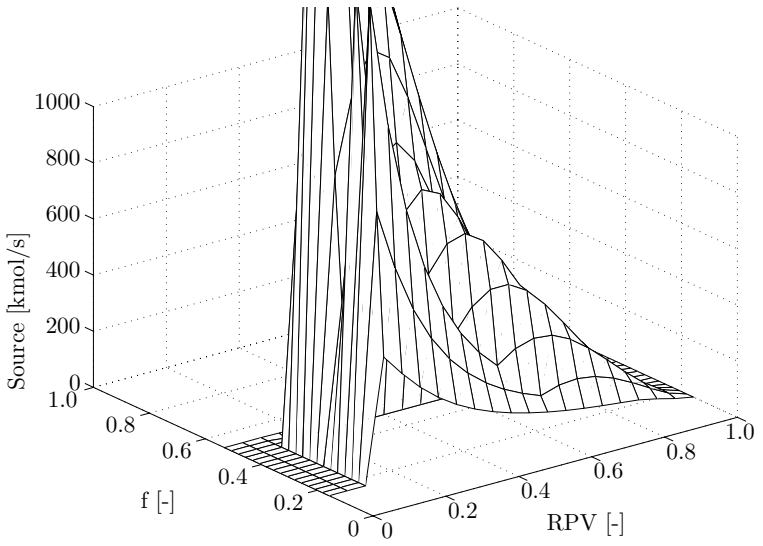

(b) Source

Figure F.2: Chemical source term dependent on the RPV and mixture fraction in the laminar database of Meth1Cold.

G
Measured Flame Transfer Functions

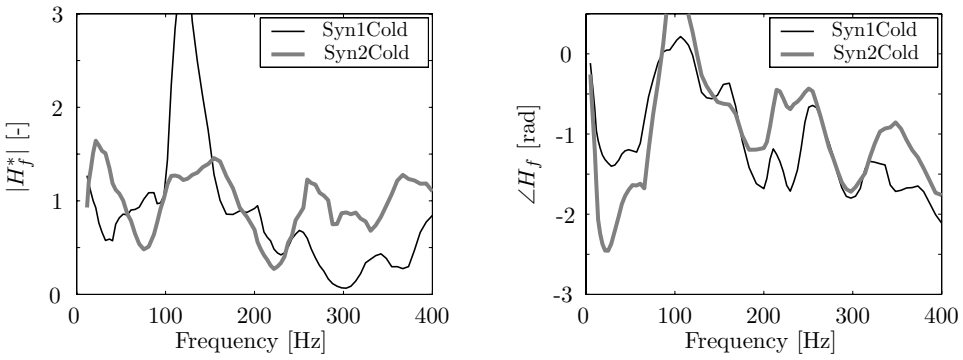

(a) Amplitude (b) Phase angle

Figure G.1: Results of the measured flame transfer functions of cases Syn1Cold and Syn2Cold.

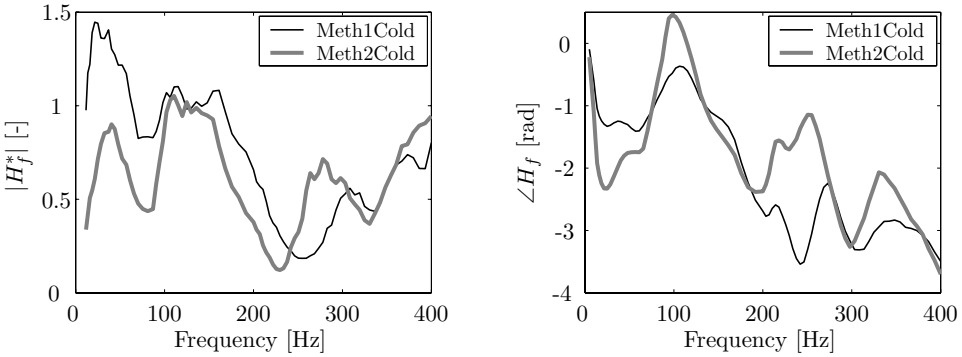

(a) Amplitude (b) Phase angle

Figure G.2: Results of the measured flame transfer functions of cases Meth1Cold and Meth2Cold.

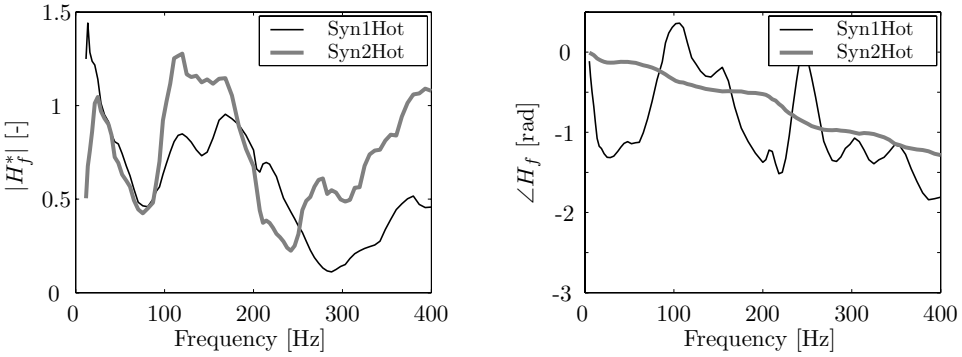

(a) Amplitude (b) Phase angle

Figure G.3: Results of the measured flame transfer functions of cases Syn1Hot and Syn2Hot.

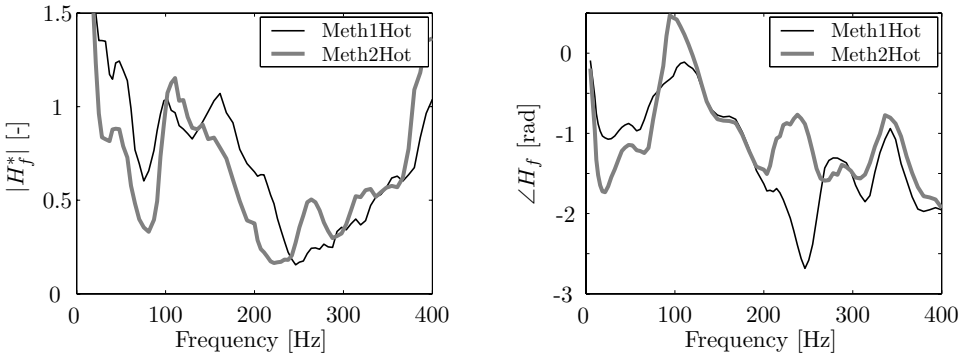

(a) Amplitude

(b) Phase angle

Figure G.4: Results of the measured flame transfer functions of cases Meth1Hot and Meth2Hot.

H
Predicted Flame Transfer Functions

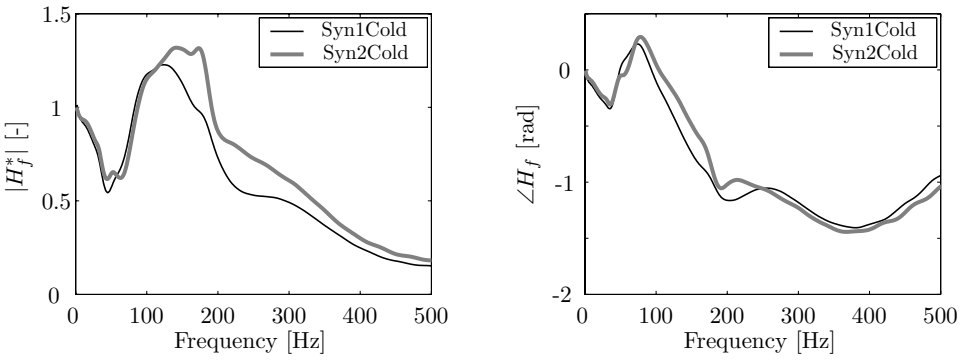

(a) Amplitude

(b) Phase angle

Figure H.1: Results of the predicted flame transfer functions of cases Syn1Cold and Syn2Cold.

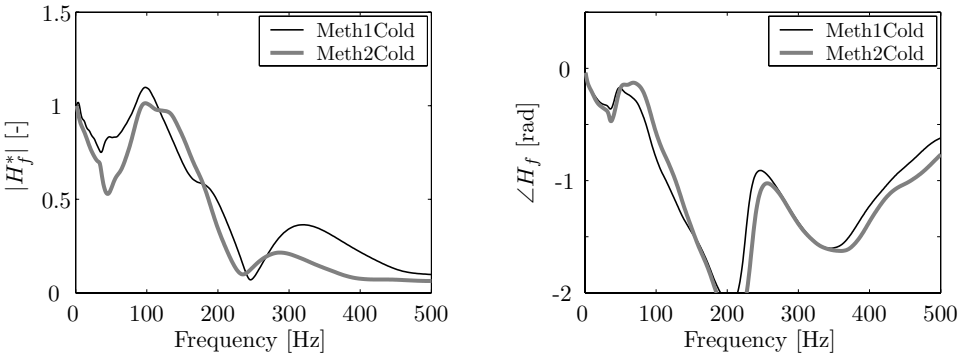

(a) Amplitude (b) Phase angle

Figure H.2: Results of the predicted flame transfer functions of cases Meth1Cold and Meth2Cold.

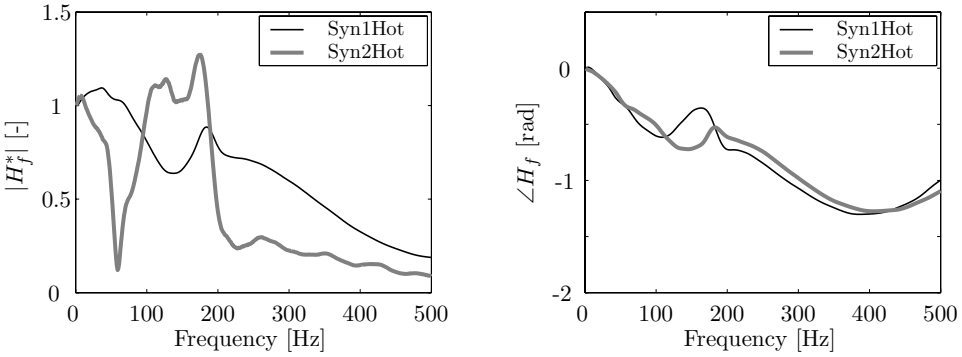

(a) Amplitude (b) Phase angle

Figure H.3: Results of the predicted flame transfer functions of cases Syn1Hot and Syn2Hot.

Bibliography

[1] Wikipedia. Fossil fuel. *http://en.wikipedia.org/wiki/Fossil_fuel*.

[2] T. Poinsot and D. Veynante. *Theoretical and Numerical Combustion*. R.T. Edwards, 2005.

[3] S.A. Klein. *On the acoustics of turbulent non-premixed flames*. PhD thesis, University of Twente, 2002.

[4] K. Ramamurthi and R.K. Patnaik. Noise reducion in non-premixed lifted-jet flames. *Flow, Turbulence and Combustion*, 72:49–67, 2003.

[5] A.H. Lefebvre. *Gas turbine combustion, second edition*. Taylor & Francis, 1998.

[6] A.P. Dowling. Singing flames - the coupling of acoustics and combustion. *Proceedings of Tenth International Congres of Sound and Vibration*, July 2003.

[7] A.A. Putnam. *Combustion - Driven Oscillations in Industry*. American EL Sevier Publishers, 1971.

[8] J.W.S. Rayleigh. The. *Nature*, XVIII:319–321, 1878.

[9] W. Polifke, A. Poncet, C.O. Paschereit, and K. Döbbeling. Reconstruction of acoustic transfer matrices by instationary computational fluid dynamics. *Journal of Sound and Vibration*, 245(3):483–510, 2001.

[10] F.Nicoud and T. Poinsot. Thermoacoustic instabilities: Should the rayleigh criterion be extended to include entropy changes? *Combustion and Flame*, 142(1):153–159, 2005.

[11] P.L. Rijke. Notitz uber eine neue art, die luft in einer an beiden enden offenen rohre in schwingungen ze versetzen. *Annalen der Physik*, 107(339343), 1859.

[12] J.W.S. Rayleigh. *The theory of sound*. Macmillan and Co. Ltd, London, 1878.

[13] M.A. Heckl. Active control of the noise from a rijke tube. *Journal of Sound and Vibration*, 124:117–133, 1972.

[14] A. Hirschberg and C. Schram. A primitive approach to aeroacoustics. *Sound-Flow Interactions*, pages 1–30, 2002.

[15] S.M. Candel and T.J. Poinsot. Interactions between acoustics and combustion. *Proceedings of The Institute of Acoustics*, 10(2):103–153, 1988.

[16] F.A. Williams. *Combustion Theory*. The Benjamin/ Cummings Publishing Company, Inc., 1985.

[17] G.I. Sivashinsky. Instabilities, pattern formation and turbulence in flames. *Annual Review of Fluid Mechanics*, 15:179, 1983.

[18] M.L. Frankel and G.I. Sivashinsky. Fingering instability in nonadiabatic low-lewis number flames. *Pshysical Review*, 52(6):6154–6157, 1995.

[19] C. Kaiser, J.-B. Liu, and P.D. Ronney. Diffusive-thermal instability of counter-flow flames at low lewis number. *38^{t}h Aerospace Sciences Meeting & Exhibit, Reno*, (AIAA 2000-0576), 2000.

[20] V.V. Toro. *Experimental Study of the Structure of Laminar Axisymmetric H_2/Air Diffusion Flames*. PhD thesis, Rijks Universiteit Groningen, 2006.

[21] J.S. Kim, F.A. Williams, and P.D. Ronney. Diffusive-thermal instability of diffusion flames. *Journal of Fluid Mechanics*, 327:273–301, 1996.

[22] M. Tsurikov, W. Meier, and K.-P. Geigle. Investigations of a syngas-fired gas turbine model combustor by planar laser techniques. *Proceedings of ASME Turbo Expo 2006*, (GT2006-90344), 2006.

[23] N. Slavinskaya, M. Braun-Unkhoff, and P. Frank. Reduced mechanisms for methane and syngas combustion in gas turbines. *Proceedings of ASME Turbo Expo 2004*, (GT2005-68287), 2005.

[24] M.A.F. Derksen. *On the influence of steam on combustion*. PhD thesis, University of Twente, 2005.

[25] J.F. van Kampen. *Acoustic pressure oscillations induced by confined turbulent premixed natural gas flames*. PhD thesis, Universityof Twente, 2006.

[26] A.K. Gupta, D.G. Lilley, and N. Syred. *Swirl flows*. Abacus Press, 1984.

[27] C.O. Paschereit, B. Schuermans, W. Polifke, and O. Mattson. Measurement of transfer matrices and source terms of premixed flames. *Journal of Engineering for Gas Turbines and Power*, 124:239–247, 2002.

[28] B. Schuermans, V. Bellucci, F. Guethe, F. Meili, P. Flohr, and C.O. Paschereit. A detailed analysis of thermoacoustic interaction mechanisms in a turbulent premixed flame. *Proceedings of ASME Turbo Expo 2004*, (GT2004-53831), 2004.

[29] W.S. Cheung, G.J.M. Sims, R.W. Copplestone, S.R. Stow, and A.P. Dowling. Measurement and analysis of flame transfer function in a sector combustor under high pressure conditions. *Proceedings of ASME Turbo Expo 2003*, (2003-GT-38219), 2003.

[30] A. Gentemann, C. Hirsch, F. Kiesewetter, T. Sattelmayer, and W. Polifke. Validation of flame transfer function reconstruction for perfectly premixed swirl flames. *Preceedings of ASME Trubo Expo 2004*, (GT2004-53776), 2004.

[31] E. Freitag, H. Konle, M. Lauer, C. Hirsch, and T. Sattelmater. Pressure influence on the flame transfer function of a premixed swirling flame. *Proceedings of ASME Turbo Expo 2006*, (2006-GT-90540), 2006.

[32] D. Bernier, S. Ducruix, F. Lacas, and S. Candel. Transfer function measurements in a model combustor: application to adaptive instability control. *Combustion Science and Technology*, 175:993–1013, 2003.

[33] M. Harleman. *Characterizing flame behavior in a lean premixed turbulent methane burner with optical techniques.* Master Thesis, University of Twente, 2005.

[34] Y. Ikeda, J. Kojima, and T. NakaJima. Local damkohler number measurement in turbulent methane/air premixed flames by local oh*, ch* and $C_2{}^*$ chemiluminescence. *Proceedings of the 36th AIAA/ASME/SAE/ASEE Joint Propulsion Conference and Exhibit*, (AIAA-2000-3395), 2000.

[35] J.O. Keller and K. Saito. Measurements of the combusting flow in a pulse combustor. *Combustion Science and Technology*, 53:137–163, 1987.

[36] B.O. Ayoola, R. Balachandran, J.H. Frankc, E. Mastorakos, and C.F. Kaminski. Spatially resolved heat release rate measurements in turbulent premixed flames. *Combustion and Flame*, 144:1–16, 2006.

[37] M.J. Lighthill. On sound generated aerodynamically. i. general theory. *Proceedings of Royal Society of London. Series A, Mathematical and Physical Sciences*, 211(1107):564–587, 1952.

[38] M.J. Lighthill. On sound generated aerodynamically. ii. turbulence as a source of sound. *Proceedings of Royal Society of London. Series A, Mathematical and Physical Sciences*, 222(1148):1–32, 1954.

[39] M.J. Lighthill. The bakarian lecture, 1961. sound generated aerodynamically. *Proceedings of Royal Society of London. Series A, Mathematical and Physical Sciences*, 267(1329):147–182, 1962.

[40] A.P. Dowling and J.E. Ffowcs Williams. *Sound and sources of sound.* Ellis Horwood Limited, 1983.

[41] R.I. Sujith, G.A. Waldherr, and B.T. Zinn. An exact solution for one-dimensional acoustic fields in ducts with an axial temperature gradient. *Journal of Sound and Vibration*, 184(3):389–402, 1995.

[42] C. Zwikker and C. Kosten. Sound absorbing materials. *Amsterdam: Elsevier*, 1949.

[43] H. Tijdeman. On the propagation of sound waves in cylindrical tubes. *Journal of Sound and Vibration*, 39:1–33, 1975.

[44] U. Ingard and V.K. Singhal. Sound attenuation in turbulent pipe flow. *Journal of the Acoustical Society of America*, 55(3):535–538, 1974.

[45] F. van der Eerden. *Noise reduction with coupled prismatic tubes.* PhD thesis, University of Twente, 2000.

[46] Vakgroep Technische Mechanica. Manual to use the transfer matrix method. 2001.

[47] K.K. Singh, S.H. Frankel, and J.P. Gore. Study of spectral noise emissions from standard turbulent nonpremixed flames. *AIAA Journal*, 42(5):931–936, 2004.

[48] W.C. Stahle. Some results on combustion generated noise. *Journal of Sound and Vibration*, 23:113–125, 1972.

[49] J.C. Lagarias, J.A. Reeds, M.H. Wright, and P.E. Wright. Convergence properties of the nelder-mead simplex method in low dimensions. *SIAM Journal of Optimization*, 9(1):112–147, 1998.

[50] W. Krebs, R. Walterkotter, P. Flohr, P. Walz, and S. Hoffman. Effect of burner design parameters on thermo acoustic stability of annular gas turbine combustor. *Proceedings of ECOS 2000, Biomass, coal oil gasification and acoustic of combustion, University of Twente*, 4, 2000.

[51] A. Linan. The asymptotic structure of counterflow diffusion flames for large activation energies. *Acta Astronautica*, 1:1007, 1974.

[52] J.K. Mason. Cfd model of a parker hanninfin airspray fuel injector. 1997.

[53] P. Wesseling. *Principles of computational fluid dynamics*. Springer-Verlag, 2001.

[54] B.E. Launder and B.I. Sharma. Application of the energy-dissipation model of turbulence to the calculation of flow near a spinning disc. *Letters in Heat and Mass Transfer*, (1):131–138, 1974.

[55] *CFX-5 Manual*. ANSYS-CFX, 2003.

[56] J.B.W. Kok and S.A. Klein. Sound generation by turbulent non-premixed flames: Effect of chemical reaction delay. *Proceedings 6th International Conference On Sound and Vibration*, (ISBN 87-987457-7-8):3385–3392, June 1999.

[57] B. de Jager. *Noise prediction with the TFC combustion model*. Master Thesis, University of Twente, 2002.

[58] J.B.W. Kok and B. de Jager. Modeling of combustion noise in turbulent, premixed flames. *Proceedings of ASME Turbo Expo 2006*, (GT2006-90567), 2006.

[59] S.A. Klein and J.B.W. Kok. Sound generation by turbulent non-premixed flames. *Combustion Science and Technology*, 149:267–295, 1999.

[60] U. Maas and S.B. Pope. Simplifying chemical kinetics: Intrinsic low-dimensional manifolds in composition space. *Combustion and Flame*, 88(239), 1992.

[61] R.L.G.M. Eggels, J.J.J. Louis, J.B.W. Kok, and L.P.H. de Goey. Comparison of conventional and low-dimensional manifold methods to reduce reaction mechanisms. *Combustion Science and Technology*, 123:347–362, 1997.

[62] S.H. Lam and D.A. Gousis. The csp method ofr simplifying kinetics. *International Journal of Chemical Kinetics*, 26:461–486, 1994.

[63] J.B.W. Kok, J.J.J. Louis, and J.H. Yu. The irst model for turbulent premixed non-adiabatic flames. *Combustion Science and Technology*, 149:225–247, 1999.

[64] A.L. Kuhl, J.R. Bowen, J.-C. Leyer, and A. Borisov. *Dynamics of reactive systems*. AIAA, 1988.

[65] J.H. Yu. *On the formation of* NO_x *and CO in turbulent premixed flames*. PhD thesis, University of Twente, 1996.

[66] J.J.J. Louis. *On turbulent combustion of coal gas*. PhD thesis, University of Twente, 1997.

[67] J.J.J. Louis, J.B.W. Kok, and S.A. Klein. Modeling and measurements of a 16-kw turbulent nonadiabatic syngas diffusion flame in a cooled cylidrical combustion chamber. *Combustion and Flame*, 125:1012–1031, 2001.

[68] B. de Jager, J.B.W. Kok, and T.H. van der Meer. Comparison of conventional and low-dimensional manifold methods to reduce reaction mechanisms. *Proceedings of the annual meeting Combustion Institue, Heidelberg*, 2006.

[69] B. de Jager. *Combustion and noise phenomena in turbulent alkane flames*. PhD thesis, University of Twente, 2007.

[70] A. Massias, D. Diamantis, E. Mastorakos, and D.A. Gousis. An algorithm for the construction of global reduced mechanisms with csp data. *Combustion and Flame*, 117:685–708, 1999.

[71] D.G. Goodwin. *Building Cantera 1.7 with visual C++ .NET*. CalTech, 2006.

[72] J.O. Hinze. *Turbulence: an introduction to its mechanism and theory*. McGraw-Hill, 1959.

[73] K. Kohse-Höinghaus. Laser techniques for the quantitative detection of reactive intermediates in combustion systems. *Progress in Energy and Combustion Science*, 20:2003–279, 1994.

[74] A.C. Eckbreth. *Laser diagnostics for combustion temperature and species*. Gordon and Breach Publishers, 1996.

[75] W. Meier. Private communication with wolfgang meier, dlr stuttgart. 2007.

[76] S. Tribuzi. Very rough grid approach for cfd modelling of thermoacoustic oscillations inside an annular premixed combustor. *Proceedings of ASME Turbo Expo 2006*, (GT2006-90055), 2006.

[77] H. Tijdeman. *Voortgezette dynamica - mechanische trillingen*. Twente University, 2000.

[78] R. Rajaram and T. Lieuwen. Parametric studies of acoustic radiation from premixed flames. *Combustion Science and Technology*, 175:2269–2298, 2003.

[79] M. Drabbels, W.L. Meerts, and J.J. ter Meulen. Determination of electric dipole moments and transition probabilities of low-lying singlet states of co. *Journal of chemical physics*, 99(4):2352–2358, 1993.

[80] L. Crocco and S.I. Cheng. *Theory of Combustion Instability in Liquid Propellant Rocket Motors*. Butterworths Scientific Publications, 1956.

[81] L. Crocco. Aspects of combustion instability in liquid propellant rocket motors. part i. *Journal of the American Rocket Society*, 21:163–178, 1951.

[82] L. Crocco. Aspects of combustion instability in liquid propellant rocket motors. part ii. *Journal of the American Rocket Society*, 22:11–26, 1952.

[83] D. Bohn and E. Deuker. Prediction of flame transfer function of non-premixed flames. *Journal of Combustion and Flame*, 1998.

[84] C. Hirsch, D. Fanaca, P. Reddy, W. Polifke, and T. Sattelmayer. Influence of the swirler design on the flame transfer function of premixed flames. *Proceedings of ASME Turbo Expo 2006*, (2005-GT-68195), 2005.

[85] A. Kaszap. *Determination of Burner Transfer Function in the Fuel Supply Line on Turbulent Non-premixed Syngas Flames*. Master Thesis, University of Twente, 2005.

[86] A. N. Lipatnikov and P. Sathiah. Effects of turbulence flame development on thermoacoustic oscillations. *Combustion and Flame*, 142:130–139, 2005.

[87] T.C. Lieuwen. *Investigation of combustion instability mechanisms in premixed gas turbines*. Georgia Institute of Technology, 1999.

[88] S.G.M. Pater, J.B.W. Kok, and T.H. van der Meer. Flame transfer function prediction for non-premixed syngas combustion. *12th International Congress on Sound and Vibration,*, 2005.

[89] H. Herlufsen. *Technical Review - Dual Channel FFT Analysis (Part I)*. Brüel & Kjær, 1984.

[90] W.-S. Choi, J. Kim, Y. Neumeier, and J. Jagoda. Preliminary study of low power plasma radical jet generator for comubustion systems. *Proceedings of ASME Turbo Expo 2006*, (GT2006-91254), 2006.

[91] J.F. van Kampen. Private communication with jaap f. van kampen. 2003-2005.

[92] D.G. Crighton, A.P. Dowling, J.E. Ffowcs Williams, M. Heckl, and F.G. Leppington. *Modern Methods in Analytical Acoustics*. Springer-Verlag, 1996.

Nawoord

Denkend aan Twente zie ik verzamelde pyramides en mastaba's met stompe toppen in de bossen staan, een Campus, waar sport en cultuur al jaren hand in hand gaan .. ..
Een dichter zoals Marsman schuilt er niet in mij. Dat zal voor niemand een verrassing zijn. Dan zou ik ook geen techniek hebben gestudeerd. Maar de goede herinneringen aan Twente, die zijn er zeker wel. Wat een leuke plek om te studeren, te werken en om te wonen. Wat een fijne plek ook, om een proefschrift te schrijven. Echter, dat kun je niet alleen .. ..

Dit proefschrift was er natuurlijk nooit gekomen zonder de hulp van velen. En hoewel ik hiermee het risico loop mensen te vergeten ga ik het toch gewoon doen.
Na het afronden van mijn studie heb ik een aantal sollicitaties gedaan. Maar de mogelijkheid om binnen de academie te blijven greep ik snel aan. Jim, jou wil ik bedanken dat je me de mogelijkheid hebt gegeven te gaan promoveren, voor al je tips en de gesprekken die we gehad hebben. En Theo, ook van jou kreeg het vertrouwen voor een stuk werk van vier jaar. Hartelijk bedankt daarvoor. En ook voor de motivatie, de ideeen en alle andere input die ik nodig had tijdens mijn werk.
De eerste lange periode zat ik bij Jaap op de kamer. Wat ik van jouw allemaal heb geleerd is echt enorm! Super bedankt voor al je uitleg over allerhande theorien en modellen. Naast werk werden er natuurlijk natuurlijk ook andere zaken besproken. Het was altijd erg gezellig vond ik. Ook wil ik je natuurlijk bedanken voor onze ijzersterke samenwerking in het legen van al die pakken chocoladevlokken. Ze staan er nog!
Een van de andere kennisbronnen die ik vele malen heb mogen raadplegen was Bram. Jouw kennis over het CFI model heeft me veel verder geholpen. Dank je wel! Daarnaast was je altijd in voor een praatje over het nieuws, was

je een goede luisteraar in geval van tegenslag en kon ik met jou ook af en toe heel goed lachen.
In het lab ben ik ook door een aantal mensen geholpen. Chris, jou wil ik natuurlijk bedanken voor alle hulp bij het bouwen van de opstelling. Zelfs als ik dacht dat het echt niet meer ging werken, dan kwam het eigenlijk toch gewoon weer goed. Wat jij allemaal kon maken heeft me echt verbaasd. Dank je wel! Eise, je gaf ons altijd veel vrijheid om onze eigen PC te beheren en als het dan een keertje misliep, dan was je altijd bereid even te helpen. Tevens wil ik Willy hier bedanken, want ook jij hebt nog aan mijn opstelling gewerkt. Ook gaf Eddy me altijd goede adviezen op het experimentele vlak. En met Eddy was er altijd vermaak in het lab. Bedankt! Nutte wil ik bedanken voor alle adviezen op gebied van het ontwerpen van mijn opstelling en het bedrijven van de opstelling, heel erg handig!
Voor al die chemiluminiscentie metingen wil ik graag Genie en Ashiq bedanken. Elke stooksessie waren jullie erbij. Ook al die keren dat de opstelling niet deed wat we wilden. Enorm bedankt!
Ook Bert Wolbert verdient een pluim. Zonder problemen kreeg ik elke keer die SigLab kastjes mee, samen met een laptop. Heel erg bedankt, het heeft me waanzinnig veel werk bespaard.
Sally, hoe zou de vakgroep er uitzien zonder jou? Na al die jaren van dienst waren klussen die voor mij veel uitzoekwerk waren voor jou een peulenschil. Bedankt voor alles!
De laatste jaren deelde ik de kamer met Artur. Ook met jou heb ik de nodige discussies gehad en het was altijd gezellig. Bedankt!
Het werk was natuurlijk ook leuk door al die andere AIO's en studenten die er in de loop van de jaren zijn geweest. De koffie- en lunchpauzes, het voetballen (nouja, het lomp en onbenullig tegen een bal trappen), de borrels, de stapavonden, de feestjes, het was altijd onwijs gezellig. Dus, Marcel, Marc, Anton, Maarten, Joost, Michiel, Martin, Maarten, Timo, Uros, Ashiq, Marco, Bogdan, Ziad, Genie, Eddy, Jim, Theo, Sally, Bram, Jaap, Nutte, Artur, Jan, Jimke, Geert, Michiel, Albert, allemaal bedankt!
In parts of the project I cooperated with visitors from abroad. At first, from Hungary, Akos Kaszap did his master thesis in our group. He delivered a nice piece of work. Thanks a lot. In the final year, Ricardo Hernandez, a PhD student from Spain visited us. It was a pleasure to work with you, Ricardo and your delivered very good work. Thank you for both!
Also with the partners I cooperated in a good atmosphere. To specify the burner and other parts of the setup, I worked together with Michael Tsurikov, staff at DLR. I have learnt a lot and have enjoyed it very much. Thanks! But also with the remaining staff from DLR and other project partners I enjoyed

the cooperations. I would like to thank the participating staff from Siemens PG, Ansaldo Energia, Enel Produzione S.p.A. and NUON NV for the good cooperation and hopsitality during the project meetings.
Voor de momenten dat het tegenzat, als ik even geen zin had, trek had in koffie, zin had om even bij te kletsen, te lunchen of trek had in een mensa-hap dan had ik zo mijn vaste klanten. Marten, Roy, Viola en Annelies, allemaal bedankt voor de gezellige tijd in de Horst! Viola wil natuurlijk ook bedanken voor het maken van de foto voor de omslag. Supermooi!
Ook heb ik die laatste jaren heerlijk kunnen genieten van mijn vrije tijd en ontspanning. Dat kwam door iedereen bij DAV Kronos voor de laatste atletiekloodjes. De heerlijke trainingen bij Boksclub Twente. De leerzame repetities en het gezellige naborrelen bij het Binnenstads Jongerenkoor en de heerlijke yogalessen bij Bodywise. Ik heb er echt van genoten, allemaal enorm bedankt!
En dan heb ik nog al die vrienden die er waren in tijden van voor- en tegenspoed. Om mee te eten, om te kletsen, filmpjes te pakken, te sporten, vakantie mee te vieren, om weekendjes weg te gaan, dagjes uit, te zeilen, te skien, te feesten en weet ik wat niet allemaal meer. Ik kan niet anders zeggen: Errug relaxed!
Tot slot natuurlijk het hele gezin Pater. Hoewel we allemaal ver bij elkaar vandaan wonen is het altijd supergezellig als we bij elkaar zijn. Bedankt allemaal, gewoon, voor het „er zijn".

Mijn tijd zit erop in Twente, ik heb er veel geleerd en waanzinnig genoten.
Zie jullie in Utrecht!

Sjoerd
Utrecht, oktober 2007